Yield-stress drops.

Guy German

Ph.D. Thesis

The University of Edinburgh

2009

‘παντα ρει’ Simplicius (490-560 A.D)

‘Some drops splat and some drop squidge
the latter display viscoplasticity,
the regime change, as we show in this work
is the Bingham number times the Capillary’ G.German (2009)

Acknowledgements

My sincerest thanks to Volfango for his invaluable support, insight and guidance through what I hope is to be the fledgling years of my academic career. Thank you also for introducing me to a truly fascinating topic of fluid dynamics. My gratitude goes to the E.P.S.R.C for providing me with a DTA studentship as well as the Royal Society of Edinburgh and the Aerosol society for their financial support in the form of scholarships. Finally thank you to my wife Rosie for all her support. I know you think you deserve a degree for listening to all my engineering talk. I agree, but I hope this recognition will do for starters.

Abstract

The behaviour of viscoplastic drops during formation and detachment from a capillary nozzle, free-fall, impact on a solid substrate and subsequent spreading are investigated experimentally by high-speed imaging. Drop dynamic behaviour is an integral component of many contemporary industrial processes ranging from fuel-injection systems in combustion engines to spray coating, agrochemical and pharmaceutical delivery, fire extinguishment and ink-jet printing. Yield-stress fluids are commonly used nowadays in products ranging from mayonnaise to hair-gel. It is hoped that through understanding the dynamics of viscoplastic fluids, additional spray applications can be developed that will help to advance and optimise industrial processes. Viscoplastic fluids exhibit shear-thinning behaviour when the applied stress exceeds a certain threshold value, called the yield-stress. Below this threshold however, the fluid behaves like an elastic solid. By comparing the behaviour of viscoplastic drops with both Newtonian and shear-thinning fluids, yield-stress is shown to be capable of altering detachment behaviour, drop shape during free-fall, impact morphology and the final sessile shape of drops after spreading. For drops attached to the end of a capillary tube, growth continues until a maximum supportable tensile stress is reached in the drop neck. After this critical point, drops become unstable and detach. The critical break-up behaviour of low yield-stress drops is found to be similar to those of Newtonian and shear-thinning fluids. Above a threshold value however, characterised in terms of the ratio between yield-stress magnitude and capillary pressure, yield-stress forces exceed surface tension forces and the maximum tensile stress achievable in the drop neck at critical stability is governed by the extensional yield-stress, established using the von Mises criterion. This threshold value can also be used to characterise equilibrium drop shapes during free-fall. Whereas Newtonian, shear-thinning and low yield-stress fluids form near spherical equilibrium drop shapes, fluids above a threshold value become increasingly more prolate as the yield-stress increases. Upon impact, viscoplastic drops can exhibit central peaks at the end of inertial spreading. The influence of yield-stress magnitude on impact behaviour is qualitatively established by measuring the size of these peaks. Peaks indicate that deformation during impact is localized and within a threshold radius, shear stresses will not be large enough to overcome the yield-stress, therefore fluid within this region will not deform from the drop shape prior to impact. After impact, spreading will be dependent on the surface energy. Again, the ratio of the yield-stress magnitude to the capillary pressure can be used to characterise the final sessile drop shape. Whilst the equilibrium contact angle of Newtonian, shear-thinning and low yield-stress drops is independent of the yield-stress magnitude, above a threshold value, contact angles vary as a function of yield-stress magnitude. Whilst the research presented in this thesis highlights how fluid yield-stress can influence drop dynamics, some results are only qualitative. To establish more quantitative results, computational fluid dynamics methods should be used to examine viscoplastic drop dynamics. This research should focus primarily on impact behaviour, an aspect that has not received much attention previously. Modelling shear-thinning and viscoplastic fluid behaviour can be achieved by incorporating the relevant rheological models into the flow equations and examining impact morphology using a volume of fluid method. Numerical results can then be directly compared with the experimental results. Useful further experimentation could examine the relaxation behaviour of diamagnetically levitated viscoplastic drops. The results from this work could provide further insight into what rheological model best describes viscoplastic behaviour for shear-stresses below the yield-point.

Table of Contents

List of Tables

List of Figures

Nomenclature

a,n,m,p	exponent coefficients
a	capillary length [m] or [mm]
A_0	capillary tube area [m^2]
A	Cross sectional area [m^2]
A_{wet}	drop wetted area [m^2]
b_n	damping parameter
$\hat{B}$	Bingham-Capillary number
$\hat{B}_E$	extensional Bingham-Capillary number
Bo	Bond number
Bm	Bingham number
C	parameter accounting for surface tension [Nm^{-1}]
Ca	Capillary number
C	Cross time constant [s]
C.M.C	critical micelle concentration [mg/ml]
D(t)	drop diameter [m] or [mm]
D_E	equivalent drop diameter [m] or [mm]
D	strain (symmetric component of the velocity gradient tensor) rate tensors [s^{-1}]
D_0	capillary tube diameter [m]
D_{Max}	maximum inertial expansion diameter [m] or [mm]
D_N	drop neck diameter [m]
$D_{N,crit}$	drop neck diameter at the point of critical breakup [m] *(drop detachment dynamics)*
D_{Peak}	drop peak diameter [m]
$D_{sessile}$	sessile state drop diameter [m] or [mm]
D_{II}	second invariant of the strain rate tensor [s^{-1}]
De	Deborah number
e	drop shape eccentricity *(drop free-fall dynamics)*
E_{ERE}	excess recoil energy [J]
E_g	gravitational potential energy [J]
E_k	kinetic energy [J]
E_σ	surface tension energy [J]
$E_{\sigma,\beta_{Max}}$	surface tension energy at maximum inertial spread [J]
F	force [N]
F_m	surface tension force driving spreading [N]
F_v	viscous braking forces in spreading [N]
g	gravitational acceleration [ms^{-2}]
G	shear modulus [Pa]
h	lamella height [m] (*drop impact dynamics)*
h	height dimension [m]
h_{Max}	maximum drop height after impact [m] or [mm]
h_{min}	minimum drop height after impact [m] or [mm]
h_{rim}	drop rim height [m] *(drop impact dynamics)*

H_f	Fall height [m] or [mm]
$I_n(kR_0)$	modified Bessell function of the first kind
I	unit tensor
k	longitudinal wave number $k = 2\pi/\lambda$ [m^{-1}] (*drop detachment dynamics)*
K	Sping constant [Nm^{-1}]
K	power law model consistency coefficient [Pas^n]
L	drop length [m] (*drop detachment dynamics)*
L	length parameter associated with rim size of rimmed disk model [m] *(drop impact dynamics)*
L_{Crit}	drop height at critical breakup [m] or [mm]
L_{neck}	drop neck length [m] (*drop detachment dynamics)*
n	Power law index
Oh	Ohnesorge number
p	temporal spreading exponent (*Drop spreading dynamics*)
P	pressure [Pa]
Q	volume flow rate [m^3s^{-1}]
r_f	roughness coefficient
R(t)	drop radius [mm]
Re	Reynolds number
Re_c	critical Reynolds number relating to splashing
R_0	capillary radius [m]
R_E	equivalent drop radius [m]
s	empirical term for Attané et al.[48] drop impact prediction model
S	spreading coefficient [Nm^{-1}] (*spreading dynamics*)
S	drop shape factor (*free fall dynamics*)
S_e	equilibrium drop shape factor (*free fall dynamics*)
S_i	initial spreading coefficient [Nm^{-1}]
ST	dimensionless surface tension *(drop impact dynamics)*
t	time [s]
t^*	dimensionless time
t_0	time of detachment [s] (*drop impact dynamics)*
$t(D_{N,crit})$	time prior to pinch off of the critical breakup point [s] *(drop detachment dynamics)*
t_p	observed time scale of an experiment [s]
t_q	quarter wavelength timescale of an oscillating inviscid drop [s]
t_r	relaxation time scale [s]
t_{si}	characteristic timescale of crossover from inertial to capillary spreading regime [s]
T_v	large scale deformation period of a viscous drop [s]
T_I	oscillation period of a perturbed inviscid drop [s]
T_{II}	second invariant of the stress tensor [Pa]
$v_r(t)$	radial velocity [ms^{-1}]
$v_z(t)$	vertical velocity [ms^{-1}]
V_{ideal}	attached drop volume [m^3]
V_f	detached drop volume [m^3]
VIS	dimensionless viscosity term *(drop impact dynamics)*

W_{crit}	drop weight at the critical point of instability [g]
$\dot{W}$	rate of energy loss from viscous dissipation [W]
We	Weber number
We_c	critical Weber number relating to splashing
X	displacement [m]
X	Xanthan gum mass fraction
X_c	length of drop at critical point of instability [m]
Y	hair-gel mass fraction
Z	vertical length along drop [m] *(drop detachment dynamics)*

Greek symbols

$\alpha(t)$	perturbation amplitude [mm]
β	dimensionless Spread factor
β_m	maximum inertial spread factor during inertial spreading
β_{Peak}	measured dimensionless drop peak diameter
$\beta_{Sessile}$	sessile drop spread factor
β_T	predicted dimensionless drop peak threshold diameter
χ	universal scaling parameter for viscous drop detachment
$\dot{\chi}$	retraction rate [s^{-1}] (*drop impact dynamics)*
ρ	fluid density [kgm^{-3}]
Δ	positive parameter introduced by Papageorgiou[23] to control the extent of the similarity region
ε	dimensionless viscosity (*drop free-fall dynamics)*
ε	ratio of viscosity
$\dot{\varepsilon}$	apparent rate of elongation [s^{-1}] *(drop detachment dynamics)*
ζ	tensile stress [Pa] *(drop detachment dynamics)*
ζ_{crit}	critical tensile stress [Pa] *(drop detachment dynamics)*
Σ	stress tensor [Pa]
$\xi(t)$	drop height factor: drop height scaled with respect to D_E
ξ_m	minimum drop height factor during inertial spreading
γ	shear strain
$\dot{\gamma}$	shear rate [s^{-1}]
$\dot{\gamma}_c$	critical shear rate [s^{-1}]
$\dot{\gamma}_{max}$	maximum predicted shear rate [s^{-1}]
κ	empirical term for modified Mao et al.[47] prediction model *(drop impact dynamics)*
κ	normalised time
λ	wavelength [m]
λ_{cr}	critical wavelength defining onset of perturbation instability [m]
μ	fluid viscosity [Pas]
μ_0	zero shear rate viscosity (Cross[129] & Carreau[130] models) [Pas]
μ_∞	inifinite shear rate viscosity (Cross & Carreau models) [Pas]
μ_{wall}	fluid viscosity evaluated at substrate temperature [Pas]

ν	kinematic viscosity [mm^2s^{-1}] or [m^2s^{-1}]
ω_d	natural damped frequency [Hz]
ω_n	drop natural frequency [Hz]
ω_v	viscous growth rate [s^{-1}]
ϕ	dissipation function [$kgm^{-1}s^{-3}$]
Ω	drop volume [m^3]
ψ	ratio of detached to attached drop volume $\psi = V_f / V_{ideal}$ *(drop detachment dynamics)*
ψ	empirical term for modified Mao et al.[47] prediction model *(drop impact dynamics)*
Φ	Harkin and Brown[27] defined parameter $\Phi = R_0 / V_f^{1/3}$
σ	surface tension (subscripts s, l and v are the solid liquid and vapour phases respectively) [Nm^{-1}]
$\sigma_{dyn}(t)$	dynamic surface tension [Pas]
τ	shear stress [Pa]
τ_c	yield-stress magnitude [Pa]
τ_{max}	maximum predicted shear stress [Pa]
$\tau_{1/2}$	Ellis model shear stress at which μ is exactly half of the μ_0 value [Pa]
θ_e	equilibrium contact angle [deg]
θ_a	advancing contact angle [deg]
θ_r	retraction contact angle [deg]
θ_{av}	average apparent angle of contact [deg]

1. Introduction

It is interesting to note how all of us have a relatively good understanding of fluid dynamics and complex fluid behaviour without having studied it in great deal. When we turn on a tap, we expect fluid to flow out in a jet. If we don't turn it off fully, we expect it to drip. When we see raindrops hit the ground, we expect to see them splash or when landing in a puddle, ripples to form. We also know that honey or shampoo will flow differently from water due to increased viscosity. Moreover, we know quite a lot about yield-stress fluids too. Should we knock over a jar of mayonnaise, peanut butter or hair gel on the counter top, we know that unless we are very unlucky, it won't spill because it acts like a solid. We also know that when we rub gel through our hair or spread mayonnaise on our sandwich with a knife it will spread smoothly, like that of a viscous fluid. The really interesting point however is that when we see all these phenomena, oftentimes we don't think about why it is happening.

The research presented in this thesis examines the effects of fluid viscosity, shear-thinning and yield-stress magnitude on drop dynamic behaviour. More concisely, the work examines how changing these rheological properties influences behaviour during the lifetime of a drop; from growth at the end of a capillary tube through detachment, free-fall, impact on a solid surface and subsequent spreading until it reaches an equilibrium state. This work is not only of interest to academia, drop dynamics are integral to many industrial processes such as spray cleaning and painting, ink-jet printing, crop spraying and fire-extinguishment. With advancements in our understanding of complex fluids, many industries have improved and optimized their industrial processes. The work presented in this thesis shows that using a yield-stress fluid as the working medium allows for further control of drop dynamic behaviour. This may be advantageous in further optimizing industrial processes.

This thesis contains 6 chapters, the first of which (**§1)** is a literature review of published research on the behaviour of both Newtonian and complex fluid drops during growth, detachment from a thin nozzle, free-fall, impact and subsequent spreading.

Included in this section is a description of Newtonian and non-Newtonian fluid rheology. Very simply, a shear stress applied to a linearly elastic solid will result in a finite shear strain. When the stress is removed, the solid will return to its original position. For fluids, the application of a shear stress will result in a shear rate within the liquid. This means that when the stress is removed, the fluid will not return to its original position. The ratio of the applied shear stress to the resultant shear rate is constant for a Newtonian fluid, and called the viscosity. The value of the viscosity for non-Newtonian fluids can vary both as a function of time and of the shear rate. Fluids whose viscosities decrease with increasing shear rate are called shear-thinning (with the opposite being shear thickening). Fluids whose viscosities decrease with time when subject to a constant shear rate are called thixotropic (with the opposite being rheopectic). Viscoplastic fluids exhibit both solid like and liquid like states. When subject to a low shear-stress, the fluids act like a linearly elastic solid. When shear-stresses rise above the 'yield point', they typically exhibit shear-thinning fluid properties.

The literature review on complex fluids highlights the significant work completed on viscoplastic drop behaviour, most of which examines high yield-stress magnitude fluids. The work presented in this thesis however explores the territory between the classical Newtonian and fully viscoplastic regimes. It is surprising to note that whilst both Newtonian and viscoplastic regimes are now relatively well understood, the 'grey area' in between has, rather remarkably, been overlooked until now.

Rheological characterisation of the Newtonian, shear-thinning and viscoplastic fluids is presented in **§2**, along with descriptions of the experimental apparatus used for each of the detachment, free-fall, impact and spreading investigations. This chapter also describes specific characteristics of fluid drops such as the average detached drop mass, equivalent spherical diameter and evaporation rate in ambient atomospheric conditions and in the humidity chamber, designed and utilised for the drop spreading study.

Aspects of drop growth and detachment dynamics are considered in **§3.** Both the onset of breakup and detachment dynamics are examined for Newtonian, shear-thinning and viscoplastic fluids. Unlike Newtonian and shear-thinning fluids, where the onset of

breakup occurs at a near constant tensile stress in the neck filament (where flow is nearly purely extensional) irrespective of changes in the viscous fluid properties, we demonstrate that increasing yield-stress magnitude results in a clear increase of tensile stress. We find that this behaviour can be characterised in terms of the extensional Bingham-Capillary number, describing the ratio of extensional yield-stress magnitude to capillary forces. For extensional Bingham-Capillary numbers less than unity (where capillary forces exceed extensional yield-stress forces), Newtonian, shear-thinning and viscoplastic fluids exhibit a near constant tensile stress at the critical point of breakup (although the critical stress will vary with surface tension). For extensional Bingham-Capillary numbers greater than unity, the critical tensile stress varies linearly with (shear) yield-stress magnitude. This relationship closely agrees with the von Mises relationship between shear and elongational yield-stress. Moreover, the intersection of these two regimes occurs at a Bingham-Capillary number close to unity, where yield-stress forces equal surface tension forces. This work may be useful to spray painting and ink-jet printing industries.

Following detachment, drops will undergo a period of free-fall. In this regime, the only forces acting on the drop are those of gravitation, viscosity, surface tension and yield-stress (where present). Directly after detachment, the neck filament remaining attached to the drop is quickly absorbed into initially prolate main body. Depending on the viscous properties of the fluid, drops can exhibit either periodic oscillations or aperiodic relaxation. The dynamic relaxation behaviour of Newtonian drops of varying viscosity is compared with well established theory describing drop relaxation behaviour. Measurements and theory are shown to agree closely. Shear-thinning drops are also compared with the same theory (with the viscosity term in the equations replaced with an apparent viscosity, equal to the consistency coefficient; a term that describes the viscosity of the shear-thinning fluid at very low shear-rates). This comparison qualitatively highlights the shear-thinning nature of the fluids. Fluids exhibiting a measurable yield-stress were found only to exhibit aperiodic relaxation.

In the absence of inhibiting yield-stress forces, both theory and experiment in **§4** show that drops will tend towards a spherical equilibrium shape. Whilst viscous

properties vary the timescale over which equilibrium is obtained, it does not alter the final state. Low yield-stress magnitude fluids exhibit a near-spherical shape in equilibrium, however as yield-stress magnitude is increased, equilibrium drop shapes increase in prolateness (become taller and thinner). We demonstrate that this can be characterised in terms of the Bingham-Capillary number. For fluids with a Bingham-Capillary number less than unity, where surface tension forces exceed yield-stress forces, the final drop shape will be near spherical. For fluids with a Bingham-Capillary number greater than unity, viscoplastic effects dominate and inhibit the formation of spherical drops. As the Bingham-Capillary number is increased in this regime, drops become increasingly more prolate.

Aspects of drop impact on a solid substrate are considered in **§5**. Research can be split into the effects of substrate wettability on impact behaviour and the effects of fluid properties on impact behaviour. This section focuses primarily on the inertial expansion and retraction phase behaviour of drops impacts.

As highlighted in the literature review, substrate wettability has a measurable influence on the impact behaviour of low viscosity Newtonian drops (such as water with μ = 0.001 Pa.s). Increasing the wettability of the substrate decreases the advancing contact angle and increases the maximum drop diameter at the end of inertial expansion. The experimental results presented in this thesis however show that for Newtonian fluids with $\mu \geq$ 0.056 Pa.s, the effect of substrate wettability on impact behaviour is decreased. Inertial spreading on both glass (hydrophilic) and parafilm (hydrophobic) substrates is found to be nearly identical with no significant variation in drop diameter at the end of the expansion phase. This indicates that the difference between impacts on different wettability substrates reduces as fluid viscosity increases. For the shear-thinning and viscoplastic fluids, the maximum diameter at the end of inertial expansion is also the same irrespective of substrate wettability. The effect of substrate wettability on drop impact dynamics can clearly be observed during the retraction phase however; retraction on a hydrophobic substrate is more pronounced in comparison with the hydrophilic surface.

A review of existing drop impact prediction models is also presented within this chapter. This review, whilst not exhaustive, provides an in depth assessment of numerous models, ranging from simple order of magnitude scaling laws to complex models that account for flow physics like flow circulation close to the contact line and lamella rim formation during high velocity impacts of low viscosity drops. Moreover, all models are compared with a standardised set of experimental results; an analysis which has not been done until now. Typically, models predict either the maximum drop diameter or minimum drop height at the end of inertial expansion using dimensionless numbers that describe the impact conditions and fluid properties, such as the Reynolds number, Weber number of Ohnesorge number. These parameters describe the ratios of inertial to viscous forces, inertial to capillary forces and viscous to capillary forces respectively. The more complex models utilising an energy balance approach are found to provide the most accurate predictions, however all models typically show poor predictive capabilities for high viscosity drops at low impact velocities. Empirical modifications were therefore made to the model exhibiting the overall best predictive capability. These modifications were found to significantly improve model predictions of high viscosity, low impact velocity drop behaviour. It is hoped this review will aid industries that use drop impact dynamics as part of their manufacturing process choose a model that can satisfactorily predict drop impact phenomenon without the need for employing complex and time-consuming numerical analyses.

Drop impact behaviour of viscoplastic fluids is also examined in this chapter. Low yield-stress fluids at relatively high impact velocities exhibit qualitatively similar impact behaviour as shear-thinning and Newtonian fluids; forming a thin flat lamella during inertial expansion. In contrast, some high yield-stress fluid drops do not deform fully upon impact and central drop regions (corresponding to the upper prolate drop region prior to impact) can exhibit a characteristic peak. This suggests that deformation is localized and will only occur in regions where shear-stresses exceed the yield-stress magnitude. Based on this hypothesis, an equation is derived that predicts the ratio of peak diameter to maximum impact diameter. This equation assumes that there is a stagnation point in the drop centre during deformation and the radial velocity varies linearly from zero at the drop centre to a maximum at the drop edge. Experimental results agree

reasonably well with this theory. It is hoped that this research may be of use in new paint-spraying, microlens or ink-jet technologies, where more control of impact behaviour can be achieved by using a viscoplastic fluid.

Dynamic and static aspects of drop spreading on a solid substrate are finally considered in **§6**. Unlike Newtonian and shear-thinning drops, whose final shape after impact varies both with the surface tension and the wettability of the substrate but not with the impact velocity (drops of an identical Newtonian or shear-thinning fluid impacting at different velocities will exhibit the same shape in sessility), viscoplastic drops in sessility change shape with surface tension, substrate wettability, impact velocity and yield-stress magnitude. For low yield-stress fluids, final diameters and equilibrium contact angles are similar irrespective of impact velocity. For larger yield-stresses, the final diameter and equilibrium contact angle vary with impact velocity. This behaviour can again be characterised by the Bingham-Capillary number. For fluids with a Bingham-Capillary number less than unity, yield-stress effects are small and capillarity dominates. In this regime, the equilibrium contact angle does not vary significantly with yield-stress magnitude or impact velocity. Above unity however, yield-stress forces exceed those arising from surface tension. In this regime, we show the equilibrium contact angle increasing linearly as a function of yield-stress magnitude. Moreover, we demonstrate that fluid yield-stress inhibits retraction and spreading on hydrophobic and hydrophilic substrates respectively. Changing the yield-stress magnitude thus alters the amount that spreading can be inhibited. It is hoped that this control of final drop shape may be of use in paint spraying or ink-jet printing technologies to optimize coating processes.

1.1 Literature Review

The study of yield-stress fluid drops combines the well established research discipline of drop dynamics with complex fluid rheology. The study of drop dynamics is not only an interesting free-boundary fluid dynamics problem, it is also an integral component of many contemporary industrial processes ranging from carburettors and fuel-injection systems in combustion engines to spray cooling[1] and coating[2] processes, agrochemical[3] and pharmaceutical delivery[4], fire suffocation/extinguishment[5,6] and ink-jet printing[7,8]. Yield-stress fluids are commonly used nowadays. Products range from ketchup and mayonnaise to hair-gel and offshore drilling mud. Moreover, they are also truly nature-inspired; their use is integral in gastropod locomotion, allowing snails and slugs to crawl up walls[9]. It is hoped that through understanding the dynamics of complex liquids such as yield-stress fluids, additional spray and atomisation applications can be developed that will help to advance and optimise industrial processes.

Historically, the implementation of drop dynamics in industry is well established; one of the most common examples is lead shot towers used in the manufacture of shot-gun pellets. The first lead shot tower was built in Bristol in 1782 by William Watts. The process involved molten lead being dripped through a copper sieve at the top of a tall tower and allowed to form a spherical shape during free-fall through capillary action before being caught in a water basin at the base. Figure [1] displays the famous '*Opening of Waterloo Bridge 1832'* by John Constable that now hangs in the Tate gallery. The two shot towers, built in 1789 and 1826 can be seen to the right of St Paul's cathedral in the background towards the right of the picture.

The study of drop dynamics however dates back considerably farther. Leonardo da Vinci first recognised in the Codex Leicester[10] that the detachment of drops is governed by competition between cohesive surface tension forces and gravity. Since then, significant research has been performed and a good understanding of drop dynamic behaviour has been achieved. There are however numerous areas in which further studies are needed in order to advance our current understanding.

Figure 1. *'Opening of Waterloo bridge 1832'* by John Constable. The painting shows the two shot towers to the right of the picture (to the right of St Paul's cathedral). The inset image shows a blow-up of the shot-towers.

Drop dynamics in a low density environment such as air is both complex and varied. Behaviour will vary with the properties of the fluid, the substrate characteristics that the drop impacts or spreads on, environmental conditions such as air pressure and temperature and experimental properties such as the drop size and fall height. Typically however, drop dynamics can be separated into four distinct phases; drop detachment, free-fall, impact and subsequent spreading. These phases are displayed in Figure [2] and will here be considered separately.

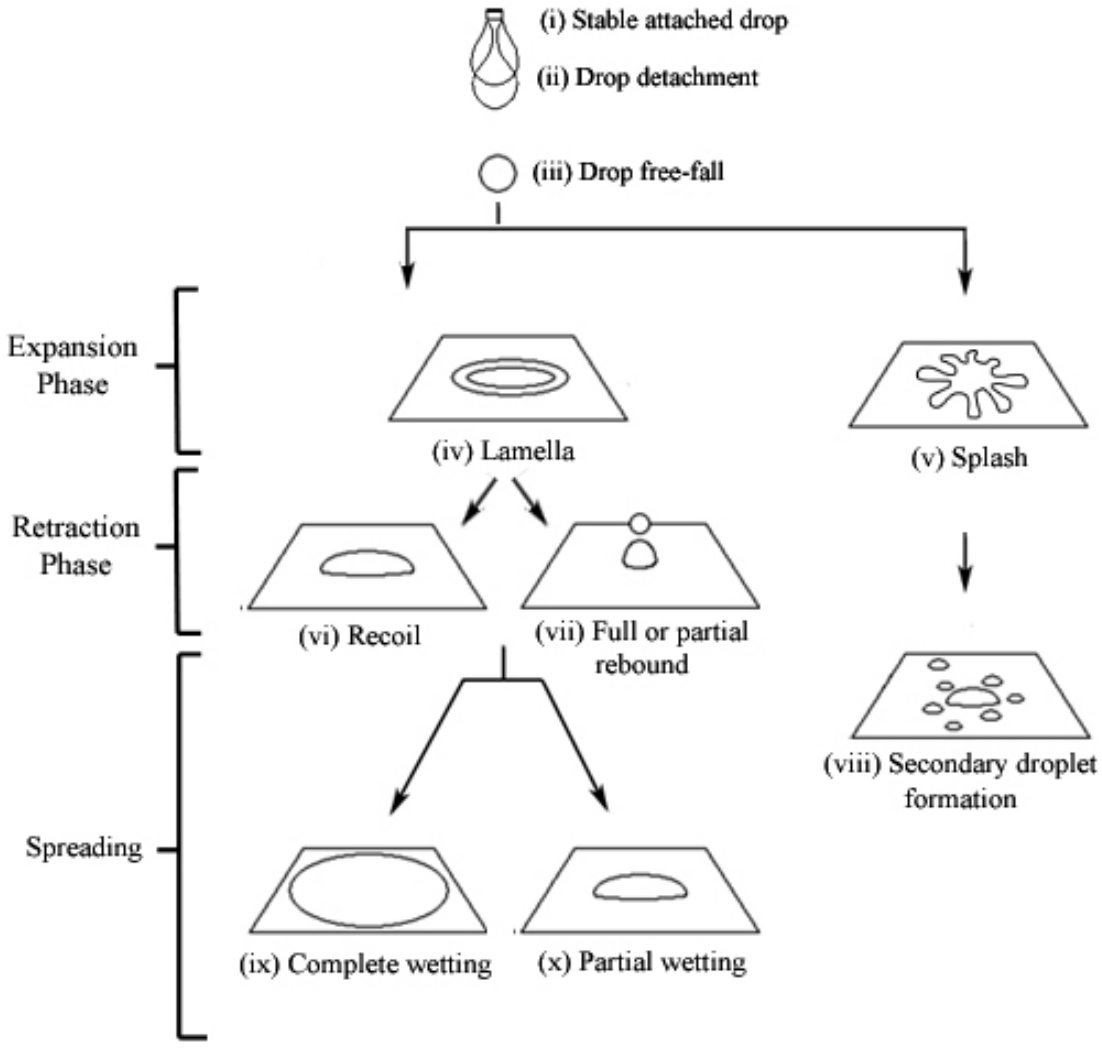

Figure 2. Generalised characteristics of drop dynamics from detachment through to sessility.

1.1.1 Newtonian drop growth, stability and detachment behaviour.

Whereas daVinci correctly established that the detachment of drops is governed by competition between cohesive surface tension forces and gravity, he incorrectly[11] assumed that it is gravity itself that governs the separation process. It was Laplace[12] and Young[13] who first recognized the crucial role of mean curvature; a combination of the axial and radial curvature. They found that once a cylindrical shape is reached in a hanging drop, it is the radial curvature, not the gravitational force that drives the breakup.

This describes a system that is driven towards a state with a smaller surface area once a critical point of stability is reached.

The role of surface tension in breakup was recognized experimentally by Savart[14], who noted that in jets, breakup occurred independently of any external force or the direction in which the jet was projected, thus negating the influence of gravity as the cause of breakup. Plateau[15], in observing the decay of fluid jets traveling through a medium of the same density recognized that perturbations would become unstable if their wavelength λ was greater than a critical value $\lambda_{cr}/R_0 = 2\pi$, corresponding to a decrease in the surface area. The wavelength corresponding to the fastest breakup was however found to be $\lambda_{opt}/R_0 = 8.76$, significantly higher than the critical value, where R_0 is the capillary tube radius. Upon introducing his method of linear stability, Rayleigh[16] recognised that the dynamics of the jet had to be taken into account. He determined that for all unstable wavelengths with $\lambda > \lambda_{cr}$, the one with the fastest growth rate is selected. For inviscid jet dynamics, he found $\lambda_{opt}/R_0 = 9.01$, in close agreement with Plateau.

Rayleigh's linear stability method (henceforth denoted as LSM) established that an initial disturbance in a jet will exhibit an exponential growth with a perturbation amplitude, α, of the form:

$$\alpha(t) = \alpha_0 e^{-i\omega t} \qquad [1]$$

where the inviscid dispersion relation is given by:

$$\omega^2 = -\frac{\sigma}{\rho R_0^3}(kR_0)\left[1-(kR_0)^2\right]\frac{I_1(kR_0)}{I_0(kR_0)} \qquad [2]$$

and ω(k) is the growth rate. In Equation [2], σ is the surface tension, k is the longitudinal wave number, ρ is the fluid density and $I_n(kR_0)$ is a modified Bessel function of the first kind. The largest growth rate occurs at $kR_0 = 0.697$, which corresponds to $\lambda_{opt} = 9.01R_0$ ($k = 2\pi/\lambda$). This however does not account for viscous effects. The effects of viscosity on capillary breakup were first investigated by Plateau[15] and Weber[170]. Plateau found

viscosity to play an important role in the growth rate of instabilities. As described by Eggers[17], Plateau found that as viscous forces become increasingly dominant with respect to inertial forces, the most unstable wavelength increases; corresponding to the greatest reduction in surface area. The growth rate is eventually determined by a balance between surface tension and viscous forces, most simply characterised by the Reynolds number $\mathrm{Re} = \rho v_z D_0 / \mu$, where μ is the fluid viscosity, v_z is the vertical velocity and D_0 is the capillary diameter. Chandresekhar[18] analysed the problem using the full Navier-Stokes equations and found a complicated implicit equation that in the limit of both small kR_0 and Re can be given by:

$$\omega = \omega_0 \left(\left[\frac{1}{2} x^2 (1 - x^2) + \frac{9}{4} \mathrm{Re}^{-2} x^4 \right]^{1/2} - \frac{3}{2} \mathrm{Re}^{-1} x^2 \right) \qquad [3]$$

where $x = kR_0$. The viscous dispersion relation for the fastest growing mode is given by:

$$\omega = \frac{1}{6} \omega_\nu \left(1 - kR_0 \right) \qquad [4]$$

where $\omega_\nu = (\sigma / R_0 \rho \nu)$ is the viscous growth rate[17] and ν is the kinematic viscosity. Experimental comparisons[19,20,21] show a good agreement with Chandrasekhar's theory with the exception[21] of low viscosity fluids with $\nu < 100$ $\mathrm{mm^2 s^{-1}}$, where significantly lower growth rates than Equation [4] are observed. Rothbert et al.[21] conclude that this is due to the omission of gravitational effects in the derivation of Equation [3]. This suggests that whilst gravity is not the cause of breakup, it has an influential role in detachment dynamics. This influence becomes increasingly more apparent as fluid viscosity decreases.

It has been well established[11,17.22] that in regions close to drop pinch-off, the classical LSM breaks down and the fluid behaviour enters a regime of self-similar flow, wherein flow lacks a typical scale and the balance of inertial, surface tension and viscous forces become independent of the minimum thickness of the neck filament attaching the

falling drop to the capillary. In other words the flow dynamics of viscous fluids in this regime can be characterised by universal scaling functions. In the last stages of detachment, viscous fluid drops can exhibit long and thin threads. Papageorgiou[23] established that after the breakdown of the LSM, the fluid enters a regime of viscous dominated self-similar Stokes flow. Temporal variations in minimum axisymmetric drop neck thickness vary as:

$$D_N\big|_{Stokes} = \chi \frac{\sigma}{\upsilon\rho}(t_0 - t) \qquad [5]$$

where χ = 0.0709 is the established universal scaling function determined from $\chi = 1/12(1+\delta)$ and δ = 0.175 is a positive parameter introduced by Papageorgiou to control the extent of the similarity region. This was found to show a good agreement with experimental results[21]. Whereas the self-similar Stokes flow regime is valid when viscous effects dominate over inertial forces, as the detachment process reaches near pinch off, inertial effects cannot be ignored due to increasing flow velocity inside the filament. Here the Stokes flow regime breaks down. A second regime of inertial-viscous flow arises that requires a solution using the full Navier-Stokes equations. This was investigated by Eggers[22], who established an identical relationship to that given in Equation [5] only with a universal scaling function of χ = 0.0304. Subsequent experimental measurements[21,25] show a good agreement with this value.

Zhang and Basaran[33] describe well the influence of fluid surface tension and viscosity on growth and detachment characteristics of drops. The major role of surface tension is to govern the volume and shape of the drop. Increasing the surface tension enforces a growing drop to remain more spherical during the first stages of growth and increase the volume of the detaching drop. As the drop grows however, gravitational forces will eventually become influential. This can be considered in terms of the Bond number $Bo = \rho D^2 g/\sigma$, which characterises the ratio of gravitational to surface tension forces. As the drop grows in size, the initially small Bond number will increase and eventually, gravitational forces will dominate over surface tension forces. As the drop volume become sufficiently large, the drop weight causes deformations in the drop neck.

These surface deformations become unstable and the drop subsequently detaches due to capillarity.

Fluid viscosity influences the stability of growing drops, making it possible to achieve larger drop elongations during detachment by damping oscillations in the liquid surface, however it has no influence on detached drop size. This can be considered in terms of the Capillary number $Ca = \mu Q/A_0\sigma$, where Q is the volume flow rate and A_0 is the capillary tube area. This dimensionless number characterises the ratio of viscous to capillary forces. For vanishingly small Capillary numbers in Newtonian fluids, where the growth rate is small or the drop is quiescent, the ratio of viscous to capillary forces is also near zero. For larger Capillary numbers, corresponding to increased flow rates or flow in the filament of detaching drops, viscous effects will become more dominant. In other words, whilst the viscous characteristics of fluids influence the growth and detachment dynamics of drops, they do not influence stability characteristics since they are proportional to the rates of deformation[11].

After pinch-off of a drop, the majority of liquid will be contained in the detached portion, however a small percentage will remain attached to the end of the capillary. In his formulation of a drop weight method to predict fluid surface tension, Tate[26] correctly assumed that the drop weight W_{crit} at the critical point of instability will equal the cohesive surface tension forces, such that:

$$W_{crit} = \rho g V_{ideal} = 2\pi R_0 \sigma \qquad [6]$$

He incorrectly assumed however that all of the fluid in the hanging drop would detach. This approximate force balance is now known as Tate's law. Harkins and Brown[27] (henceforth denoted as HB) developed this theory and through careful experimentation, established a relationship between maximum attached drop volume and the combined volume of the detached primary and satellite drops over a range of R_0. The method relates the attached drop volume V_{ideal} to the detached drop volume V_f (where $V_f < V_{ideal}$) via a master curve of ideal volume fraction $\psi = V_f / V_{ideal}$ plotted against

dimensionless tube radius $\Phi = R_0 / V_f^{1/3}$. Once V_f and Φ are established, the surface tension is readily calculated from determining ψ from the master curve and using $\psi = \rho g V_f / 2\pi R_0 \sigma$. Wilkinson[28] later extended the HB master curve ($0.25 \leq \Phi \leq 1.6$) to encompass much smaller nozzle radii ($0.05 \leq \Phi \leq 0.25$). Figure [3] displays the HB master curve for the combined range from Harkins and Brown and Wilkinson. A theoretical understanding of the HB master curve has been proposed and developed by both Rayleigh[29] and Ferguson[30], however only recently have the effects of flow rate and viscosity been included[31], based on one dimensional slender jet approximation of the Navier-Stokes equations[32].

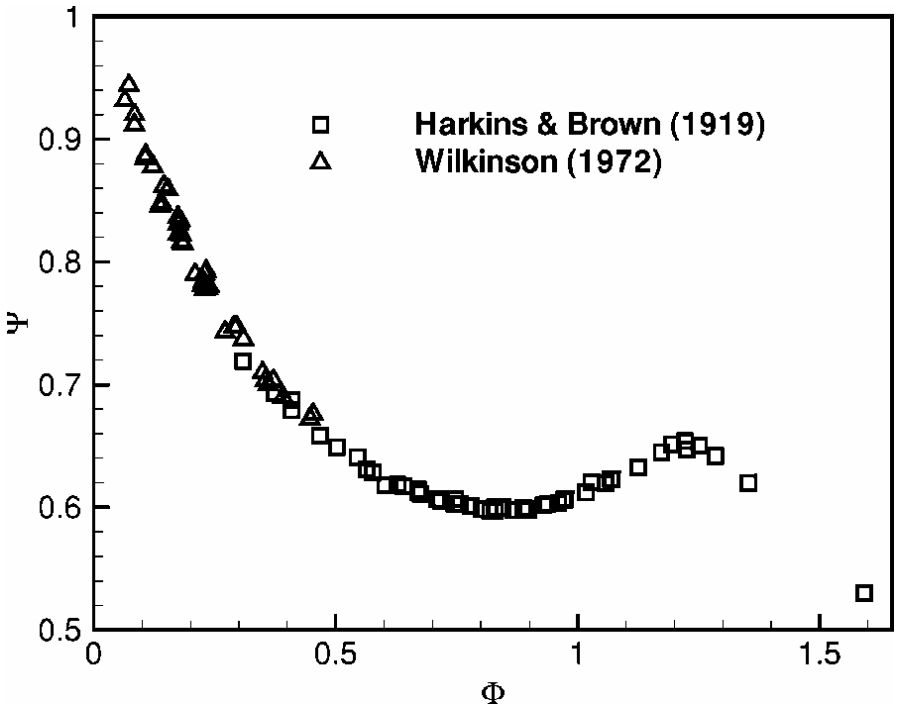

Figure 3. Harkins and Brown[27] master curve (open square symbol) overlaid with the extended results from Wilkinson[28] (open triangle) extracted from Yildrim et al.[31]: Ideal volume fraction ψ plotted against dimensionless capillary tube radius Φ.

1.1.2 Newtonian drop dynamics during free-fall

The dynamics of drops in free-fall have been examined in general by Kelvin[34], Lamb[35] and Chandrasekhar[18] and specifically for applications such as spray cooling[1] and nuclear physics[36]. At pinch-off, drops will typically be non-spherical. This induces an

inertial forcing term that can induce small-amplitude oscillatory behaviour about a spherical shape (surface tension drives a drop in free-fall towards a spherical shape to minimise surface area). A free-falling drop will be subject only to gravitational, capillary and viscous forces. When viscous effects cannot be neglected, additional damping effects must be considered. Prosperetti[37] highlights that through varying the fluid properties, drop dynamic behaviour will change.

The motion of drops in free-fall is analogous to a spring-dashpot system, with the spring constant k and displacement x from Hooke's law (F = -kx) related to the surface tension and the dashpot damping coefficient related to the viscosity of the fluid. The characteristics of liquid drop motion falling through a host liquid were established theoretically by Prosperetti in terms of a drop natural frequency ω_n and a damping parameter b_n. For an underdamped system, the equation of motion is:

$$\ddot{x} - 2b_{n0}\dot{x} + \omega_{n0}^2 x = 0 \qquad [7]$$

where:

$$\omega_{n0}^2 = n(n-1)(n+2)\frac{\sigma}{\rho R_E^3} \qquad [8]$$

is the natural frequency; consistent with that derived by Lamb[35].

$$b_{n0} = (n-1)(2n+1)\frac{\mu}{\rho R_E^2} \qquad [9]$$

is the damping parameter. Solving for x with n = 2 (the most common mode of vibration) results with:

$$x(t) = e^{-b_{n0}\omega_{n0}t}\left(A\cos(\omega_d t) + B\sin(\omega_d t)\right) \qquad [10]$$

where $\omega_d = \omega_{n0}\sqrt{1-b_{n0}^2}$ is the natural damped frequency, A = x(0) and $B = \left(b_{n0}\omega_{n0}x(0) + \dot{x}(0)\right)/\omega_d$. For an overdamped system this becomes:

$$x(t) = Ae^{\gamma_- t} + Be^{\gamma_+ t} \qquad [11]$$

where $\gamma = \omega_{n0}(-b_{n0} \pm \sqrt{b_{n0}^2 - 1})$, $A = 2x(0) - [\gamma_- x(0) - \dot{x}(0)]/[\gamma_- - \gamma_+]$ and $B = [\gamma_- x(0) - \dot{x}(0)]/[\gamma_- - \gamma_+]$.

Below a critical damping condition, drop motion will exhibit a damped periodic motion; above this limit the motion will be aperiodic. In either case the final equilibrium state will be spherical. The size and temporal shape of drops exhibiting oscillations during free-fall were characterised by Ford and Furmidge[53] in terms of an equivalent spherical radius and a drop eccentricity e = H(t)/D(t). Typically for water drops, the eccentricity varies in the range $0.8 \leq e \leq 1.2$.

Prosperetti established that the initial and asymptotic frequencies of the drop vanish for $\varepsilon = 2\sqrt{2}/5 \approx 0.5657$ and $\varepsilon \approx 0.7665$ respectively, where:

$$\varepsilon = \nu\left(\frac{\rho}{R_E \sigma}\right)^{1/2} \qquad [12]$$

is the dimensionless viscosity. This corresponds to a transition from periodic to aperiodic decay, equivalent to going from an underdamped to an overdamped system. The two values indicate that it is possible for the motion to start out as an aperiodic decay and to evolve into a periodic oscillation by way of the large velocity gradients in the initially irrotational flow being transformed to flow circulation within the drop. Ultimately however, no periodic oscillations are predicted for fluid drops with $\varepsilon > 0.7665$.

1.1.3 Newtonian drop impact dynamics

Research into drop impact behaviour dates back to Osbourne Reynolds[38] (who established that vortex rings produced by raindrop impacts on water transport liquid well

below the surface and thereby damp wave motion) and pioneering work by Worthington[39], who observed the phenomenon of rebound during milk drop impacts on a smoked glass plate. Whilst Worthington achieved sharp photographic images by illuminating the impacting drops with electric sparks; from which he was able to achieve exposure times of a few microseconds, it was not until Edgerton[40] established a stroboscopic photography method and observed milk drop splashes on a solid surface that a greater understanding of drop impact dynamics was achieved. Not only did his work provide a fascinating insight into high-speed impact events, his photographic method also paved the way for more quantitative studies of drop impact behaviour.

Drop impacts are complex and will vary with impact velocity[41-62], drop size[47,62,63] the rheological properties and surface tension characteristics of the liquid[43,45-49,57-70], the inclination[65,71] and type of substrate (surface roughness[47,72,73] and wettability[47,65,74] or rheological properties of the liquid substrate), type of thermal effects such as substrate [6,42,75-79] and liquid[80-82] temperature, non-isothermal effects such as evaporation or liquid solidification rates[79,81,82] and environmental conditions such as air pressure[83]. Furthermore, impacts can occur on liquid surfaces (both thin liquid films[14,57,84] and deep pools of fluid[14,57,85]), solid surfaces[57] (both unyielding and yielding; flat, curved or surfaces of only a finite size[86]), porous surfaces[87] and granular surfaces[88]. Rioboo et al.[89] classifies 6 types of differing morphologies of drop impact on a solid substrate: *deposition, prompt splash, corona splash, receding break up, partial rebound* and *full rebound*.

Previous research into drop impact dynamics is both extensive and diverse, as highlighted by the numerous review papers on the topic; each of which focus on different drop impact aspects. Yarin[62] and Rein[57] review the behaviour of drops impacting on thin films of liquid as well as on solid surfaces. Topics that are reviewed include the examination of normal and oblique impacts, conditions for the onset of splashing and shock wave transmission during the early periods of inertial impact on solid substrates. For liquid substrates, Prosperetti and Oguz[85] and Rein[57] review drops impacting into deep liquid pools, where liquid motion is not constrained and the velocities of impacts are large enough to cause the pushing apart of significant liquid mass under the location of

impact. These reviews also examine liquid drop bouncing, coalescence, floating, splashing, jet formation, gas bubble entrainment and vortex ring behaviour. In addition to experimental research, extensive theoretical studies into drop impact behaviour have also been completed. Rein, Healy et al.[74] and Attané et al.[48] all review existing models that predict the maximum inertial diameter reached from impacting drops on solid substrates during the inertial expansion phase. Each of these reviews however is not exhaustive and provides only a limited selection of all the published models. Moreover, the reviews by Rein and Healy et al. examine only models prior to 1995; significantly more of which have been proposed since.

In order to limit the review to research more relevant to this thesis, we consider only drops impacting on dry, flat, horizontal and unyielding surfaces. This reduces the experimental variables to those of drop size, impact velocity, substrate wettability, substrate roughness, temperature and pressure characteristics and the rheological properties of the impacting liquid drop. Each of these variables will subsequently be considered separately.

There are a number of important dimensionless numbers that govern drop impact dynamics. These are:

$$We = \frac{\rho . D_E . v_z^{\,2}}{\sigma} \qquad [13]$$

$$\mathrm{Re} = \frac{\rho . D_E . v_z}{\mu} \qquad [14]$$

$$Ca = \frac{v_x . \mu}{\sigma} \qquad [15]$$

$$Oh = \frac{\mu}{(\rho . \sigma . D_E)^{1/2}} = \frac{We^{1/2}}{\mathrm{Re}} \qquad [16]$$

where D_E and v_z are the drop diameter and vertical velocity prior to impact respectively. v_r corresponds to the horizontal velocity; in terms of drop impacts, this corresponds to the axisymmetric radial velocity. We, Re, Ca and Oh are the:

- *Weber number*, characterising the ratio of inertial to capillary forces.
- *Reynolds number*, characterising the ratio of inertial to viscous forces.
- *Capillary number*, characterising the ratio of viscous to capillary forces and redefined here in terms of the radial velocity.
- *Ohnesorge number*, characterising the ratio of viscous to capillary forces in terms of the drop size.

A drop impacting on a solid surface will in general have two distinct dynamic regimes; an inertial expansion stage and a retraction stage. During the inertial expansion stage, a drop will impact on a surface and deform. Most of the inertial energy will be converted into capillary energy via the creation of new surface regions. Some energy however will remain in the form of flow recirculations[44] close to the contact line of the drop and some will be lost due to viscous dissipation[42,43,46,47]. Drops during inertial expansion can also splash and form secondary droplets[57,84,89]. For impacts where this does not occur, the inertial expansion phase ends when deformation due to inertial forces ceases and a maximum diameter is reached (although this is not necessarily the maximum drop diameter when considering subsequent spreading on wettable surfaces). This typically occurs very quickly; of the order of 3-8 milliseconds and can be characterised by the Weber number (Equation 13).

1.1.3.1 Influence of drop size

Whilst drop size will significantly influence drop impact dynamics, its effect can be eliminated from analyses by way of scaling dimensional parameters with respect to the drop size prior to impact and plotting these against Re, We or Oh, whose terms are directly related to maximum spread and rebound and incorporate the drop diameter D_E[42,47]. Reducing the drop size will therefore reduce both Re and We and increase Oh. Drop impact behaviour will not be identical for all drop scales. An upper limit can be defined in terms of the capillary length[90], a, where:

$$a = \sqrt{\frac{\sigma}{\rho g}} \qquad [17]$$

A drop with $R_E \leq a$ can be considered to be a low Bond number surface, where gravitational effects will not be dominant. A sessile drop on a solid surface will therefore take the shape of spherical cap; the solution to the Young equation with gravity absent (Equation 26). Drops with radii R_E greater than the capillary length will therefore differ increasingly from typical impact behaviour.

1.1.3.2 Influence of impact velocity

The variable that most significantly influences drop impact dynamics is the impact velocity, based primarily on its square proportionality to We (Equation 13) and linear proportionality to Re and Ca (Equations 14 and 15). At low We, drop deformation and hence the maximum inertial impact diameter will also be small. Deformation will increase with We, eventually taking on a thin flat disk shape called a *lamella.* Drop shape is usually characterised in terms of the dimensionless diameter $\beta = D/D_E$ and apex height $\xi = H/D_E$, where D_E is the equivalent diameter of a drop during free fall based on drop weight measurements (see **§2.4)** and D and H are the measured drop diameter and height. Not only does the maximum spread factor $\beta_m = D_{Max}/D_E$ increase[42,47] and minimum apex height factor $\xi_m = h_{Min}/D_E$[72] decrease as a function of increasing impact velocity, the period of deformation will also decrease[72]. Loehr[93,57] established that the impact behaviour of drops of different viscosities over the range $200 \leq We \leq 1500$ and $4200 \leq Re \leq 19700$ was consistent with $\beta(\kappa) = 1 - \exp(-c\,\kappa)$, where $\kappa = 2tu_z/D_E$ is the normalised time and c is a non-dimensional parameter that accounts for influential variables such as surface tension. Chandra and Avedisian[42] confirmed this relationship by comparing their results of β with both numerical[94] and analytical[95] results and established that as long as β was small, the spreading process would be independent of viscosity and surface tension effects.

At sufficiently high impact velocities, radial arms will begin to form at the edge of spreading drops. As the velocity increases further, the radial arms become more prominent and elongated. Eventually splashing occurs through pinch-off in the arms, forming secondary droplets. The splashing threshold is determined as the condition at which transition from spreading to splashing takes place; a drop is said to splash whenever it forms two or more secondary droplets after impact. Levin and Hobbs[96] and Stow and Stainer[97] recognised the importance of inertial forces on drop impact dynamics by observing that drop splash is promoted by increasing impact velocity and drop size. A critical Weber number We_c is often used to report where splashing begins[57], however this parameter is not the sole defining parameter and the threshold will depend on other fluid and surface properties. Stow and Hadfield[41] established the splashing/deposition limit as:

$$Re_c^{0.31} We_c^{0.69} = \Xi \qquad [18]$$

where Ξ is the splash deposition value; a parameter dependent on the surface roughness.

For non-splashing dynamics, the contact angle (Figure 4) that drops make with the surface will vary during impact. During inertial spreading, the advancing contact angle θ_a will be large (typically > 90^o). Dynamic contact angles are known to increase with the velocity of a moving solid–liquid–air contact line. Elliot and Riddiford[92] measured the dynamic contact angles in liquid flow between two parallel plates, and found that they increased linearly with contact line velocity until finally an upper limiting value of θ_a was reached. Contact angles were then independent of further increases in velocity. Pasandideh-Fard et al.[43] made identical conclusions when measuring the dynamic contact angle during drop impacts.

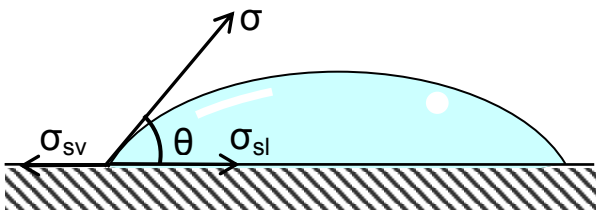

Figure 4. Measurement of dynamic contact angle

At the end of the expansion phase, surface tension forces can induce recoil. Before this however, non splashing drops will undergo contact angle hysteresis. The drop diameter remains constant whilst contact angles decrease to a minimum called the receding contact angle θ_r (where $\theta_r < \theta_a$). This hysteresis is well established and reviewed[53,91]. Subsequently, a number of processes can occur. Drops can either retract whilst adhering to the surface or rebound either partially or fully from the surface[57,62] (Figure 2). Impact velocity will affect retraction phase dynamics; increasing the impact velocity will result in increased deformation and thereby, the maximum energy available for recoil, however this excess energy will also be reduced from increased viscous dissipation attributed to shear-stress at the wall on the (larger) area of solid-liquid contact[47]. It is not only the balance of these factors that controls retraction phase behaviour, the wettability of the surface[47,57], viscosity[47,49,71] and surface tension of the fluid[49,61,65] have all been shown to be influential.

When drops do not rebound there can be multiple spread and retraction phases[47,49], each with diminished height and diameter oscillations due to damping by viscous dissipation. Drop height oscillations can continue well after oscillations in diameter cease and the drop contact line with the surface becomes fixed. It should be noted that contact angle hysteresis will occur in between each subsequent spread-recoil phase, although with a diminished variation between θ_a and θ_r. Van Dam and Le Clerc[8] established the oscillation period of water drop spread-retraction oscillations to be well represented by:

$$T = \sqrt{\frac{\rho D_E^3}{6\sigma(1-\cos(\theta_{av}))}} \qquad [19]$$

where θ_{av} is the time averaged contact angle. This prediction was established by fitting experimental drop height measurements with a function of the form $h(t) = \varsigma_0 + \varsigma_1 e^{-\varsigma_2 t} + \varsigma_3 e^{-\varsigma_4 t}\cos(\varsigma_5 t + \varsigma_6)$. For complete rebounds, Biance et al.[100] recognised that capillary forces driving the retraction must exceed the drop weight. Moreover, they analogise the drop after detachment to that of a system comprised of two

equal point masses (of half the mass of the drop each) joined by a spring, whose spring constant k is a function of the surface tension. Their expressions for drop dynamic behaviour were found to be in good agreement with the experimental findings.

1.1.3.3 Influence of fluid viscosity

The influence of fluid viscosity μ on impact behaviour is commonly reported in terms of Oh or Re, where increasing μ corresponds to an increase in Oh and a decrease in Re respectively. Increases in viscosity decrease the maximum inertial spread factor β_m[42,47,61] and increase the minimum apex drop height factor ξ_m[49]. During the early period of inertial spreading, where inertial forces will be much larger than the viscous forces (high Re), spreading rates are independent of fluid viscosity drops. As the drops approach their maximum spread however and spreading slows (decreasing Re), viscous effects will play a more dominant role[47,61] and the spreading rates will reduce as a function of increasing viscosity. At higher viscosities, drops at maximum spread will not only have less excess surface energy available for retraction, the excess energy must overcome higher viscous dissipation during recoil. The tendency for recoil/rebound is therefore reduced.

There have been a number of studies into the effects of fluid viscosity on retraction dynamics. Bechtel et al.[49] established that increasing the viscous dissipation arising during spread-recoil oscillations (by increasing Oh) increases the damping of the oscillations. This research highlights the well established notion that increased energy dissipation results from larger fluid viscosities.

A later experimental investigation of fluid drops with $0.001 \leq \mu \leq 0.205$ Pas by Bartolo et al.[98] confirmed that the maximum retraction rate after β_m is reached is independent of the impact velocity for strong enough impacts with $We > 10$, $Re > 10$ (characterising inertial forces at least an order of magnitude larger than both capillary and viscous forces). This research also noted the existence of two distinct retraction regimes. For $Oh \leq 0.05$, characteristic of low viscosity fluids, retraction rates were found to be

independent of μ and proportional to the inverse of the capillary oscillation period of a perturbed inviscid drop, $T_I = (4\pi\rho R_E^3/3\sigma)^{1/2}$. For Oh > 0.05, retraction rates were found to decrease significantly with increasing Oh and to be proportional to the inverse of a large scale deformation period of a viscous drop, $T_v = \mu R_E/\sigma$.

Whereas significant experimental research has been completed on low viscosity drop impact behaviour at moderate and high We, research into low We, high Oh drop impacts is limited. Typically for high We impacts or for fluid drops with low viscosities, deformation is significant and can be approximated by a thin flat cylinder. In some high velocity impact cases the lamella may be bounded by a toroidal rim. In contrast however, for low We impacts or for fluids with a relatively high viscosity, a cylindrical approximation becomes invalid and impacting drops show deformations similar in shape to that of a spherical cap[49], as shown in Figure [5].

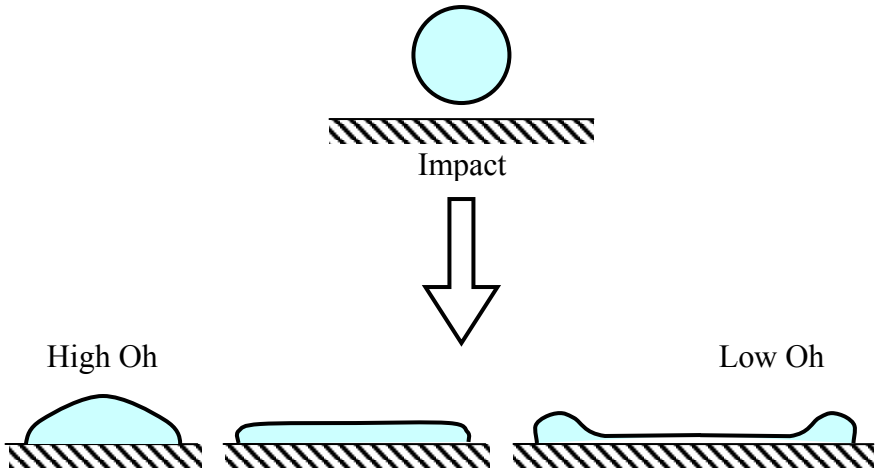

Figure 5. The variable nature of non-splashing drop impacts near the end of the inertial expansion phase. Drops can appear like a spherical cap (left), thin cylinder (centre) or toroidal rimmed disk (right).

Research completed into high Oh, low We impacts includes Attané et al.[48], who established a cylindrical approximation drop impact model capable of adequately predicting maximum spread factors to within approximately ± 15% for fluid drops with $0.6 \leq We \leq 2000$ and $0.002 \leq Oh \leq 0.585$ (with significant improvements in predictive capability towards high We and low Oh) and Schiaffino and Sonin[101], who examined the deposition and solidification characteristics of water (μ = 0.0016 Pas), molten wax (μ =

0.018 Pas), glycerol (μ = 0.93 Pas) and an aqueous solution of glycerol with a mass fraction of 0.8 (μ = 0.045 Pas) at low and moderate We.

For low and moderate We across a large range of Oh, Schiaffino and Sonin proposed separating drop dynamic behaviour into four distinct regimes, characterised by similarity parameters Oh, We, Re, θ_e and the spreading coefficient S (Equation 28). These parameters are based on dimensional analysis of the terms in the radial component of the Navier-Stokes equation in the appropriate limits and each regime is separated by Oh and We limits. These regimes are details in Figure [6] and Table [1]. This characterisation is limited to low Bo (D_E < a) numbers and moderate contact angles that are not close to either θ_a = 180^o or θ_a = 0^o. Moreover, the limits do not to apply at high We; close to break-up and splashing of drops and only serves as an order of magnitude argument with regard to the similarity parameters.

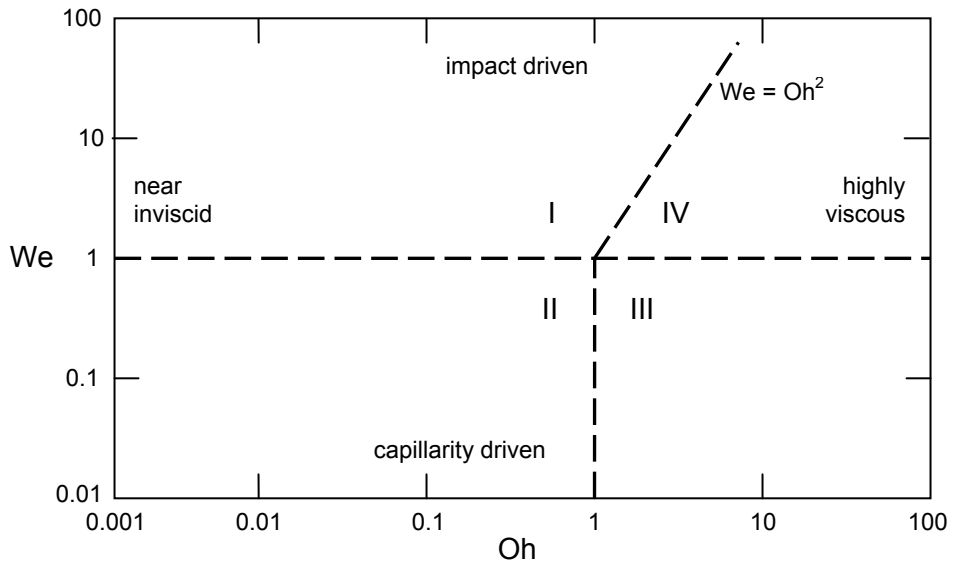

Figure 6. The characterisation of drop impact dynamics[101] based on similarity parameters using Oh and We

Table 1. Characteristics of drop dynamic behaviour for low and moderate We, as proposed by Schiaffino and Sonin[101].

Region			Characteristic Velocity in expansion phase [ms^{-1}]	Characteristic timescale in expansion phase [s]	Driving Force	Inhibiting force
I	We >> 1	Oh << $We^{1/2}$	V	D_E/V	Impact pressure	Inertia
II	We << 1	Oh << 1	$(\sigma/\rho D_E)^{1/2}$	$(\rho D_E^3/\sigma)^{1/2}$	Capillarity	Inertia
III	We << 1	Oh >> 1	σ/μ	$\mu D_E/\sigma$	Capillarity	Viscosity
IV	We >> 1	Oh >> $We^{1/2}$	$\rho V^2 D_E/\mu$	$\mu/\rho V^2$	Impact pressure	Viscosity

The four regions in Figure [6] are:

(I) *Inviscid, impact-driven spreading*. Spreading during the expansion phase occurs over a short time period and flow is driven by inertial forces and resisted by inertia. Impact velocity and drop size govern the velocity and time scales and viscous effects are weak. Underdamped oscillations arise during retraction and subsequent spreading phases with a period longer than the characteristic timescale of the expansion phase detailed in Table [1]; an observation in agreement with the oscillation timescales established by Van Dam and Le Clerc[8] (Equation 19). Viscous effects act to damp subsequent oscillations. The limit in Figure [6] between impact driven regimes (I) and (IV) ($We = Oh^2$) corresponds to Re = 1 given that $Re = \sqrt{We}/Oh$. For Re < 1, inertial forces will dominate over viscous forces; the opposite is true for Re > 1. Typically drop splashing will occur in this regime, although it is possible for it also to occur in (IV).

(II) *Inviscid, capillarity driven spreading*. During the expansion phase, impact velocity effects are negligible and most of the initial spreading is driven by capillarity and resisted by inertia. The timescale detailed in Table [1] is valid initially and in agreement with Van Dam and Le Clerc[8] (Equation 19), however towards the end of the stage viscous forces take effect and spreading slows. As with regime (I), underdamped oscillations are present in the retraction and subsequent spreading phases with a period of the same order as that given in Table [1]. In terms of dimensional analysis, this timescale is the same as Equation [19]. Viscous effects eventually damp out oscillations.

(III) *Highly viscous, capillarity driven spreading*. Initial spreading during the expansion phase is driven by capillarity and retarded by viscosity. The impact velocity in this regime has a negligible effect and the high viscosity of the fluid results in an overdamped system, so no oscillations are present in subsequent retraction or spreading.

(IV) *Highly viscous, impact-driven spreading*. Initial spreading is driven by inertial forces and retarded by viscous effects. The effect of surface tension during this phase is negligible. As with regime (III), the system is overdamped and no oscillations arise during the retraction and subsequent spreading phases.

As highlighted by van Dam and Le Clerc[8], this description of drop impact behaviour based on dimensionless numbers acts as a good summary and is useful when first trying to establish the expected dynamic characteristics.

Research into predicting the maximum inertial drop diameter and minimum apex heights of impacting drops at the end of the inertial expansion stage is extensive. Theoretical, empirical and semi-empirical prediction models range from simple order of magnitude studies to more technical energy conservation models, which account for more complex flow physics including deformed drop shape and additional dissipative effects arising from the rolling motion of liquid near the contact line. Kurabayashi[102], Bechtel et al.[49] and Chandra and Avedisian[42] were amongst the first to utilise the energy balance method to estimate β_m and ξ_m. In general, the energy balance can be expressed as:

$$\frac{d}{dt}(E_k + E_g + E_\sigma) + \dot{W} = 0 \qquad [20]$$

where E_k is the kinetic energy, E_g is the gravitational potential energy, E_σ is the surface energy and $\dot{W}$ is the rate of energy loss from viscous dissipation, considered the most difficult quantity to estimate accurately because flow velocity profiles and the degree of flow recirculation can only be approximated.

One of the difficulties in developing a model is the estimation of the surface tension term at the end of the inertial expansion phase. Models can approximate the shape of the drop at maximum spread to be a cylinder, resulting in the equation[53]:

$$E_{\sigma,\beta_{Max}} = \frac{\pi}{4} D_{Max}^2 \sigma (1 - \cos\theta_a) \qquad [21]$$

Equation [21] can be re-written in terms of the equilibrium contact angle θ_e[47]:

$$E_{\sigma,\beta_{Max}} = \sigma \left[\frac{\pi}{4} D_{Max}^2 (1 - \cos\theta_e) + \frac{2}{3} \pi \frac{D_E^3}{D_{Max}} \right] \qquad [22]$$

Alternatively, the drop shape can be approximated by a spherical cap[49,57], whereupon the applicable equation is:

$$E_{\sigma,\beta_{Max}} = \frac{\pi}{3} D_E^2 \sigma \left[\left(\frac{h}{D_E} \right)^{-1} + 2 \left(\frac{h}{D_E} \right)^2 - \left(\left(\frac{h}{D_E} \right)^{-1} - \left(\frac{h}{D_E} \right)^2 \right) \cos\theta_e \right] \qquad [23]$$

The diverse range of drop shapes arising during inertial expansion has already been highlighted; the application of these approximations typically limits the models to ranges of Weber numbers where deformation is consistent with the approximation used. A cylindrical approximation is most commonly used, however this can become an increasingly poor approximation towards impacts with smaller We and higher Oh. In order to improve model predictive capability for high viscosity low energy impacts, existing models need to be assessed over larger ranges of We and Oh than previously established[48]. Moreover a review of both old and new models needs to be completed that includes contemporary models not covered in previous reviews[51,74]. Models exhibiting the best predictive capability can then optimised for low inertial energy, high Oh impacts. To aid clarity, this work is presented separately in **§5.3.2** as part of a research project objective.

1.1.3.4 Thermal influences

Research into the effects of temperature on drop impacts is extensive and includes investigations into the solidification of molten drops upon impact[51,79,81] and ambient isothermal drops on heated surfaces[42,100,108,109]. The current research examines liquid drop impacts on solid isothermal surfaces, therefore previous thermodynamic research is not directly relevant and therefore will only be considered in passing.

Substrate temperature effects on drop impact behaviour were first observed by Johann Leidenfrost[75]. Drops impacting on a heated surface were found to boil nearly instantaneously, causing secondary atomisation. Heating the surface further however can cause drops to rebound from a thin, cushioning vapour layer formed between the drop and the surface, preventing direct contact. This is known as the *dynamic Leidenfrost phenomenon* and was originally investigated in detail by Wachters and Westerling[108]. Subsequent studies include: Wang et al.[110], who reclassified the *Leidenfrost temperature* as the wall temperature at which the total drop evaporation time on a heated surface was longest and the *critical temperature of dry impact* as the minimum temperature above which the drop has no direct contact with the solid surface due to the formation of a vapour layer, Yao and Cai[111] who established that the Leidenfrost temperature varied with We and Sawyer et al.[112], who determined the effect of drop size, impact frequency and impact velocity on the critical heat flux[1] of impacting water drops on a solid surface.

1.1.3.5 Influence of static and dynamic surface tension

Whereas the effect of surface tension on drop impacts has already been described in terms of dimensionless We, Ca and Oh numbers, dynamic surface tension effects can result in a non-uniform surface tension on the fluid/gas interface, which can vary throughout the impact process. Extensive research has been completed into the effect of

[1] Critical heat flux occurs just prior to the onset of the Leidenfrost regime, where a maximum heat transfer from a heated surface to a liquid drop is reached.

surfactants on drop impact dynamics[43,67-70], primarily because different surfactants have different adsorption kinetics.

Dynamic surface tension effects are dependent on the migration rate of surfactant molecules to newly formed interface regions. Different surfactant molecules exhibit considerably different migration timescales, ranging from the order of milliseconds to minutes. The molecules are comprised of a water-loving (hydrophilic) head and a water-hating (hydrophobic) tail; they find it energetically favourable to position themselves at the fluid/gas interface and act to lower the surface tension. Dynamic surface tension effects arise when surfactant concentrations are not in equilibrium, giving rise to Marangoni[113] forces. Surface tension effects only occur at fluid interfaces, therefore cannot be described as rheological characteristics because by definition; rheological fluid properties are homogenous within the fluid.

For slow surfactant migration periods or high flow rates, newly formed surface regions are created faster than surfactant molecules can be transported to them; the local surface tension in newly formed regions is therefore greater than the equilibrium surface tension. Faster migration rates or slower flow rates improve the efficiency of adsorption kinetics, allowing surfactants to more easily maintain the equilibrium surface tension.

Since a liquid with a high surface tension pulls more strongly on the surrounding liquid than one with a lower surface tension, the presence of a gradient will naturally cause liquid to flow away from low surface tension regions. Zhang and Basaran[33] investigated the influence of Triton X-100 and SDS surfactants on drop impact dynamics and established that dynamic changes in the surface tension from accumulation of surfactant molecules at the gas-liquid interface enhanced the spreading of drops on a solid substrate and reduced the likelihood of rebound. In addition to providing evidence supporting the notion that surfactants increase damping of spread-recoil oscillations by stabilizing interfacial waves (due to the redistribution of surfactant molecules by convection and diffusion), they also highlight the complicated relationship between dynamic surface tension and impact velocity. The maximum inertial spread diameter at low impact velocities can be increased by increasing the surfactant concentration,

however the opposite tendency is observed at high impact velocities. This complicated relationship is due to the existence of three competing mechanisms during impact dynamics; (a) the dilution of surfactants due to new surface creation, (b) the convection of surfactants toward the contact line whose intensity increases with impact and (c) the repopulation of the interface by surfactant molecules from the bulk of the drop. For low velocity impacts, surface creation rates are low and surfactants have time to repopulate new regions. In contrast, the large surface creation rate in high velocity impacts leads to dilution of surfactants and an inequality of the surface tension. At the same time, the radial spreading of the drop in the expansion phase gives rise to interfacial flows from the axis of symmetry at the centre of the drop towards the expanding contact line. The flow sweeps the surfactant molecules on the surface towards the contact line and causes it to accumulate there. The rate at which this occurs increases with interfacial velocity and hence, impact velocity.

Crooks et al.[69] examined the effects of differing adsorption kinetics on drop impact dynamics for surfactants in glycerol/water solutions. Their results indicate that the recoil height after the inertial expansion phase decreases as surfactant concentration increases even when β_m remains constant. Whereas their findings agreed with those of Zhang and Basaran[68] for fluids with surfactant additives below the critical micelle concentration (C.M.C, where this denotes a surfactant concentration above which micelles are spontaneously formed due to the interfacial surface becoming crowded with surfactant molecules), additional experiments performed for fluids with surfactant concentrations above the C.M.C showed significantly different drop impact behaviour.

Below the C.M.C, the radial flow during inertial expansion convects surfactants already present at the interface to the leading edge. Above the C.M.C, in response to the non-equilibrium conditions (from surfactants being diluted at newly formed surfaces), micelles disintegrate and supply molecules to the surface. The characteristic time of demicellisation for the surfactants studied is significantly shorter than the transport rate of free molecules to the surface[114,115]. This implies that demicellisation will respond nearly immediately to drop deformation and will swamp any hydrodynamic convection of free molecules to the contact line. The overall result is the dramatic decrease in dynamic

surface tension by way of increasing the rate at which surfactants reach newly formed surface regions. Demicellisation kinetics govern the surface excess of surfactant molecules and the subsequent surface relaxation characteristics of impacted drops with surfactant additives above the C.M.C. Below the C.M.C, hydrodynamic effects are controlling.

In their investigation into drop impact dynamics for surfactant solutions well (10X) above the C.M.C, Mourougou-Candoni et al.[70,116] highlight that the characteristic timescale of adsorption kinetics for different surfactants in water will influence both the inertial spreading and retraction phases. When the maximum inertial spread diameter is reached, the dynamic surface tension is found to be almost constant on the whole drop free surface, however this value is not necessarily the equilibrium surface tension value after complete adsorption of the surfactants. This indicates that the rate at which surfactants migrate to the surface will influence the maximum spread diameter. Moreover, adsorption kinetics also affects the retraction phase dynamics. Studies of the dynamic behaviour of drops were performed for surfactant additives whose equilibrium surface tensions ranged between $0.025 \leq \sigma \leq 0.0372$ N/m and dynamic surface tensions σ_{dyn} at maximum inertial spread β_m ranging between $0.0397 \leq \sigma_{dyn} \leq 0.0722$ N/m. Each of the surfactants also had differing adsorption kinetics. β_m was observed to vary by up to ± 14% due to the variation in dynamic surface tension. Retraction dynamics also differed significantly, varying with both excess surface tension recoil energy and surfactant adsorption kinetics.

The influence of dynamic surface tension effects on impact dynamics is complex due to the many variables including surfactant concentration and adsorption kinetics. Studies currently appear to be limited to the analysis of specific types of surfactants and no generalised theories exist at present that can predict drop dynamic behaviour irrespective of surfactant type. Existing research does however highlight the significant influence of adsorption kinetics and surfactant concentration on impact behaviour and their increasingly influential role for higher impact velocities.

1.1.3.6 Influence of surface roughness

The effect of surface roughness on splashing was first recognised by Engel[103], who observed that splashing was reduced when highly polished surfaces were used. Subsequent research after Stow and Hadfield's[41] proposed correlation between the splashing/deposition limit, We_c, Re_c and the surface roughness has concentrated predominantly on the effects of the surface. Wu[104] determined that the influence of fluid viscosity on splashing for small values of Oh was small and could be neglected; reducing Equation [18] to:

$$We_c = a \log^b \left(\frac{R_E}{R_a} \right) \qquad [24]$$

where a = 6.47, b = 1.87, R_E is the drop radius and R_a is the roughness coefficient[2]. Values for a and b were established by fitting Equation [24] to the experimental data of Stow and Hadfield[41] using a least square method. Range and Fuillebois[73] experimentally confirmed the hypothesis of Wu with regard to the influence of viscosity at low Oh and the splashing limit proposed by Stow and Hadfield for water drop impacts on rough aluminium surfaces. Moreover, their results also confirm that the splashing limit depends on the substrate roughness in a way that can be described by Equation [24] (the parameters a and b having to be adapted for each liquid-substrate combination). Furthermore, perturbations appearing on the rim during the expansion phase prior to splashing were found to vary with surface roughness. The number of perturbations decreased with increasing surface roughness, however each perturbation increased in size.

[2] Surface roughness can be either random or periodic (typically man made) variations in the surface topography. Measurements can be made using contact (involving dragging a measurement stylus across the surface) or non-contact methods (such as interferometry, confocal or electron microscopy and photogrametry). The roughness coefficient R_a is the most common term employed to describe roughness. It is the arithmetic average of the absolute roughness values. Absolute roughness values are calculated as the vertical distance from the calculated mean profile line.

An underlying mechanism by which surface roughness influences splashing was proposed by Levin and Hobbs[96]. The resultant of the surface tension forces in the convex region between the undeformed drop and the outspreading liquid film is directed at an angle to the flat substrate surface. If these forces are of a sufficient magnitude relative to the inertial spreading forces of the liquid film then it could introduce a vertical flow component, lifting the spreading film from the surface. The lifted sheet could then form a crown shape and subsequently breakup. Whilst increased surface roughness may enhance this mechanism, Range and Fuillebois[73] highlight that there is not yet enough data to ascertain this effect.

Mundo et al.[105] investigated the splashing/deposition limit of impacting drops (R_E = 60-150μm) on rotating surfaces (a smooth surface with R_a = 2.8μm and a rough surface with R_a = 78μm; of the order of the drop size) for liquids with a variety of fluid properties as a function of Oh and Re. They established an expression of the form $OhRe^{1.25} = 57.7$, however this correlation was only obtained if the normal velocity component of the impacting drop was used. Walzel[106] derived a correlation between the critical Weber number and the Ohnesorge number, given by $We_c = 7.9 \times 10^{10} Oh^{2.8}$. Whereas Mundo et al. established no difference between two surfaces with different roughness characteristics, Cossali et al.[107] highlight that those surfaces used had roughness characteristics falling within an asymptotic region, such that Ξ in Equation [18] achieves a near constant value. Vander Wal et al.[84] investigated the splashing/deposition limit for water drops (R_E = 2 mm) with $300 \leq Re \leq 15000$ and $0.0019 \leq Oh \leq 0.021$ on an aluminium substrate with a roughness less than 10 nm. Whilst this study did not examine the effects of either surface roughness or surface wettability, an empirical splashing limit of the form $OhRe^{0.609} = 0.85$ was established; clearly different from that of Mundo et al. This indicates a clear variation in the splash/deposition limit due to surface roughness, in agreement with initial observations by Engel[103].

A generalized theory of drop splashing that incorporates the influence of surface roughness for all surface types has yet to be established. This is due primarily to the complexity of splashing events and the significant influence of numerous parameters (Oh, Re, R_a). Moreover, surface roughness characteristics are typically non-uniform and drops

can splash in a variety of ways (ranging from prompt splash upon impact to crown splashing towards the end of inertial spreading). Both aspects contribute significantly to the complexity of the system.

1.1.3.7 Influence of spreading and the dynamic contact angle.

Research into the effects of surface wettability on impact dynamics is extensive, however investigations have primarily focussed on low viscosity fluids close to that of water (μ = 0.001 Pas). The equilibrium contact angle θ_e of sessile water drops is often used to characterise the wettability of substrates. As governed by the Young equation (Equation 35), hydrophilic surfaces such as clean glass will have small values of θ_e and can be completely wetting ($\theta_e = 0^o$); hydrophobic surfaces like parafilm-M will have significantly larger values. Ford and Furmidge[53] were amongst the first to investigate the influence of surface wetting effects on impact dynamics and discovered that the maximum spread of water drops increased as θ_e decreased; later confirmed by numerous experimental investigations including Mao et al.[47], Pasandideh-Fard et al.[43] (who obtained a similar conclusion in terms of the advancing contact angle θ_a) and Sikalo et al.[61]. The influence of surface wettability was found to be negligible[45,47,61] during the early stages of water drop impact, where spreading is dominated by inertial and viscous effects, and grows only towards the end of inertial spreading.

Both Pasandideh-Fard et al.[43] and Mao et al.[47] quantified the influence of substrate wettability on β_m for varying impact velocities of water drops on wax and glass surfaces; Pasandideh-Fard et al. over the ranges $59 \leq We \leq 271$ and $2084 \leq Re \leq 5833$ and Mao et al. over the ranges $11.3 \leq We \leq 518$ and $1482 \leq Re \leq 10024$. Whereas both investigations conclude that the influence of wettability on maximum inertial spread decreases as the impact velocity increases; a characteristic later confirmed by Sikalo et al.[61], the maximum variation in β_m over $27 \leq \theta_e \leq 111^o$ measured by Pasandideh-Fard et al. (up to $\Delta\beta_m = 23.6\%$ for We = 59 and Re = 2084) was significantly larger than that

measured by Mao et al. over $37 \leq \theta_e \leq 97^o$ (up to $\Delta\beta_m = 10.4\%$ for We = 37 and Re = 2694).

By comparing impacts on glass and wax surfaces, both Sikalo et al.[61] and Mao et al.[47] established that recoil is significantly larger on less wettable substrates; whereas partial and complete drop rebounds were observed on wax surfaces, equivalent impacts on glass surfaces produced only spread-recoil oscillations. Both investigations conclude that retraction dynamics will vary as a function of θ_r and the excess surface tension energy at the end of the inertial spreading phase; where excess energy is defined as the difference in surface tension energy between a sessile drop shape and a drop at maximum inertial spreading. Drops therefore will reach an equilibrium state when the excess energy reduces to zero. Furthermore, both studies highlight that the time to reach an equilibrium state on the wax surface is longer than for a glass surface. Mao et al. attribute this to a slower energy dissipation rate for decreasingly wettable surfaces. Furthermore, Mao et al. established a theoretical expression describing the excess recoil energy E_{ERE} in terms of the dimensionless maximum inertial spread diameter β_m and θ_e, given by:

$$E_{ERE} = \frac{1}{4}\beta_m{}^2(1-\cos\theta_e) - 0.12\beta_m{}^{2.3}(1-\cos\theta_e)^{0.63} + \frac{2}{3}\beta_m - 1 \qquad [25]$$

For positive values of E_{ERE}, the drop will rebound. Negative values correspond to drops remaining on the surface during retraction. Upon impact on a wettable surface, the more a drop spreads, the less likely is the tendency to rebound. As substrate wettability decreases however, the likelihood increases for equivalent values of β_m. Through comparison with experiments, Mao et al. found this expression to be capable of predicting rebound events, although the accuracy of predicting events diminished significantly for values of E_{ERE} close to zero.

1.1.4 Newtonian drop spreading dynamics on solid surfaces

The spreading of drops on solid surfaces is a complex process, made increasingly more so by the preceding dynamics of the expansion and retraction phases. When a liquid

drop is deposited on a solid horizontal surface it will eventually either form a film or a spherical cap (for $R_E < a$), depending on the wettability of the surface. The timescale of spreading is typically much longer than the impact process and has been found to vary significantly with θ_e and viscosity. By balancing the equilibrium interfacial energies for a sessile drop, shown in Figure [4] where $\theta = \theta_e$, Young[13] established the equation:

$$\sigma_{sv} - \sigma_{sl} - \sigma \cos\theta_e = 0 \qquad [26]$$

where σ is the surface tension and subscripts s, l and v are the solid liquid and vapour phases respectively. Due to its frequency of appearance, the liquid-vapour interfacial tension is denoted throughout this thesis without subscripts. Complete wetting ($\theta_e = 0^o$) results with $\sigma_{sv} - \sigma_{sl} = \sigma$. Wenzel[118] modified this equation to account for surface roughness, giving:

$$\sigma \cos\theta_{av} = r_f (\sigma_{sv} - \sigma_{sl}) \qquad [27]$$

where θ_{av} is the average apparent angle of contact and r_f, the roughness factor, is the ratio of true to apparent area of the solid. Harkins and Feldman[119] established that for drops where interfacial energies are not in equilibrium, the spreading coefficient S is given by:

$$S = \sigma_{sv} - \sigma - \sigma_{sl} \qquad [28]$$

In equilibrium, the spreading coefficient, where $S = S_{eq}$, can never be positive[120]. Whereas complete wetting corresponds to $S_{eq} = 0$, $S_{Eq.} < 0$ corresponds with partial wetting.

The spreading may be positive initially[99] however, wherein the difference between initial and equilibrium spreading coefficients is due to vapour molecule adsorption to the substrate, reducing σ_{sv} to less than the surface free energy in the absence of vapour σ_{s0}. Substituting these terms gives:

$$S_i = \sigma_{s0} - \sigma - \sigma_{sl} \quad [29]$$

where the initial spreading coefficient, $S_i > S_{Eq}$. S_i can be both positive and negative, however when S_i is negative, so will S_{eq} and the drop will not spread. In contrast, for $S_i > 0$, S_{eq} can be both positive and negative.

De Gennes[99] highlights in his review that drop spreading velocities v_r are large at first and then decrease significantly. This is often represented by a power law and in terms of the wetted area $A_{wet} = \pi R^2(t)$, is given by:

$$\pi R^2(t) \cong t^n \Omega^q \quad [30]$$

where Ω is the fluid volume. The parameter n has been obtained by a number of investigations[121,122], however one of the most accurate and well established studies was by Tanner[123], who obtained n = 0.21. Values of q have not been investigated as thoroughly, however Lelah and Marmur[122] established a value of 2/3. Moreover, Hoffman[124] established through experimental investigations of silicone oil drop spreading that the capillary number Ca in the limit of low velocity could be related to the advancing contact angle θ_a by:

$$Ca = K\theta_a^m \quad [31]$$

where K is a constant and m = 3 ± 0.5. This describes a relationship between the contact line velocity and the advancing contact angle of the form:

$$\frac{dR}{dt} \cong \frac{\sigma}{\mu}\theta_a^m \quad [32]$$

For drop radii less than the capillary length (Equation 17), the drop will take on a spherical cap shape, where drop height h(t) and radius R(t) are related by:

$$h = \frac{1}{2} R\theta_a \qquad [33]$$

$$\frac{\pi}{2} hR^2 = \Omega, \qquad [34]$$

where h is considered small in comparison with R. Substituting Equations [33] and [34] into Equation [32] and integrating gives:

$$R(t)^{3m+1} \cong \frac{\sigma}{\mu} \Omega^m t \qquad [35]$$

Comparing Equation [30] with Equation [35] indicates n = 2/(3m+1) and q = 2m/(3m+1). Taking Hoffman's value of m = 3 gives n = 0.2 and q = 0.6, in close agreement with experimental results. Equation [35] is commonly known as Tanner's law.

Research has also established the way the contact line advances during spreading. On a macroscopic level, the contact line forms an advancing contact angle θ_a with the surface. Through marking the upper surface of viscous spreading drops with spots of dye, Dussan and Davis[125] established that a characteristic rolling motion occurs, similar to that of a caterpillar track vehicle; this motion gives rise to viscous friction effects. Ahead of the wedge is a precursor film, extending in front of the apparent contact line. Whereas extensive investigations on this film have been performed and reviewed[99], this is considered outwith the scope of the research, where we concentrate on macroscopic events and phenomena.

It should be noted that there are several schools of thought when considering dynamic contact angle. The two main approaches are hydrodynamic and molecular dynamic theories; the first of which is described within this section. In molecular dynamic theory, the motility of molecules in the liquid and at the solid-liquid interface are considered. Ruijter et al[171] show that molecular dynamic calculations of contact angles and flow fields agree with experimental observations of spreading drops,

supporting the validity of the molecular-kinetic model of wetting. Using this molecular-kinetic approach, changes in the strength of the solid-liquid interactions varied the wettability of the system.

Research cited so far in this chapter details the spreading dynamics of drops deposited on a surface. Drop impact dynamics prior to drop spreading must however also be taken account and consideration given to the crossover period between inertial expansion or retraction phases and the spreading phase.

Biance et al.[100] investigated the early stages of spreading for drops deposited on a solid surface and established that spreading has two regimes; a fast inertial regime with $R(t) \alpha t^{1/2}$, followed by the well established viscous regime described by Tanner's law where $R(t) \alpha t^{1/10}$ (Equation 35). The inertial regime was found to eventually crossover to the conventional spreading regime after the characteristic timescale:

$$t_{si} = \left(\frac{\rho \sigma R_E}{\mu^2} \right)^{1/8} \sqrt{\frac{\rho R^3}{\sigma}} \qquad [36]$$

The physics behind drops deposited slowly on a surface are therefore not dissimilar to drop impacts. Both will exhibit an inertial regime followed by a viscous regime and whilst the drop morphology and timescales to reach a sessile state may differ considerably, the final sessile state will ultimately be governed by Equation [26].

1.1.5 Complex fluids

With a better understanding of rheology and rheological techniques, industries have realised that working fluids can be tailored specifically to their intended purpose and be used to optimise existing industrial processes. Contemporary research into complex fluid drop dynamics, particularly for impact and deposition processes is therefore of interest. A classic example of industrial optimisation is the work by Bergeron et al.[3], who

established that rebound and splashing of impacting aqueous based pesticide drops on the upper surface of waxy, hydrophobic leaves could be suppressed through the addition of small amounts (~100 p.p.m) of flexible polymers. Not only does this improve application efficiency, it also reduces environmental impact from ground contamination.

Sections **§1.2.1 - 1.2.4** detail existing research into Newtonian fluid drop dynamic behaviour as well as some additive effects such as surfactants that act at the fluid interface. Unlike dynamic surface tension effects, changes in fluid drop dynamics arise most commonly from variations in the rheological composition of the fluid; which describe homogenous fluid properties, albeit not necessarily isotropic when subject to external forces. Unlike Newtonian fluids, where the applied shear stress is proportional to the rate of strain (the constant of proportionality being the viscosity μ), non-Newtonian fluids exhibit variations in this proportionality; either as a function of applied shear-stress (shear thickening or thinning fluids) as displayed in Figure [7] or with time when subject to a constant shear-stress (rheopectic or thixotropic fluids).

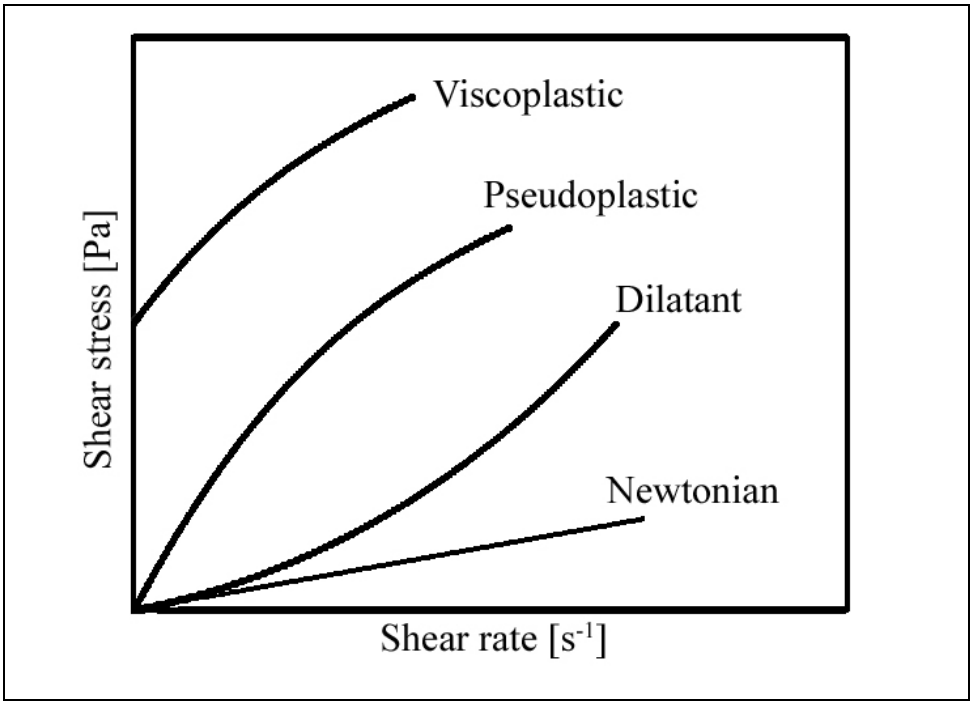

Figure 7. The characteristics of common non-Newtonian fluids, plotted on a graph of shear-stress τ against shear rate $\dot{\gamma}$.

Some fluid types can exhibit solid-like and fluid-like properties; these are called viscoplastic or 'yield-stress' fluids. This fluid type forms the focus of the research

project. Rather surprisingly, very little research into yield-stress drop dynamics has been published to date. Viscosplastic fluids can exhibit both shear-thinning and yield-stress characteristics. With the exception of viscoelastic fluids, which are currently a popular research topic and will be briefly discussed here, complex fluids that do not exhibit these characteristics are considered outwith the scope of the research and will not be considered further.

As the name suggests, viscoelastic fluids exhibit both viscous and elastic components. These fluids are easily produced by adding small amounts of polymer (of the order parts per million) such as polyethylene oxide (P.E.O) to water. Research is extensive and includes rheological characterisation[126,127] and the behaviour of viscoelastic drop dynamics[3,67,77,128,159,165]. The research by Bergeron[3], which details the retraction phase and splash suppression effects of small amounts of P.E.O in impacting water drops has already been highlighted. We describe here some other aspects of dynamic viscoelastic drop behaviour, specifically with regard to drop detachment.

As described in **§1.2.1**, unstable Newtonian fluid drops detaching from a capillary tube will initially exhibit exponential increases in the perturbation amplitude at the point of minimum drop neck thickness followed by a transition to Stokes and then Navier-Stokes self-similar flow regimes. Amarouchene et al.[159] however show experimentally that a remarkably different behaviour can occur with the addition of minute amounts of polymer to a low viscosity Newtonian fluid. Whilst the initial behaviour of these viscoelastic fluids is similar to that of the Newtonian fluid drops up to and including the transition to the Stokes flow self-similar regime, subsequent behaviour shows inhibition of self-similar breakup. The drop neck instead forms a long thin filament which continues to elongate and thin but at a much slower rate. This rate is found to be exponential. Filament formation is found to occur when the critical elongation rate in the neck becomes comparable to the reciprocal of twice the polymer relaxation time[164]. In other words, the interaction of the polymer with the flow is found to occur when the elongation rate is sufficiently large enough to stretch the polymer coils. Increasing either the additive concentration or the polymer molecular weight is also found to slow the filament thinning.

Experimental and numerical studies by Wagner et al.[165] show that viscoelastic fluids can also inhibit satellite drop formation. Satellite drop formation in Newtonian fluids occurs when pinching in the neck occurs simultaneously at the end close to the capillary tube and the end closest to the drop. This produces a much smaller satellite drop above the detached primary drop. With the addition of small amounts of polymer additive to Newtonian fluids, pinching is inhibited and thin cylindrical threads remain connected to the small satellite bead in the middle, forming a 'bead on a string' appearance. For small enough capillary tube diameters, no satellite bead is formed and the thread remains uniform.

1.1.5.1 Shear-thinning fluids

The viscosity of a shear-thinning fluid decreases as a function of increasing shear-stress. A number of rheological models have been proposed to characterise this shear-thinning behaviour. These include:

$$\mu = K\dot{\gamma}^{n-1} \qquad \text{(Power-law model)} \qquad [37]$$

$$\frac{\mu - \mu_\infty}{\mu_0 - \mu_\infty} = \frac{1}{1 + (C\dot{\gamma})^{1-m}} \qquad \text{(Cross model)}^{129} \qquad [38]$$

$$\frac{\mu - \mu_\infty}{\mu_0 - \mu_\infty} = \frac{1}{\left[1 + (C\dot{\gamma})^{a}\right]^{(1-m)/a}} \qquad \text{(Carreau model)}^{130} \qquad [39]$$

$$\frac{\mu_0}{\mu} = 1 + \left(\frac{\tau}{\tau_{1/2}}\right)^{n-1} \qquad \text{(Ellis model)}^{131} \qquad [40]$$

where τ is the applied shear stress. K is the consistency coefficient, which describes the viscosity at low shear-rates; this gives an idea of the overall range of viscosities across

the part of the flow curve that is being modeled. The exponent n is the power law index, where $0 < n < 1$; the more shear-thinning the fluid, the closer n is to zero. A value of $n = 1$ corresponds to a Newtonian fluid. μ_0 and μ_∞ are the viscosities at zero shear and infinite shear respectively and C is the cross time constant. This parameter is the reciprocal of the strain rate at which the zero strain rate component and the power-law component of the flow curve intersect. (1-m) is the rate constant describing fluid shear-thinning for the Cross and Carreau models. $\tau_{1/2}$ in the Ellis model is the shear stress at which μ is exactly half of the μ_0 value.

It is important to choose a rheological model that provides the best correlation to experimental data. Equation [37] is the simplest model with only two fitting parameters. Whilst this can adequately model shear-thinning characteristics, it fails to describe very low and high shear rate regions[132]. The Cross model is more complex and has the added capability of modelling low ($\mu \sim \mu_0$) and high shear ($\mu \sim \mu_\infty$) Newtonian regions. Additional models have been proposed (Equation 39) that include a fifth fitting parameter, a. The Carreau model designates $a = 2$ and has been found to fit experimental data better than the Cross model. Frequently the high shear rate Newtonian region is not observed, common for fluids such as polymer melts[132]. The Ellis model (Equation 40) sets μ_∞ in the Cross model (Equation 38) to zero and is usually expressed in terms of a stress variable.

One of the difficulties in studying fluids exhibiting shear-thinning characteristics is that during any drop dynamic process, the viscosity will vary both spatially and temporally as a function of the local shear-rate. This is unlike Newtonian fluids, whose viscosity remains constant. This additional complexity increases the difficulty in establishing relationships between the macroscopic drop dynamic behaviour and the underlying viscometric properties of the fluid. Moreover, common parameters used to characterise drop behaviour such as Re, Oh and Ca cannot be defined adequately because they are not fixed for any given process due to the variation of the viscosity term. Whilst computational studies can be used to model the drop dynamic behaviour of fluids exhibiting shear-thinning characteristics[145], establishing empirically derived models is

difficult and observing dynamic behaviour qualitatively is often the limit to what can be expected.

Existing research into shear-thinning fluid drops focuses mainly on detachment dynamics from capillary tubes and the spreading behaviour on solid surfaces. Davidson et al.[145] investigated the detachment dynamics of both shear-thinning and yield-stress fluids detaching from a thin capillary tube using computational methods. This is discussed collectively in section **§1.2.5.2**.

Carre and Eustache[152] examined the spreading behaviour of shear-thinning fluids on solid surfaces by equating surface tension forces driving the spreading, F_m:

$$F_m = \sigma\left[\cos\theta_e - \cos\theta_a(v_r)\right] \qquad [41]$$

with viscous braking forces F_v:

$$F_v = K\left(\frac{v_r}{\theta_a(v_r)}\right)^n \qquad [42]$$

where $\theta_a(v_r)$ is the advancing contact angle at a spreading velocity of v_r. The logarithmic form of the resultant expression:

$$\log\left[\cos\theta_e - \cos\theta_a(v_r)\right] = n\log\left(\frac{v_r}{\theta_a(v_r)}\right) + \log\left(\frac{K}{\sigma}\right) \qquad [43]$$

was assessed by plotting the values of the left hand side of Equation [43] with the first term on the right hand side and comparing the slope of the line (the power law index n)

with experiment results. The theory was found to be in good agreement with experimental results.

Advancing upon gravitational and capillary spreading of Newtonian drops, whose spreading laws have been well established theoretically[99,123] as $R(t) \sim t^{1/8}$ and $R(t) \sim t^{1/10}$ respectively and confirmed by experiment[153], Starov et al.[154] established theoretical spreading laws for non-Newtonian power law fluids with both shear-thinning and dilatant characteristics. Analyses were performed for both gravitationally driven ($R_E > a$) and capillary driven ($R_E < a$) spreading regimes, where a is the capillary length (Equation 17). Drops were assumed to be completely wetting with small dynamic contact angles. Reynolds numbers were also small and drop radii were significantly larger than the height. The evolution of drop shapes for each regime was deduced to have self-similar solutions, from which spreading laws were obtained. For the case of an axisymmetric non-Newtonian drop within the capillary spreading regime, a self-similar relationship of the form:

$$R(t) = \left(\frac{D_E}{2}\right)\left[1 + \frac{n}{2n+1}\frac{\lambda}{\alpha}\left(\frac{\sigma}{K}\right)^{1/n}\frac{\Omega^{(n+2)/N}}{(2\pi^m)^{(n+2)/n} R_E^{1/\alpha}}t\right]^p \qquad [44]$$

was established, where:

$$p = \frac{n}{mn + 2m + 5 + 2n} = \frac{n}{7 + 3n} \qquad [45]$$

Ω is the drop volume, λ is dimensionless constant, n is the power law index (Equation 37) and for axisymmetric spreading drops, m = 1.

Experimental analyses by Rafaï et al.[156] measured temporal variations in drop radius and established best fit power law curves of the form $R(t) = Ct^p$ for shear-thinning fluids in the range $0.3 \leq n \leq 0.9$. The results agreed with predictions by Starov et al., indicating that the temporal spreading exponents of shear-thinning fluids are less than

those predicted by Tanners law ($p = 1/(3m+1) = 0.1$, Equation 35). For shear-thinning fluids with $n \geq 0.6$ however, error margins were sufficiently large for spreading exponents to agree with both predictions by both Starov et al. and Tanners law. Rafaï et al.[156] conclude that Tanner's law is remarkably robust, with neither strong shear-thinning nor large normal stress effects (found in viscoelastic fluids) significantly affecting spreading rates.

1.1.5.2 Yield-stress fluids

Yield-stress fluids exhibit two distinct regimes. For applied shear stresses below a critical value the fluid behaves like an elastic solid. Above the critical value or 'yield-stress', fluids exhibit shear-thinning behaviour. Measurement of the yield-stress magnitude, τ_c, is most commonly performed by determining the intersection of the solid-like and fluid like regimes via extrapolation as shown in Fig [8][133].

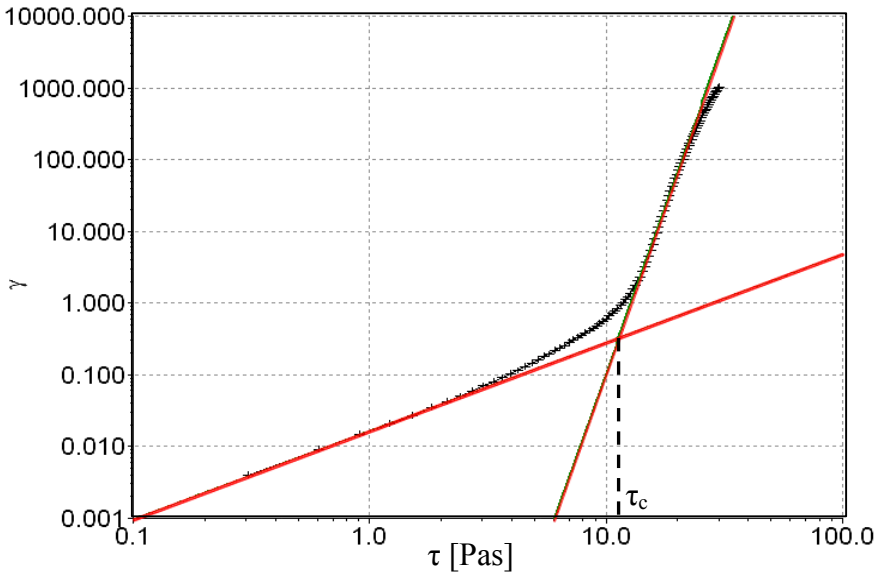

Figure 8. Shear strain plotted against shear stress for a 0.3 mass fraction hair-gel solution in water, replotted from Bertola[133]. The data is used to establish yield-stress magnitude; defined as the extrapolated intersection of the solid-like and liquid-like regimes.

The viscometric properties of each fluid solution can be fitted using a Herschel-Bulkley[134] rheological model, given by:

$$\begin{aligned} \tau &= G\gamma \qquad for\ \tau < \tau_c \\ \tau &= \tau_c + K\dot{\gamma}^n \quad for\ \tau \geq \tau_c \end{aligned} \qquad [46]$$

where G is the shear modulus, γ is the shear strain and τ_c is the yield-stress magnitude. Whilst this model is well established[135] and amongst the most commonly used when analyzing yield-stress behaviour, other models include:

$$\tau = \tau_c + \mu\dot{\gamma} \quad for\ \tau \geq \tau_c \qquad \text{(Bingham model)}^{136} \qquad [47]$$

$$\sqrt{\tau} = \sqrt{\tau_c} + \sqrt{\mu\dot{\gamma}} \quad for\ \tau \geq \tau_c \qquad \text{(Casson model)}^{137} \qquad [48]$$

The Bingham model assumes a Newtonian fluid flow for in the liquid-like region and the Casson model has a more gradual transition from the Newtonian to the yield region.[132]

Research into viscoplastic fluids; their measurement and characterisation is extensive and has been summarised in numerous reviews[132,135,138,139] with the term now commonly used to describe fluids that exhibit solid-like and fluid-like characteristics. Barnes[135] highlights that references to this term in research number 2500 alone from 1985-1998. Bingham[136] was not the first to study these types of fluids; rather it was Schwedoff[140], who first experimented on gelatine solutions in 1900. Bingham however left rather a greater impression; coining the term ‘rheology’, commencing the first society of rheology and describing through experimental research the first non-Newtonian characteristic, that of a ‘Bingham yield-value’; now more commonly known as the ‘yield-stress’.

There are ongoing debates as to the validity of the previous description of a yield-stress fluid; these centre on whether fluids can actually exhibit a 'yield-stress'. The review by Barnes[135] examines the evidence for and against its existence and argues that whereas the concept of a definable yield-stress has and continues to prove useful in a whole range of applications, when carefully measured rheological data is plotted on a logarithmic scale, a Newtonian\power-law\Newtonian behaviour is seen, as described by the Cross shear-thinning model and displayed in Figure [9]

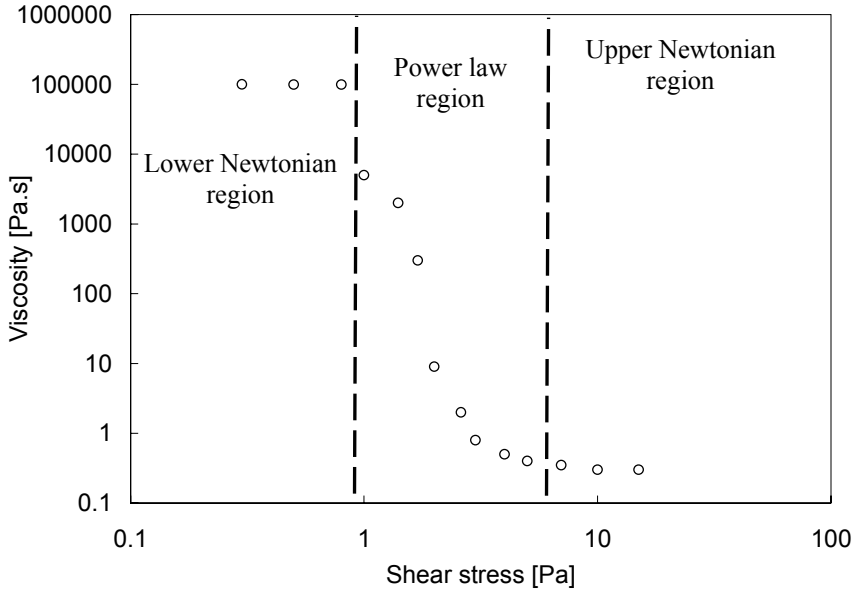

Figure 9. The variation of viscosity with applied shear-stress for a 6% (by volume) suspension of iron oxide dispersed in mineral oil (replotted from Macosko[132]).

The viewpoint highlighted in this review is that at low shear-rates (typically less than 10^{-5} s^{-1}), yield-stress fluids exhibit creep; a slow moving viscous flow regime instead of a solid-like regime whose viscosity tends towards an infinite value. This lower Newtonian regime can be seen in Figure [9]. This contradicts many of the numerous definitions of yield-stress including;

'where no flow can be observed under the conditions of experimentation',[141]

'yield stress is a limiting shear stress at which the material starts to flow; below the yield value the material behaves as an elastic solid'[142] and

'A plastic material is one that shows little or no deformation up to a certain level of stress'[132].

In his definition of yield-stress;

'*a stress below which no unrecoverable flow occurs'*,

Barnes highlights that such a definition effectively rules out experimental proof of the existence of a yield-stress since it would require an infinite amount of time to show that the shear rate, at any given stress is actually zero. Moreover, he systematically argues against all experimental data suggesting the existence of a yield-stress, as the title of his review suggests ('παητα ρει' - everything flows). These arguments are reasoned and not without validity, however he on occasion adopts a fervent and (rather ironically) unyielding stance that no yield-stress can exist on an absolute level.

Barnes does however recognise the counterpoint that is most eloquently detailed by Malkin[143];

'*even though the* (yield-stress) *material is a liquid and flows though its viscosity is very high, it is reasonable to treat the behaviour of a yield-stress material as solid-like*'.

This argument is further supported by Coussot[138] in his review of the rheophysics of pastes. Coussot highlights with regard to Barnes's review, subsequent authors have demonstrated that although they are unable to ascertain the absolute absence of flow below the yield-stress, some viscoplastic fluids exhibit negligible flow characteristics with regards to the time frame of observation. This can be most easily understood by introducing the dimensionless Deborah number[144]:

$$De = \frac{t_r}{t_p} \qquad [49]$$

The dimensionless Deborah number is the ratio of the relaxation time scale t_r, characterising the fluidity of a material, to the observed time scale of an experiment probing the response of the material t_p. Whereas yield-stress fluids may exhibit low-shear rate flows, this fluidity can only be observed over long timescales. For shorter timescales;

characteristic of rheometric measurement and drop dynamic phenomena, the dynamic behaviour of fluids for stresses less than the yield-stress magnitude are negligible. Furthermore, Coussot details that when observing the temporal deformation of a bentonite suspension (a yield-stress fluid) subject to sufficiently low stresses, the slopes of the deformation curves continuously decrease with time; eventually levelling out at a finite value. This limited deformation at low stresses is highlighted as being the hallmark of a solid regime; deformations over long time periods are observed in solids and attributed to ageing effects. For higher stresses the rate of deformation tends towards a constant value consistent with flowing material.

Research into the influence of shear-thinning and yield-stress fluids on drop dynamic behaviour is limited. Both computational fluid dynamic and experimental measurements of drop detachment dynamics from a thin capillary were analysed by Davidson and Cooper-White[145] for both fluid types, using a volume of fluid (VOF) approach, wherein fluid location is recorded by employing a colour function which defines a value of unity within the fluid region, zero outside of the fluid and within these limiting values for cells on the free surface. A Carreau model (Equation 39) was used to reproduce shear-thinning fluid behaviour and a Bingham model implemented with a bi-viscosity approximation[160] (Equation 50) was used for the yield-stress fluids, where:

$$\mu(\dot{\gamma}) = \frac{\tau_c}{\dot{\gamma}} + \mu_2 \quad for\ \dot{\gamma} > \dot{\gamma}_c$$
$$\mu(\dot{\gamma}) = \mu_1 \quad for\ \dot{\gamma} \le \dot{\gamma}_c \qquad [50]$$

In Equation [50], μ_1 is a large Newtonian viscosity below the critical shear rate $\dot{\gamma}_c$ (of regime change), μ_2 is a significantly smaller Newtonian viscosity above the critical shear rate $\dot{\gamma}_c$ and the critical shear rate $\dot{\gamma}_c = \tau_c/(\mu_1-\mu_2)$. ε_μ is a dimensionless ratio μ_1/μ_2, such that as $\varepsilon_\mu \rightarrow 1$ the fluid becomes Newtonian. This model assumes that the material behaves as a Newtonian fluid with a very large viscosity until the critical yield-stress is exceeded, whereupon it exhibits a rapidly decreasing viscosity.

Changes in the temporal variations of minimum neck thickness D_N and drop length L (**§2.8.1**) were used to observe the influence of shear-thinning properties. Fluid shear-thinning was varied by changing μ_∞ and Re independently, where the Reynolds number was defined in terms of the zero shear viscosity μ_0. This definition is counterintuitive however because Re characterises the ratio of inertial to viscous forces and μ_0 defines the flow under zero shear, where inertial forces are zero.

Decreases in both μ_0 and μ_∞ were found to increase the rapidity of neck narrowing; for a fixed volume flow rate Q, pinch off occurs sooner after the onset of instability. This effect is consistent with the influence of viscosity on Newtonian fluid pendent drops; during the detachment process, where liquid flows out of the thinning neck filament as it thins due to increased pressure induced from the curvature, the fluid will exit towards the detaching drop in the lower region and towards the capillary tube in the upper region. Decreasing the viscosity will reduce the normal viscous stresses whilst the induced pressure from the surface tension forces remains the same. This increases neck squeezing and therefore the rate of outflow, resulting in a more rapid onset of pinch off. The maximum drop length at pinch-off also varies considerably with shear-thinning characteristics. Drop lengths become shorter for decreases in both μ_0 and μ_∞. This is expected given that the fluid in the neck will drain more rapidly as the viscosity decreases.

Davidson and Cooper-White only perform one computational analysis of a detaching viscoplastic fluid drop with τ_c = 20 Pa. Whereas satellite droplets formed during the detachment of shear-thinning fluids and a reduction of surface tension increased the likelihood of formation, no droplets were observed in the yield-stress fluid. This is due to the initial resistivity to flow, followed by a rapid reduction in viscosity as the fluid yields. This reduction results in the filament length remaining short.

Prior to the formation of a filament, the shear rate was found to be zero except at the expanding drop surface, corresponding to plug flow (or in the case of a biviscosity model $\mu_1 \sim O(10^{10})$ Pas). As a neck is formed, the shear rate becomes much larger and rises towards pinch-off, considerably reducing the fluid viscosity ($\mu_2 \sim O(0.1 - 1)$ Pas).

This large variation in local viscosity results in rapid drainage of the neck. Furthermore, the drop was observed to be torpedo shaped at pinch-off, rather than spherical or ellipsoidal. They highlight that the drop is expected to eventually obtain a spherical shape, but this does not occur by the time it reaches the limit of the computational domain.

Viscoplastic fluid drop detachment dynamics are also examined by Coussot and Gaulard[146], who demonstrated that high yield-stress magnitude fluid drops become unstable when the weight of the material supported by a fluid element becomes larger than the inhibiting yield-stress forces. Moreover, high yield-stress magnitude fluid drops appear like a cylindrical extrudate instead of a typical pendant shape because capillary forces cannot overcome the inhibiting yield-stress. In order to establish a relationship between drop length at critical breakup and yield-stress magnitude, Coussot and Gaulard assume the drop length is much larger than its diameter. Fluid rheological properties are also modelled using the constitutive equation:

$$\begin{aligned} D &= 0 && \text{for} \quad \sqrt{-T_{II}} < \tau_c \\ \Sigma &= -pI + \frac{2^n K}{\left(\sqrt{-D_{II}}\right)^{1-n}} + \frac{\tau_c D}{\sqrt{-D_{II}}} && \text{for} \quad \sqrt{-T_{II}} \geq \tau_c \end{aligned} \qquad [51]$$

where Σ and D are the stress and strain (symmetric component of the velocity gradient tensor) rate tensors, p is the pressure, I is the unit tensor, T_{II} and D_{II} are the second invariants of the stress and strain tensor and the final term on the right hand side of the $\sqrt{-T_{II}} \geq \tau_c$ case equation is the Herschel-Bulkley rheological model. The normal stress resulting from purely elongational flow (with radial and longitudinal velocity components v_r = -rd/2 and v_z = zd respectively with $d = -\dot{R}/R$) is established as:

$$\tau_{zz} = \varepsilon\left[\frac{2\tau_c}{\sqrt{3}} + 2\sqrt{3}^{n-1} K|d|^n\right] \qquad [52]$$

$\sqrt{-D_{II}} = \sqrt{3}\,|d|/2$ was calculated for uniaxial extensional flow, where $\varepsilon = |d|/d$ and z is the vertical distance along the drop length. This formulation utilises the von-Mises yield criterion that states the yielding of materials will arise when the second deviatoric invariant of the stress tensor reaches a critical value, equivalent to the square of the yield-stress magnitude. Moreover, the stress resulting from the weight of the material below a fluid element $\rho g \pi X R_0^2 e_z$ in cylindrical coordinates is of the form:

$$\Sigma = \frac{\rho g X R_0^2}{R^2}\left[I + (2e_{zz} - e_{\theta\theta} - e_{rr})\right] \qquad [53]$$

The second invariant of the stress tensor was determined as $\sqrt{-T_{II}} = \rho g X R_0^2/\sqrt{3}\,R^2$, where $\sqrt{-T_{II}} = \tau_c$ at critical breakup. The resultant drop length X_c was established as:

$$X_c = \frac{\sqrt{3}\tau_c}{\rho g} \qquad [54]$$

Predictions were found to show a reasonable correlation with measured results.

A similar study by Al Khatib and Wilson[147] interestingly reveals an identical result even though a biviscosity model (Equation 50) is used instead of a Herschel-Bulkley model. At the critical yield point, the relationship at the critical yield point was established as:

$$A = \frac{\rho g Q T}{\sqrt{3}\tau_c} \qquad [55]$$

where A is cross sectional area of the fluid, Q is the volume flow rate and T defines the time at which a fluid element emerges from the capillary nozzle (the base of the fluid drop being T = 0). For a cylindrical drop, the value QT/A is dimensionally equivalent to a

drop length, and thus Equation [55] is equivalent to Equation [54]. Both equations describe a critical drop length increasing proportionally with the yield-stress magnitude.

The only published investigation of yield-stress fluid drop impacts in open literature is by Nigen[148], who examined how impact dynamics on a solid plexiglass surface vary with changes in inertial energy. Fluid rheological behaviour was modelled using a Cross model, modified to include a yield-stress component. Whilst this was found to provide a good fit with viscometric measurements in the range $10^{-2} \leq \dot{\gamma} \leq 10^{3}$ s^{-1}, the 'double-definition' of combining both a Cross model (which models low and high shear-rate Newtonian regimes) and a yield-stress term (defining a yield-limit below which the fluid is solid-like) is rather ambiguous.

Upon pinch-off from a thin capillary tube (0.4 mm inner diameter), drops were observed to be prolate in shape, however drop heights in free-fall decrease asymptotically in time towards a non-spherical equilibrium shape; in disagreement with Davidson and Cooper-White[145] who expected viscoplastic drops to form an equilibrium spherical shape.

Upon impact at low velocities (v_z = 0.67 ms^{-1}), drops decrease sharply in height, however inertial spreading is small with no lamella formation; drops appear to be gently deposited on the surface and behave like a deformable solid. Nigen highlights that a slow creeping flow is observed thereafter until drops assume a sessile state after approximately 5 minutes. At slightly larger velocities (v_z = 0.85 ms^{-1}), drops retract after maximum inertial spreading and height oscillations are observed. After retraction, the diameter continues to spread at a near constant rate. At high impacts (v_z = 2.3 ms^{-1}), recoil is inhibited with wetted area retractions of no greater than 5% of the maximum spreading. Again, creeping flow is observed, however this is small and does not affect the maximum drop diameter.

Sessile drop shapes were established to be independent of the impact velocity (to within experimental error) for $v_z \leq 0.85$ ms^{-1}. For $v_z \geq 0.85$ ms^{-1} however the opposite is true; sessile drop shapes differ for impacts at different velocities. This variation in final shape indicates that yield-stress effects dominate over capillary forces during both the retraction and capillary driven spreading phases and inhibit drops from taking on final equilibrium states governed by Equation [26].

Nigen concludes that upon characterising the impact dynamics with respect to the Bingham number:

$$Bm = \frac{\tau_c D_E}{\mu\, v_z} \qquad [56]$$

where μ in Equation [56] is defined as the zero shear rate viscosity μ_0, the inertial spreading of low velocity drop impacts with Bm > 0.004 is small and subsequent creeping flow will occur towards a final sessile state[3]. The final sessile state of high velocity impacts with Bm < 0.004 however, will be identical to the diameter reached at the end of inertial spreading. In a similar fashion to Davidson and Cooper-White, Nigen's definition of the dimensionless Bingham number by attributing μ_0 to the viscosity term is not well posed because whilst the Bingham number characterises the ratio of viscous to yield-stress forces, viscous dissipation only occurs during fluid motion and the μ_0 term is only valid at zero shear rate. Moreover, the characterisation of sessile drop shapes using this dimensionless number is not appropriate because Equation [56] characterises the inhibiting yield-stress forces with respect to the viscosity and not the driving surface tension forces (it has been well established that sessile drop shapes vary with surface energies and not the fluid viscosity, which acts only to vary the rate at which sessility is reached). Nigen however does recognise that significantly more research into drop impact behaviour of yield-stress drops is required and should include investigations to assess the influence of shear-thinning and yield-stress magnitude.

[3] It is not clarified however whether it is capillary forces driving the spreading or the hydrostatic pressure from the weight of the undeformed prolate drop.

Yield-stress fluid studies also include gravitationally driven spreading of yield-stress fluids down an inclined plane[150], surface tension driven spreading through thin capillary tubes[133] and the behaviour of Saffman-Taylor instabilities (an overdamped case of Rayleigh-Taylor instability) forming within a host fluid[151]. These investigations are considered outside the framework of drop dynamics however, and will not be further discussed.

To summarise; currently there is a good understanding of Newtonian fluid drop dynamics, achieved through extensive theoretical and experimental research. This framework of understanding has been used as a basis from which more complex non-Newtonian fluid drop dynamic behaviour has been studied. Whilst this research is relatively new, it has produced significant advances, however there are numerous avenues of research that remain unexplored in detail, primarily due to the many different types of non-Newtonian fluids in existence. With regard to yield-stress fluids, there is scope for significant improvement of our understanding of drop dynamic behaviour by advancing upon limited existing studies; the current research is thus not only timely, it also has the opportunity to be extremely novel.

1.2 Aims and Objectives

The primary aim of this research is to establish, through experimentation, the influence of fluid yield-stress on drop dynamic behaviour from initial growth and detachment from a thin, flat ended capillary to the end of spreading after impact on a solid substrate. This research can be divided into four main research areas, namely;

A. drop detachment behaviour,
B. drop behaviour during free-fall,
C. drop impact behaviour and
D. drop spreading dynamics on a solid substrate.

This research describes each research area chronologically. Drops grow at the end of a capillary tube, then detach and fall towards the solid substrate, whereupon they impact and subsequently spread until they assume an equilibrium state. Dynamic behaviour during each stage is significantly different due to the varied inertial, surface tension and dissipative forces experienced by the drop.

In order to distinguish viscoplastic yield-stress characteristics from shear thinning and more classical Newtonian effects, the behaviour of viscoplastic fluid drops across a wide range of yield-stress magnitudes were compared with those of shear-thinning and viscous Newtonian fluid drops, ranging in their degree of shear-thinning and viscosity respectively. Due to the complex rheological characteristics of viscoplastic fluids however, the independent influence of yield-stress effects often cannot be established directly (i.e. direct comparison of two sets of experimental data or experimental data with theory) and indirect methods must be used.

The research objectives for each area are;

A. Drop detachment behaviour

To establish the influence of fluid shear-thinning and yield-stress magnitude on:

- the stability characteristics of drops attached to a thin capillary tube and
- the initial exponential growth of perturbations and transition to self – similar flow after the onset of instability.

Whereas the behaviour of Newtonian drops detaching under their own weight has been well established, the influence of fluid shear-thinning and yield-stress effects have not been analysed in detail. These objectives intend to progress existing research[145-147] by investigating how variations in both shear-thinning and fluid yield-stress magnitude influence drop detachment dynamics and how these may differ from well established Newtonian fluid behaviour.

B. Drop behaviour during free-fall

To establish the influence of shear-thinning and fluid yield-stress on the dynamic and equilibrium shapes of drops during free-fall. It has been well established that capillary forces drive the drop during free-fall towards an equilibrium spherical shape whilst changes in Newtonian viscous characteristics alter drop dynamic behaviour. This objective will provide experimental data expected to validate existing drop oscillation dynamic theories[37,100] and develop initial observations of detached yield-stress drops[145,148] by investigating whether fluid yield-stress can inhibit the formation of spherical drops and if so, whether there is a definable correlation between equilibrium drop shape and yield-stress magnitude.

C. Drop impact behaviour

To provide experimental evidence expected to support existing theories of Newtonian drop dynamic behaviour and establish the independent influence of shear-thinning effects and yield-stress magnitude on:

- the inertial impact phase of drop impact; from initial deformation up until a maximum inertial deformation is reached and
- the retraction phase driven by capillarity.

The research also reports on a number of additional objectives. These are;

- to establish the influence of surface wettability on Newtonian, shear-thinning and yield-stress fluid drop impact dynamics and
- to evaluate the predictive capability of existing drop impact prediction models through comparison with standardized experimental results and optimize those exhibiting the best performance for low impact velocity, high viscosity fluids; an impact regime where the predictive capability of existing models has not been studied in detail.

Research examining the effects of surface wettability on drop impact dynamics has been completed only for low viscosity fluids (μ~0.001 Pas). The current research extends this investigation by examining how surface wettability effects influence drop impact dynamics for increasingly viscous fluids.

D. Drop spreading dynamics

To provide evidence expected to support theoretical models describing the drop spreading behaviour of shear-thinning fluids and establish the independent influence of yield-stress magnitude on:

- the rate of drop spreading and
- the sessile shape of drops on surfaces of differing wettability.

The drop spreading behaviour of Newtonian and some shear-thinning fluids is well established, however very little research has yet been published that focuses on the inhibiting influence of fluid yield-stress on spreading drops after inertial impact. This objective will answer whether fluid yield-stress effects can influence the evolution of spreading drops and prevent the formation of sessile drop shapes according to classical theory over a wide range of impact velocities.

2. Methodology

2.1 Test fluid preparation and rheology

2.1.1. Newtonian fluids

Six Newtonian fluids, with viscosities in the range $0.001 \leq \mu \leq 0.925$ Pas were prepared by dissolving glycerol, with mass fractions 0.98, 0.96, 0.94, 0.9, 0.8 and 0.0 in de-ionised water. Glycerol solutions were mixed for approximately 2 hours to ensure homogeneity using a magnetic stirrer and then re-stirred before use. Table [2] displays the fluid properties of each solution.

Table 2. Fluid properties measured at 296 K for aqueous solutions of glycerol.

Glycerol mass fraction	Density [kgm^{-3}]	Viscosity [Pas] Error ± 0.005	Surface Tension* [Nm^{-1}]	Abbreviations used in figure captions
0.98	1256	0.925	0.069 ± 0.003	GL098
0.96	1251	0.631	0.069 ± 0.003	GL096
0.94	1248	0.428	0.069 ± 0.003	GL094
0.9	1236	0.213	0.069 ± 0.003	GL090
0.8	1211	0.056	0.070 ± 0.003	GL080
0.0	998	0.001	0.075 ± 0.003	Water

* Measured on a Kruss EasyDyne surface tensiometer using a Du Nouy ring method. Errors are based on the correct reading of de-ionised water at 296K.

Viscosity measurements for fluids with $0.056 \leq \mu \leq 0.925$ Pas are displayed in Figure [10] and were obtained by performing a controlled rate (CR) test across the shear rate range $0 \leq \dot{\gamma} \leq 100\ s^{-1}$ using a Haake-Mars rotational rheometer with a cone-and-plate configuration (35mm diameter, 2^o angle).

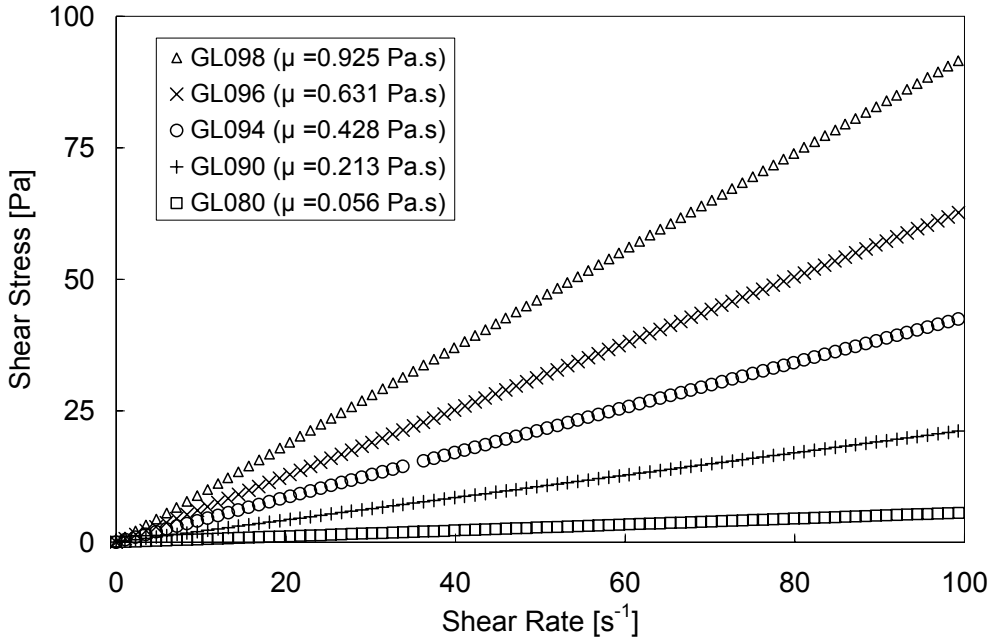

Figure 10. Shear stress (τ) versus shear rate ($\dot{\gamma}$) for glycerol solutions with μ = 0.925 Pas (triangle symbol), μ = 0.631 Pas (cross), μ = 0.428 Pas (circle), μ = 0.213 Pas (plus) and μ = 0.056 Pas (square) determined using a Haake-Mars rotational rheometer with a cone and plate configuration (35mm diameter, 2^{o} angle).

2.1.2. Shear-thinning fluids

Four shear-thinning fluids were prepared by dissolving Xanthan gum with mass fractions 0.00125, 0.0025, 0.005 and 0.01 in de-ionised water. The solutions; none of which exhibit yield-stress characteristics, were prepared by slowly adding the Xanthan gum whilst continuously swirling the fluid in order to disperse the powder and avoid agglomeration. The solutions were then subjected to continued mixing using a magnetic stirrer for two hours and re-stirred before each use. Each fluid sample was used within 48 hours to avoid changes in viscometric characteristics due to bacterial degradation. The fluid properties of each solution are detailed in Table [3].

Viscosity measurements are displayed in Figure [11] and were obtained by performing a controlled rate (CR) test across the shear rate range $0\ s^{-1} \leq \dot{\gamma} \leq 100\ s^{-1}$ using a Haake-Mars rotational rheometer with a cone-and-plate configuration (35mm diameter, 2^o angle).

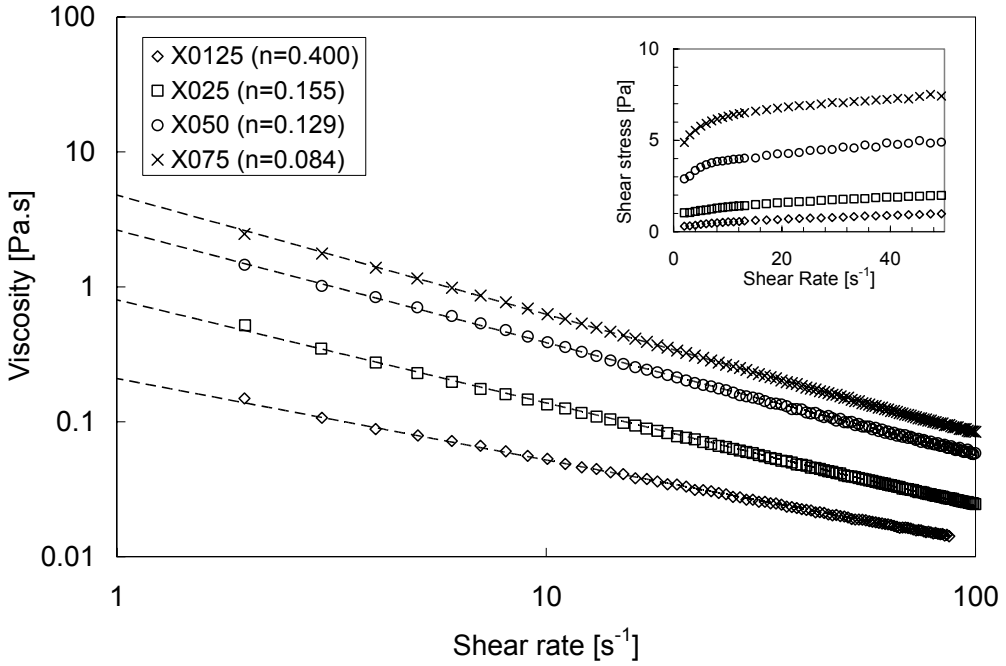

Figure 11. Viscosity (μ) plotted against shear rate ($\dot{\gamma}$) and (inset) shear stress (τ) plotted against shear rate ($\dot{\gamma}$) for shear-thinning fluid solutions of Xanthan gum in de-ionised water with mass fractions ranging between 0.00125 and 0.01. Dashed lines represent best fit power law model distributions (Equation 37).

To characterise each fluid solution, rheological measurements were fitted with a power law model (Equation 37); chosen to allow fluid shear-thinning properties to be most simply characterised in terms of the power law index n and the consistency coefficient K. The fluids investigated did not show appreciable low and high Newtonian regions, therefore the Cross (Equation 38) and Carreau (Equation 39) models were deemed overly complex. Table [3] displays the fitted parameters for each fluid solution.

Table 3. Fluid properties measured at 296 K for aqueous solutions of Xanthan gum and power law model fitted parameters n and K.

Xanthan Gum mass fraction	Density [kgm^{-3}]	Surface Tension* [Nm^{-1}]	Consistency coefficient K [Pas^n]	Power law index n	Abbreviations used in figure captions
0.00125	998	0.0713 ± 0.0015	0.208 ± 0.001	0.400 ± 0.003	X0125
0.0025	998	0.0714 ± 0.0001	0.962 ± 0.006	0.155 ± 0.005	X025
0.0050	998	0.0704 ± 0.0008	2.846 ± 0.015	0.129 ± 0.004	X05
0.0075	998	0.0717 ± 0.0012	5.064 ± 0.027	0.084 ± 0.005	X075

*Measured on a Kruss EasyDyne surface tensiometer using a Du Nouy ring method . Errors are based on the standard deviation of five samples for each shear thinning fluid solution.

2.1.3. Yield-stress fluids

Seven yield-stress fluid solutions were prepared by dissolving a commercial hair-gel, with mass fractions 0.2, 0.25, 0.3, 0.35, 0.4, 0.45 and 0.5 in de-ionised water; hair-gel is comprised of a mixture of alcohol, water, carbomers, surfactants and glycerin and mixes readily with water. The solutions were mixed slowly in a container to avoid the formation of bubbles, left to settle for 24 hours and then thoroughly mixed to ensure homogeneity using a magnetic stirrer. The fluid properties of each solution are detailed in Table [4]. Each hair-gel solution was used within 48 hours of preparation to minimise any changes in viscometric properties, which can become visibly apparent after 1-2 weeks.

Yield-stress magnitudes were measured by performing a controlled stress (CS) test on a Haake-Mars rotational rheometer using a plate-and-plate configuration with the surfaces covered with sandpaper to avoid slip. Measurements were made within the range 0 Pa $\leq \tau \leq$ 50 Pa. Aqueous solutions of hair-gel are model yield-stress fluids; altering the mass fraction of the hair-gel allows τ_c to be varied in a continuous fashion. Fluid yield-stress magnitudes were found to vary as a linear function of the solution concentration, as detailed in Figure [12].

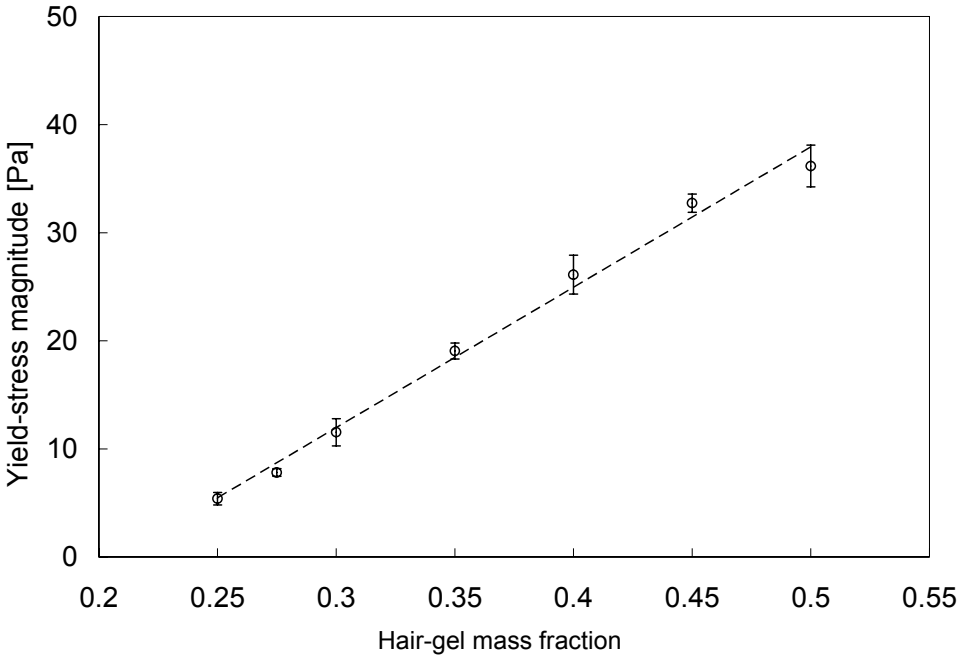

Figure 12. Variation of fluid yield-stress magnitude τ_c with hair-gel mass fraction.

Whereas there is continued debate over whether it is entirely accurate to define a fluid as having a yield-stress, as discussed in **§1.2.5.2**, the ratio of the fluid relaxation time-scale for applied stresses less than τ_c to the observed experimental time-scale in each of the drop dynamic processes investigated is very high (Equation 49), indicating that it is reasonable to assume the fluid exhibits solid-like behaviour. The viscometric properties of each fluid solution were therefore fitted using a Herschel-Bulkley rheological model (Equation 46). Table [4] displays the fitted model parameters for each solution.

Table 4. Fluid properties, measured yield-stress and Herschel Bulkley model (Equation 46) fitted parameters n and K for yield-stress fluid solutions at 296K.

Hair-gel mass fraction	Density [kgm^{-3}]	Surface Tension* [Nm^{-1}]	Measured Yield-stress, τ_c [Pa]	Consistency coefficient K [Pas^n]	Power law index n	Abbreviations used in figure captions
0.2	1037	0.0341 ± 0.0008	0	1.443 ± 0.009	0.4747 ± 0.005	YSF020
0.25	1047	0.0343 ± 0.0008	5.4 ± 0.6	3.096 ± 0.019	0.4311 ± 0.007	YSF025
0.3	1057	0.0340 ± 0.0015	11.5 ± 1.3	5.533 ± 0.015	0.3775 ± 0.004	YSF030
0.35	1067	0.0340 ± 0.0024	19.1 ± 0.7	6.982 ± 0.030	0.3730 ± 0.005	YSF035
0.4	1076	0.0340 ± 0.0031	26.1 ± 1.8	7.936 ± 0.033	0.3727 ± 0.004	YSF040
0.45	1086	0.0340 ± 0.0040	32.7 ± 0.9	12.05 ± 0.039	0.3579 ± 0.007	YSF045
0.5	1096	0.0340 ± 0.0041	36.2 ± 1.9	19.93 ± 0.051	0.3116 ± 0.006	YSF050

* Measured on a Kruss EasyDyne surface tensiometer using a Du Nouy ring method. Errors are based on the standard deviation of ten samples.

Viscosity measurements for fluids with $0 \leq \tau_c \leq 26.1$ are displayed in Figure [13]. These were obtained by performing a controlled rate (CR) test across the shear rate range $0 \leq \dot{\gamma} \leq 100\ s^{-1}$.

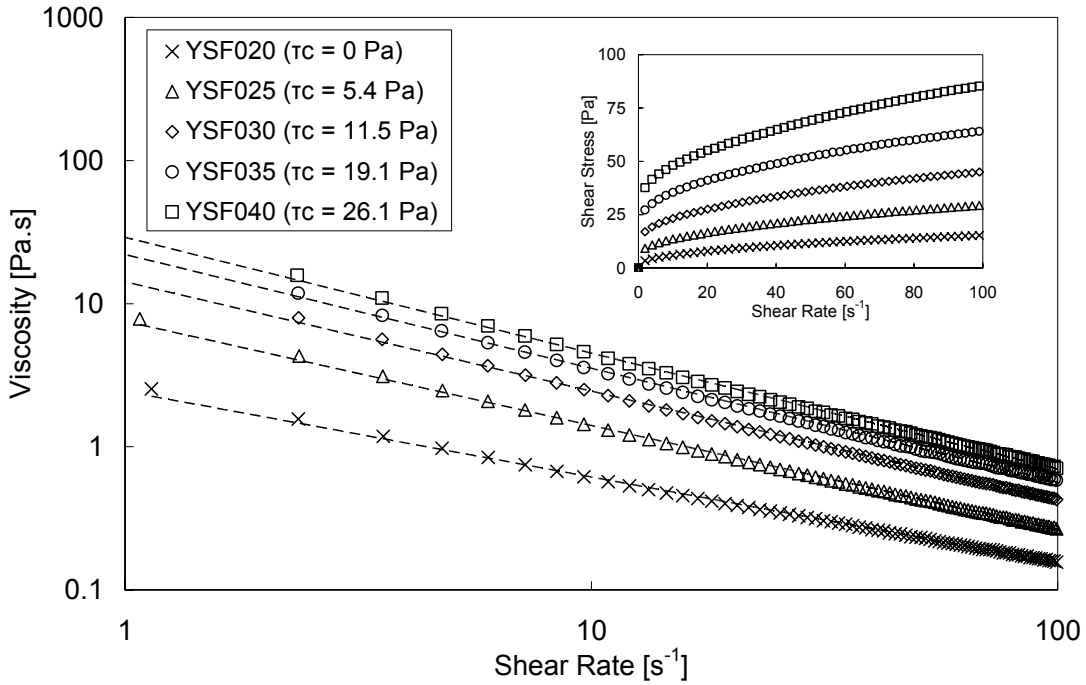

Figure 13. Viscosity (μ) plotted against shear rate ($\dot{\gamma}$) and shear stress (τ) plotted against shear rate ($\dot{\gamma}$) (inset) for yield-stress fluid solutions with τ_c= 0 Pa (cross), τ_c=5.4 Pa (triangle), τ_c=11.5 Pa (diamond), τ_c= 19.1 Pa (circle) and τ_c= 26.1 Pa (square), measured using a Haake-Mars rotational rheometer with a 35mm plate and plate configuration. Dashed lines represent best fit Herschel-Bulkley model distributions (Equation 46).

The influence of dynamic surface tension effects on yield-stress drop dynamic behaviour must also be considered due to the presence of surfactants. Surfactants act to reduce the interfacial surface tension. Reducing the surface tension of a fluid drop typically decreases the rate of pinch-off during detachment, increases the maximum spread upon impact and reduces the likelihood of retraction/rebound. Dynamic surface tension indicates non-equilibrium surface tension characteristics and is usually brought about by the creation of new interface regions. Drop dynamic behaviour can occur over very short time intervals, typically;

- Drop detachment (~10-30 ms)
- Drop impact – Inertial expansion phase (~3-7 ms)
- Drop impact – Retraction phase (~15-30 ms)
- Drop spreading – (~ms - minutes)

Significant amounts of new liquid-gas interface can be created during these periods, especially for high velocity impacts. The drop dynamic behaviour of fluids containing surfactant molecules exhibiting long migration periods can therefore be significantly influenced by dynamic surface tension effects.

The surfactant Polysorbate 20 is present in each of the yield-stress fluid solutions at concentrations significantly higher than the C.M.C. Equilibrium surface tension measurements of each solution, displayed in Table [4] correlate with previous measurements[157] of Polysorbate 20 in de-ionised water (σ = 0.034 Nm^{-1}) for concentrations at and above the C.M.C (0.06 mg ml^{-1}). Previous research establishes that above the C.M.C., adsorption kinetic timescales will be drastically reduced due to demicellisation close to the surface, as highlighted in Figure [14] and described in **§1.2.3.5**. The surface tension of the viscoplastic fluids was therefore assumed to be constant during each drop dynamic process.

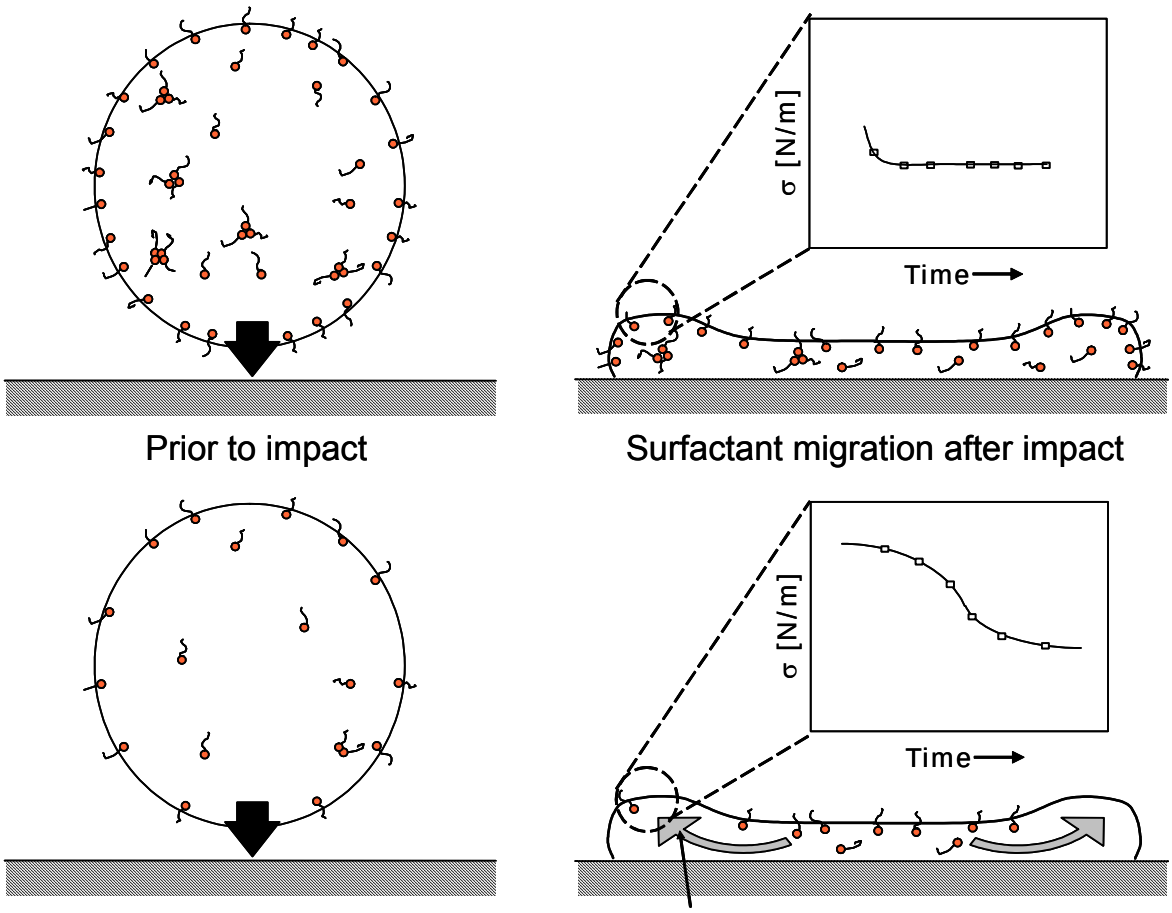

Figure 14. Migration of surfactant molecules during drop impact and the temporal variation of surface tension σ in regions of newly created surface for (lower) a fluid containing a surfactant concentration significantly below the C.M.C and (upper) a fluid containing a surfactant concentration significantly greater than the C.M.C.

2.2 Experimental apparatus

2.2.1 General experimental apparatus design

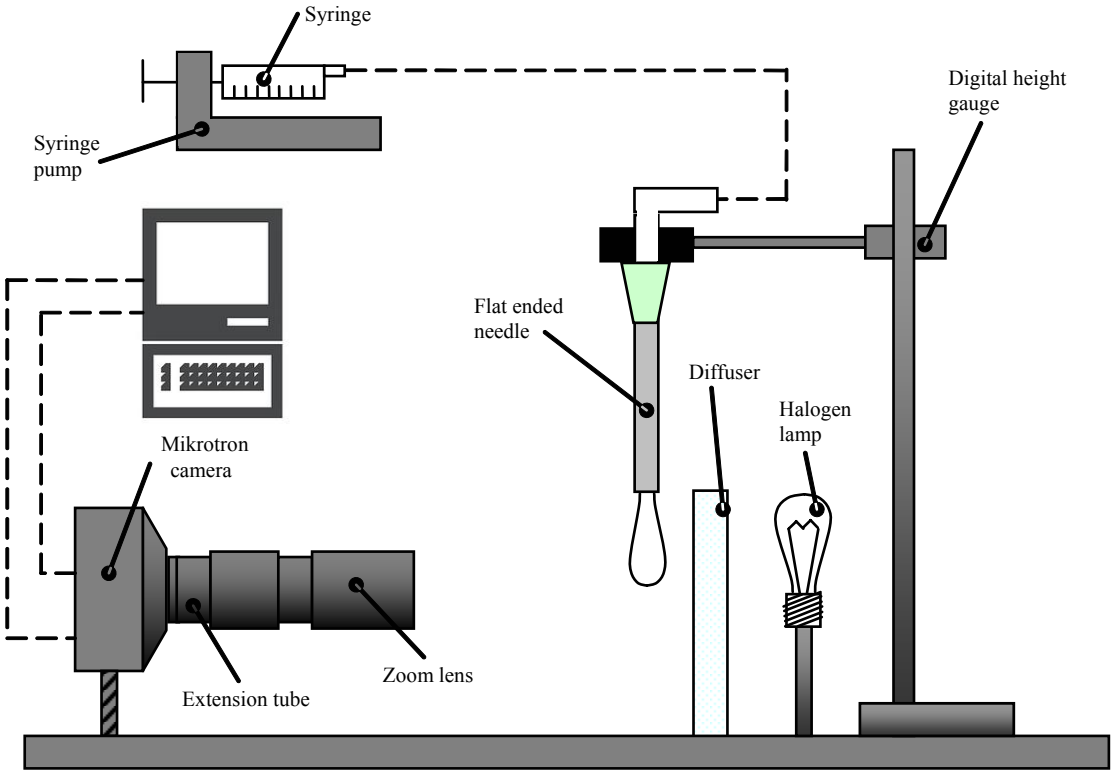

Figure 15. Drop generation and image capturing equipment.

The general configuration of the experimental apparatus is shown in Figure [15] and comprises a 1.27mm outer diameter (O.D.), 0.838mm inner diameter (I.D.) Needle gauge 18 flat-ended metallic hypodermic needle attached to a digital height gauge with a precision of ± 0.01 mm. Control of drop detachment was achieved using a screw driven mechanical syringe pump. Drops were allowed to form slowly at the end of the needle and detach under their own weight. The formation process could take up to a minute for the higher mass fraction hair-gel solutions, however timescales for typical drop formation were of the order of seconds.

Drop dynamic behaviour was observed and recorded using a high frame rate Mikrotron MC1311 camera, equipped with a Sony 18mm-108mm / f2.5 zoom lens and

30mm extension tube, aligned orthogonally to the substrate. The substrate was backlit using a 100W halogen lamp positioned behind a light diffuser. Digital images were recorded at 1000 f.p.s (frames per second) with a maximum achievable resolution of 1280 x 1024 pixels. To achieve a frame rate of 1000 f.p.s however, the image resolution was decreased to 720 x 512 pixels. The magnification was manipulated so that the image could accommodate the maximum spread of impacting drops or the full height of detaching drops and was kept constant throughout each study with a typical spatial resolution of 32.6 mm/pixel. Lighting positions and camera settings were also maintained to ensure conditions were identical for each drop impact recording. The light source could heat up significantly over short periods of time, therefore to ensure temperature consistency to within ± 2 ^{o}C of room temperature (23 ^{o}C), the light was switched on only when needed. When the light was switched on, it was allowed to reach a maximum intensity before any experimentation was performed. This took no longer than 30 seconds. Vibrational isolation and fine optical alignment were achieved by attaching the apparatus to an optical bench. The calibration of drop dimensions was achieved by establishing the ratio of pixilated to measured needle outer diameter.

2.2.2 Adaptation for drop stability and detachment studies

The arrangement shown in Figure [15] is used with the needle reduced to a fall height of H_f = 15mm so that both the needle and drop were sufficiently backlit. Drop stability and detachment characteristics were analysed through the measurement of minimum neck width, drop height and the vertical distance between the base of the drop and the position of minimum neck thickness, as detailed in **§2.8.1**. For each fluid solution, the growth and detachment dynamics of five drops were recorded and averaged to establish errors magnitudes and ensure repeatability.

2.2.3 Adaptation for drop impact and free-fall studies

The experimental apparatus was modified so that the needle was centered over an aluminium square block (40mm x 40mm) upon which different substrates were placed. Studies of drop impacts were made for fall heights of 7.5, 10, 25, 50, 100 and 200mm, corresponding to a Weber number range of $1.7 \leq We \leq 240$ for the Newtonian solutions, $0.8 \leq We \leq 194$ for the shear-thinning fluids and $0.7 \leq We \leq 340$ for the yield-stress fluids. Drop impact behaviour was analysed through the measurement of axisymmetric drop diameter and apex height, as detailed in **§2.8.2** and **§2.8.3** respectively. For each fall height, the impact dynamics of five drops were recorded and averaged to establish errors magnitudes and ensure repeatability.

The influence of surface wettability was determined by comparing equivalent drop impacts on two different substrates; a hydrophobic Parafilm-M coating and a hydrophilic clean glass surface. To characterise the properties of each surface, the equilibrium contact angles of de-ionised water drops were measured.

Drops of the YSF040 solution could not be analysed from fall heights lower than 10 mm because impacts were observed to occur before complete detachment from the needle. Furthermore, for fall heights greater than 100mm, drops with yield-stress magnitudes greater than or equal to the YSF030 solution (τ_c = 11.5 Pa) were observed to occasionally rotate during free fall, resulting in an angled impact. This phenomenon could be observed because of the prolate drop shapes. Nigen[148] also observed this phenomenon and noted that even plastic tubing surrounding the falling drop and shielding it from external air currents did not eliminate the effect. All angled drop impacts were discounted from the experimental results.

The experimental configuration and methodology used for the examination of drop impacts was also used for drop free-fall studies with a number of alterations. Firstly, additional viscoplastic fluid solutions were studied to obtain a more detailed relationship between fluid yield-stress magnitude and free-fall drop shape. Viscoplastic fluids with

hair-gel mass fractions of 0.275 (τ_c = 7.8 ± 0.36 Pa, σ = 0.034 N.m^{-1}) and 0.325 (τ_c = 15.4 ± 0.4 Pa, σ = 0.034 N.m^{-1}) were created for this specific study. Additional experiments were also completed so as to incorporate the influence of drop size on viscoplastic fluid free-fall equilibrium drop shape. These experiments were completed using a smaller 0.813 mm O.D, 0.495 mm I.D. (Needle gauge 21) flat ended hypodermic needle. The characteristics of viscoplastic drops detaching from this smaller nozzle are detailed in Table [5]. Finally, to lengthen the periods over which free-fall drop dynamics were studied, some experiments (where necessary) also included additional fall heights of 300, 400 and 500mm. These additional heights were only used when drop shapes in free-fall did not reach equilibrium within a fall height of 200 mm. For each fluid solution, the free-fall dynamics of five drops were recorded at each fall height to establish errors magnitudes and ensure repeatability.

2.2.4 Adaptation for drop spreading studies

Drop spreading experiments were designed to be performed within a translucent acrylic box, built to surround the substrate region with saturated air to eliminate evaporative effects whilst allowing digital images to be recorded. With the aim of minimising the box volume and thus the time period required to obtain complete saturation, the minimum box width and breadth dimensions were constrained by the size of the substrate to be placed inside. The minimum height was constrained by the requirement that the camera field of view contained no box edges or corners; the visual clarity of the images being of importance to ensure accurate drop dimensional measurements. The box was designed to include a moat following the internal perimeter through which the enclosed air could become saturated. The moat (15mm wide, 13.5 mm tall) was designed to contain a volume of de-ionised water greater than that required to saturate the enclosed air and to maximise the surface area of water (56 cm^2 for a box volume of 721 cm^3) and hence the evaporation rate.

To ensure an airtight seal, internal corner and edge seals of the box were coated with paraffin wax along with holes in the optical bench. The seals were then tested for

leaks by filling the box completely with water. To minimise changes in image clarity, surfaces were cleaned thoroughly and the box sealed to the optical bench, where it remained static thereafter. Access to the box was achieved through a side window. Once the substrate was inserted and correctly positioned, the window was closed and sealed along the edges with putty. The box was then left for an hour to allow the enclosed air to become re-saturated. Impacting drops entered the box via a 10 mm circular hole drilled in the top of the box. A plug was removed just prior to drop detachment and quickly replaced after impact to prevent the escape of saturated air. For drop impacts at fall heights below 25 mm, the needle protruded through the plug. A schematic of the acrylic box design and its position within the experimental apparatus is displayed in Appendix A and Figure [16] respectively.

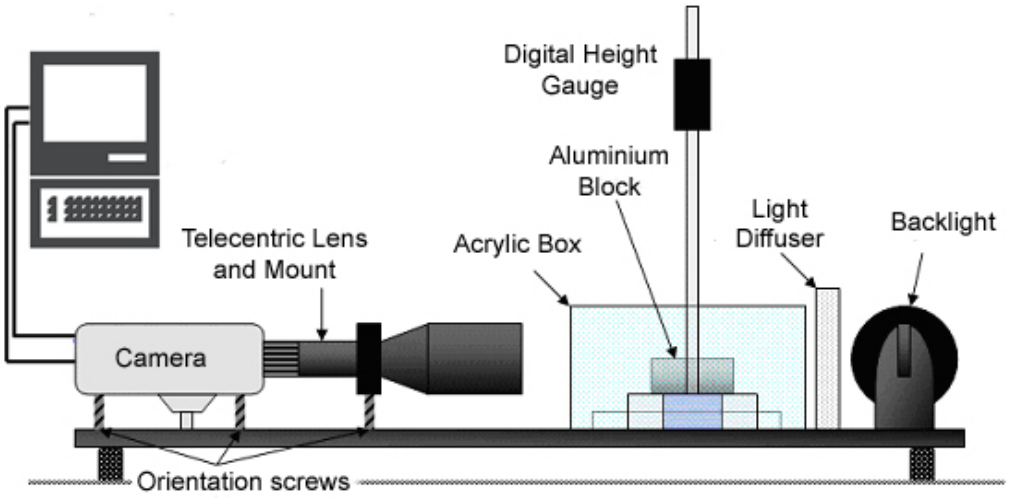

Figure 16. Side view of experimental apparatus used for drop spreading experiments.

The spreading dynamics of drops on surfaces after inertial impact can occur over timescales significantly longer than either drop detachment or impact processes. A low speed Sony black and white video CCTV CCD camera was therefore utilized to record spreading processes. The camera was connected to a computer via a live-feed frame grabber adaptor and recordings were made using Capture Studio Professional v4.05. The camera was capable of 30 f.p.s (interlaced) or 15 f.p.s (single frame) however digital images were recorded between 1 and 5 f.p.s for up to 15 minutes with a maximum achievable resolution of 768 x 576 pixels. The camera was equipped with a Vicotar Type:

T150/0.19 114 mm/ 25.7 x 19.3 mm F.O.V (field of view based on 1/3" sensor size) telecentric measurement lens combined with a 10mm extension tube to produce a correct image focus. A telecentric lens was used primarily to ensure a consistent magnification over every part of the object image and eliminate optical distortion, which could introduce inaccuracies in measured drop dimensions; for drops on wettable surfaces where spreading is significant and extends towards the edges of the image, distortions would become influential. Figure [17] highlights image differences between conventional and telecentric lenses.

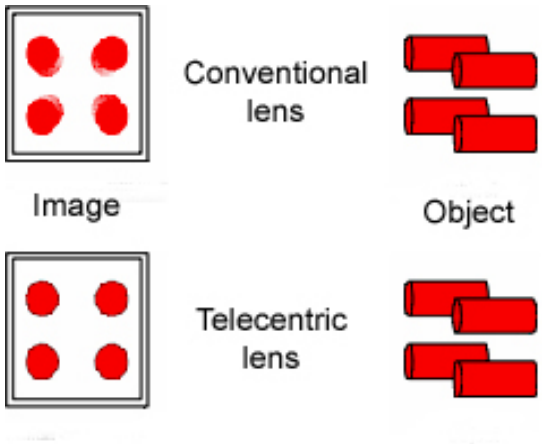

Figure 17. A comparison of images produced by conventional and telecentric lenses.

The experiments performed were identical to the drop impact study, however recordings were made over longer periods so that sessile drop shapes could be established.

2.3 Image post-processing

Digital image processing was performed using the IMAQ functionality suite in Labview v6.1. An 8-bit digital image is a matrix of pixel intensities, ranging from black [0] to white [255]. Iterative routines can be employed to perform fast arithmetic, filtering and measurement processes on the image matrices in a data set, typically consisting of close to a thousand images. Figures [19] and [20] detail the flow diagrams of the programmed routines. The first routine was used to extract relevant information for the drop free-fall, impact and spreading experiments. The second routine was used for drop

detachment experiments. Typically the algorithm processes include the subtraction of the background image, image filtering and de-speckling to identify and remove unwanted pixels originating from dust or airborne particulates, the retrieval of relevant pixel information used to establish drop widths, heights and pixel areas and the storage of this information in a simple array string. Drop width and height dimensions were obtained by establishing the lowest and highest row and column numbers where the variation of pixel intensities over 3 pixel lengths exceeds a threshold intensity value of 60, as displayed in Figure [18]. The rake function in Figure [20] performs a sub-routine where the smallest horizontal pixel distance between the two edges of the drop neck was established. The horizontal row where this occurs was also recorded. This sub-routine required the manual selection of an area around the neck region to avoid values of zero that would otherwise arise if the whole image was used. The outer diameter of the flat ended needle was measured for each results set and used as a dimensional calibration to convert pixel dimensions to S.I unit lengths. These calibration measurements were extracted manually from the images using a simple routine programmed specifically for the task.

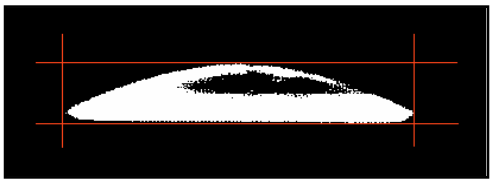

Figure 18. Drop pixel width and height measurement through establishing the maximum and minimum row and column where pixel light intensities exceed a threshold value.

Background image subtraction and filtering (removal of pixels with intensities less than 30) was performed to improve image consistency by reducing small fluctuations in background light intensity due to the light source. De-speckling removed erroneous regions with less than 30 pixels (drop areas in contrast show measured areas of greater than 3000 pixels) that would ordinarily be recognized by the algorithm. Image inversion was performed prior to subtraction of the background image because drops appear as a dark image on a light background; inversion results in high image intensities in the drop region (near 255) with low intensities in the background (near 0). Subtraction of the background image therefore does not significantly affect the drop region in the image. Schematics of both Labview post-processing routines are displayed in Appendix B.

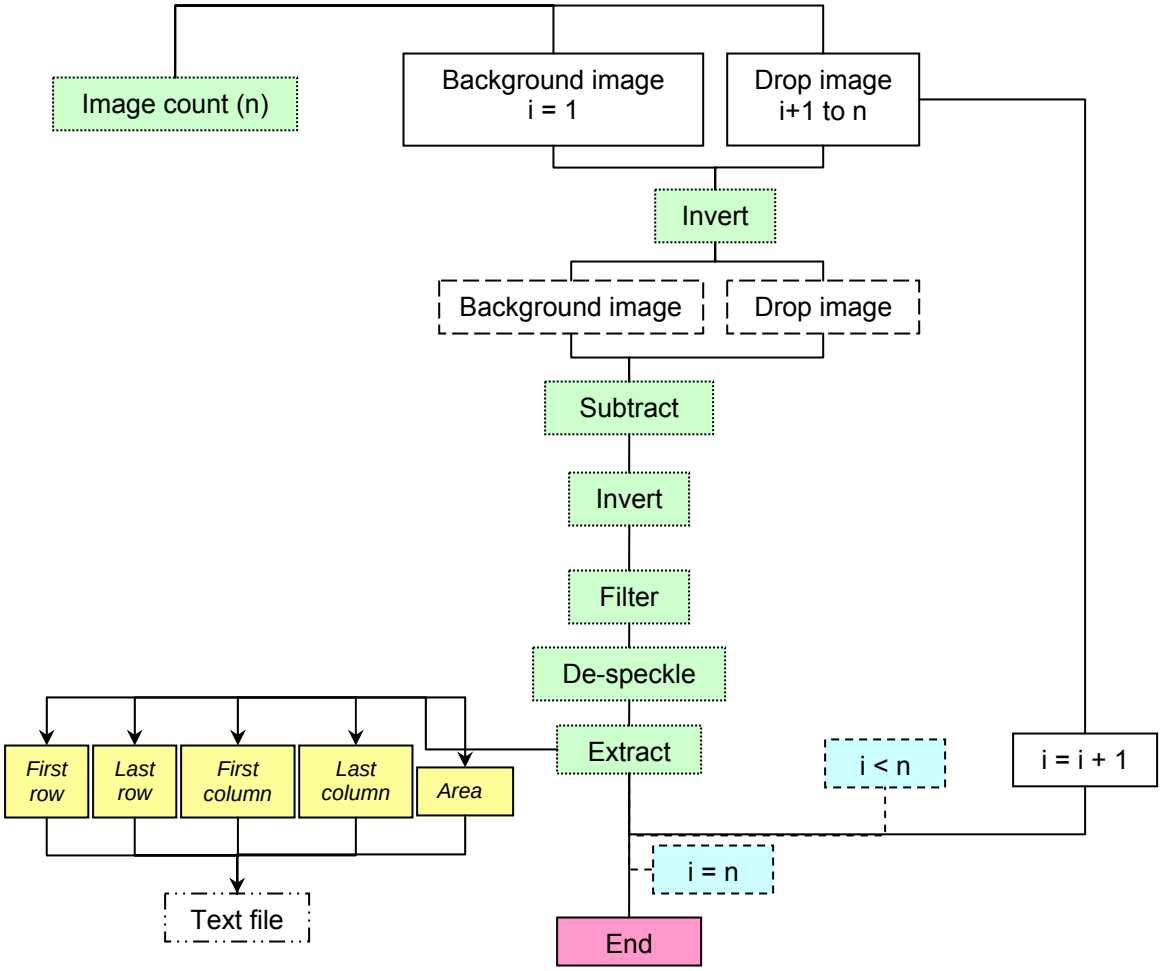

Figure 19. Flow diagram of image processing algorithm used to extract drop width, height and area for free-fall, impact and spreading experiments.

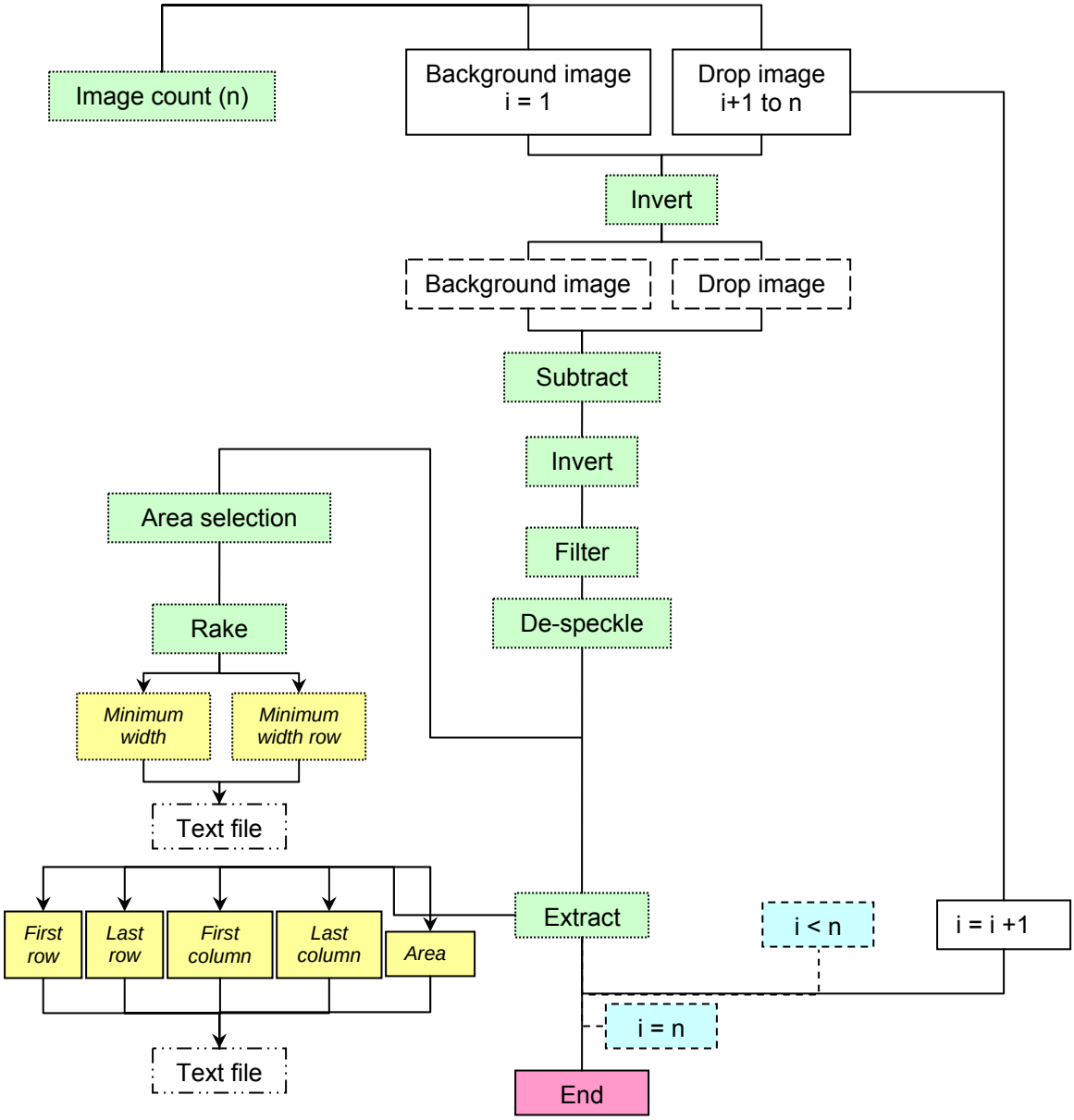

Figure 20. Flow diagram of image processing algorithm used to extract minimum drop neck widths, heights and areas for detachment experiments.

2.4 Drop production and characterization

The equivalent spherical diameter D_E of each fluid solution was established by averaging 50 drop weight measurements made using a Mettler Toledo MT100 precision balance and substituting into:

$$D_E = \sqrt[3]{\frac{6m}{\pi\rho}} \qquad [57]$$

where m is the average drop weight. Values of D_E were not extracted directly from the digital images because of limitations in measurement accuracy arising from both drops oscillations during free-fall and non-spherical equilibrium shapes of some yield-stress fluid drops. The average drop mass[4] and D_E for each solution is detailed in Table [5].

Table 5. Drop weight, capillary length and equivalent diameter measurements for drops produced using both the 0.838mm I.D. (Needle gauge 18) and 0.495mm I.D. (Needle gauge 21) flat-ended metallic needles.

Fluid Abbreviation	Capillary tube I.D. Diameter [mm]	Average Drop mass [mg]	Measurement error [mg]	D_E [mm]	Standard Deviation [mm]	Capillary length a [mm]
GL098	0.838	19.64	0.332	3.102	0.0175	2.37
GL096	0.838	19.81	0.329	3.116	0.0172	2.37
GL094	0.838	19.50	0.166	3.101	0.0087	2.37
GL090	0.838	20.06	0.474	3.141	0.0248	2.39
GL080	0.838	19.50	0.293	3.133	0.0157	2.43
Water	0.838	22.07	0.482	3.480	0.0254	2.77
X0125	0.838	21.96	0.324	3.474	0.0171	2.70
X025	0.838	20.50	0.583	3.396	0.0322	2.70
X05	0.838	21.10	0.127	3.428	0.0069	2.68
X075	0.838	19.63	0.115	3.347	0.0065	2.70
YSF020	0.838	12.10	0.224	2.848	0.0176	1.83
YSF025	0.838	10.81	0.336	2.743	0.0284	1.82
YSF030	0.838	10.05	0.308	2.678	0.0273	1.81
YSF035	0.838	9.59	0.275	2.636	0.0142	1.80
YSF040	0.838	9.39	0.147	2.617	0.0136	1.79
YSF045	0.838	9.44	0.168	2.619	0.0156	1.79
YSF050	0.838	9.22	0.164	2.602	0.0154	1.78
YSF030	0.495	7.12	0.086	2.344	0.0094	1.81
YSF0325	0.495	6.83	0.083	2.307	0.0093	1.81
YSF035	0.495	6.39	0.165	2.253	0.0194	1.80
YSF040	0.495	6.00	0.129	2.200	0.0158	1.79

[4] Drop mass measurements were performed at the lowest achievable flow rate (allowing drops to detach under their own weight). This detachment process was employed for all the experiments presented in this thesis. Mass measurements show a good repeatability. To ensure small variations in flow rate did not result in changes in detached drop mass, measurements were also made at slightly larger flow rates. Drop masses were found not to differ from the original measurements by amounts larger than the experimental error. This indicates that small variations in the flow rate (close to the minimum rate achievable) do not significantly influence drop mass.

Figure [21] displays the variation of D_E with glycerol, Xanthan gum and hair-gel mass fraction respectively. Whereas the drop diameters of the Newtonian fluids in the range $0.056 \leq \mu \leq 0.925$ Pas (upper figure) do not vary significantly ($D_E = 3.118 \pm 0.016$ mm), shear-thinning drop diameters (middle figure) vary as a linear function of the Xanthan gum mass fraction, X, and are well represented by $D_E = 3.48 - 16.483X$ mm (short dashed line). The variation in D_E with shear-thinning characteristics is thought to be due both to changes in the volume of fluid remaining attached to the capillary after drop detachment and the formation of satellite droplets during detachment.

Viscoplastic fluid drop diameters (lower figure) also vary as a linear function of the hair-gel mass fraction, Y, and are well represented by $D_E = 3.059 - 1.222Y$ mm (short dashed line). The zero mass fraction viscoplastic fluid measurement (filled circle symbol on the y-axis) corresponds to a dilution of Polysorbate 20 in de-ionised water with a concentration of 0.08mg/ml; chosen to be well above the C.M.C to minimise dynamic surface tension effects during drop detachment. This fluid is Newtonian with the same surface tension as the viscoplastic fluids (σ = 0.034 Nm^{-1}). Decreases in D_E with increasing hair-gel mass fraction are thought to originate primarily from changes in fluid density. Although changes in fluid density do not appear to significantly influence D_E for the Newtonian fluids, the Bond number $Bo = \rho D^2 g/\sigma$ of the viscoplastic fluids in comparison is nearly double ($\sigma \sim 0.07$ N/m for the Newtonian fluids, σ = 0.034 N/m for the viscoplastic fluids) due to the significantly smaller surface tension. This dimensionless parameter characterises the ratio of gravitational forces to surface tension forces. A larger Bond number indicates that surface tension effects are less dominant (i.e. capillary forces are comparatively weaker) and changes in fluid density are more likely to have an influence on the final drop diameter.

The significant difference in D_E between a drop of de-ionised water (D_E = 3.48 mm, open triangle symbol) and an equivalent drop with a Polysorbate 20 additive (D_E = 3.048 mm, open square symbol) in the lower figure of Figure [21] highlights the effect of surface tension on drop detachment and agrees with previous observations of drop detachment behaviour[10,11,16]; where decreases in surface tension reduce the maximum supportable weight of hanging drops from a thin capillary tube.

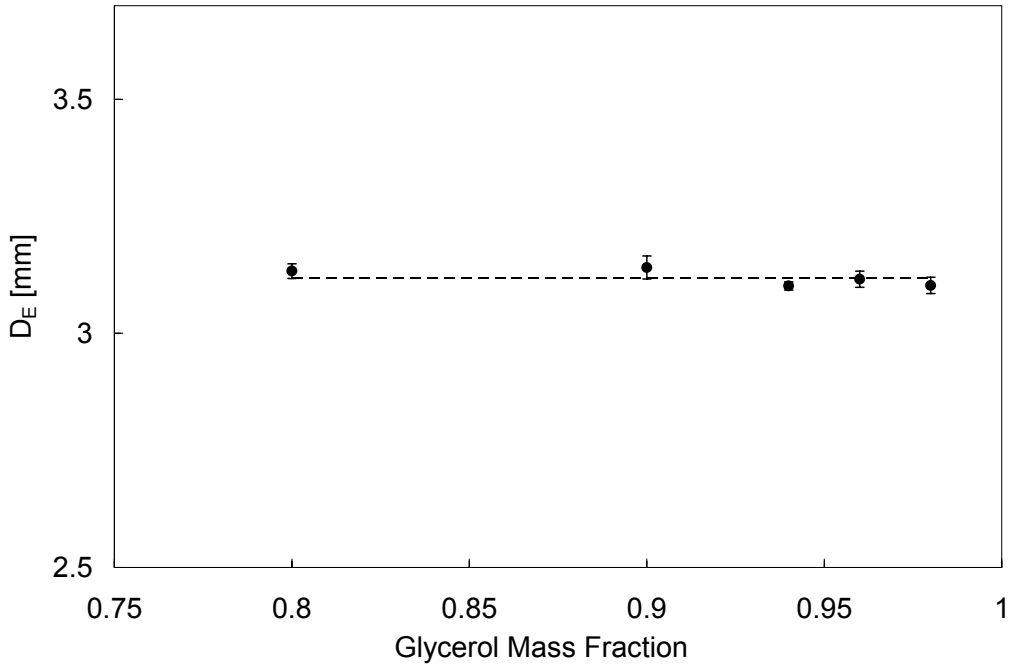
3.5
3
2.5
D_E [mm]
0.75
0.8
0.85
0.9
0.95
1
Glycerol Mass Fraction

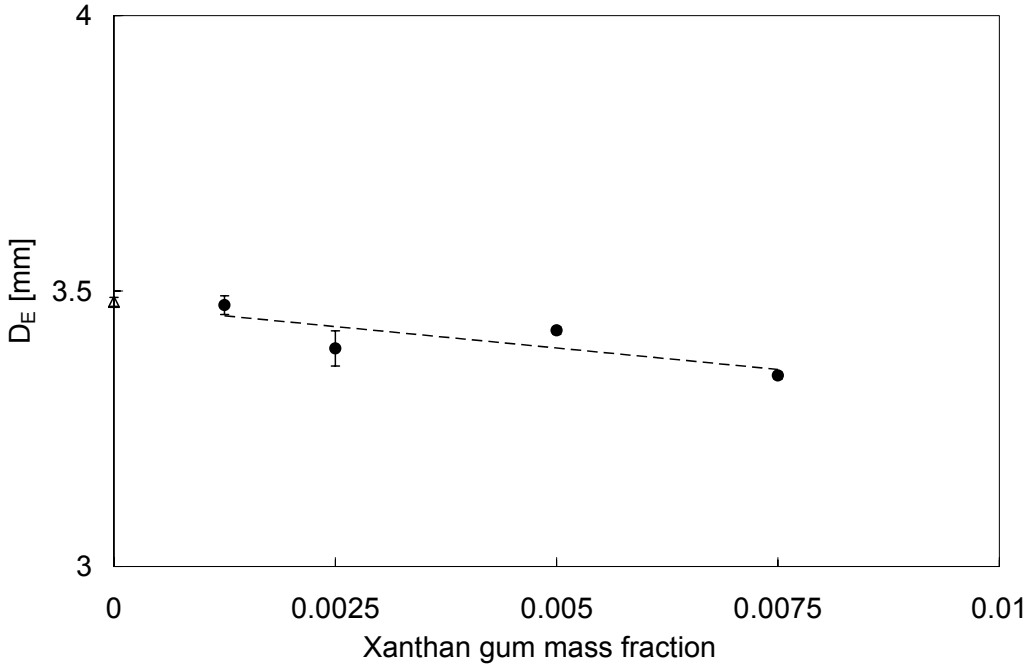
4
3.5
3
D_E [mm]
0
0.0025
0.005
0.0075
0.01
Xanthan gum mass fraction

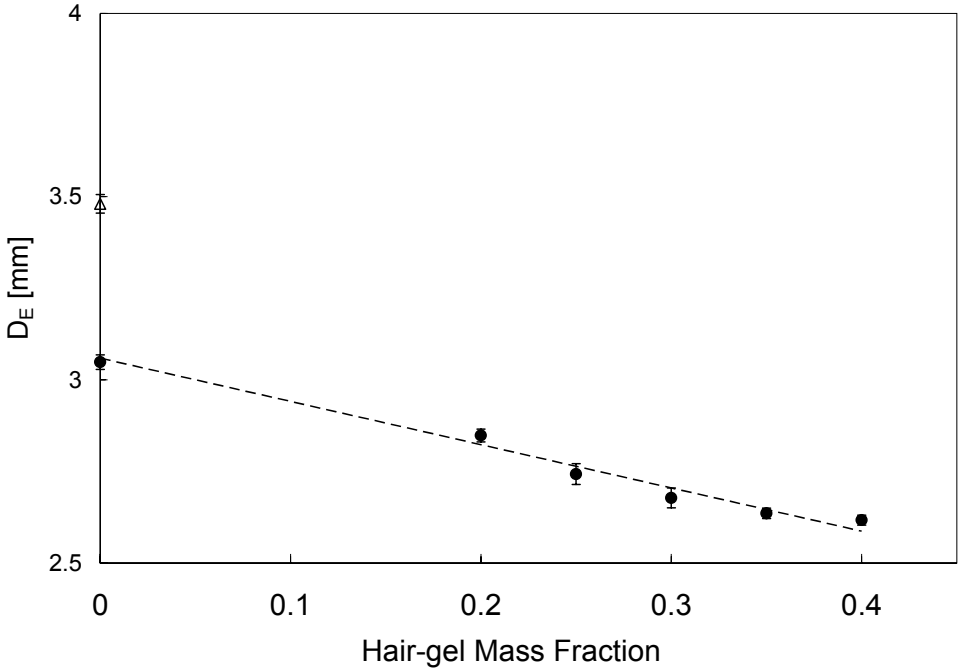

Figure 21. Drop D_E produced using the 0.838mm I.D. (Needle gauge 18) needle and plotted against (upper figure) glycerol, (middle figure) Xanthan gum and (bottom figure) hair-gel mass fraction. In all figures, the short dashed line corresponds to a least square linear best fit of the experimental results (filled circle). (upper figure) Experimental data is well represented by $D_E = 3.118$ mm. (middle figure) Experimental data is well represented by $D_E = 3.48 – 16.483X$ mm where X is the Xanthan gum mass fraction. (bottom figure) Experimental data is well represented by $D_E = 3.059 – 1.222Y$ mm where Y is the hair-gel mass fraction. The filled circle symbol on the y-axis in the bottom figure corresponds to a zero hair-gel mass fraction measurement. This is the measured value of D_E for drops of de-ionised water containing concentrations of Polysorbate 20 well above the C.M.C. ($\sigma = 0.034$ Nm^{-1}) The open triangle symbol corresponds to a measurement of D_E for de-ionised water ($\sigma = 0.075$ Nm^{-1}). Each symbol corresponds to an average of 5 drop measurements. Where not observed, errors are comparable in size to symbol dimensions.

To characterise the shape of drops, comparisons of their radii were made with the capillary length, a (Equation 17). The capillary length for each fluid solution was found to be larger than the drop radius R_E, as detailed in Table [5]. This indicates that gravitational effects are not dominant and the drop will assume a spherical cap shape when sessile on a substrate. This characteristic is also true for the drops produced using the smaller 0.495 mm O.D. needle.

2.5 Impact Velocity

Drop impact velocities just prior to impact were extracted directly from the digital images and compared with the theoretical free-fall velocity:

$$v_z = \sqrt{2g(H_f - H)} \quad [58]$$

where H_f denotes the fall height and v_z is the vertical impact velocity. Equation [58] incorporates the height of the pendant drop, H, to account for changes in the drop centre of mass prior to detachment. This modification was made because the height of attached yield-stress pendant drops could be greater than twice the value of D_E. Figure [22] compares predicted impact velocities from Equation [58] with measurements for fluids within the range $0 \leq \tau_c \leq 26.1$ Pa. Predictions closely agree with the measurements for fall heights ranging between 7.5 mm $\leq H_f \leq$ 200 mm.

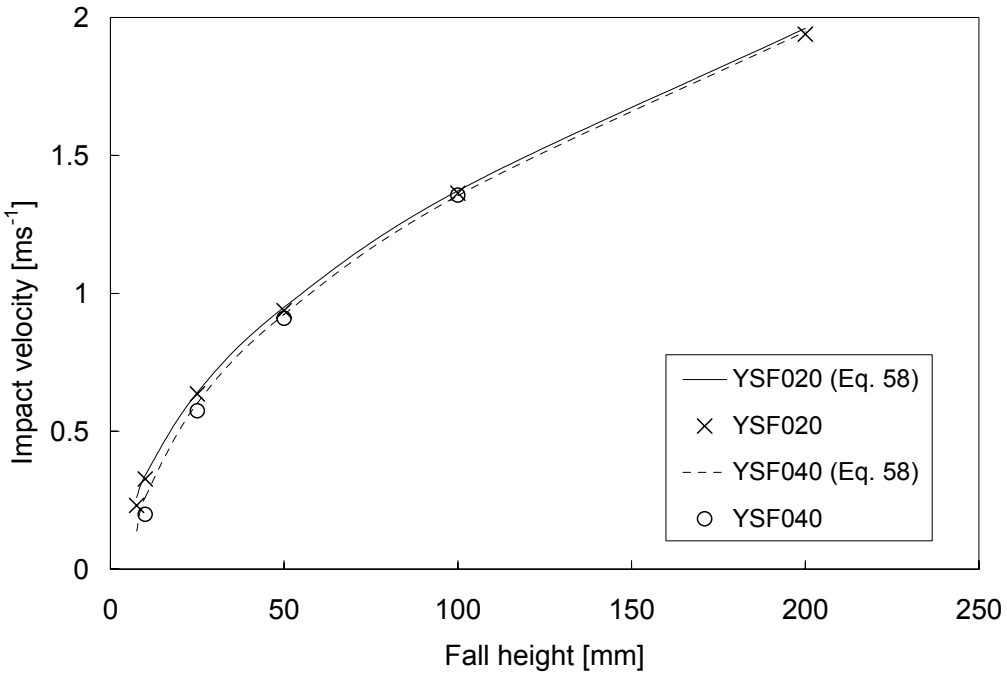

Figure 22. Comparison of measured drop impact velocities with those predicted by Equation (58). The YSF020 (cross) and YSF040 (circle) viscoplastic solutions (respectively) typically represent spherical and prolate drop shapes upon detachment. The solid and short dashed lines represent predicted impact velocities for the YSF020 and YSF040 solutions respectively.

2.6 Surface preparation

In order to examine the influence of surface energy on drop impact and spreading behaviour, comparisons of impact and spreading behaviour were made on two different substrates; a hydrophobic parafilm-M film and a hydrophilic glass slide. Hydrophobic parafilm-M substrates were created by stretching the film tightly over the aluminium

block. Hydrophilic glass was prepared by washing standard glass slides with a surfactant solution, rinsing the surface with de-ionised water, repeatedly washing the surface with acetone and ethanol to remove chemical contaminants, subjecting the slide to an ultrasound bath in a surfactant solution for 10 minutes to remove any residual traces of particulates and finally washing with de-ionised water and allowing to dry in a clean heated cabinet to accelerate evaporation and minimise the likelihood of particles settling on the surface. The slides were then transferred to a sealed container until they were used.

The equilibrium contact angles of de-ionised water drops (D_E = 3.48 mm) were measured to characterise the properties of each surface. A contact angle of $\theta_e = 95 \pm 2^o$ was determined for the Parafilm-M substrate averaged over five drop measurements; the glass substrate was found to be completely wetting ($\theta_e = 0^o$). Drop contact angles were measured manually using a contact angle measurement plug-in to the ImageJ software called BigDrop[158].

2.7 Evaporative effects

The spreading of viscous fluid drops on wettable substrates can take in the order of minutes to reach a sessile state. The elimination of evaporative effects is therefore necessary to prevent changes in drop volume during this period.

Sessile drop evaporation rates (in ambient air conditions) were initially established for de-ionised water, YSF020, YSF030 and YSF040 yield-stress fluid solutions. Drops were allowed to detach from a needle and impact from a fall height of 150 mm on to a substrate placed on a precision balance. The ratio of the instantaneous drop weight, m(t), to original drop weight, m, was calculated for five drops of each solution over a 10 minute period and averaged. Average fractional mass losses are displayed in Figure [23] for both parafilm and glass substrates.

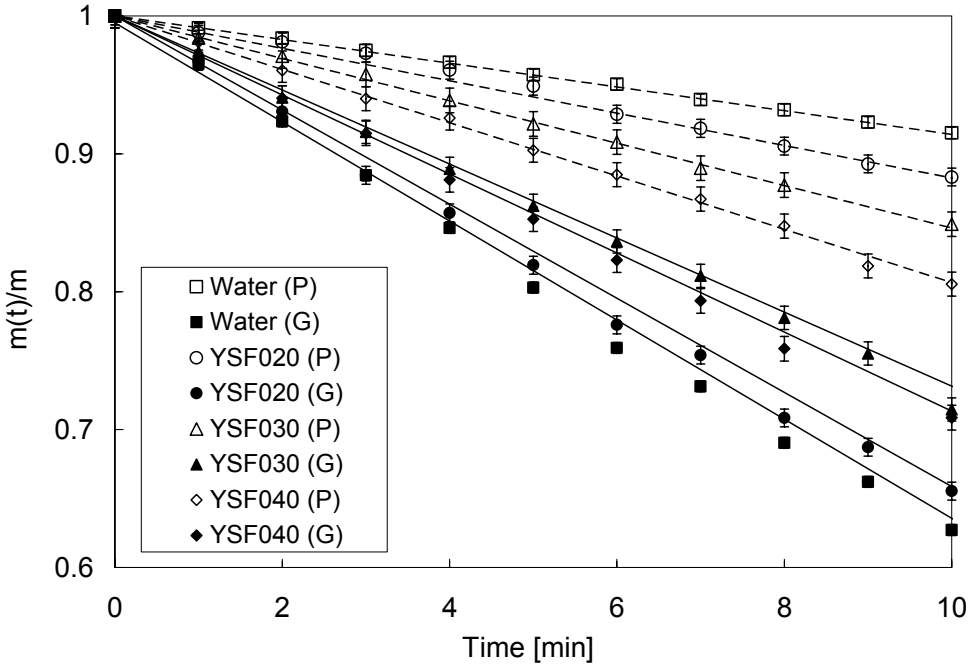

Figure 23. Fractional mass loss through evaporation m(t)/m plotted against time for drops of de-ionised water (square) (μ = 0.001 Pas, D_E = 3.48 mm), YSF020 (circle) (D_E = 2.85 mm, τ_c = 0 Pa), YSF030 (triangle) (D_E = 2.68 mm, τ_c = 11.5 Pa) and YSF040 (diamond) (D_E = 2.617 mm, τ_c = 26.1 Pa) impacting from a fall height of 150mm on to a parafilm substrate (open symbols and dashed line) and a glass substrate (filled symbols and solid line). Each set of data points corresponds to the average of five drop measurements.

A minimum evaporation rate of 3.4 x 10^{-6} gs^{-1} was recorded for drops of de-ionised water on a parafilm substrate. Over the three second high speed camera recording period this constitutes a mass loss of 0.05% (for a D_E = 3.48 mm). In contrast, the maximum recorded evaporation rate for water drops on the glass substrate (1.24 x 10^{-5} gs^{-1}) causes a mass loss of 0.17% over the same period. This increased rate is due to continued drop spreading after the inertial expansion phase of the impact, increasing the liquid-vapour surface area. For similar sized drops of the hair-gel solutions, both the YSF020 and YSF030 solutions show increased evaporation rates on the parafilm substrate and decreased rates on the glass substrate. On the parafilm substrate, the viscoplastic fluids exhibit decreased retraction rates (after β_m is reached) over the same measurement period as the water drop, resulting in a comparatively larger liquid-vapour surface area. On the glass substrate, spreading after inertial impact is retarded, resulting in lower liquid-vapour surface areas. These phenomena are caused by the combined

effect of increased average viscosity retarding the spreading/retraction rate and yield-stress effects inhibiting spreading motion.

Drops of the YSF040 solution continue the trend of increased evaporation rate on the parafilm surface, however the evaporation rate increases rather than decreases on the glass surface. Whilst the cause of this not immediately recognisable, it is likely that this is due to the highly prolate shape of the impacting drops; whilst lower yield-stress fluid drops completely deform; creating a lamella upon impact, higher yield-stress fluid drops do not completely deform and the upper part of the drop is still visible in the centre of the drop in the form of a peak. This increases the drop surface area, thereby increasing the evaporation rate.

Unlike high yield-stress magnitude fluids, both low yield stress magnitude fluids (YSF020, τ_c = 0 Pa) and water with drop radii below the capillary length will exhibit spherical cap shapes when sessile on the substrate. For these fluids it is interesting to note that the mass appears to vary linearly with time. This is unexpected seeing as evaporation occurs at the liquid-vapour interface and should vary as a function of D_E^2 (Surface area), not D_E^3 (volume). Existing published research however highlights the non-trivial behaviour or evaporating drops. Subsequent studies are considered outwith the scope of the research however because evaporation studies were performed primarily to determine whether a saturated air environment was needed for each of the drop dynamic studies. Furthermore, whilst there is scope for further research into the effects of yield-stress and fluid shear-thinning on drop evaporation, the underlying spreading dynamics and sessile state characteristics need first to be examined; an understanding of which is one of the objectives of the research project. This study highlights however that mass losses over the period of drop detachment and impact are too small to influence drop dimensions noticeably.

The minimum and maximum fractional mass losses over a typical spreading period of 5 minutes[148] were 4.3% and 19.7%, achieved by de-ionised water drops on parafilm-M and glass substrates respectively. In both cases, mass losses significantly influence the drop dimensions during this period, therefore evaporative effects must be eliminated or accounted for in experiments over this time-period.

To further assess the effectiveness of saturated air within the acrylic box on retarding evaporative losses, a comparison of de-ionised water drop evaporation rates was made with those in an ambient air environment. Drops were deposited on the surface of a parafilm substrate (chosen so that a sessile state is reached after a very short period) and images were recorded once a minute over a 20 minute period. This period exceeds the maximum recording periods for drop spreading studies. Both internal and ambient air temperatures remained at a constant 23^{o}C over this period. The air within the acrylic box was left to saturate for 24 hours prior to experimentation. Figure [24] highlights that whilst evaporation is noticeable after only 5 minutes in the open air environment (most clearly as a decrease in contact angle), no noticeable differences are observed for the drop within the casing. Figure [25] shows the temporal variation of maximum apex drop height and width averaged over 5 drop experiments and confirms this observation. The figure also highlights that evaporative effects are noticeable only when observing drop height; drop diameters remain nearly constant over the recorded period.

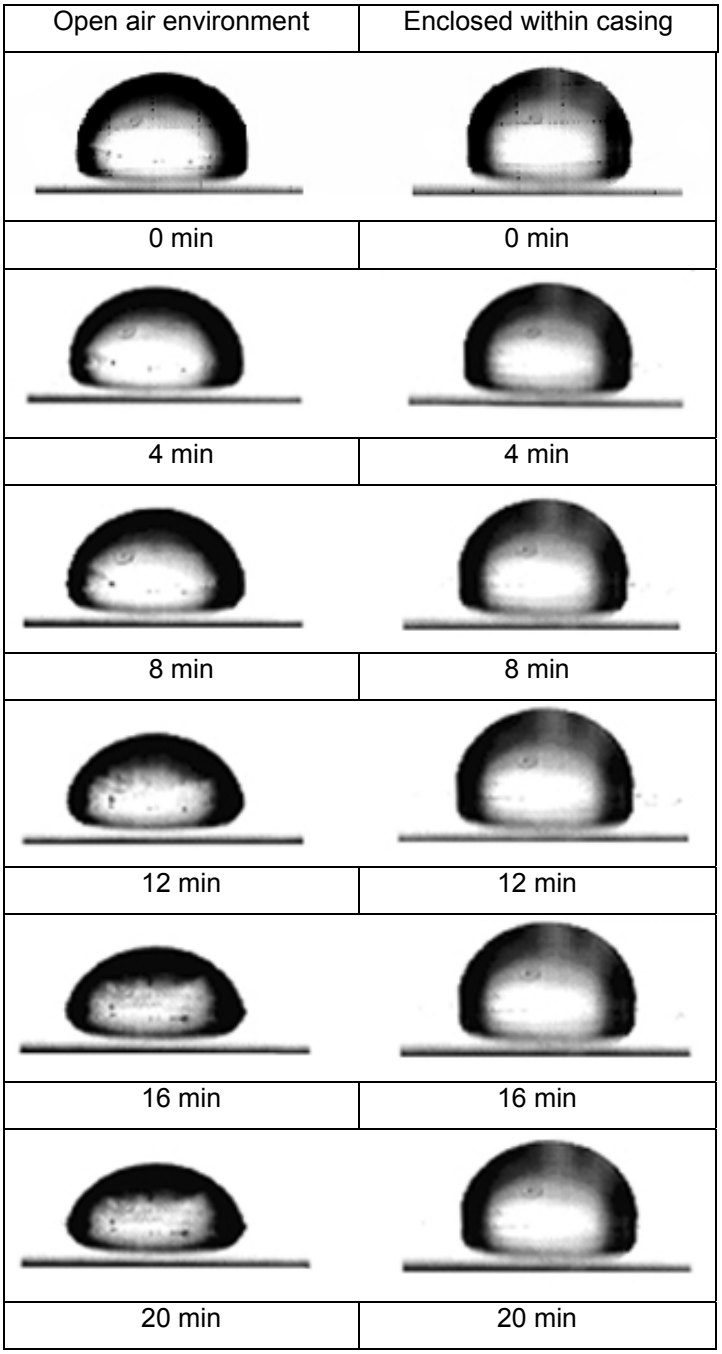

Figure 24. The temporal variation of drop shape with evaporation in (left) an ambient air environment and (right) saturated air confined within the acrylic box.

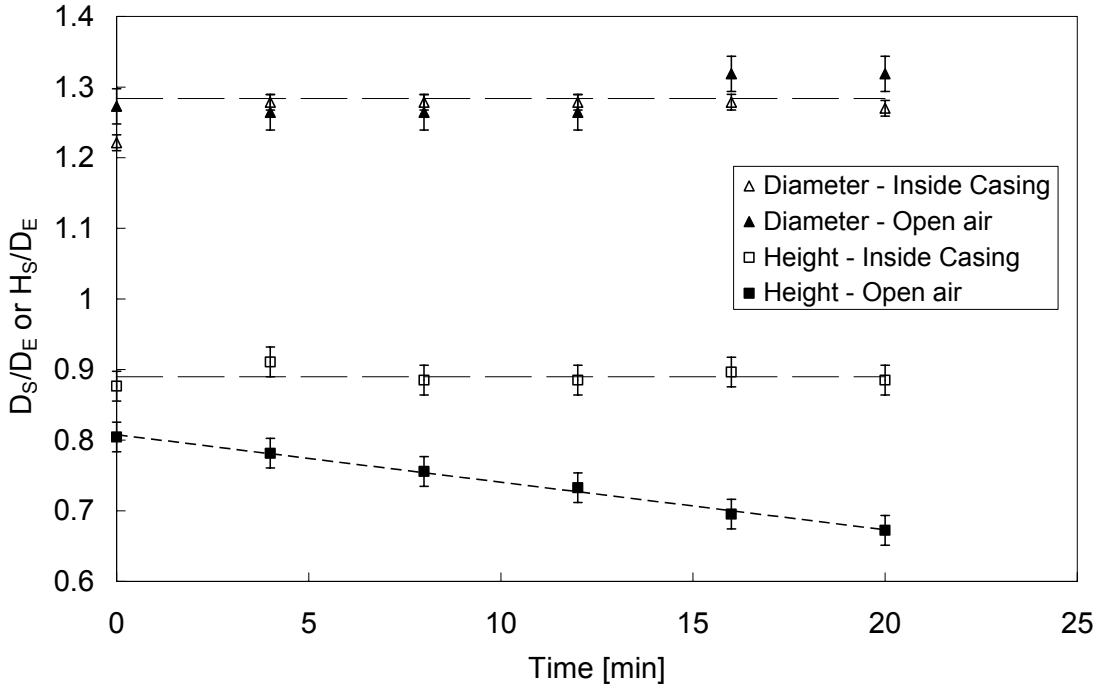

Figure 25. The temporal variation of dimensionless drop height and diameter with evaporation in an ambient air environment (open symbols) and saturated air confined within the acrylic box (filled symbols).

2.8 Drop shape Characteristics

2.8.1 Drop detachment parameters

Drop detachment dynamics were analysed through the measurement of drop height L, minimum axisymmetric filament neck diameter D_N and both the position of the neck from the end of the capillary tube $L_{neck}/2$ and its velocity, v_{neck}, as defined in Figure [26]. Drop dimensions were non-dimensionalised with respect to the inner diameter of the capillary tube D_0. Five drop measurements were recorded and averaged for each fluid sample to establish errors magnitudes and ensure repeatability.

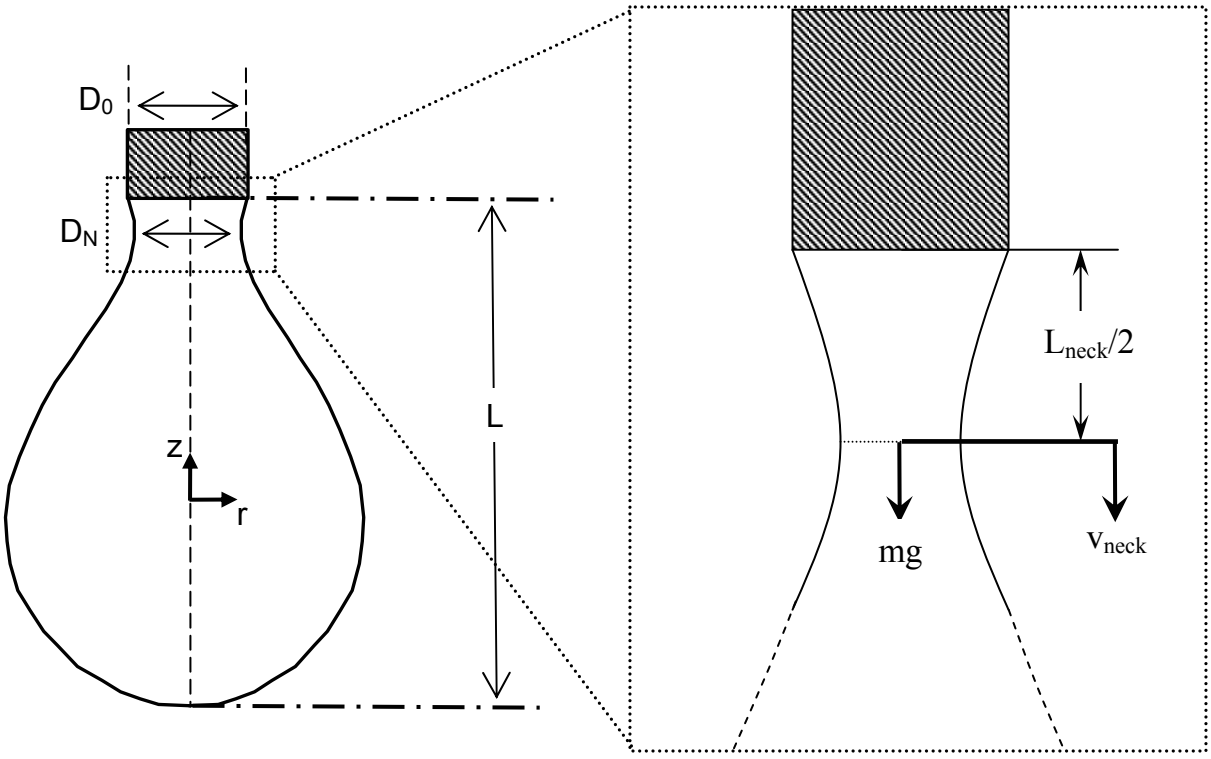

Figure 26. Drop shape and dimensional parameters.

2.8.2 Drop free-fall parameters

Drop shapes during free fall were analysed using the dimensionless shape factor S, where:

$$S = \frac{H(t) - D(t)}{H(t) + D(t)} \qquad [59]$$

In the absence of inhibiting forces, free-falling drops with radii smaller than the capillary length take on a spherical shape in equilibrium[37] by action of capillarity, where the equilibrium shape is denoted as S_e. Using Equation [59], prolate drop shapes (where the maximum axisymmetric height is larger than the maximum diameter) have a positive value and oblate shapes produce a negative value. This factor characterises drop shapes in terms of their deviation from a spherical shape, as detailed in Figure [27].

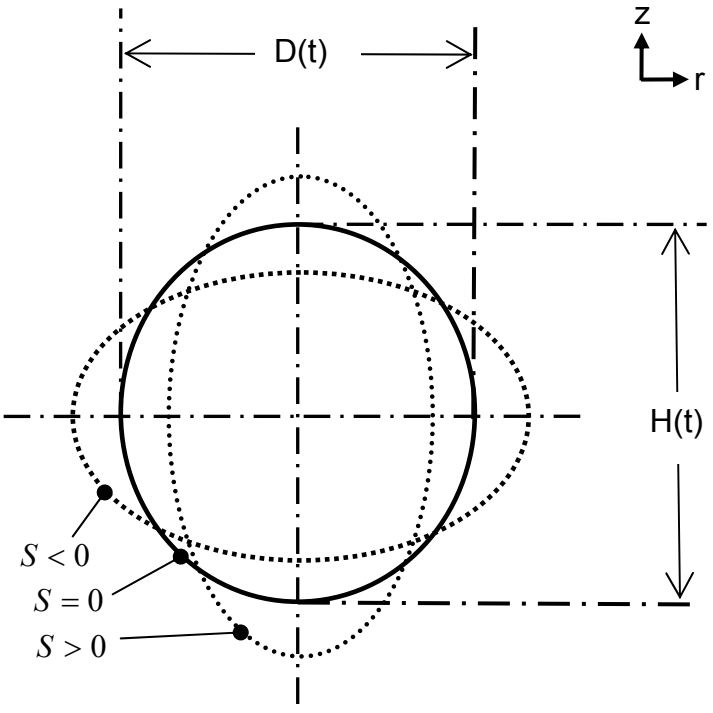

Figure 27. Drop free-fall shape and dimensional parameters.

2.8.3 Drop impact and spreading parameters

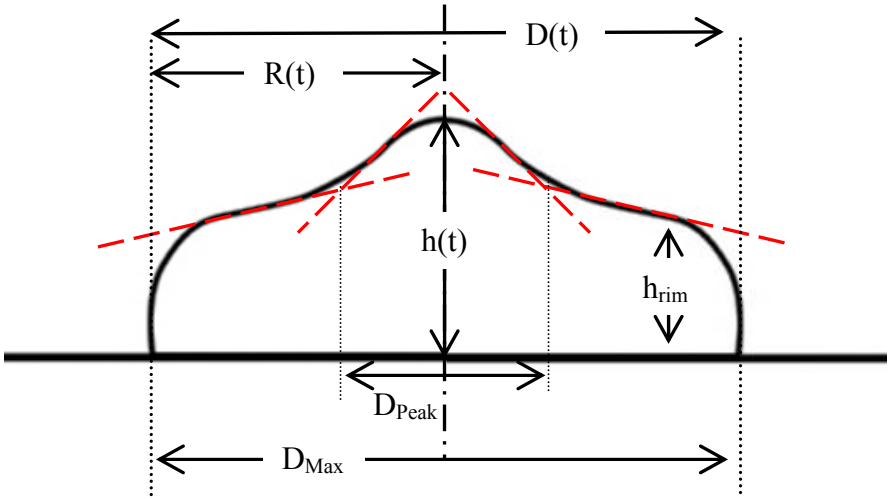

Figure 28. Drop impact and spreading dimensional parameters including drop peak measurement for yield-stress fluid drops using the intersection of surface tangents (dashed lines).

Drop shapes during inertial impact, retraction and subsequent spreading were analysed primarily through the measurement of maximum drop width D_{Max} and maximum apex drop height h_{Max}. In terms of dimensionless numbers, the drop diameter D(t) scaled with respect to D_E is denoted as the dimensionless spread factor β with a maximum where $\beta_m = D_{Max}/D_E$. Equivalently drop height h(t) scaled by D_E is denoted as the dimensionless height factor ξ with a minimum where $\xi_m = h_{Min}/D_E$. Furthermore, the influence of fluid yield-stress magnitude on drop shape was established by analysing the size of drop peaks; observed at the centre of some axisymmetric viscoplastic drops after impact. Peak diameters D_{Peak} were measured by extrapolating the length between intersections of surface tangents to the undeformed peak regions and outlying deformed regions of the drop, as displayed in Figure [28]. This length was non-dimensionalised by scaling with respect to the maximum drop impact diameter D_{Max} and denoted as β_{Peak}.

3. Results and Discussion - Drop detachment dynamics

We consider here the formation and detachment behaviour of liquid drops from a thin 0.838 mm I.D. capillary tube to establish influences from Newtonian viscosity, shear-thinning and fluid yield-stress. Typically, drops grow at the end of a capillary needle and take on a pendent shape appearance with the maximum drop width larger than the capillary diameter D_0. Classically for viscous Newtonian fluids after the onset of instability, perturbations will initially grow exponentially with a rate determined by Equations [1] and [4]. A critical point of instability can therefore be defined as the intersection of the exponential and zero growth rate regimes. The point of critical breakup, denoted as $D_{N,Crit}$ can most clearly be observed in temporal variations of D_N. The drop height at $D_{N,Crit}$ is denoted as L_{Crit}.

Figures [29] – [31] display drop images at the onset of instability overlaid with outlines of drop shapes at instances 50ms, 20ms and 3ms prior to pinch–off as well as at the point of pinch-off for Newtonian, shear-thinning and yield-stress fluids in the range $0.056 \leq \mu \leq 0.925$ Pas, $0.084 \leq n \leq 0.400$ and $0 \leq \tau_c \leq 26.1$ Pa respectively.

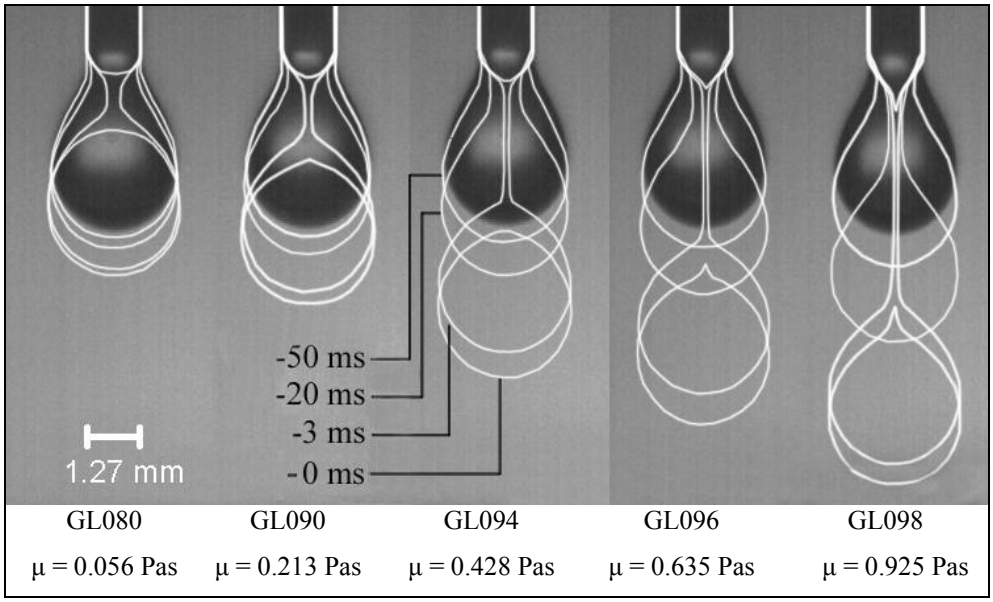

Figure 29. Newtonian fluid drop shape during detachment. Annotation corresponds to time in milliseconds prior to detachment (at which t = 0 ms)

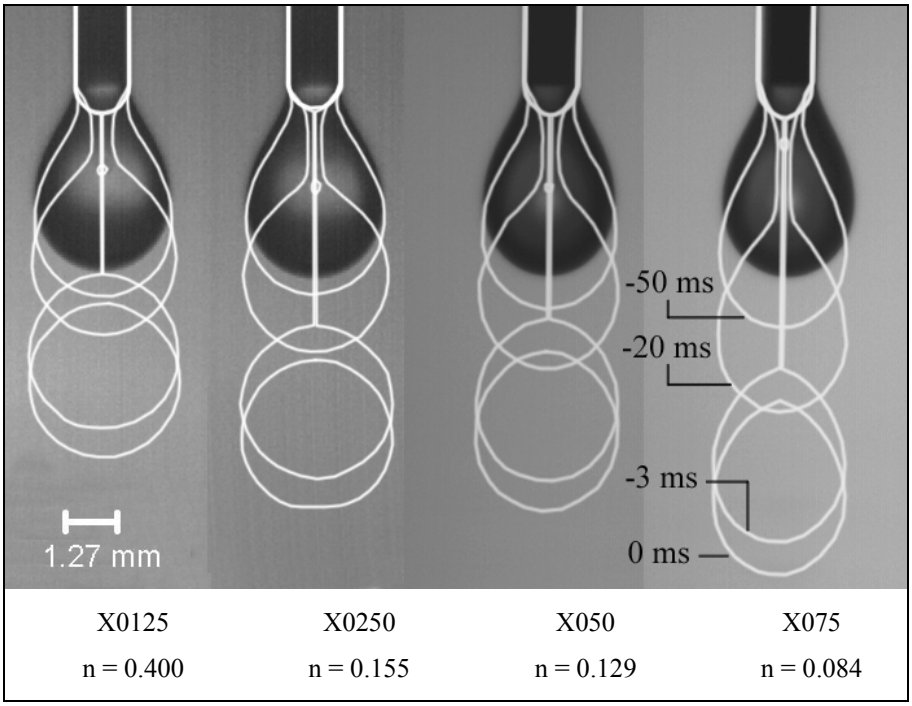

Figure 30. Shear-thinning fluid drop shape during detachment. Annotation corresponds to time in milliseconds prior to detachment (at which t = 0 ms)

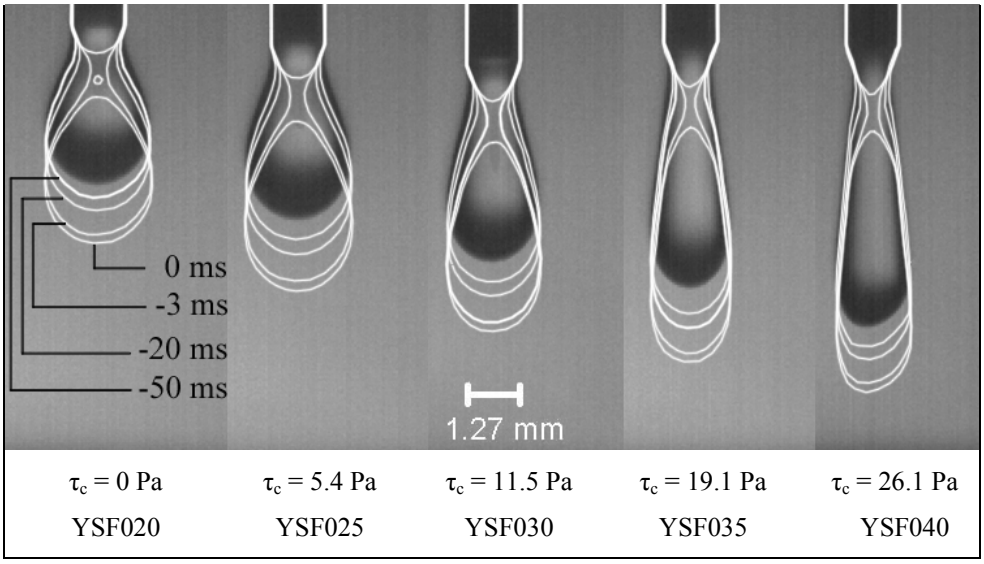

Figure 31. Yield-stress fluid drop shape during detachment. Annotation corresponds to time in milliseconds prior to detachment (at which t = 0 ms)

The shapes of some yield-stress fluid drops during detachment are clearly different from the Newtonian and shear-thinning fluids, varying in prolateness as a function of increasing τ_c (Figure 31). Differences are only visibly apparent for fluids with $\tau_c \geq 11.5$ Pa. Prolate drop shapes within this yield-stress magnitude range have previously

been observed in fluids with $\tau_c \geq 11$ Pa. by Nigen[148] and $\tau_c \geq 20$ Pa by Davidson and Cooper-White[145]. After the onset of instability, drop neck thicknesses decrease non-linearly with time, however long, thin filaments are not observed and pinch-off occurs quickly and at a similar position below the end of the capillary. This behaviour is considerably different from that of both the Newtonian and shear-thinning fluids, whose filament lengths and drop lengths at pinch-off vary as a function of the viscosity and shear-thinning characteristics respectively. Moreover, with the exception of the YSF020 solution where the yield-stress magnitude is negligible, no satellite droplets are formed, unlike those observed during the pinch-off process of both Newtonian (with $\mu \leq 0.056$ Pas) and shear-thinning fluids (observed in all four fluids). This final characteristic agrees with previous observations made by Davidson and Cooper-White.

3.1 Detachment dynamics and stability of Newtonian fluid drops.

3.1.1 Drop stability

Figures [32] and [33] display the dimensionless drop length L/D_0 and minimum neck diameter D_N/D_0 plotted against time for Newtonian fluids with $0.056 \leq \mu \leq 0.925$ Pas respectively. Prior to $D_{N,Crit,}$ D_N/D_0 remains constant (with $D_N/D_0 = 1$) and the drop height grows slowly in time (in the range $1.17 \leq m \leq 2.53$ mms^{-1}, where m is the drop height growth rate prior to the onset of instablity). Thereafter, D_N/D_0 and L/D_0 respectively decrease and increase non-linearly as the drop gains inertia, neck filaments form and subsequently stretch to become longer and thinner. The position of $D_{N,Crit}$ has been marked on both Figures.

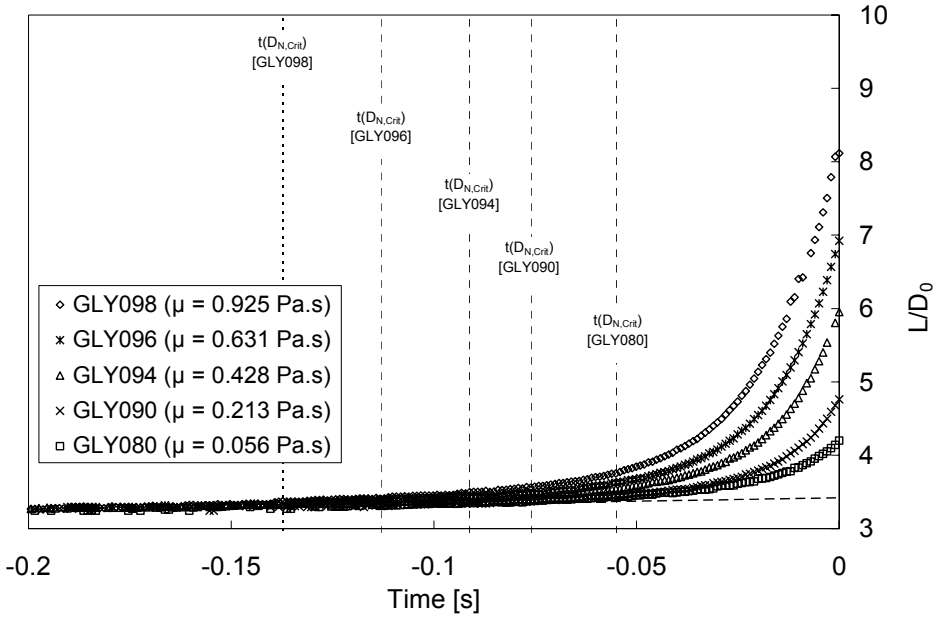

Figure 32. Temporal variations in drop height L/D_0 for Newtonian fluids with viscosities in the range $0.056 \leq \mu \leq 0.925$ Pas. Each set of experimental results constitutes the average of 5 drop measurements. Linear best fit trendlines of the form $L/D_0 = -mt + C$ were fitted to the experimental data of each results set prior to $D_{N,Crit}$ (critical breakup denoted by short dashed lines). Drop height growth with time varies in the range $1.17 \leq m \leq 2.53$ mms^{-1}. This is due to the limited control of flow rate, not the physics of drop breakup. These variations however, do not alter the breakup behaviour. All of the lines of best fit are not displayed in the Figure. To aid visual clarity, only the line of best fit for the GLY080 solution is displayed, denoted by the long dashed line. Moreover, measurement errors are not displayed for visual clarity, however are comparable with symbol size.

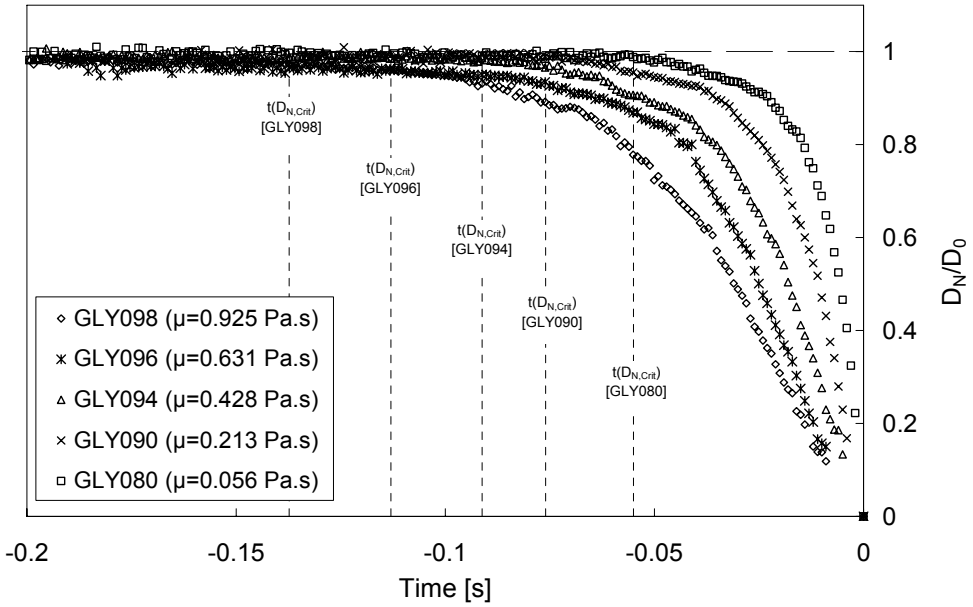

Figure 33. Temporal variations in minimum dimensionless drop neck thickness D_N/D_0 for Newtonian fluids with viscosities in the range $0.056 \leq \mu \leq 0.925$ Pas ($D_0 = 1.27$ mm). Each set of experimental results constitutes the average of 5 drop measurements.The short dashed lines correspond to the time of the onset of instability, where D_N/D_0 deviates from a value of 1, denoted by the long dashed line. Measurement errors are not displayed for visual clarity, however are comparable with symbol size.

Whereas the onset of instability begins earlier for fluids with increasing viscosity; varying linearly in the range -0.055 ≥ t ($\widetilde{D}_{N,Crit}$) ≥ -0.137 ms for 0.056 ≤ μ ≤ 0.925 Pas (Figure 34), the magnitudes of $D_{N,Crit}/D_0$ and L_{Crit}/D_0 remain nearly identical for each fluid ($D_{N,Crit}/D_0 = 1$, $L_{Crit} = 4.28 \pm 0.058$ mm), indicating that fluid viscosity does not alter the equilibrium shape of attached drops at the critical breakup point; in agreement[11] with the fact that viscous effects are only influential in the presence of motion since they are proportional to the rates of deformation.

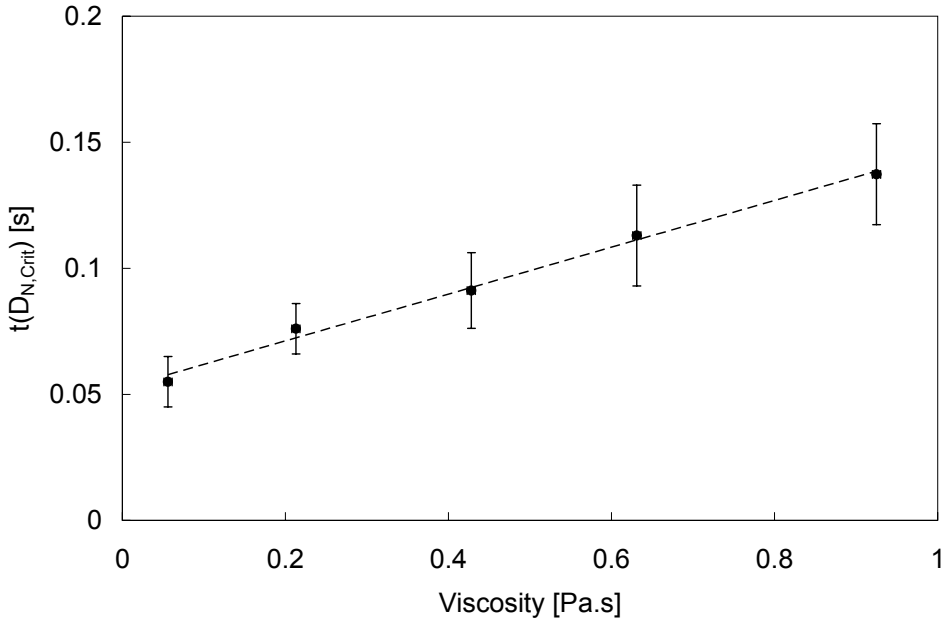

Figure 34. Time prior to pinch-off at which the onset of instability occurs in detaching drops plotted against Newtonian viscosity. The dashed line corresponds to a linear fit of the experimental data with a gradient of 0.093 Pa^{-1}.

3.1.2 Drop detachment behaviour.

Figure [35] compares measured temporal variations in D_N/D_0 with those predicted using Equations [1], [4] and [5] during the detachment process. Whereas the predicted behaviour in both the initial exponential instability growth regime and subsequent Stokes flow self-similar regime closely match the experimental results for fluids with $0.213 \leq \mu \leq 0.925$ Pas, significant differences are observed for $\mu < 0.213$ Pas. This discrepancy is due to the omission of gravitational effects in the formulation of Equation [3] during pinch-off[18] and has previously been highlighted in equivalent work by Rothbert, Richter and Rehberg[21]. Furthermore, analysis of the Navier-Stokes self-similar regime (Equation 5 with $\chi = 0.0304$) is limited; the resolution of the images prevents accurate measurement of very small filament thicknesses.

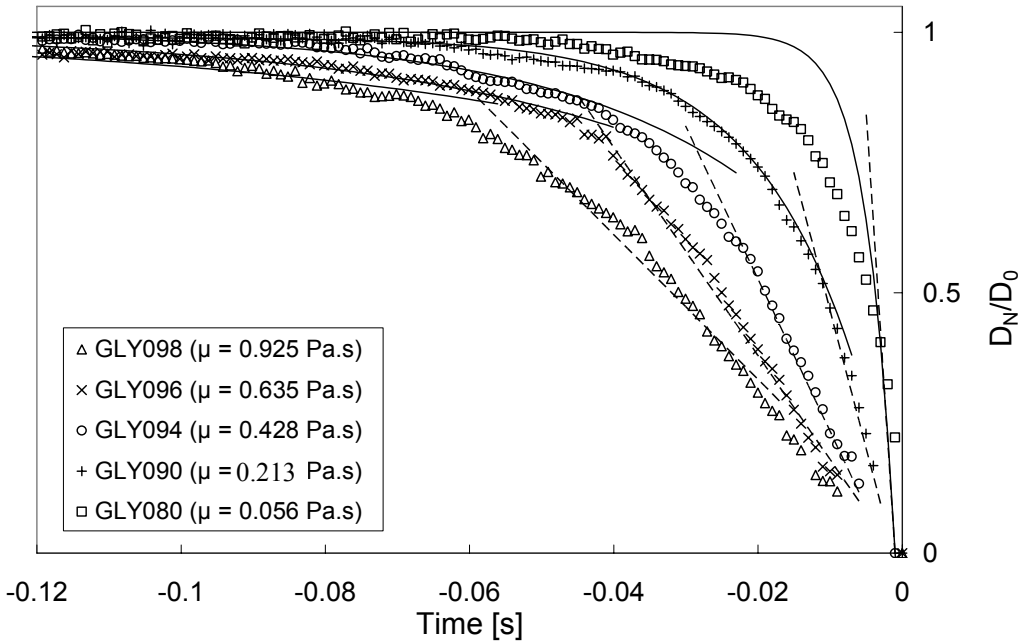

Figure 35. The temporal variation of dimensionless D_N with time for Newtonian fluids with $0.056 \leq \mu \leq 0.925$ Pas. Solid lines represent predictions of viscous exponential instability growth rate using Equations [1] and [4]. Dashed lines represent predicted self-similar Stokes flow using Equation [5]. Each experimental results set is based on the average of 5 drop measurements. Errors are not displayed for visual clarity, however are comparable with symbol size.

The intersection of the solid and dashed lines, denoted as $D_{N,Trans}$, denotes the transition from the initial exponential instability growth regime (LSM[16] regime) to the self-similar Stokes flow regime[23] (Equations 1 and 4 to Equation 5 with $\chi = 0.0709$).

Comparisons of measured $D_{N,Trans}$ with previous experimental work[21] show a reasonable agreement and are displayed in Figure [36]. These results however show that above the largest kinematic viscosity previously analysed ($\nu \sim 400$ mm^{2}s^{-1}), the minimum neck thickness at the transition of the flow regime continues to grow monotonically with ν (although less than linearly). This result weakens the conclusion by Rothbert, Richter and Rehberg[21] that $D_{N,Trans}$ does not vary as a function of ν, although it is difficult to conclude otherwise even based on their original experimental data.

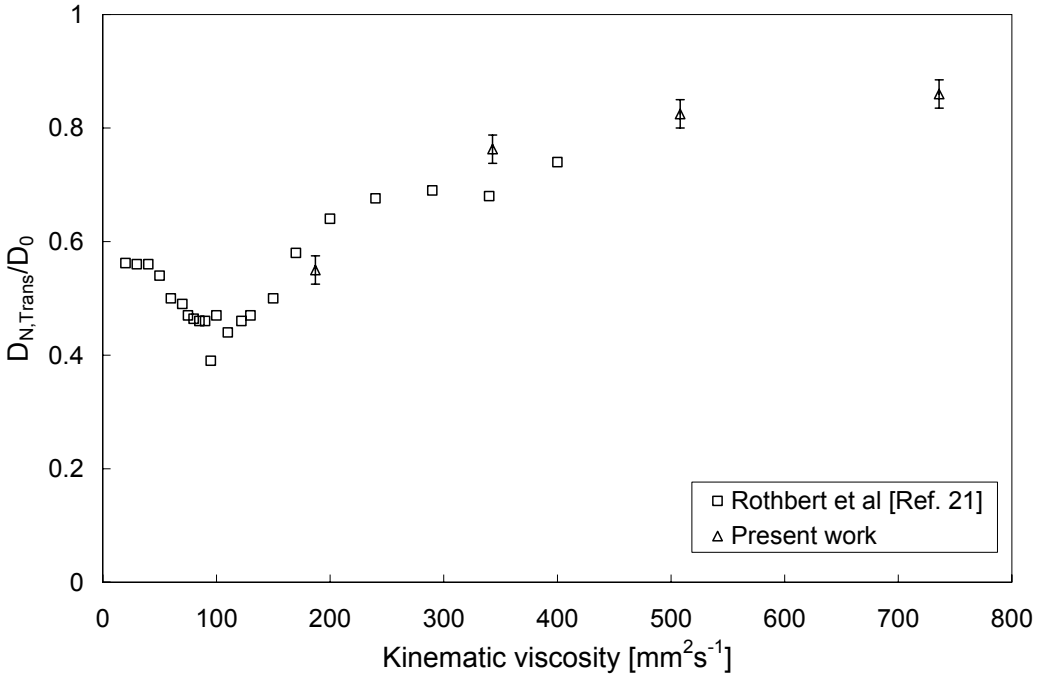

Figure 36. The variation of $D_{N, Trans}$ with kinematic viscosity ν for Newtonian fluids.

3.2 Detachment dynamics and stability of shear-thinning fluid drops.

3.2.1 Drop stability

Figures [37] and [38] display D_N/D_0 and L/D_0 plotted against time for the shear-thinning fluids. Prior to the onset of instability, $D_{N,Crit}$ remains nearly identical for each of the four fluids and variations in L_{Crit} are small with $4.8 \leq L_{Crit} \leq 5.3$ mm. This indicates that fluid shear-thinning characteristics do not significantly alter the shape of attached drops at the critical breakup point.

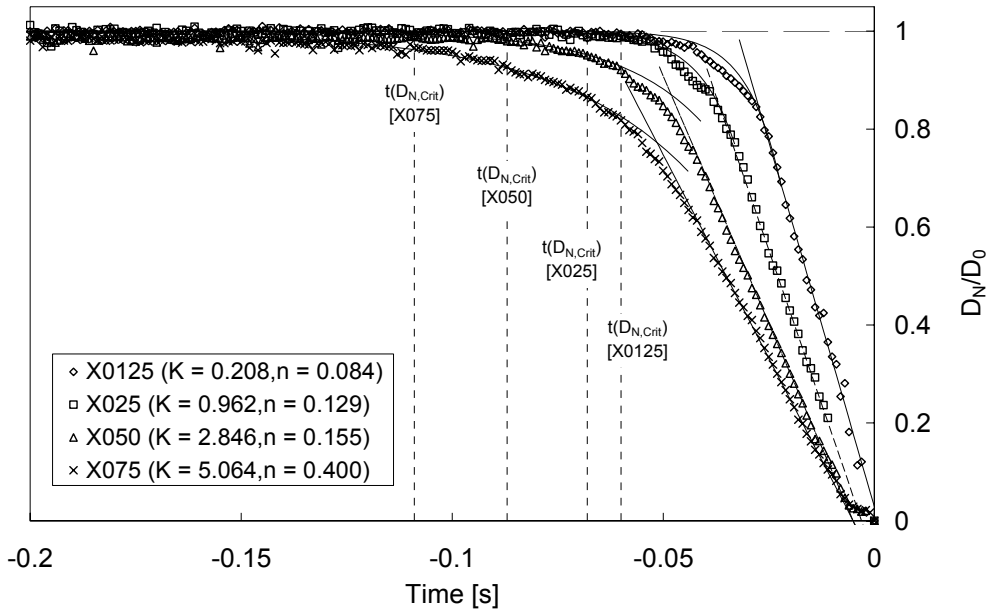

Figure 37. Temporal variations in dimensionless minimum drop neck thickness D_N/D_0 for shear thinning fluids with power law indices in the range ($0.084 \leq n \leq 0.4$). Solid lines represent best fit predictions of viscous exponential instability growth rate using an apparent viscosity μ_{app} in Equation [4]. Long dashed lines represent best fit predictions for the self-similar Stokes flow using μ_{app} in Equation [5]. Short dashed lines correspond to the time of $D_{N,Crit}$ prior to pinch-off. Each experimental results set is based on the average of 5 drop measurements. Errors are not displayed for visual clarity, however are comparable with symbol size.

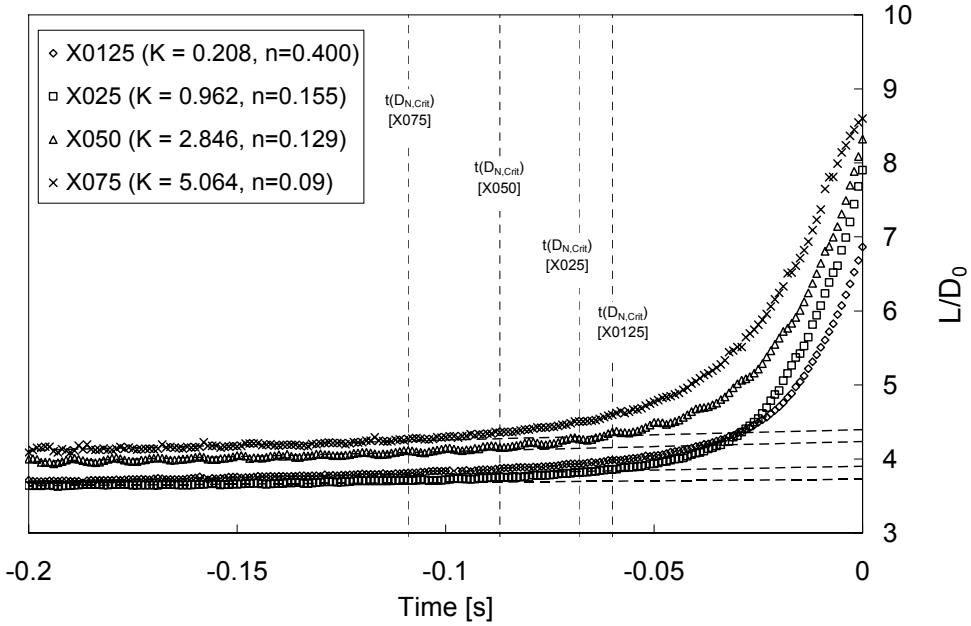

Figure 38. Temporal variations in dimensionless drop height L/D_0 for shear thinning fluids with power law indices in the range ($0.084 \leq n \leq 0.4$). Long dashed lines represent linear variations in drop height prior to the onset of instability. Short dashed lines correspond to the time of $D_{N,Crit}$ prior to pinch-off. Each experimental results set is based on the average of 5 drop measurements. Errors are not displayed for visual clarity, however are comparable with symbol size.

3.2.2 Drop detachment behaviour

As with the Newtonian fluids, the period between the onset of instability and drop pinch-off varies between fluids: increasing the shear-thinning characteristics of the fluid in the range $0.084 \leq n \leq 0.4$ (along with corresponding changes in the consistency coefficient in the range $0.208 \leq K \leq 5.064$ Pas^n) results in this period increasing in the range $-0.06 \geq t(D_{N,Crit}) \geq -0.109$ s, as displayed in Figures [39] and [40][5]. Davidson and Cooper-White[145] established numerically that decreasing μ_0 in a Cross type rheological model (Equation 37), equivalent here to decreasing K resulted in a more rapid narrowing of the neck and therefore decreased the breakup period, consistent with the results of Figure [40]. They also established that increases in μ_∞ (whilst keeping μ_0 constant), equivalent to decreased shear-thinning ($n \rightarrow 1$) retarded drop breakup. Whilst this contradicts the results of Figure [39], one further aspect that must be considered here is the relative influence of changes in the consistency coefficient K over changes in the degree of shear thinning, characterised by n. Whereas each fluid exhibits a different degree of shear-thinning, they also vary considerably in K. Increases in K result in comparatively larger average viscosities during detachment and increased detachment periods (the time between $D_{N/Crit}$ and pinch-off); consistent with that of the Newtonian fluids. The influence of changes in the degree of shear-thinning may therefore be swamped by increases in the average viscosity during detachment.

The effect of shear-thinning on drop detachment can be highlighted with a direct comparison of a shear-thinning and Newtonian fluid. The viscosity of the X025 ($K = 0.962$ Pas^n) shear-thinning fluid in the limit of a Newtonian regime (where $n \rightarrow 1$ and $K \rightarrow \mu$) at very low shear-rates is approximately the same as the GL098 Newtonian fluid viscosity ($\mu = 0.925$ Pas). The associated timescale for detachment of the shear-thinning drop ($t(D_{N,Crit}) = 0.068$ s) however is considerably smaller[6] than the maximum Newtonian detachment period ($t(D_{N,Crit}) = 0.137$ s. The cause of the increased rate of breakup

[5] It should be noted that Figures [39] and [40] are not fully representative of the relationship between $t(D_{N,Crit})$, n and K because Figure [39] does not highlight the influences of K on detachment dynamics and Figure [40] does not highlight the influences of n.

[6] Whilst the value of K (0.962 $Pa^n s$) for the X025 fluid and the viscosity of the GLY098 fluid differ by a small amount, according to Fig [32] the difference in detachment timescale between these two values in a Newtonian regime should be 3.4 ms (based on a gradient of 0.091 s^{-1}), however the measured difference is considerably larger (69 ms).

appears therefore to be shear-thinning, where increases in the strain rate during detachment reduce the local fluid viscosity in the shear-thinning fluid, reducing the break-up period. This agrees with previously established numerical findings[145].

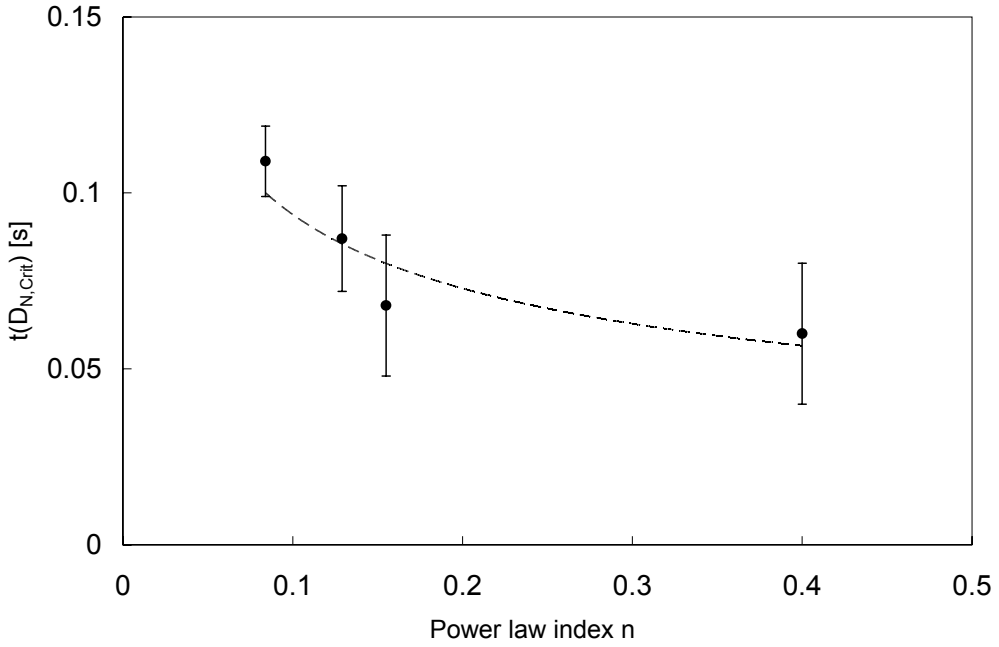

Figure 39. The time prior to pinch-off at which the onset of instability occurs in detaching shear-thinning drops plotted against power law index n (Equation 37). The dashed line corresponds to a best fit power law curve $t(D_{N,\,Crit)}) = 0.04n^{-0.37}$.

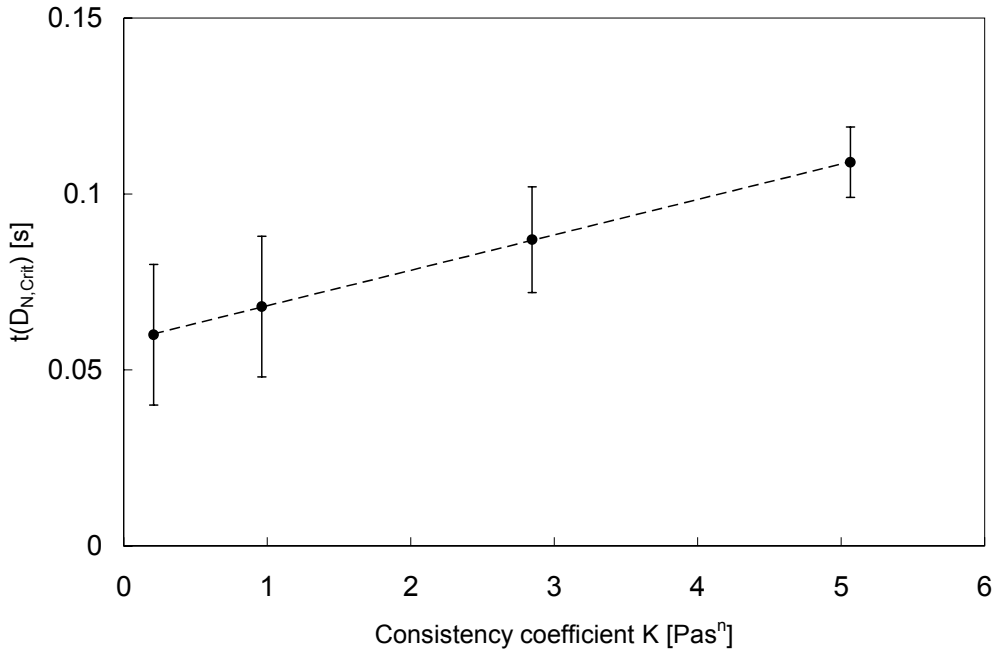

Figure 40. The time prior to pinch-off at which the onset of instability occurs in detaching shear-thinning drops plotted against consistency coefficient K (Equation 37). The dashed line corresponds to a linear fit of the form $t(D_{N,\,Crit)}) = 0.0101n\ Pa^{-1}s^{1-n}$.

To further examine the influence of shear-thinning on drop detachment dynamics, Equations [1], [4] and [5] were used to fit changes in D_N/D_0 in time for both the LSM and self-similar Stokes flow regimes (Figure 37). Best fit representations were determined by replacing the viscosity term μ with an apparent viscosity μ_{app}, Table [6] highlights that μ_{app} in both the initial exponential instability growth and self-similar Stokes flow regimes increase as the Xanthan gum mass fraction increases, indicative of a higher average viscosity and therefore the dominant influence of consistency coefficient K over the power law index. Moreover, the apparent viscosity of each fluid over the period from transition to Stokes flow to pinch-off is significantly smaller than the apparent viscosity over the period from onset of instability to the transition point, indicating that the increases in shear rate with time during the detachment process result in fluid shear-thinning.

Table 6. Variation of apparent fluid viscosity μ_{app} in both the linear stability analysis and self-similar Stokes flow regimes of shear-thinning fluids.

Xanthan Gum mass fraction	Best least square fit μ_{app} for linear instability analysis regime Equation [4] [Pas]	Best least dquare fit μ_{app} for self-similar Stokes flow regime Equation [5] [Pas]	Abbreviations used in figure captions
0.00125	0.115	0.0405	X0125
0.0025	0.13	0.048	X025
0.0050	0.29	0.059	X05
0.0075	0.47	0.073	X075

3.3 Detachment dynamics and stability of yield-stress fluid drops.

3.3.1 Drop stability

The drop stability and detachment dynamics of viscoplastic fluids can appear remarkably different from those of shear-thinning and Newtonian fluids. Figures [41] and [42] display D_N/D_0 and L/D_0 plotted against time for yield-stress fluids with $0 \leq \tau_c \leq 36.2$ Pa respectively. Whereas fluids with $\tau_c < 11.5$ Pa exhibit similar behavioral traits to those of Newtonian and shear-thinning fluids; with similar values of L_{Crit}/D_0 and values of $D_{N,Crit}/D_0$ close to unity, fluids with $\tau_c > 11.5$ Pa show increasingly small values of $D_{N,Crit}/D_0$ in the range $0.67 \leq D_{N,Crit}/D_0 \leq 0.88$ and increasingly longer drop lengths (with $3.99 \leq L_{Crit}/D_0 \leq 7.02$). Figures [43] and [44] display L_{Crit}/D_0 and $D_{N,Crit}/D_0$ plotted against τ_c respectively. There is a clear influence of yield-stress on drop behaviour at the onset of instability. Moreover, the relationship between τ_c and $D_{N,Crit}/D_0$ appears to be linear. Upon fitting a least square best fit line to the critical drop heights of fluids with $\tau_c \geq 11.5$ Pa in Figure [43] and extrapolating it back to $\tau_c = 0$ Pa, the linear relationship does not appear to be representative towards low yield-stress magnitudes. The results also show that low yield-stress drop heights at critical breakup are very similar. Whilst there may be a change in the governing fluid characteristics for detaching drops of low and high yield-stress magnitude fluids, these results are not adequately incisive to make any conclusive relationships.

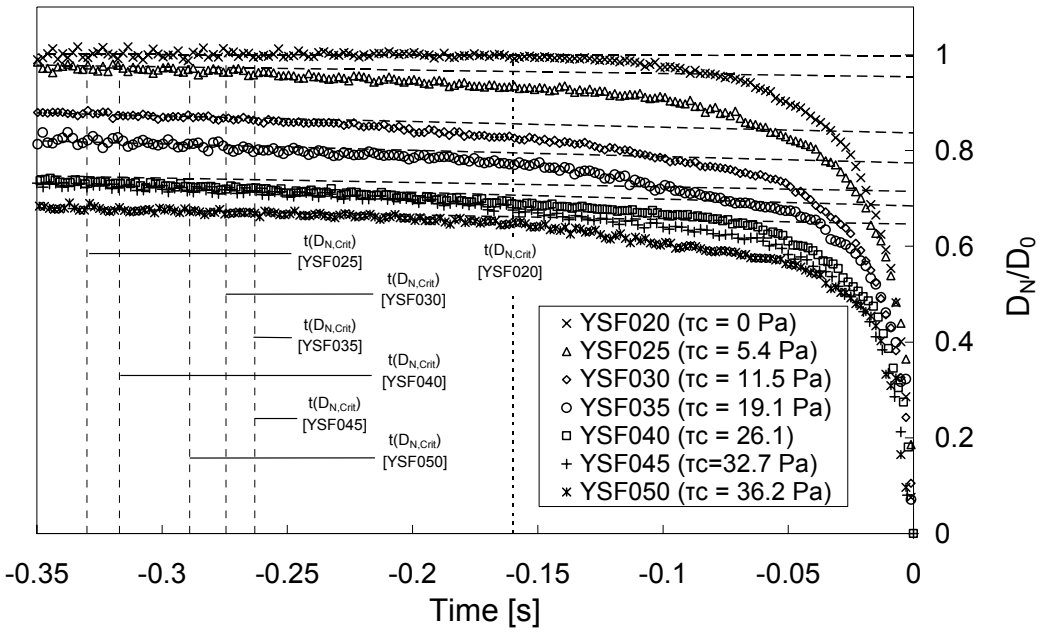

Figure 41. Temporal variations in minimum drop neck thickness (D_N/D_0) for yield-stress fluids with $0 \leq \tau_c \leq 36.2$ Pa. Long dashed lines correspond to a linear best fit variation of D_N/D_0 prior to the onset of instability. $D_{N,Crit}$ corresponds to where the experimental data points deviate from the linear trend lines, highlighted for each fluid with a short dashed vertical line. Each experimental results set is based on the average of 5 drop measurements. Errors are not displayed for visual clarity, however are comparable with symbol size.

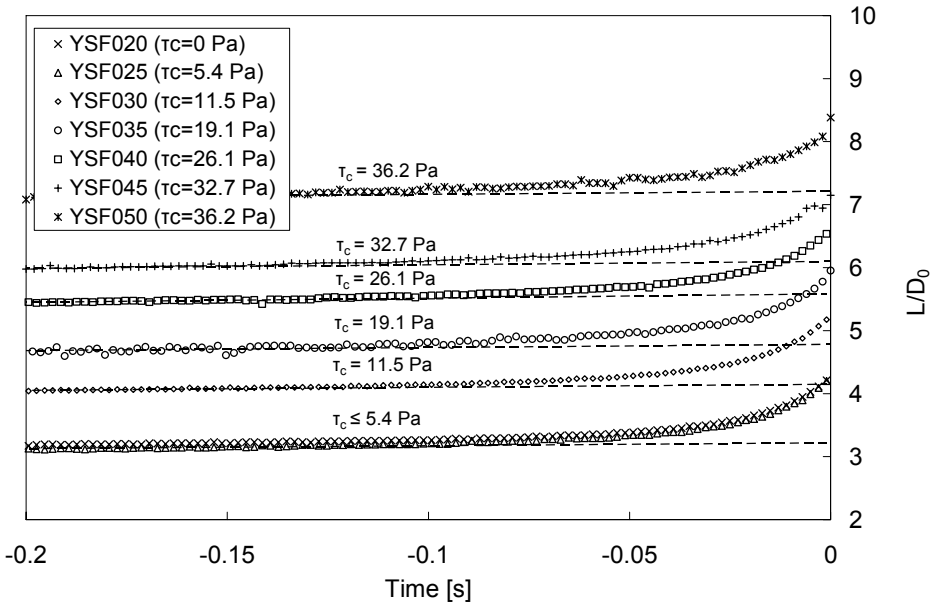

Figure 42. Temporal variations in drop height L/D_0 for yield-stress fluids with $0 \leq \tau_c \leq 36.2$ Pa. Dashed lines correspond to the linear best fit variation of L/D_0 prior to the onset of instability at $D_{N,Crit}$. Each experimental results set is based on the average of 5 drop measurements. Errors are not displayed for visual clarity, however are comparable with symbol size.

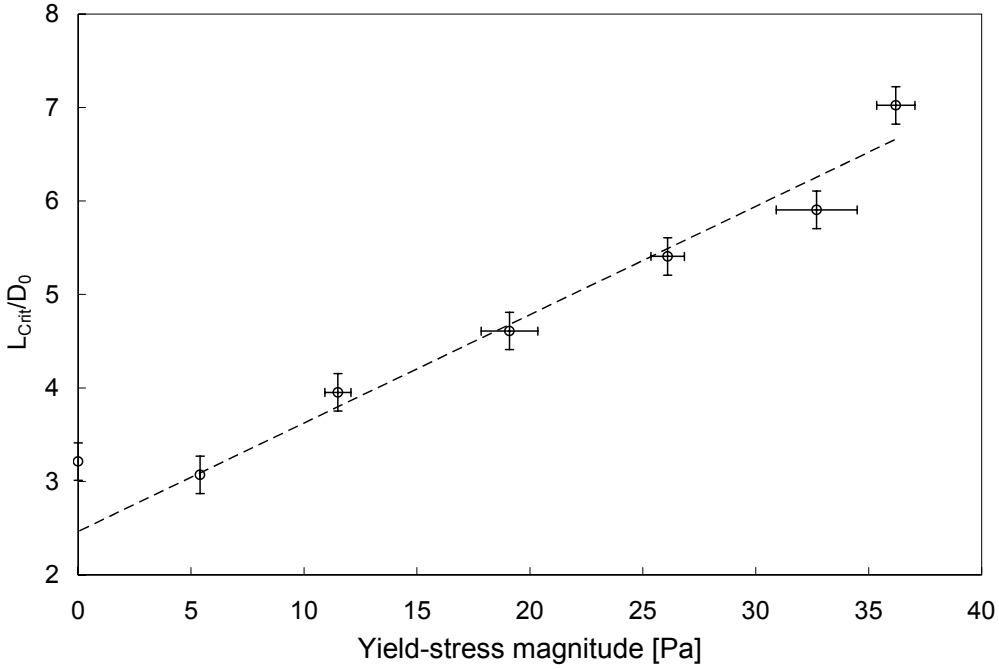

Figure 43. The variation of L_{Crit}/D_0 with yield-stress magnitude for $0 \leq \tau_c \leq 36.2$ Pa.

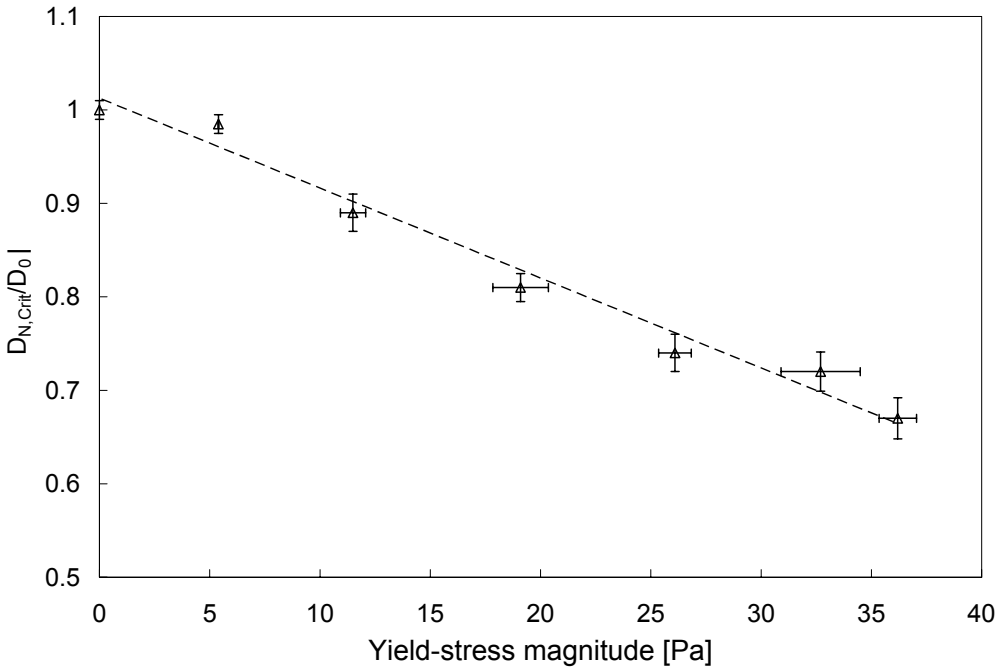

Figure 44. The variation of $D_{N,Crit}/D_0$ with yield-stress magnitude for $0 \leq \tau_c \leq 36.2$ Pa.

To establish more concisely the independent influences of viscosity, shear-thinning and yield-stress magnitude on drop detachment dynamics, the maximum tensile stress in the drop neck at the point of yielding is examined. Values of the tensile stress ζ_z at the position of minimum neck thickness were calculated using:

$$\zeta_z = \frac{F_z}{A_{neck}} = \frac{mg}{\text{minimum neck area}} = \frac{2\rho g D_E^3}{3D_N^2} \qquad [60]$$

where the tensile stress is the weight[7] of the detached drop divided by the area of the neck at the thinnest point of the filament. In all detachment experiments, the capillary pressure ($2\sigma/D_N$) is significantly smaller than the tensile stress (Eq. 60) and can therefore be considered relatively unimportant.

This stress is plotted against the apparent rate of elongation[8] $\dot{\varepsilon}$, defined as:

$$\dot{\varepsilon} = \frac{v_{neck}}{L_{neck}} \qquad [61]$$

where v_{neck} is the velocity of the minimum neck thickness position D_N and L_{neck} is the length of the neck; defined as twice the vertical length between the end of the capillary tube and the minimum neck thickness position. These parameters are displayed for clarity in Figure [26].

Figure [45] displays ζ_z plotted against $\dot{\varepsilon}$ for the most viscous GLY098 (μ = 0.925 Pas) and least viscous GLY080 (μ = 0.056 Pas) Newtonian fluids. The characteristic trends observed for these fluids are representative of all of the Newtonian fluids

[7] We assume here that the detached drop weight is comprised of all fluid below the position of the minimum neck thickness, where pinch-off occurs.

[8] The actual elongation or strain rate is $\dot{\varepsilon} = \partial u_z/\partial z$. Due to the shape of the drop neck (non cylindrical), the actual strain rate will vary throughout the filament. The apparent rate of elongation in Eq. [61] refers to the measured strain rate at the point of minimum neck filament diameter and whilst not entirely accurate, is useful for establishing where the strain begins to increase during pinch-off. Moreover, the apparent rate of elongation is defined here in terms of neck length. It can also be determined in terms of the drop radius at the point of minimum neck thickness. The mass flow, $\dot{M} = \pi D_N^{\,2} v_z \rho / 4$ of a cylindrical region of fluid of length L, density ρ and radius $D_N/2$ moving with velocity v_z can be equated to the derivative of the mass $M = \pi\rho L\, D_N^{\,2}/4$ (where $\dot{M} = 2\pi D_N \dot{D}_N L\rho/4$), giving $\dot{\varepsilon} = v_z/L = -2\dot{D}_N/D_N$. A comparison of apparent rates of elongation measured using the drop neck length and minimum neck thickness was made. Results were found to agree to within ±10%.

examined. Figure [46] displays an equivalent plot for the least shear-thinning X0125 and most shear-thinning X075 fluids. As with the Newtonian fluids, trends observed in these results are representative of the other shear-thinning fluids examined.

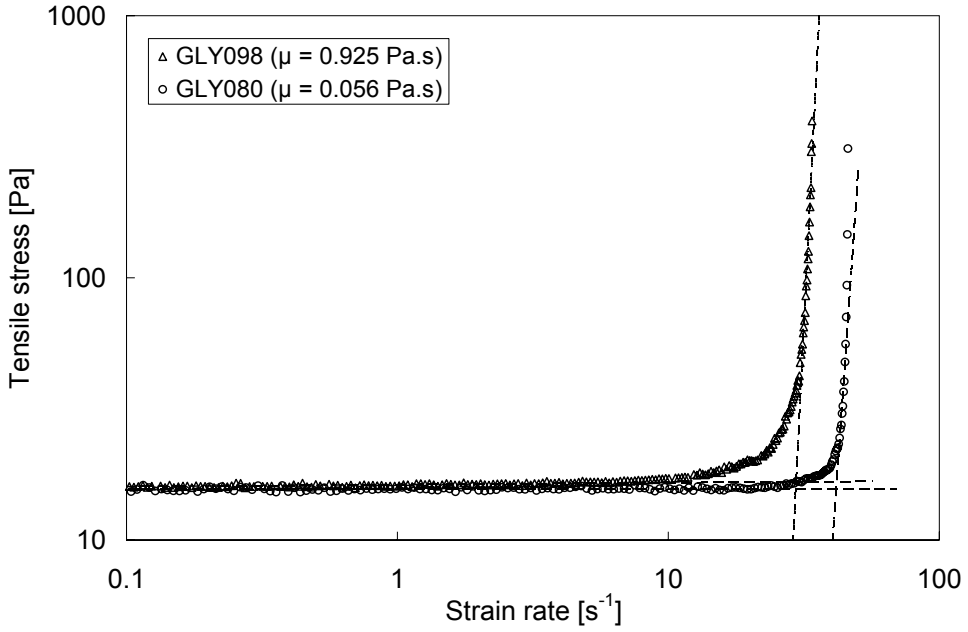

Figure 45. Tensile stress ζ_z at the position of minimum neck thickness as a function of the apparent rate of elongation $\dot{\varepsilon}$ for the GLY098 (μ = 0.925 Pas, open triangle symbol) and GLY080 (μ = 0.056 Pas, open circle symbol) Newtonian fluids. The maximum tensile stress at the point of instability corresponds to the intersection of the least square linear best fits (short dashed lines) for the near-constant stress region prior to the onset of instability and the unstable region of increasing tensile stress. Each experimental results set is based on the average of 5 drop measurements. Errors are not displayed for visual clarity, however are comparable with symbol size.

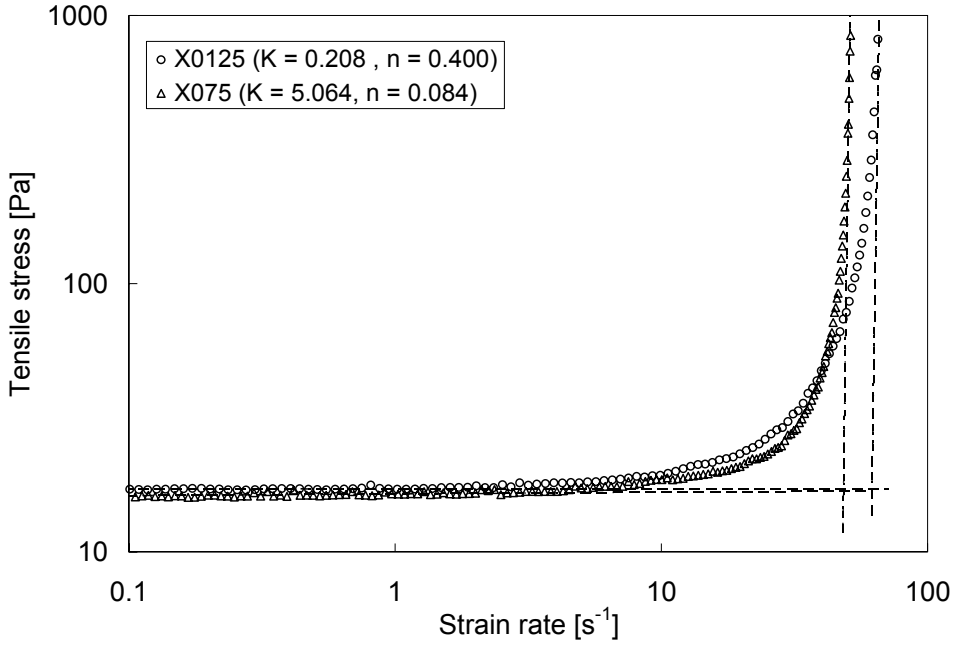

Figure 46. Tensile stress ζ_z at the position of minimum neck thickness as a function of the apparent rate of elongation $\dot{\varepsilon}$ for the X0125 (K = 0.208 Pas^n, n = 0.400, open triangle symbol) and X075 (K = 5.064 Pas^n, n = 0.084, open circle symbol) shear-thinning fluids. The maximum tensile stress at the point of instability corresponds to the intersection of the least square linear best fits (short dashed lines) for the near-constant stress region prior to the onset of instability and the unstable region of increasing tensile stress. Each experimental results set is based on the average of 5 drop measurements. Errors are not displayed for visual clarity, however are comparable with symbol size.

As Newtonian and shear-thinning drops (with similar D_E) grow on the end of the capillary tube, the tensile stress increases slowly due to increased drop mass; the minimum neck thickness prior to critical breakup remains equal to D_0. At the point of critical breakup, the maximum tensile stress of a stable drop supportable by the cohesive surface tension forces is reached. After this point, the tensile stress begins to increase significantly towards pinch-off; whilst the weight of the drop below the minimum neck thickness position remains the same (and equal to the detached drop weight), the increase is due to decreases in the minimum neck thickness. The maximum tensile stress at the point of instability, ζ_{crit}, is established by measuring the intersection of least square linear best fits of the form, $\zeta = k\dot{\varepsilon}^m$ or $\log(\zeta) = \log(k) + m\log(\dot{\varepsilon})$, representing the near-constant stress region prior to the onset of instability and the unstable region of increasing tensile stress. Measured values of ζ_{crit} plotted against viscosity are displayed in Figure [47] for the Newtonian fluids. Figures [48] and [49] plot ζ_{crit} for the shear-thinning fluids, plotted respectively against n and K.

From Figures [47] – [49], the influence of both viscosity and shear-thinning on ζ_{crit} is small. A maximum measurable difference of $\Delta\zeta_{crit}$ = 1 Pa is observed for the Newtonian fluids with an average of ζ_{crit} = 16.15 Pa. A maximum measurable difference of $\Delta\zeta_{crit}$ = 0.51 Pa is observed for the shear-thinning fluids with an average of ζ_{crit} = 17.16 Pa. These results support the previously established observation that viscous effects do not alter the stability characteristics of hanging drops[11].

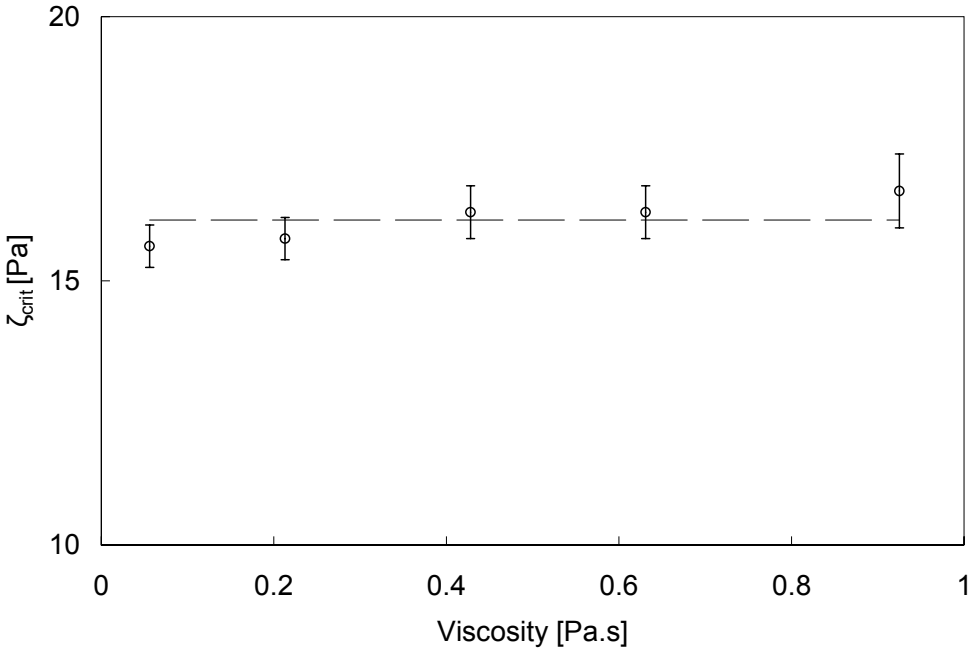

Figure 47. ζ_{crit} plotted against viscosity μ for Newtonian fluids in the range 0.056 ≤ μ ≤ 0.925 Pas. The long dashed line represents the average of ζ_{crit} for the fluids (ζ_{crit} = 16.2 Pa). ζ_{crit} varies in the range 15.7 ≤ ζ_{crit} ≤ 16.7 Pa.

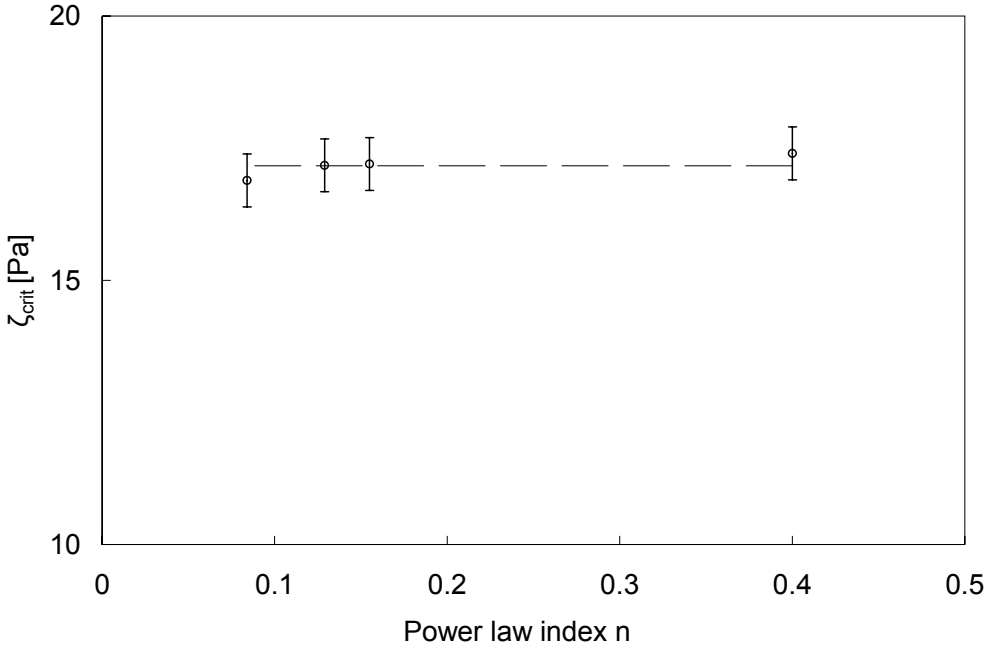

Figure 48. ζ_{crit} plotted against power law index n (Equation 37) for shear-thinning fluids in the range $0.084 \leq n \leq 0.4$. The long dashed line represents the average ζ_{crit} for the fluids ($\zeta_{crit} = 17.2$ Pa). ζ_{crit} varies in the range $16.9 \leq \zeta_{crit} \leq 17.4$ Pa.

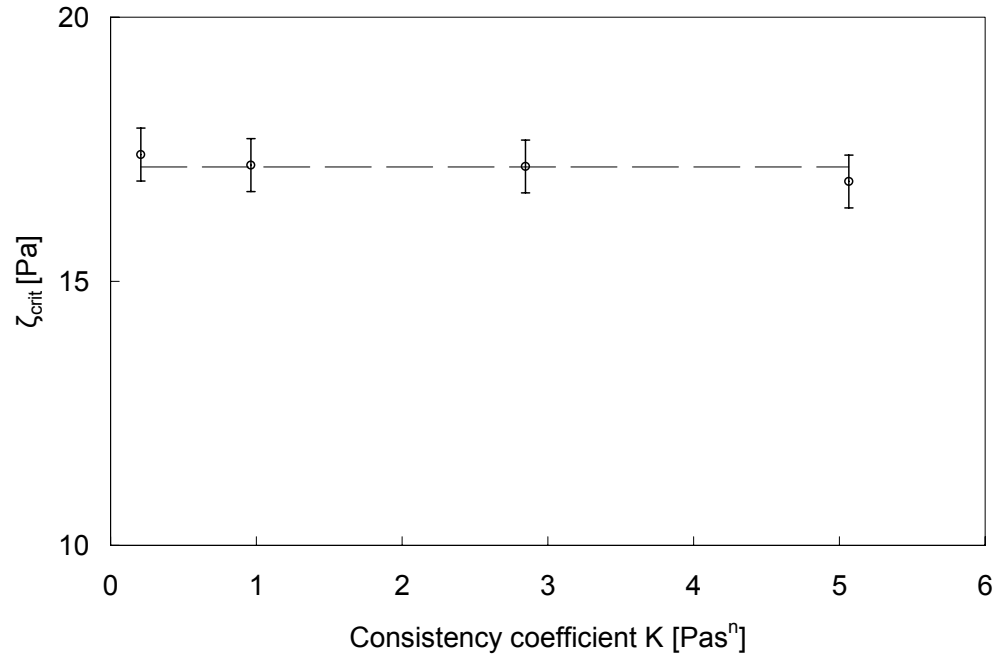

Figure 49. ζ_{crit} plotted against consistency coefficient K (Equation 37) for shear-thinning fluids in the range $0.208 \leq K \leq 5.064$ $Pa^n s$. The long dashed line represents the average ζ_{crit} for the fluids ($\zeta_{crit} = 17.2$ Pa). ζ_{crit} varies in the range $16.9 \leq \zeta_{crit} \leq 17.4$ Pa.

If one makes the conjecture that fluid yield-stress can influence the stability characteristics of hanging drops, then one should be able to measure these influences as variations in the maximum tensile stress arising in the drop neck at the onset of instability. Figures [50] – [53] display ζ_z plotted against $\dot{\varepsilon}$ for the YSF020 (τ_c = 0 Pa), YSF025 (τ_c = 5.4 Pa), YSF040 (τ_c = 26.1 Pa) and YSF050 (τ_c = 36.2 Pa) fluids. Again, least square best fit lines were applied to measurements of tensile stress in the stable and unstable linear regimes (short dashed lines in the figures); values of ζ_{crit} were determined from the intersection of these lines. From the figures, ζ_{crit} does not vary significantly for fluids with a low yield-stress magnitude, however there is a large increase in ζ_{crit} with τ_c for fluids with $\tau_c \geq 11.5$ Pa. To better understand this relationship, Figure [54] plots ζ_{crit} against τ_c. Whilst values of ζ_{crit} remain similar for low yield-stress magnitude fluids with $\tau_c < 11.5$ Pa, the critical tensile stress increases significantly with τ_c for fluid drops with $\tau > 11.5$ Pa.

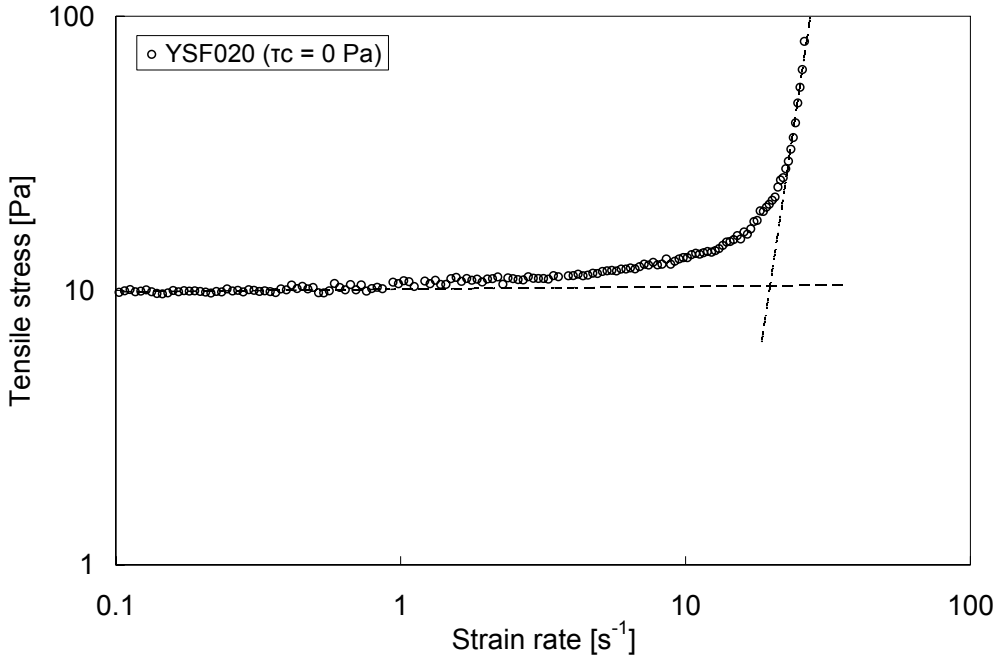

Figure 50. Tensile stress ζ_z at the position of minimum neck thickness as a function of the apparent rate of elongation $\dot{\varepsilon}$ for the YSF020 (τ_c = 0 Pa) viscoplastic fluid. Lines of best fit were made to the stress measurements in the linear stable and unstable regimes (short dashed lines); the intersection of these corresponds with ζ_{crit}. Experimental results are based on the average of 5 drop measurements. Errors are not displayed for visual clarity, however are comparable with symbol size.

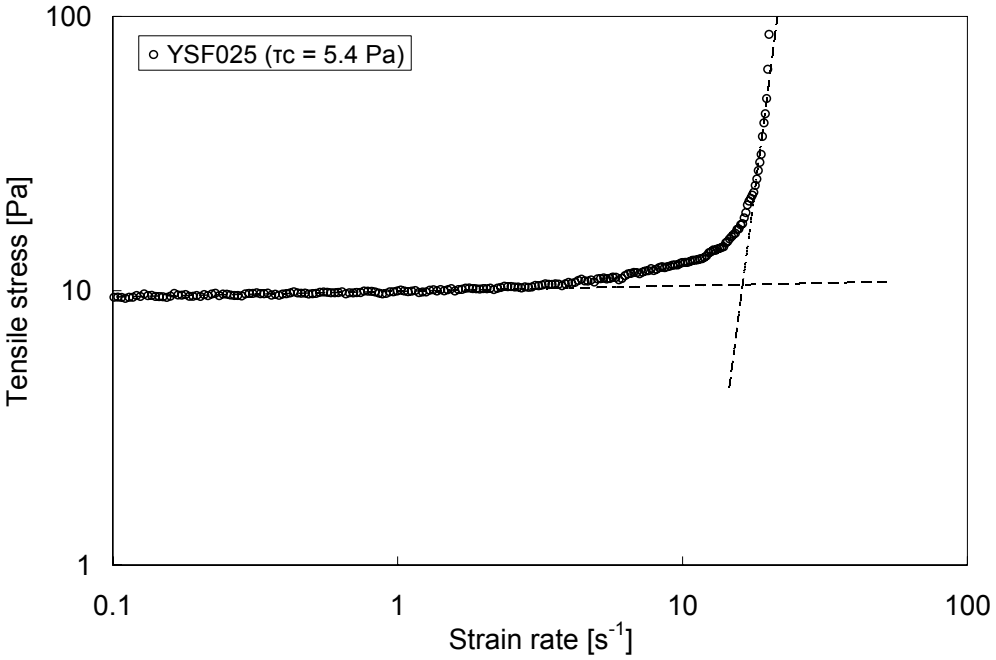

Figure 51. Tensile stress ζ_z at the position of minimum neck thickness as a function of the apparent rate of elongation $\dot{\varepsilon}$ for the YSF025 (τ_c = 5.4 Pa) viscoplastic fluid. Lines of best fit were made to the stress measurements in the linear stable and unstable regimes (short dashed lines); the intersection of these corresponds with ζ_{crit}. Experimental results are based on the average of 5 drop measurements. Errors are not displayed for visual clarity, however are comparable with symbol size.

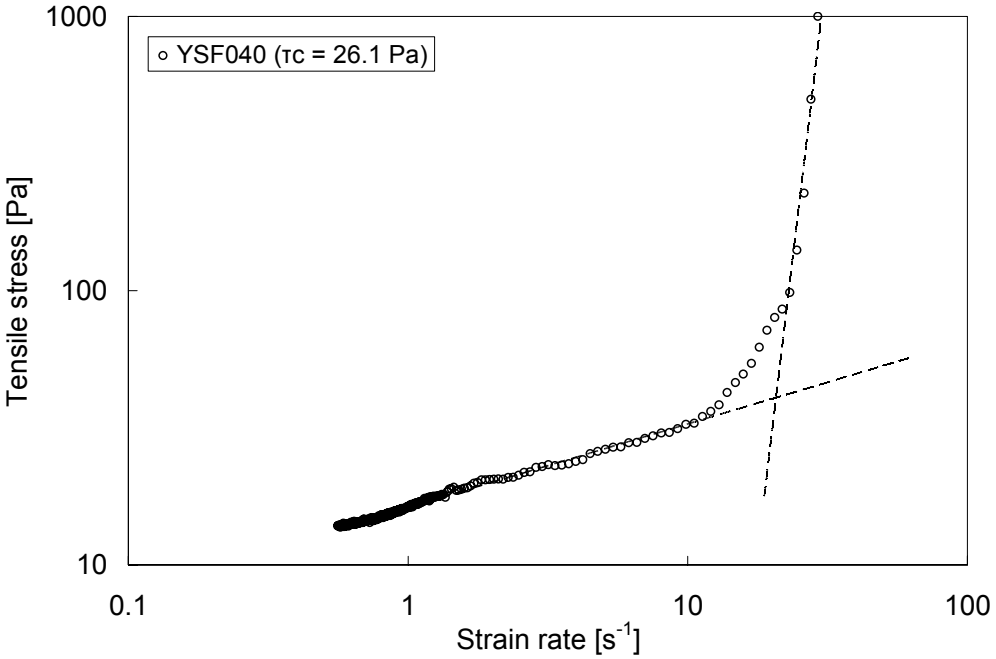

Figure 52. Tensile stress ζ_z at the position of minimum neck thickness as a function of the apparent rate of elongation $\dot{\varepsilon}$ for the YSF040 (τ_c = 26.1 Pa) viscoplastic fluid. Lines of best fit were made to the stress measurements in the linear stable and unstable regimes (short dashed lines); the intersection of these corresponds with ζ_{crit}. Experimental results are based on the average of 5 drop measurements. Errors are not displayed for visual clarity, however are comparable with symbol size.

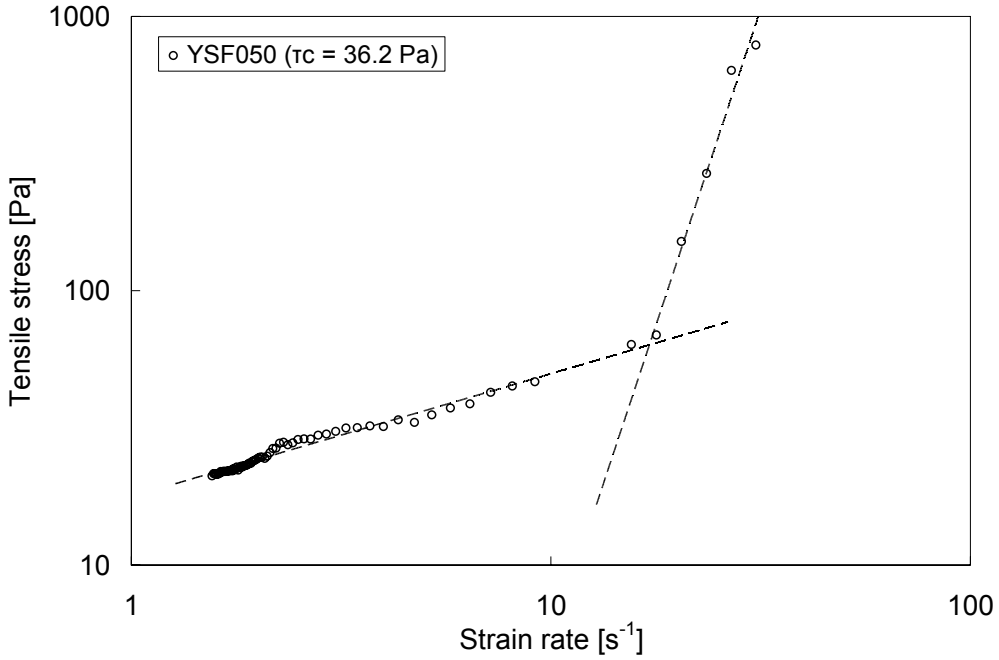

Figure 53. Tensile stress ζ_z at the position of minimum neck thickness as a function of the apparent rate of elongation $\dot{\varepsilon}$ for the YSF050 (τ_c = 36.2 Pa) viscoplastic fluid. Lines of best fit were made to the stress measurements in the linear stable and unstable regimes (short dashed lines); the intersection of these corresponds with ζ_{crit}. Experimental results are based on the average of 5 drop measurements. Errors are not displayed for visual clarity, however are comparable with symbol size.

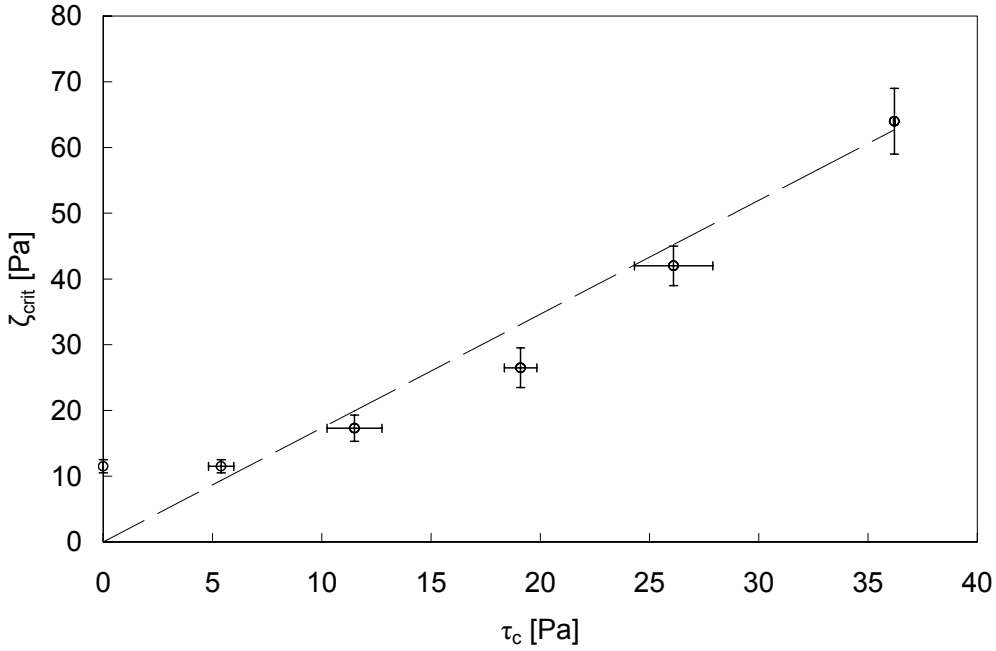

Figure 54. Measured ζ_{crit} plotted against τ_c for viscoplastic fluids with $0 \leq \tau_c \leq 36.2$ Pa. The long dashed line corresponds to the von Mises yield criterion (Equation 62).

An additional complexity is that deformation in the neck during the onset of instability and subsequent detachment is extensional, however the yield-stress magnitude is measured by applying a shear-force to a fluid sample during rheometry. Figure [54] therefore represents the relationship between the tensile and shear yield points. A relationship between these two parameters can be established using the von-Mises yield criterion[163], which states that the yielding of plastic materials begins when the second deviatoric stress tensor $\sqrt{-T_{II}}$ reaches a critical value. In the case of the generalized Herschel-Bulkley rheological model (Equation 46), this is $\sqrt{-T_{II}} = \tau_c$. Moreover, the shear stress at the onset of yielding is $\sqrt{3}$ times smaller than the tensile stress in the case of simple tension at the yield criterion:

$$\zeta_{crit} = \sqrt{3}\tau_c \qquad [62]$$

Figure [54] highlights two interesting characteristics. Firstly, fluids with $\tau_c \leq 5.4$ Pa show larger values of ζ_{crit} than those predicted using Equation [62] (long dashed line). Secondly, values of ζ_{crit} for fluids with $\tau_c \geq 5.4$ Pa generally show a good agreement with the von Mises yield relationship, although the measured critical tensile stress of the YSF035 solution is smaller than that predicted using Equation [62] and slightly outwith the margin of experimental error.

The von-Mises relationship predicts the tensile stress in the drop neck at the point of critical breakup to be zero for all fluids that do not exhibit a finite yield-stress magnitude. As the Newtonian and shear-thinning drop measurements show in Figures [47] - [49] however, this is clearly not true; both fluids types exhibit a near constant value of ζ_{crit} with changes in both viscosity and shear-thinning characteristics. Moreover, values of ζ_{crit} for yield-stress fluids with $\tau_c \leq 5.4$ Pa are nearly identical, although smaller than the Newtonian and shear-thinning fluids because the reduced surface tension lowers the supportable drop mass at critical breakup. This suggests therefore that the von Mises relationship breaks down towards low yield-stress magnitude fluids. For yield-stress

fluids with $\tau_c > 5.4$ Pa however, the relationship between the tensile and shear yield-stresses follows Equation [62], indicative of a system being governed by fluid plasticity.

In order to characterise why the behaviour of detaching drops of low and high yield-stress magnitude fluids differ, we separate stability characteristics into two regimes; a classical regime where critical breakup is governed by competition between gravity and fluid capillarity and a regime where fluid yield-stress forces are comparable with or exceed surface tension forces and govern the critical breakup of detaching drops. In the first regime; characteristic of Newtonian, shear-thinning and small yield-stress magnitude fluids, drop detachment dynamics are governed by well established classical behaviour; instabilities arise when gravity overcomes cohesive surface tension forces and once a cylindrical shape is reached on the drop surface, perturbations will increase exponentially in magnitude, driven by capillarity. In the second regime, cohesive forces originating from yield-stress characteristics can inhibit capillary driven breakup. Moreover, within this regime, critical instability is governed by yield-stress magnitude.

The two regimes can be distinguished by introducing a dimensionless number $\hat{B}$ that compares the yield-stress to the capillary pressure[133]:

$$\hat{B} = \frac{\tau_c D_E}{\sigma} \qquad [63]$$

This term is the product of the dimensionless Capillary (Equation 15) and Bingham (Equation 56) numbers and characterises the ratio of yield-stress to capillary forces. This term specifically relates capillary forces with fluid yield-stress magnitude when subject to shear forces. As previously highlighted however, the stress in the drop neck during detachment is extensional. A more appropriate parameter for characterisation in this case is therefore:

$$\hat{B}_E = \frac{\zeta_{crit} D_E}{\sigma} = \frac{\sqrt{3}\tau_c D_E}{\sigma} \qquad [64]$$

When surface tension forces exceed extensional yield-stress forces ($\hat{B}_E < 1$), ζ_{crit} remains unchanged, however when extensional yield-stress forces exceed surface tension forces ($\hat{B}_E > 1$), the critical breakup characteristics of drops are governed by yield-stress effects.

Figure [55] plots measured values of ζ_{crit} against $\hat{B}_E$, whose extensional yield-stress term is calculated in terms of the measured τ_c and Equation [62]. The two trendlines correspond to a least square best fit line representing the average ζ_{crit} for fluids with $\hat{B}_E < 1$, and a least square line of best fit applied to the results of the yield-stress fluids with $\hat{B}_E > 1$. The intersection of these lines occurs at $\hat{B}_E \sim 1.3 \pm 0.1$, close to the expected transition value of $\hat{B}_E = 1$.

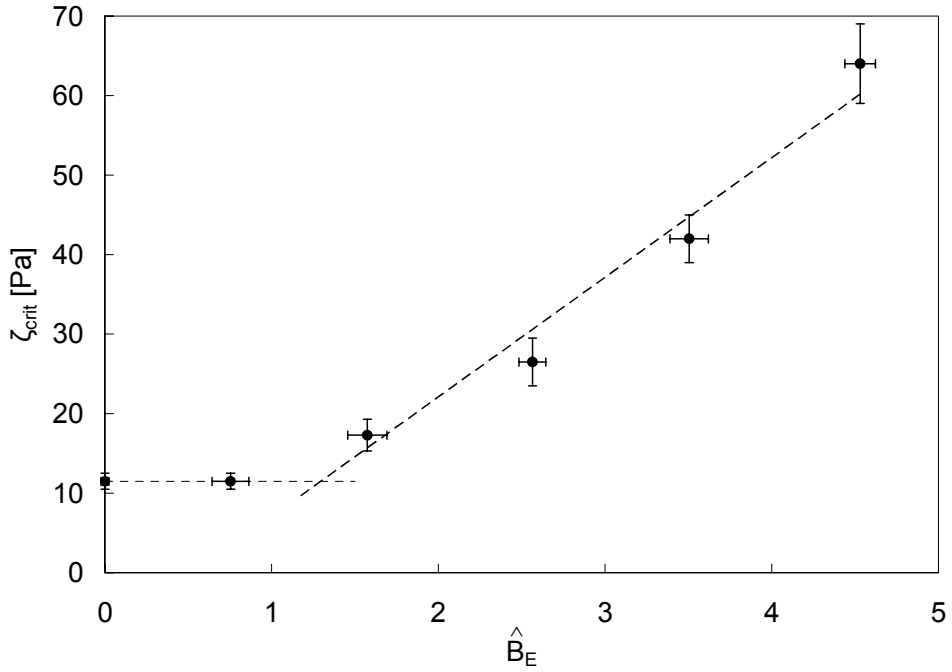

Figure 55. ζ_{crit} plotted against $\hat{B}_E$ for viscoplastic fluids in the range $0 \leq \tau_c \leq 36.2$ Pa. The short dashed line correspond to the average ζ_{crit} for $\hat{B}_E < 1$ and the long dashed line corresponds to the least square line of best fit for fluids with $\hat{B}_E > 1$. The intersection of the dashed lines corresponds with the transition point from capillary governed detachment to yield-stress governed detachment. This occurs at $\hat{B}_E \sim 1.3 \pm 0.1$.

Figure [55] supports the conjecture that surface tension and yield-stress governed regimes exist. For $\hat{B}_E < 1$, tensile stresses at critical breakup remains very similar in magnitude; a characteristic also observed in both the Newtonian ($15.7 \leq \zeta_{crit} \leq 16.7$ Pa) and shear-thinning fluids ($16.9 \leq \zeta_{crit} \leq 17.4$ Pa). This is representative of a system where the stability criterion of detachment is governed by competition between the drop weight and the cohesive surface tension forces; a near constant parameter for each fluid type. At the intersection of the two regimes close to $\hat{B}_E = 1$, the maximum stable tensile stress in the drop neck that can be supported by capillary forces is equal in magnitude to the extensional yield-stress. For $\hat{B}_E > 1$, the extensional forces required to yield the fluid are greater than those required to produce the onset of instability by overcoming capillary forces, indicative of a yield-stress governed regime[146,147].

3.3.2 Drop detachment behaviour

Unlike Newtonian and shear-thinning fluids, the period between the onset of instability and pinch-off (Figure 40) for fluids with a measurable yield-stress does not vary significantly. With the exception of the YSF020 fluids (τ_c = 0 Pa), whose detachment period is t ($D_{N,Crit}$) = - 0.16 s, the remaining fluids; all of which exhibit a measurable yield-stress , have similar detachment periods in the range $-0.337 \leq t(D_{N,Crit}) \leq -0.263$ s. This is displayed in Figure [56]. The similarity is interesting because the viscoplastic fluids each exhibit differing shear-thinning properties and shear-thinning characteristics in the absence of a yield-stress have previously been shown to produce a measurable change in the detachment period (Figure 39 and 40). This suggests that fluid yield-stress influences the detachment dynamics of the drops as well as the stability characteristics.

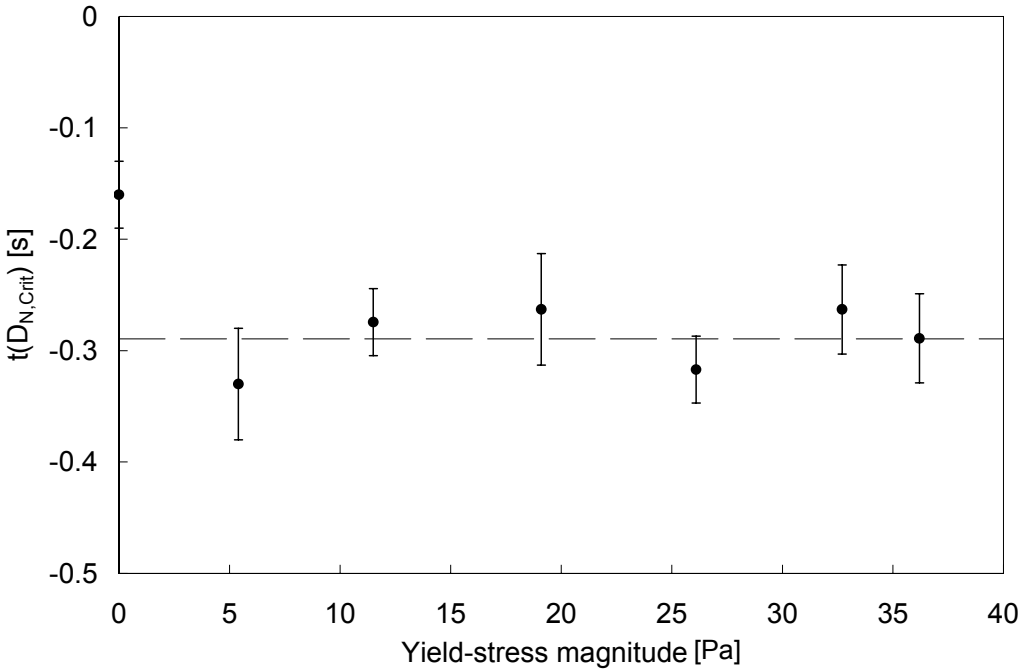

Figure 56. Detachment period or the time of the onset of instability prior to pinch off $t(D_{N,Crit})$ for viscoplastic fluids in the range $0 \leq \tau_c \leq 36.2$ Pa. The long dashed line corresponds to the average detachment period of 0.298 s for fluids with a measurable yield-stress.

Figure [57] displays the temporal variations of D_N/D_0, normalised with respect to $D_{N,Crit}$. The normalisation results with the onset of instability for each fluid occurring at the same neck diameter. The graph highlights that with exception of the YSF020 fluid ($\tau_c = 0$ Pa), drop detachment behaviour is nearly identical for each fluid and does not vary like Newtonian or shear-thinning characteristics. Whereas shear-thinning characteristics of the yield-stress fluids vary (Table 4) and should significantly influence the period of detachment, the similarity of the results in Figure [57] suggests that increasing fluid yield-stress within the range $5.4 \leq \tau_c \leq 32.7$ Pa does not change the detachment period, but instead alters the rate at which D_N/D_0 varies. In other words, increasing fluid yield-stress does not alter the detachment period, but instead reduces the rates of detachment.

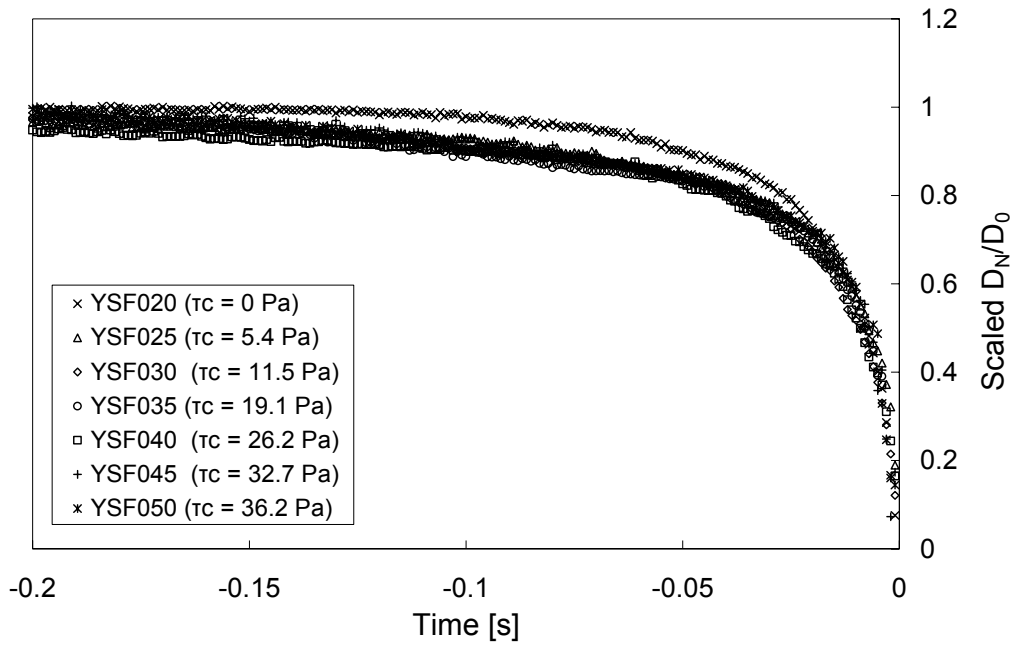

Figure 57. (D_N/D_0) normalized with respect to $D_{N,Crit}$ for each fluid plotted against time. Experimental results are based on the average of 5 drop measurements. Errors are not displayed for visual clarity, however are comparable with symbol size.

4. Results and Discussion - Drop free-fall dynamics

Directly after pinch-off, the portion of the neck filament remaining attached to the drop will be absorbed into the initially prolate main drop body. This shape will become more spherical during free-fall by action of capillary forces. Whilst a spherical drop shape is reached quickly for each of the Newtonian ($0.056 \leq \mu \leq 0.925$ Pas) and shear-thinning ($0.084 \leq n \leq 0.4$, $0.208 \leq K \leq 5.065$ Pas^n) fluid solutions, the shape of some yield-stress fluid drops can be prolate throughout the measured free-fall period. Whilst drops of the YSF020 ($\tau_c = 0$ Pa) and YSF025 ($\tau_c = 5.4$ Pa) solutions take on a near spherical equilibrium shape, increasing τ_c results in drop shapes appearing progressively more prolate, this may indicate that yield-stress can prevent spherical drop shape formation; in agreement with previous observations[148]. Figure [58] displays images of the equilibrium free fall shape (**§2.8.2**) for the Newtonian, shear-thinning and viscoplastic drops.

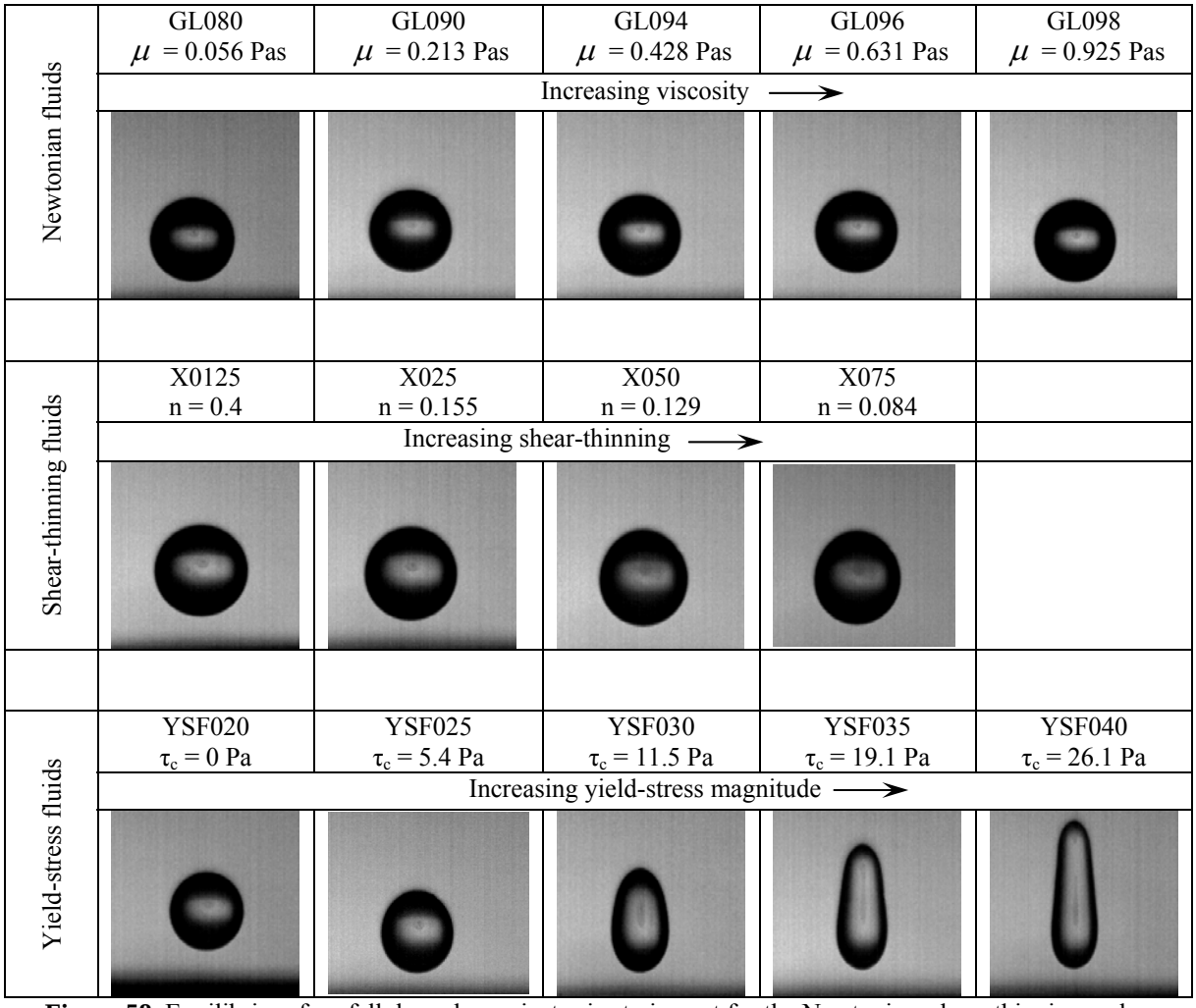

Figure 58. Equilibrium free-fall drop shapes just prior to impact for the Newtonian, shear-thinning and yield-stress fluids.

4.1 Newtonian fluid drops

Figures [59] – [63] display measured temporal variations in drop shape factor S (Equation 59) just after pinch-off for each Newtonian fluid. Experimental measurements are compared with predictions of Equations [10] and [11] using parameters detailed in Table [7]. Moreover, drop relaxation dynamics can be described in terms of the drop shape factor, S, instead of x(t) using:

$$S(t) = \frac{H(t) - D(t)}{H(t) + D(t)} \approx \frac{(D_E + x(t)) - (D_E - x(t))}{(D_E + x(t)) + (D_E - x(t))} \approx \frac{x(t)}{D_E} \qquad [65]$$

This approximation assumes that the initial drop perturbations are small and prolate. S is then simply the perturbation length non-dimensionalised by the equivalent drop diameter D_E (Equation 57). Values of S(0) used in the predictions were measured directly from drop images at the point of detachment after the absorption of the neck filament. In general these initial values fall within the observed range of eccentricities e = H/D by Ford and Furmidge[53] ($0.8 \leq e \leq 1.2$, approximately equivalent to $-0.1 \leq S \leq 0.1$), however measured values of S(0) for the GLY098 and GLY096 fluids are larger, as detailed in Table [7]. This is primarily due to the long filament attached to drop upon detachment.

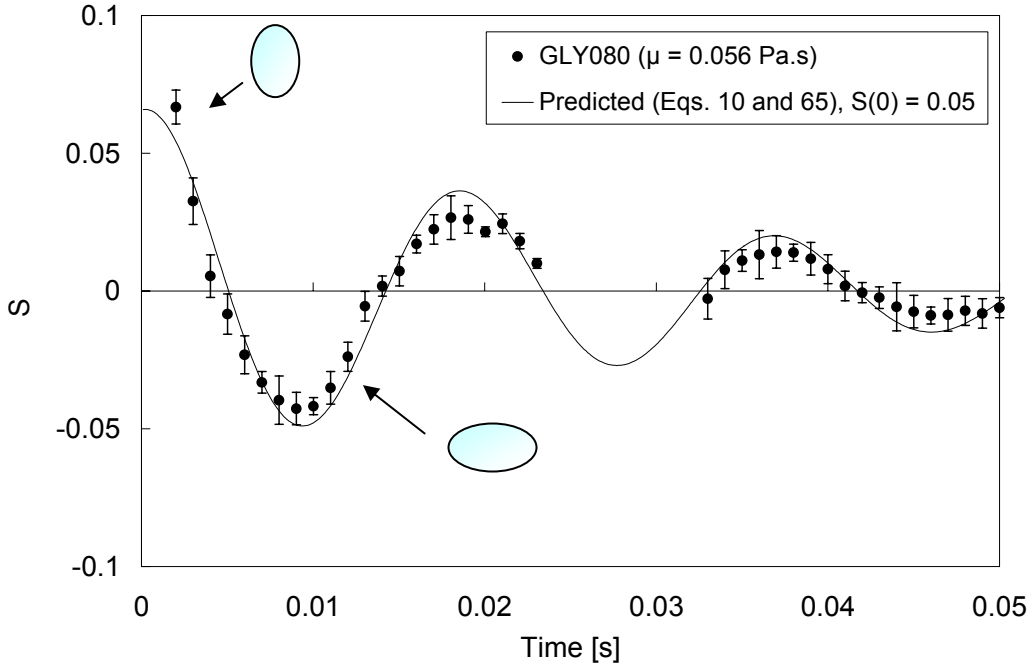

Figure 59. Temporal variation in dimensionless drop shape factor S after pinch-off for the GLY080 solution (μ = 0.056 Pas). The solid line corresponds to predictions using Equations [10] and [65] with values detailed in Table [7]. Experimental results are based on the average of 5 drop measurements.

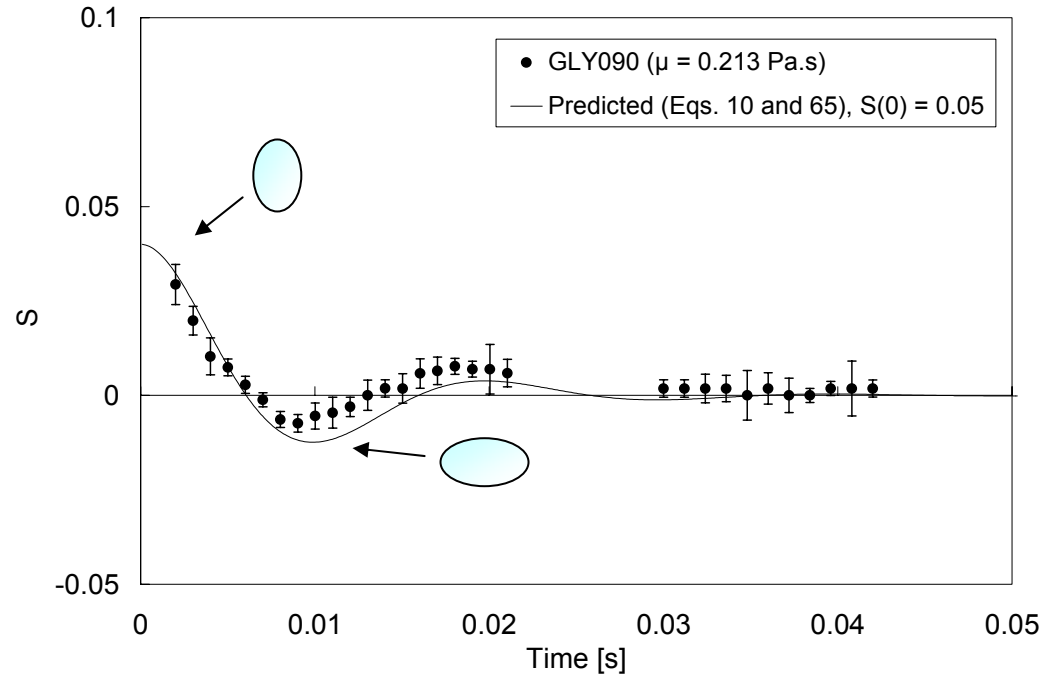

Figure 60. Temporal variation in dimensionless drop shape factor S after pinch-off for the GLY090 solution (μ = 0.213 Pas). The solid line corresponds to predictions using Equations [10] and [65] with values detailed in Table [7]. Experimental results are based on the average of 5 drop measurements.

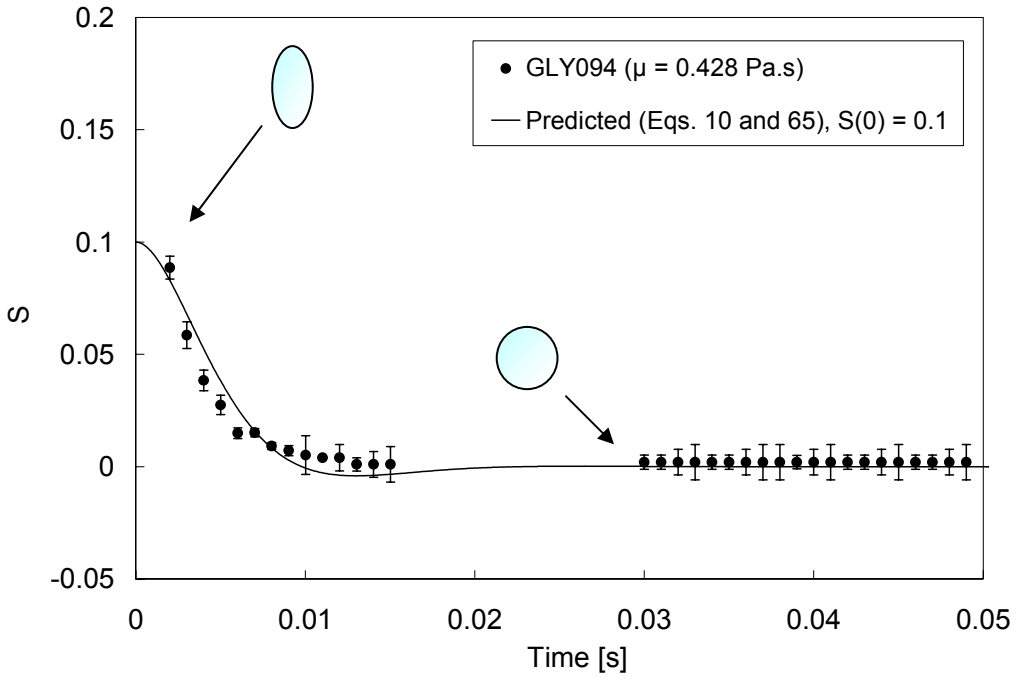

Figure 61. Temporal variation in dimensionless drop shape factor S after pinch-off for the GLY094 solution (μ = 0.428 Pas). The solid line corresponds to predictions using Equations [10] and [65] with values detailed in Table [7]. Experimental results are based on the average of 5 drop measurements.

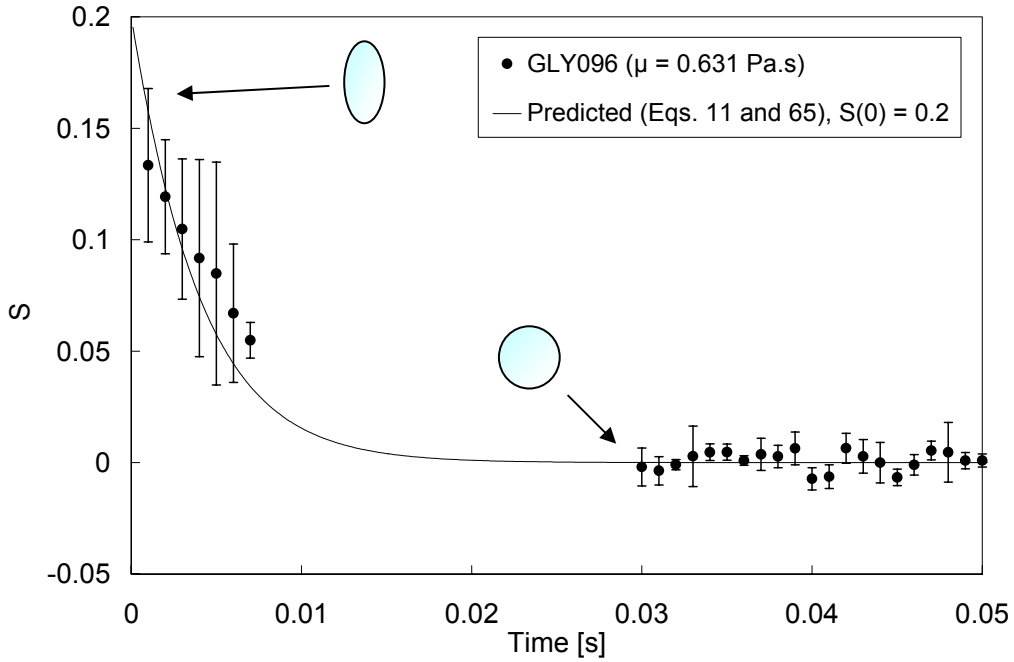

Figure 62. Temporal variation in dimensionless drop shape factor S after pinch-off for the GLY2 solution (μ = 0.631) Pas). The solid line corresponds to predictions using Equations [11] and [65] with values detailed in Table [7]. Experimental results are based on the average of 5 drop measurements.

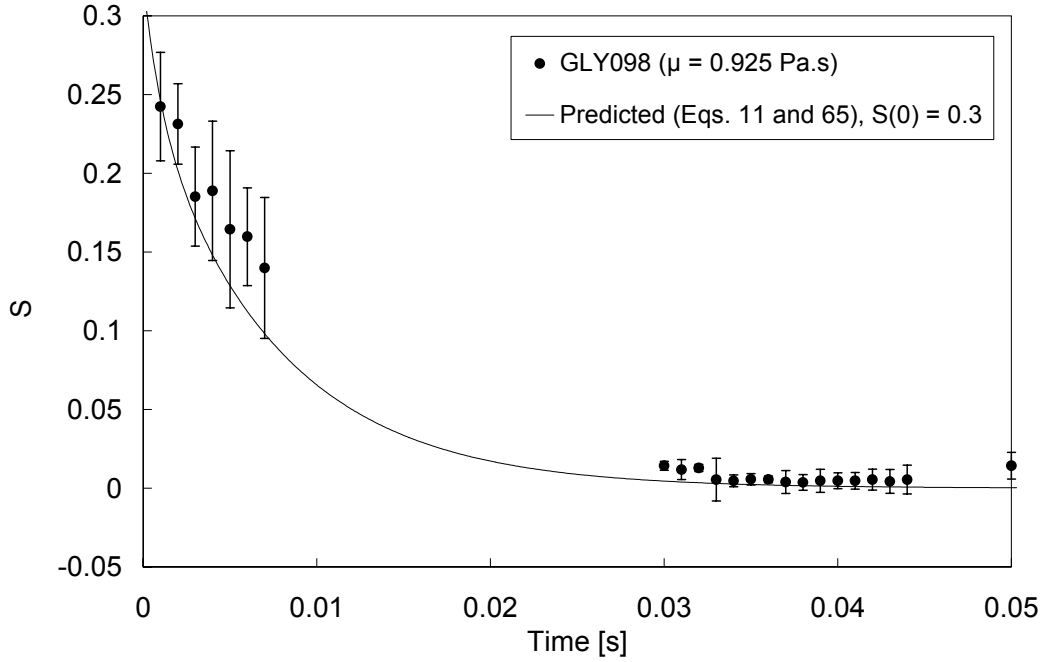

Figure 63. Temporal variation in dimensionless drop shape factor S after pinch-off for the GLY098 solution (μ = 0.925 Pas). The solid line corresponds to predictions using Equations [11] and [65] with values detailed in Table [7]. Experimental results are based on the average of 5 drop measurements.

Table 7. Parameters associated with free drop dynamic behaviour including measured initial drop shape factors S(0) used for predictions.

Material	Viscosity [Pas]	Undamped natural frequency $\omega_{n0}/2\pi$ [s^{-1}]	Damping factor b_{n0} [s^{-1}]	Approximate Eccentricity at pinch-off (H_0/D_0) e	Measured initial drop shape factor S(0)
GLY080	0.056	54.8	0.094	1.1	0.05 ± 0.01
GLY090	0.213	54.0	0.350	1.1	0.04 ± 0.02
GLY094	0.428	54.8	0.713	1.2	0.1 ± 0.02
GLY096	0.631	54.4	1.039	1.4	0.2 ± 0.02
GLY098	0.925	55.0	1.531	1.6	0.3 ± 0.02

Experimental results in Figures [59] – [63] are each comprised of a composite of measurements taken from different fall heights using a fixed camera field of view. Altering the fall height allowed different periods of free-fall to be observed. Quantification of this period was made by extracting the time of impact from the recorded images and using Equation [58], with $u = (H_f - H)/t$ to establish the total free fall time. The drop characteristics of five drops were recorded and averaged for each measurement to ensure repeatability and to establish errors.

The measured drop relaxation behaviour of each Newtonian fluid (Figures 59 – 63) agrees closely with its respective prediction curve. Fluids with $\mu \leq 0.213$ Pas show periodic behaviour, whilst aperiodic behaviour is observed for $\mu \geq 0.428$ Pas. Moreover, Table [8] compares the measured and predicted frequencies $\omega_d/2\pi$ for the GLY090 and GLY080 fluids (detailed in **§1.2.2**). Values in both cases agree to within experimental error. Increases in viscosity for the periodic regime act to increase the damping and thus reduce oscillatory behaviour and the period from pinch-off until equilibrium. The opposite is true in the aperiodic regime; increasing viscosity acts to slow relaxation driven by capillarity, lengthening the period from pinch-off until equilibrium.

Table 8. A comparison of measured and predicted damped natural frequencies for fluids exhibiting periodic behaviour along with periodic/aperiodic transition characterization parameters.

Material	Quarter wavelength period t_q [ms]	Damped natural frequency $\omega_d/2\pi$ [s^{-1}]			Dimensionless viscosity ε
		Measured	Error	Predicted	
GLY080	4.6	61.3	6.6	54.5	0.15
GLY090	4.6	59.75	10.1	50.6	0.58
GLY094	4.6	-	-	-	1.17
GLY096	4.6	-	-	-	1.72
GLY098	4.5	-	-	-	2.51

The characterisation of drop relaxation dynamics in free-fall can be made using the dimensionless viscosity ε (Equation 12). Prosperetti[37] developed the understanding of classical damped harmonic and overdamped system behaviour in free drops by establishing that fluids with $\varepsilon \geq 0.7665$ will exhibit aperiodic motion throughout their

relaxation period. Figure [64] plots dimensionless viscosity ε against μ for Newtonian fluids in the range 0.056 ≤ μ ≤ 0.925 Pas and confirms that this characterisation agrees with the observed behaviour.

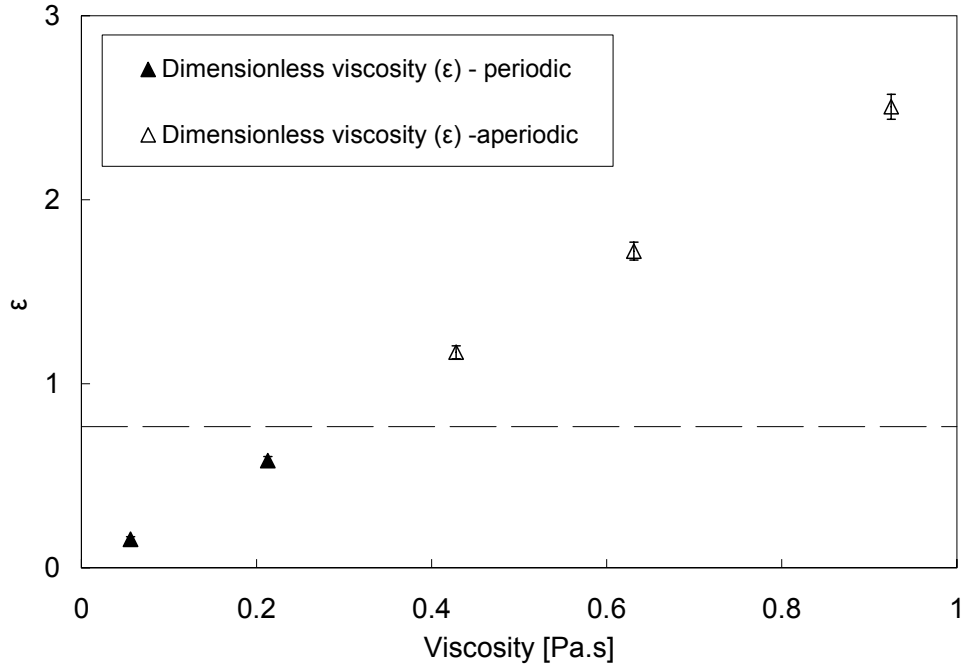

Figure 64. Dimensionless viscosity ε (Equation 12) plotted against viscosity, μ, for Newtonian fluids in the range 0.056 ≤ μ ≤ 0.925 Pas. Filled and open symbols denote periodic and aperiodic relaxation behaviour respectively. The dashed line corresponds to ε = 0.7665. Values of ε above this threshold exhibit only aperiodic motion. Where not observed, error bars are comparable in size to the symbol.

4.2 Shear-thinning fluid drops

Figures [65] – [68] display measured temporal variations in S after pinch-off for each of the shear-thinning fluids. In order to establish the effects of shear-thinning on drop dynamics during free-fall, the measured relaxation behaviour of each fluid is compared with predictions (using Equations 10, 11 and 65) of an equivalent Newtonian fluid exhibiting no shear-thinning effects. An equivalent Newtonian fluid is conceived by recognising that as shear-thinning properties decrease (n → 1), the power law model ($\tau = K\dot{\gamma}^n$) tends to the Newtonian model ($\tau = \mu\dot{\gamma}$) with the consistency coefficient K tending towards the Newtonian viscosity. Here K denotes the maximum viscosity of the shear-thinning fluids as shear-rates tend to zero. Equivalent Newtonian predictions

therefore use values of K replacing the viscosity term, with all other fluid parameters (σ, ρ and D_E) kept the same as those detailed in Tables [3] and [5]. Moreover, predicted values of S(0) correspond with those measured directly after pinch-off for each fluid.

As with the Newtonian fluid measurements, results are not continuous because of the static camera field of view through which the drop passes. Measurements are composites of recordings from several fall heights, combined in the same way as described in **§4.1**. Table [9] details the parameters used for the equivalent Newtonian predictions.

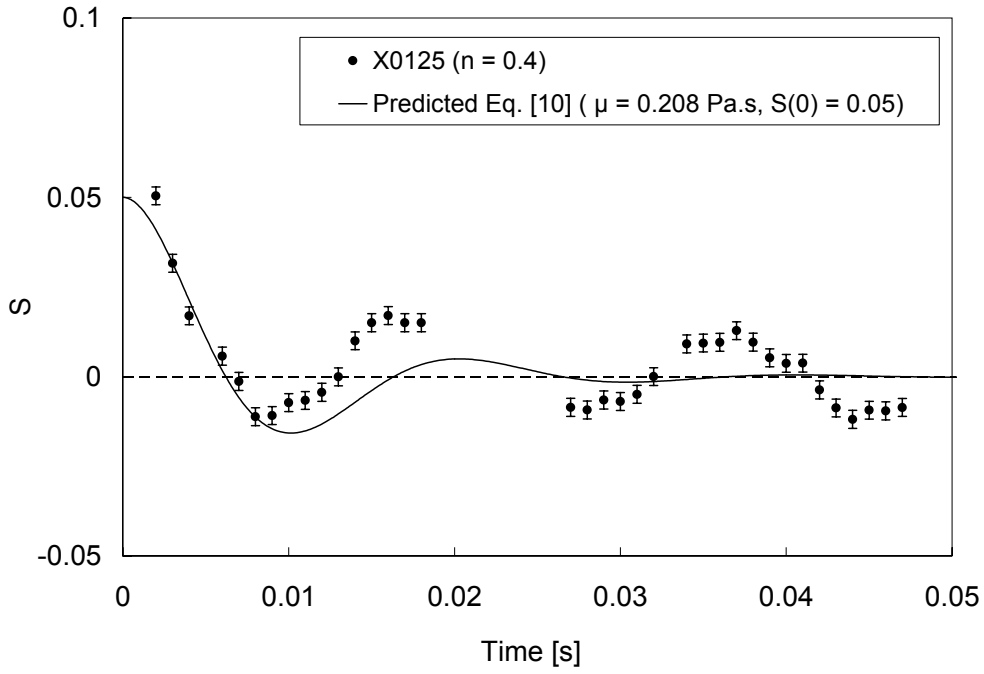

Figure 65. Temporal variation in dimensionless drop shape factor S after pinch-off for the X0125 fluid solution (n = 0.4, K = 0.208 Pas^n). The solid line corresponds to the drop shape prediction of an equivalent Newtonian fluid using Equations [10] and [65] with the viscosity replaced with the consistency coefficient K, detailed in Table [9]. Experimental results are based on the average of 5 drop measurements.

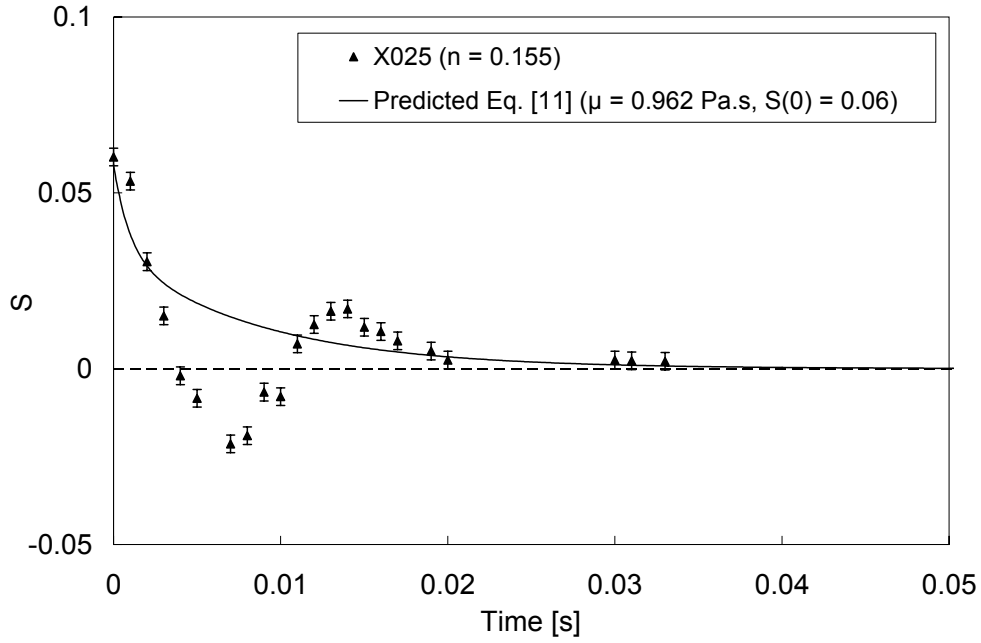

Figure 66. Temporal variation in dimensionless drop shape factor S after pinch-off for the X025 fluid solution (n = 0.155, K = 0.962 Pas^n). The solid line corresponds to the drop shape prediction of an equivalent Newtonian fluid using Equations [11] and [65] with the viscosity replaced with the consistency coefficient K, detailed in Table [9]. Experimental results are based on the average of 5 drop measurements.

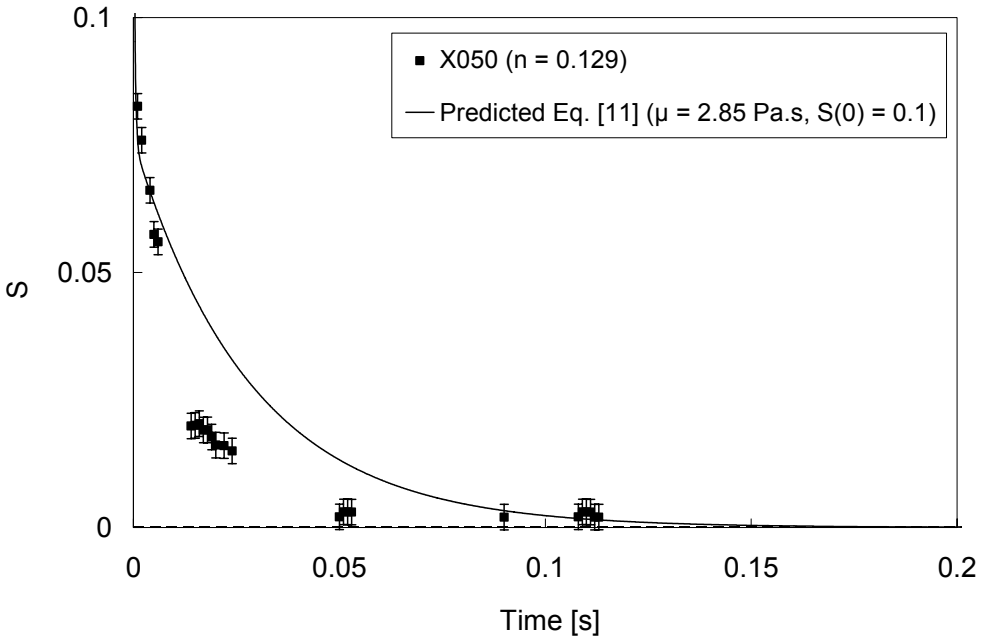

Figure 67. Temporal variation in dimensionless drop shape factor S after pinch-off for the X050 fluid solution (n = 0.129, K = 2.85 Pas^n). The solid line corresponds to the drop shape prediction of an equivalent Newtonian fluid using Equations [11] and [65] with the viscosity replaced with the consistency coefficient K, detailed in Table [9]. Experimental results are based on the average of 5 drop measurements.

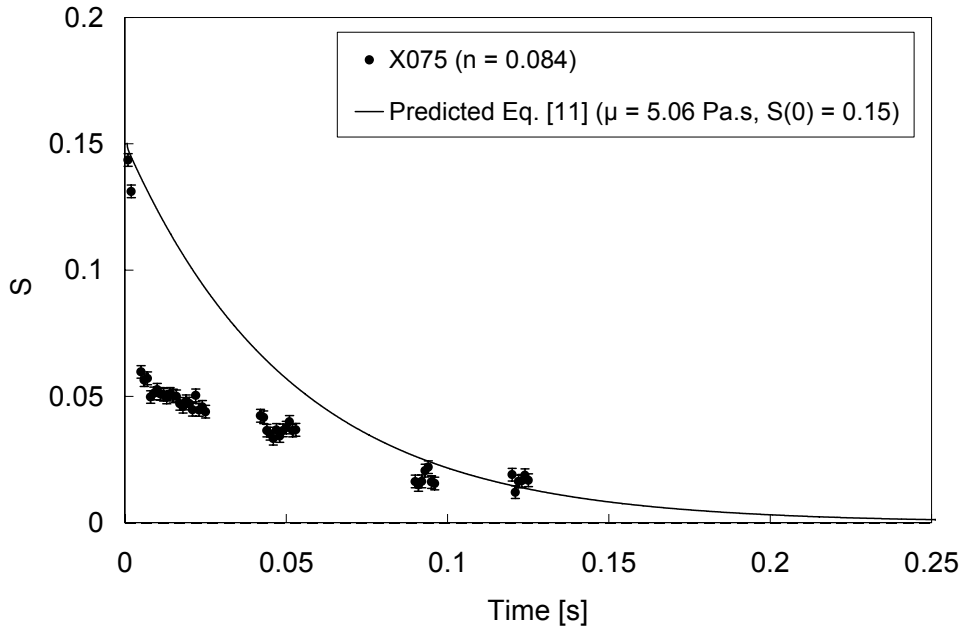

Figure 68. Temporal variation in dimensionless drop shape factor S after pinch-off for the X050 fluid solution (n = 0.084, K = 5.06 Pas^n). The solid line corresponds to the drop shape prediction of an equivalent Newtonian fluid using Equations [11] and [65] with the viscosity replaced with the consistency coefficient K, detailed in Table [9]. Experimental results are based on the average of 5 drop measurements.

Table 9. Parameters associated with shear-thinning and equivalent Newtonian fluid drop dynamic behaviour including initial measured drop shape factor S(0) used for predictions.

Material	Consistency coefficient K [Pas^n]	Undamped natural frequency $\omega_{n0}/2\pi$ [s^{-1}]	Damping factor b_{n0} [s^{-1}]	Dimensionless viscosity ε	Measured initial drop shape factor S(0)
X0125	0.208	52.55873	0.345	0.59 ± 0.022	0.05 ± 0.01
X025	0.962	54.41798	1.672	2.77 ± 0.089	0.06 ± 0.02
X050	2.846	53.2807	4.853	8.20 ± 0.268	0.1 ± 0.02
X075	5.064	55.73408	9.059	14.63 ± 0.510	0.15 ± 0.02

From the predicted values of ε (Equation 12 with μ replaced with K) given in Table [9], all fluids except the X0125 solution are expected to show overdamped aperiodic behaviour (ε > 0.7665). In contrast however, both the measured relaxation behaviour of the X0125 and X025 fluids in Figures [65] and [66] exhibit periodic relaxation. This indicates that fluid shear-thinning during relaxation reduces the dimensionless viscosity of the X025 fluid to below ε = 0.7665. Moreover, the effects of

fluid shear-thinning can also be observed for the X0125 in Figure [65]; predictions show increased damping in comparison with measured drop relaxation behaviour. In other words, the action of fluid shear-thinning decreasing local fluid viscosity during relaxation also reduces the damping (comparable to reducing the damping coefficient b_{n0} in Equation [9] by decreasing the Newtonian viscosity μ), resulting in a longer timescale of oscillation.

Shear-thinning effects can be observed for aperiodic relaxation as well in Figures [67] and [68]. For both the X050 and X075 fluids, the initial measured retraction after pinch-off is substantially faster than that predicted for the equivalent Newtonian fluids. We highlight here how this increase is indicative of shear-thinning. Figure [69] compares predicted (Equations 10, 11 and 65) and measured timescales from pinch-off until drops first assume a spherical shape (S = 0) for the Newtonian fluids in the range $0.056 \leq \mu \leq 0.925$ Pas. These results are further compared with the quarter wavelength timescale t_q of equivalent inviscid drops where:

$$t_q = \frac{\pi}{2\omega_{n0}} \qquad [66]$$

and ω_{n0} is calculated using Equation [8]. The period from pinch-off until drops first reach S = 0 corresponds to the quarter wavelength timescale for periodic relaxation and the complete relaxation period for aperiodic behaviour. Both measured and predicted timescales for low viscosity fluids with $\mu \leq 0.213$ Pas (corresponding to a periodic regime) are small and agree closely with t_q. This suggests that fluid viscosity in this regime does not play a significant role during initial retraction. Results of pure water ($\mu = 0.001 \pm 0.00012$ Pas, $\sigma = 0.075 \pm 0.002$ Nm^{-1}, $\rho = 1000$ kgm^{-3}, $D_E = 3.265 \pm 0.0137$ mm) were also included to further corroborate this observation. For aperiodic relaxation of fluids with $\mu > 0.213$ Pas, both measured and predicted timescales increase linearly with viscosity. In other words, aperiodic relaxation timescales of Newtonian fluid drops shorten with decreasing viscosity. For shear-thinning fluids therefore, a faster relaxation period in comparison with the equivalent Newtonian prediction suggests that fluid shear-thinning reduces the local viscosity in the drop.

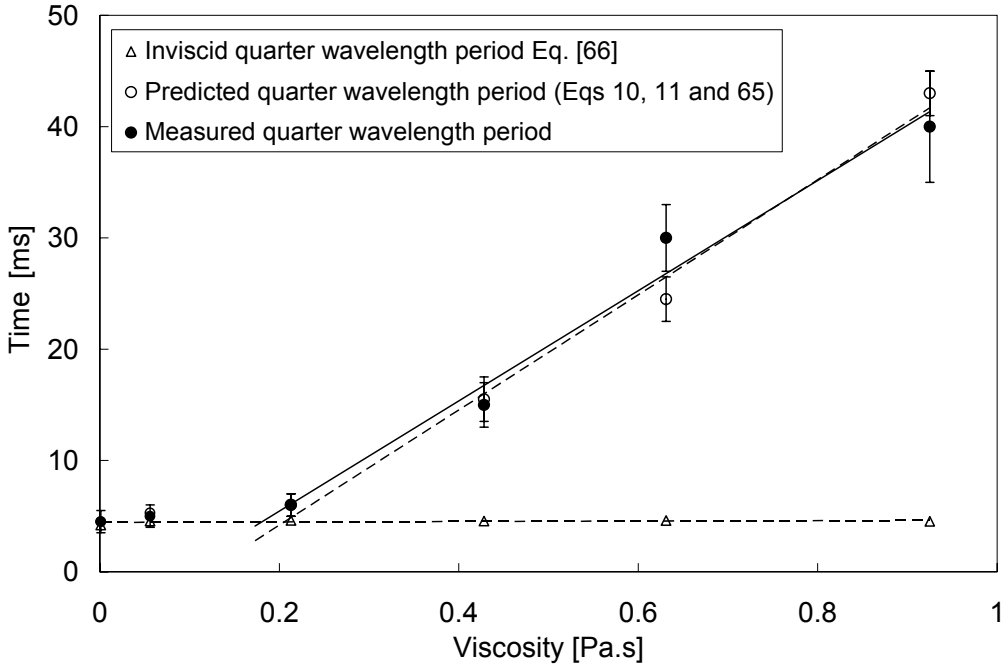

Figure 69. Measured and predicted (using Equations 10, 11 and 65) quarter wavelength relaxation periods (the period between pinch-off and when drops first reach a spherical shape (S = 0)) plotted against viscosity. Open and filled symbols correspond to predictions and measurements respectively. For aperiodic behaviour, the quarter wavelength period corresponds to the complete relaxation period. Open triangle symbols correspond to the quarter wavelength timescale t_q of an inviscid drop (Equation 66 with equal values of D_E and σ), where values of $t_q = \pi/2\omega_{n0}$ are provided in Table [8].

Whilst the effect of fluid shear-thinning on drop relaxation behaviour has been qualitatively examined, a quantitative analysis of how the degree of shear-thinning (characterised by the power law index n) influences drop dynamic behaviour has not been investigated because for the fluids considered in the present work, it is not possible to compare fluids with equal values of K and differing power law indices n, therefore this analysis falls out of the scope of the thesis.

4.3 Yield-stress fluid drops

Figures [70] and [71] display the measured temporal variations in drop shape factor S for yield-stress fluids in the range $0 \leq \tau_c \leq 36.2$ Pa detaching from a 1.27 mm O.D. and 0.813 mm O.D. flat ended needle respectively. Solid lines correspond with best fit curves of the form $S(t) = S_e + Ae^{-t/t1} + Be^{-t/t2}$. A second order exponential fitting method was used because first order fitting methods consistently over-predicted values of S_e. Details of the fitting parameters are given in Table [10].

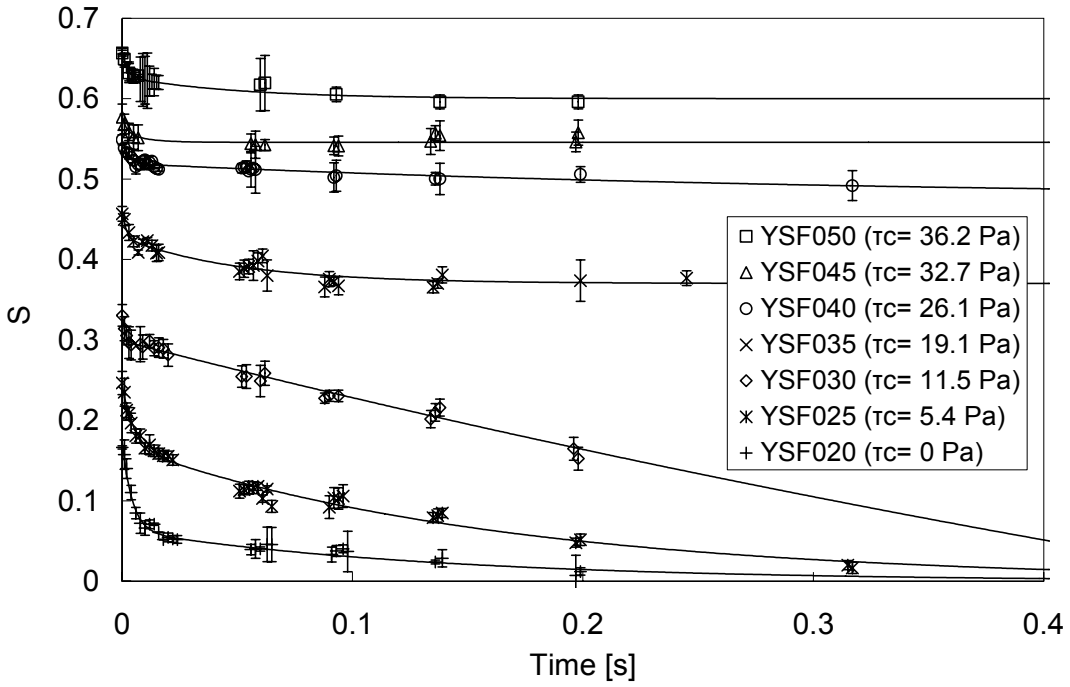

Figure 70. The temporal evolution of drop shape factor S for yield-stress fluid with $0 \leq \tau_c \leq 36.2$ Pa detaching from a 1.27 mm O.D. needle. Solid lines correspond to best fit curves of the form $S(t) = S_e + Ae^{-t/t1} + Be^{-t/t2}$ with parameters detailed in Table [10]. Experimental results are based on the average of 5 drop measurements.

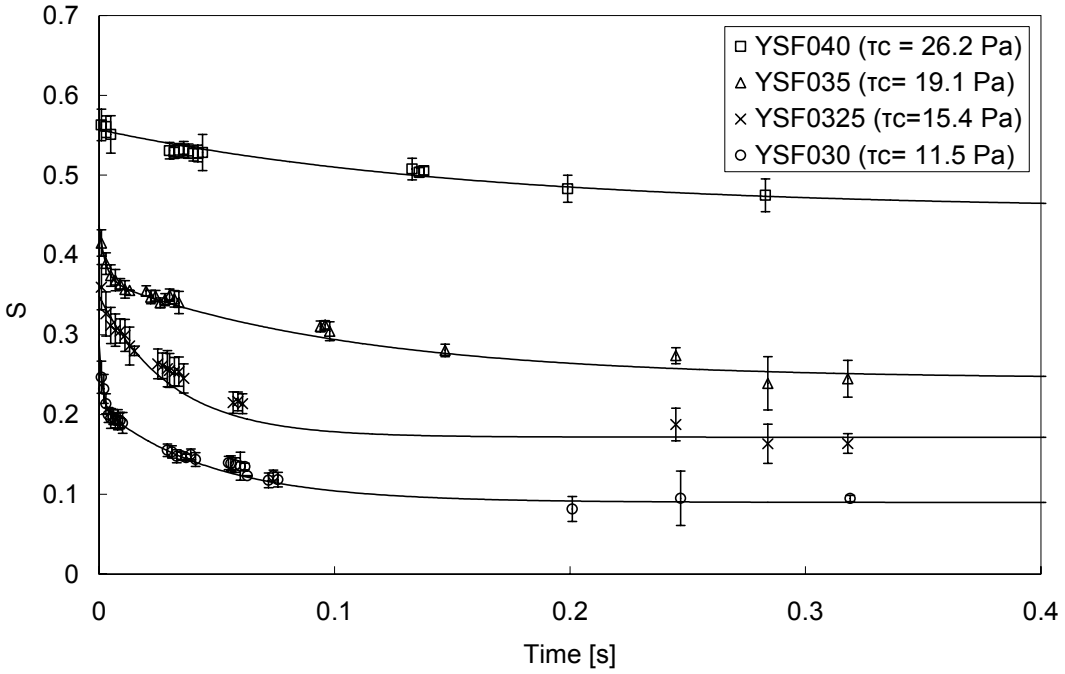

Figure 71. The temporal evolution of drop shape factor S for yield-stress fluid with $11.5 \leq \tau_c \leq 26.2$ Pa detaching from a 0.813 mm O.D. needle. Solid lines correspond to best fit curves of the form $S(t) = S_e + Ae^{-t/t1} + Be^{-t/t2}$ with parameters detailed in Table [10]. Experimental results are based on the average of 5 drop measurements.

Table 10. Free-fall drop shape characteristics: parameters associated with 2nd order exponential fitting curves of the form $S(t) = S_e + Ae^{-t/t1} + Be^{-t/t2}$ for viscoplastic fluids with $0 \leq \tau_c \leq 36.2$ Pa in free-fall after detachment from 0.838 mm and 0.495 mm I.D. flat ended needles. The negative value of S_e for the YSF030 (0.838 mm capillary tube) exponential curve is erroneous because measurements exhibit no significant asymptotic trend towards an equilibrium value.

Material	Capillary tube inner diameter D_0 [mm]	A	t_1 [s]	B	t_2 [s]	Equilibrium Drop shape S_e
YSF020	0.838	0.063 ± 0.0023	0.136 ± 0.014	0.113 ± 0.0040	0.0043 ± 0.0003	0 ± 0.0005
YSF025	0.838	0.168 ± 0.0035	0.164 ± 0.0071	0.077 ± 0.0058	0.0052 ± 0.0008	0 ± 0.0006
YSF030	0.838	0.816 ± 0.754	1.107 ± 1.120	0.0352 ± 0.007	0.0012 ± 0.0005	-0.517 ± 0.760
YSF035	0.838	0.057 ± 0.0037	0.051 ± 0.0095	0.034 ± 0.0062	0.0018 ± 0.0007	0.370 ± 0.0035
YSF040	0.838	0.030 ± 0.0037	0.003 ± 0.0006	0.044 ± 0.0015	0.3180 ± 0.049	0.476 ± 0.0020
YSF045	0.838	0.019 ± 0.0760	0.002 ± 0.0064	0.013 ± 0.078	0.0093 ± 0.0574	0.545 ± 0.0014
YSF050	0.838	0.032 ± 0.0085	0.002 ± 0.0014	0.028 ± 0.009	0.0498 ± 0.016	0.600 ± 0.0012
YSF030	0.495	0.083 ± 0.024	0.0015 ± 0.0009	0.120 ± 0.015	0.0474 ± 0.0350	0.090 ± 0.0047
YSF0325	0.495	0.0883 ± 0.009	0.03066 ± 0.003	0.0883 ± 0.009	0.0307 ± 0.003	0.1717 ± 0.005
YSF035	0.495	0.0673 ± 0.012	0.003 ± 0.001	0.12473 ± 0.005	0.108 ± 0.0179	0.2448 ± 0.09
YSF040	0.495	0.0502 ± 0.005	0.158 ± 0.016	0.0502 ± 0.005	0.158 ± 0.016	0.4567 ± 0.09

Newtonian, shear-thinning and viscoplastic fluid drops in free-fall are all subject to gravitational, viscous and capillary forces. Whilst the Newtonian and shear-thinning fluids consistently exhibit a near spherical shape in equilibrium ($0 \leq S_e \leq 0.014$) within the investigated range of viscosities ($0.056 \leq \mu \leq 0.925$ Pas), consistency coefficients ($0.208 \leq K \leq 5.064$ Pas^n) and power law indices ($0.084 \leq n \leq 0.400$), viscoplastic fluids can exhibit highly non-spherical equilibrium shapes. It can be reasonably assumed this characteristic could be caused by fluid yield-stress.

To establish the relationship between equilibrium drop shape and yield-stress, it is first necessary to rule out effects due to shear-thinning and viscosity. The consistency coefficient for the YSF035 ($K = 6.98$ Pas^n) and YSF040 ($K = 7.94$ Pas^n) viscoplastic fluids are significantly larger than the maximum measured for the shear-thinning fluids ($K = 5.064$ Pas^n for the X075 fluid). What appears therefore to be a non-spherical equilibrium state, denoted by S_e, could instead be a very slow retraction due to high fluid viscosity. In order to examine this premise, measured temporal variations in drop shape are compared with predictions of equivalent Newtonian drops with the same viscous characteristics as those of the yield-stress fluids at very small shear-rates (similar to that described in **§4.2).** Again, predictions are made using Equations [11] and [65] using identical values of σ, D_E, ρ (Table 4) and measured S(0), however the viscoplastic consistency coefficient (Table 11) replaces the Newtonian viscosity term. Equivalent Newtonian fluids associated with the viscoplastic fluids exhibit no shear-thinning or yield-stress effects ($n = 1$, $\mu = K$ and $\tau_c = 0$).

Table 11. Predicted relaxation parameters of equivalent Newtonian fluids associated with viscoplastic fluids in the range $0 \leq \tau_c \leq 26.1$ Pa.

Material	Consistency coefficient K [Pas^n]	Undamped natural frequency $\omega_{n0}/2\pi$ [s^{-1}]	Damping factor b_{n0} [s^{-1}]	Dimensionless viscosity ε	Measured initial drop shape factor S(0)
YSF020	1.44	48.97	3.57	6.55	0.166
YSF025	3.10	51.96	8.25	14.29	0.246
YSF030	5.53	53.63	15.46	25.96	0.331
YSF035	6.98	54.91	20.14	33.02	0.457
YSF040	7.94	55.51	23.22	37.66	0.549

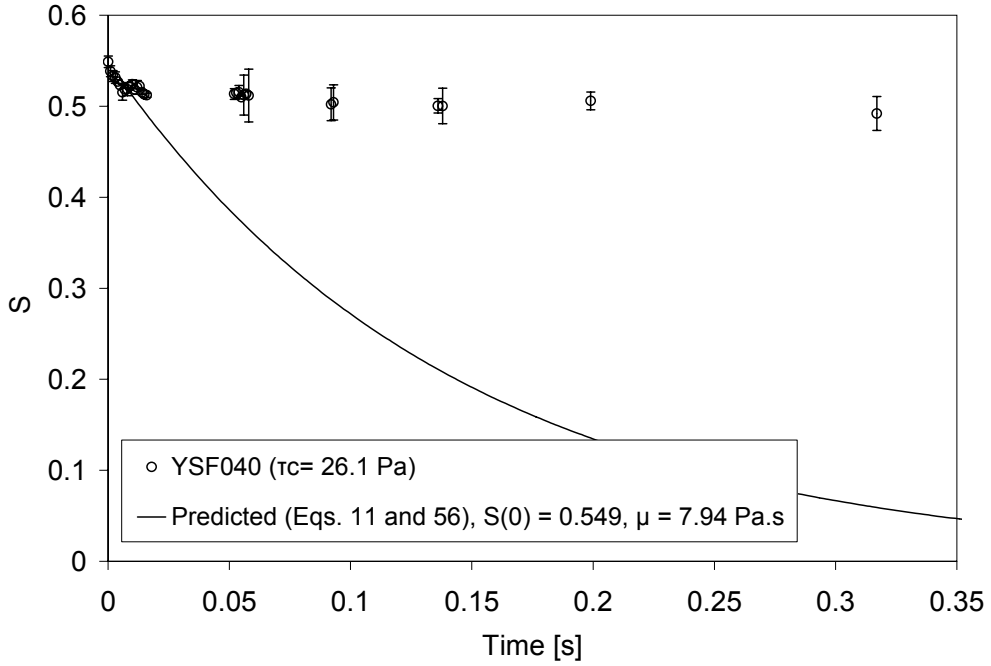

Figure 72. Measured (symbols) temporal variation in S for the high yield-stress magnitude YSF040 (τ_c = 26.1 Pa) fluid detaching from a 0.838 mm I.D. flat ended needle compared with predictions (solid line) of its equivalent Newtonian fluid (with viscosity μ terms replaced with the consistency coefficient K detailed in Table 11). Experimental results are based on the average of 5 drop measurements.

From Table [11], the dimensionless viscosity ε of each equivalent Newtonian fluid indicates that aperiodic behaviour is expected ($\varepsilon \geq 0.7665$). This flow characteristic is consistent with fluid measurements, indicating that shear-thinning does not cause transition to periodic motion. Figure [72] compares the measured relaxation behaviour of the high yield-stress magnitude YSF040 (τ_c = 26.1 Pa) fluid with the predicted behaviour of its equivalent Newtonian fluid. The equivalent Newtonian prediction shows a slow relaxation towards equilibrium, however over the maximum measurement timescale of 320 ms (equivalent to a fall height of H_f = 500 mm), drop shape decreases to within 10% of the spherical. In contrast, the measured drop shape of the YSF040 fluid decreases initially and at a similar rate to the prediction, however it then rapidly slows and forms a very prolate equilibrium shape. This difference indicates that even the high viscosities associated with low shear-rate flow in the viscoplastic fluids cannot account for the slowing and eventual cessation of the drop shape factor for high yield-stress magnitude fluids. Moreover, shear-thinning effects have been established not to cause cessation of drop shape; this property acts only to increase the rate of retraction when fluids are subject to higher shear-rates. Fluid yield-stress therefore appears capable of inhibiting the

formation of spherical drops. Further analysis examines the relationship between the equilibrium drop shape S_e and the yield-stress magnitude.

With the exception of drops of the YSF030 solution detaching from the 0.838 mm I.D. needle (Fig 70), an equilibrium drop shape, Se, is reached for all of the viscoplastic solutions. Whilst spherical or near-spherical equilibrium drop shapes are obtained for fluids solutions with $\tau_c \leq 7.8$ Pa, above this magnitude S_e increases as a function of τ_c. This is displayed in Figure [73]. The figure also indicates that for $\tau_c \geq 7.8$ Pa, S_e does not vary linearly with τ_c; the size of the drop also appears to be a dependent factor. Yield-stress magnitude alone does not therefore seem to be a suitable parameter to characterise equilibrium drop shape characteristics. Instead, the Bingham-Capillary number (Equation 63) is used.

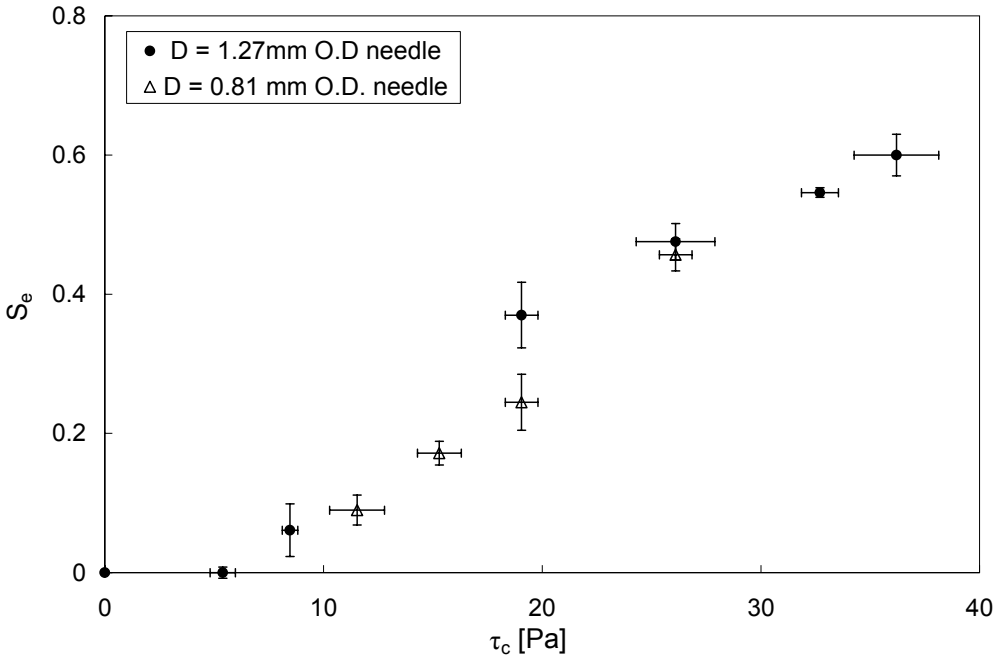

Figure 73. Equilibrium drop shape S_e plotted against yield-stress magnitude τ_c for yield-stress fluids with $0 \leq \tau_c \leq 36.2$ Pa detaching from both the 0.838 mm I.D. (filled circle) and 0.495 mm I.D. flat ended needles (open triangle).

Flow within the drop during free-fall will not be purely extensional, therefore characterisation is made with respect to τ_c and not the measured tensile yield-stress. For this investigation, $\hat{B}$ eliminates the viscosity term whilst retaining the yield-stress and surface tension terms; important factors in the framework of this experiment because they act to drive and inhibit the drop from obtaining a spherical equilibrium shape

respectively. Viscous fluid characteristics are not important here because they only influence the dynamic characteristics of fluid motion and not the equilibrium shape. Figure [74] displays the equilibrium shape factor S_e as a function of $\hat{B}$.

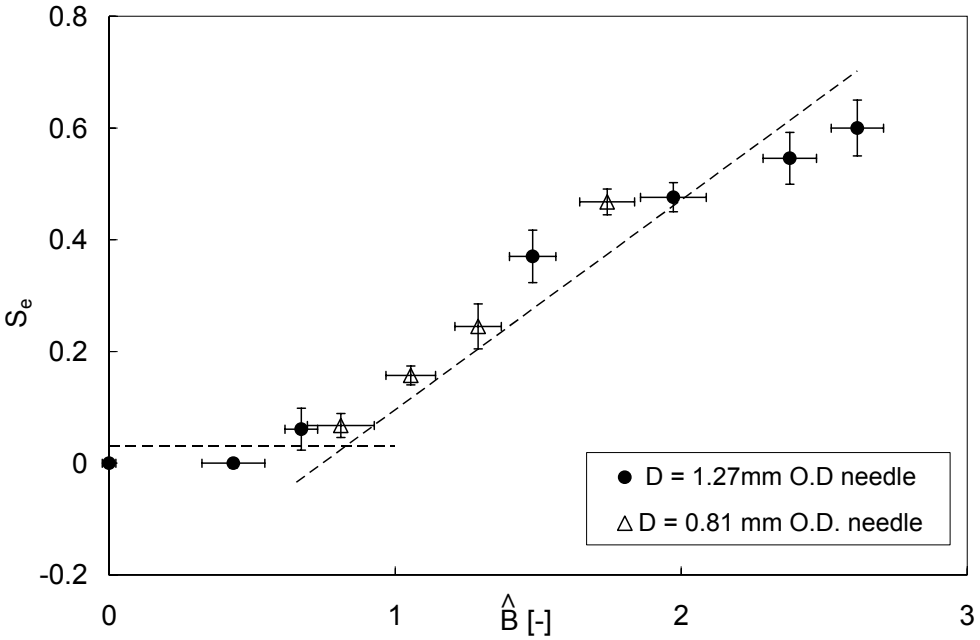

Figure 74. Equilibrium drop shape S_e plotted as a function of $\hat{B}$ for yield-stress fluids with $0 \leq \tau_c \leq 36.2$ Pa detaching from both the 0.838 mm I.D. (filled circle) and 0.495 mm I.D. needles (open triangle). The dashed line corresponds to a least square line of best fit for results in the range $\hat{B} > 1$. The solid line corresponds to the average S_e value for results with $\hat{B} \leq 1$ ($S_e = 0.0299$). The intersection of the lines occurs at $\hat{B} = 0.8 \pm 0.1$.

There are two clearly distinct regions in Figure [74]; for values of $\hat{B} < 1$, representative of drops whose surface tension forces exceed those that arise from the fluid yield-stress, the equilibrium free-fall shapes are spherical. For values of $\hat{B} > 1$, representative of fluid drops in which the yield-stress forces exceed surface tension forces, the equilibrium drop shape will be non-spherical. Moreover, S_e increases linearly with $\hat{B}$ (with a gradient of m = 0.350 based on a least square line of best fit). The critical point occurs at $\hat{B} \approx 1$ ($\hat{B} = 0.8 \pm 0.1$ in Figure 74), where surface tension forces equal those arising from fluid yield-stress.

Figure [74] suggests that an equilibrium spherical drop shape will be formed as long as inhibiting forces are not above a magnitude capable of preventing the driving capillary force from minimising the surface area. When yield-stress forces are sufficiently

large to overcome capillary forces however, a non-spherical equilibrium shape will result. Within the regime $\hat{B} > 1$, increasing the yield-stress magnitude will further inhibit relaxation by driving capillary forces, resulting in an increase in the equilibrium drop shape S_e.

5 Results and Discussion - Drop impact dynamics

Figures [75], [78], [81] and [84] show image sequences of Newtonian drop impacts (with $0.056 \leq \mu \leq 0.925$ Pas) on a parafilm-M surface from a fall height of 10, 25, 50 and 100mm. Equivalent image sequences for shear-thinning drops with $0.084 \leq n \leq 0.4$ and $0.208 \leq K \leq 5.064$ Pas^n and yield-stress fluid drops with $0 \leq \tau_c \leq 26.1$ Pa are displayed in Figures [76], [79], [82], [85] and [77], [80], [83], [86] respectively. As discussed in **§5.1**, initial impact behaviour on glass substrates is identical to that on parafilm surfaces for the fluids examined, therefore only image sequences of drop impacts on parafilm are shown here.

The influence of impact velocity and Newtonian fluid viscosity can clearly be observed from the image sequences in Figures [75], [78], [81] and [84]. The maximum spread factor β_m and minimum apex height factor ζ_m for each fluid increases and decreases respectively as impact velocity is increased. A decrease in viscosity also has a similar effect, whereby drops reach a larger maximum inertial spread diameter with the lamella appearing much thinner; this characteristic becomes more noticeable as fall height is increased. Drop shapes of low viscosity fluids ($\mu \leq 0.213$ Pas) impacting from fall heights with $H_f \geq 25$ mm typically take on a cylindrical shape at the end of inertial expansion. The deformation of higher viscosity fluids upon impact is reduced and can appear closer in appearance to that of a spherical cap (increasingly so as the fall height is reduced to $H_f = 10$ mm).

Whilst differences in impact dynamics between the different shear-thinning fluids are noticeable from the image sequences in Figures [76], [79], [82] and [85] it is not immediately obvious how the consistency coefficient K and the power law index n independently influence dynamic behaviour. Increases in β_m and decreases in ζ_m are observed for increasing n and decreasing K.

Drop impact dynamics of yield-stress fluids differ significantly from both the Newtonian and shear-thinning fluids during the expansion phase, as shown in Figures [77], [80], [83] and [86]. This is due primarily to the prolate shape of the drops prior to impact. As previously discussed in **§3.3** and **§4.3**, viscoplastic fluid drops with $\hat{B}_e > 1$,

growing on the end of a capillary tube increase in prolateness with τ_c. Moreover, fluids with a yield-stress characterised by $\hat{B} > 1$ appear to inhibit surface tension driven formation of spherical drops during free-fall. For fluids with $\tau_c \leq 11.5$ Pa, general drop impact behaviour does not appear to vary significantly from those of shear-thinning and Newtonian drops; decreases in impact velocity and increases in hair-gel mass fraction reduce β_m and increase ξ_m in a similar fashion to increasing the consistency coefficient or Newtonian viscosity. As the fluid yield-stress magnitude is increased however, drops do not deform completely and instead of the drop taking on a disk like shape at maximum spread, central peaks are observed (visible in Figures 80, 83 and 86). This suggests that flow is localised during inertial expansion; the top of the prolate drop throughout the impact process does not deform from its original shape prior to impact, resulting with a characteristic peak. Peaks are most noticeable for lower velocity impacts where deformation is relatively small. As impact velocity increases, the drop peak size decreases and eventually disappears. Peak sizes also appear to increase with τ_c. High τ_c drops impacting at low Weber numbers show very little deformation during inertial expansion.

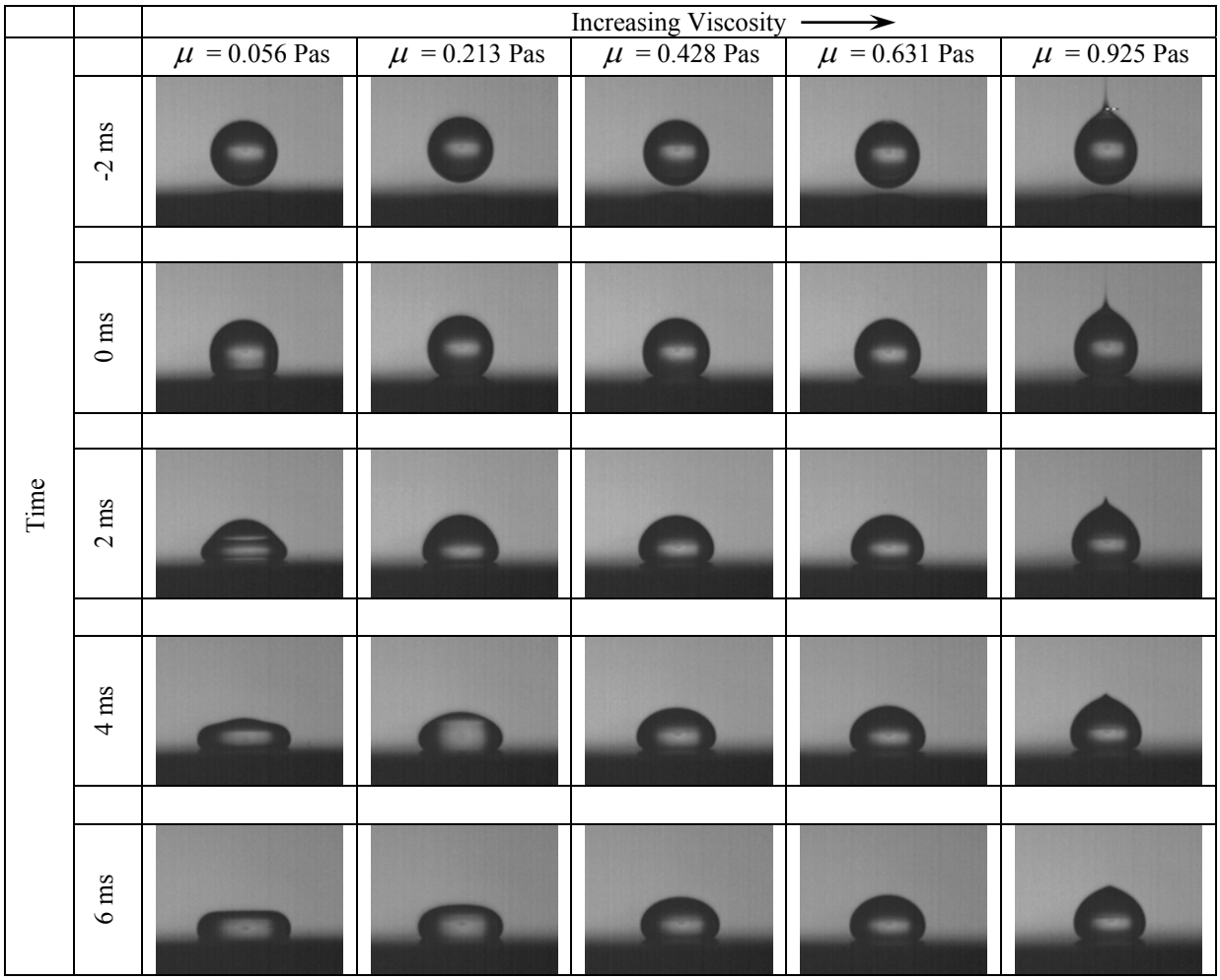

Figure 75. The parametric morphology of viscous Newtonian fluid drops impacting on a parafilm substrate from a fall height of 10 mm.

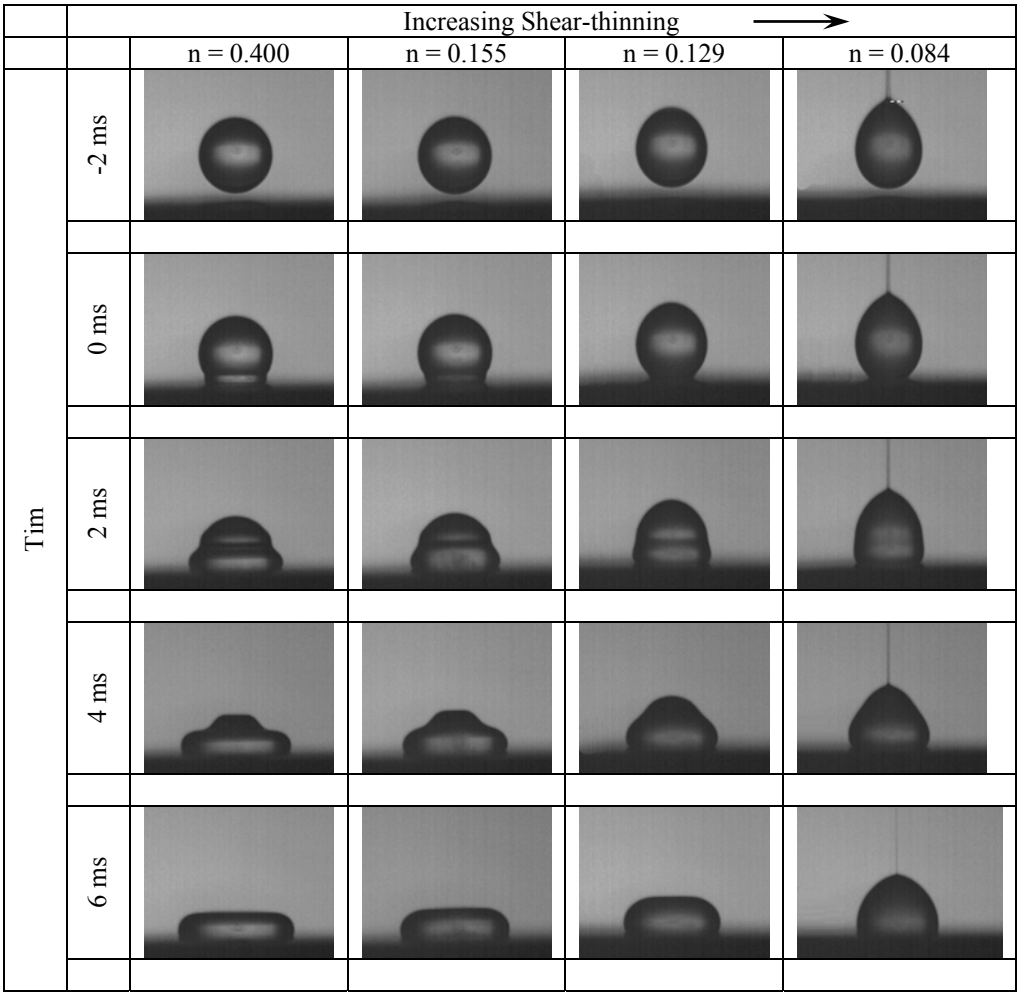

Figure 76. The parametric morphology of shear-thinning fluid drops impacting on a parafilm substrate from a fall height of 10 mm.

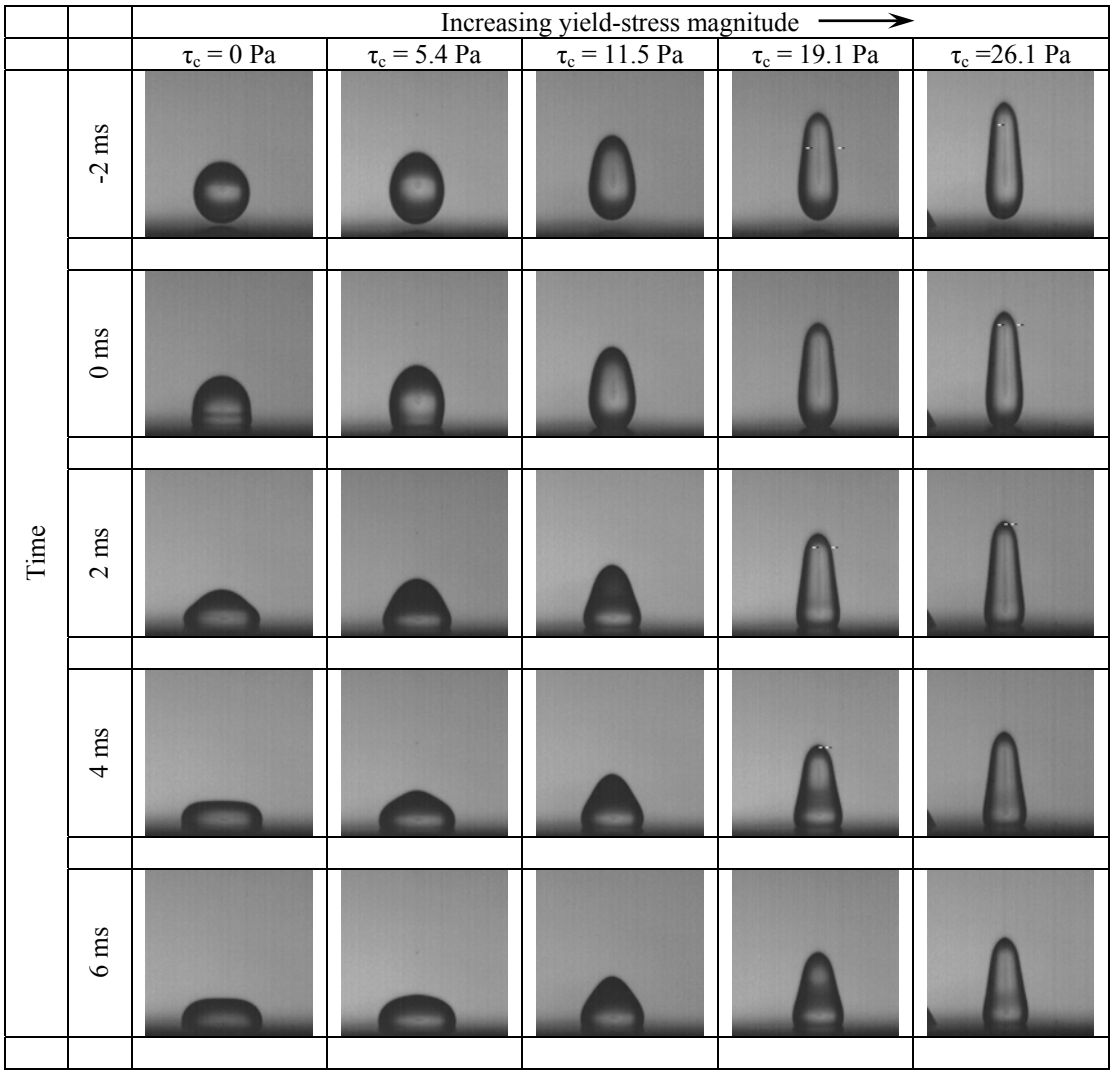

Figure 77. The parametric morphology of yield-stress fluid drops impacting on a parafilm substrate from a fall height of 10 mm.

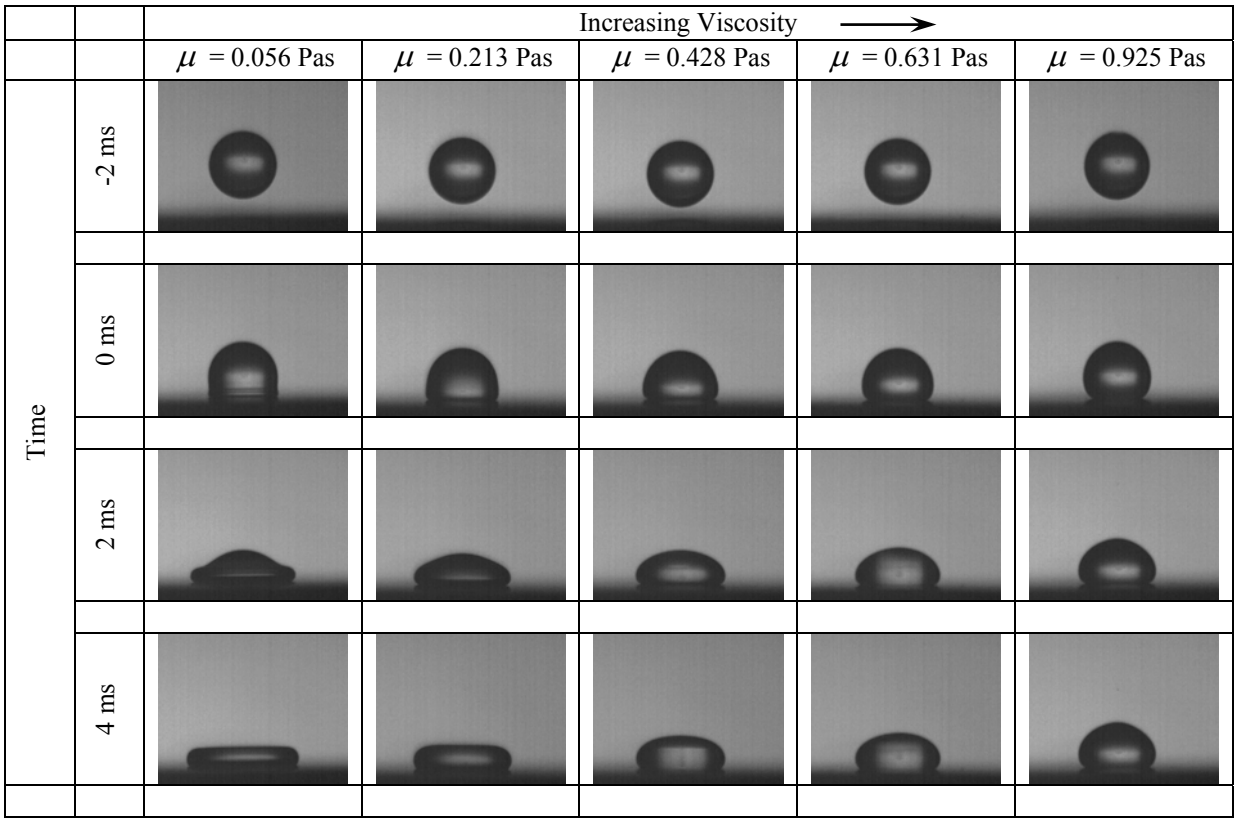

Figure 78. The parametric morphology of viscous Newtonian fluid drops impacting on a parafilm substrate from a fall height of 25 mm.

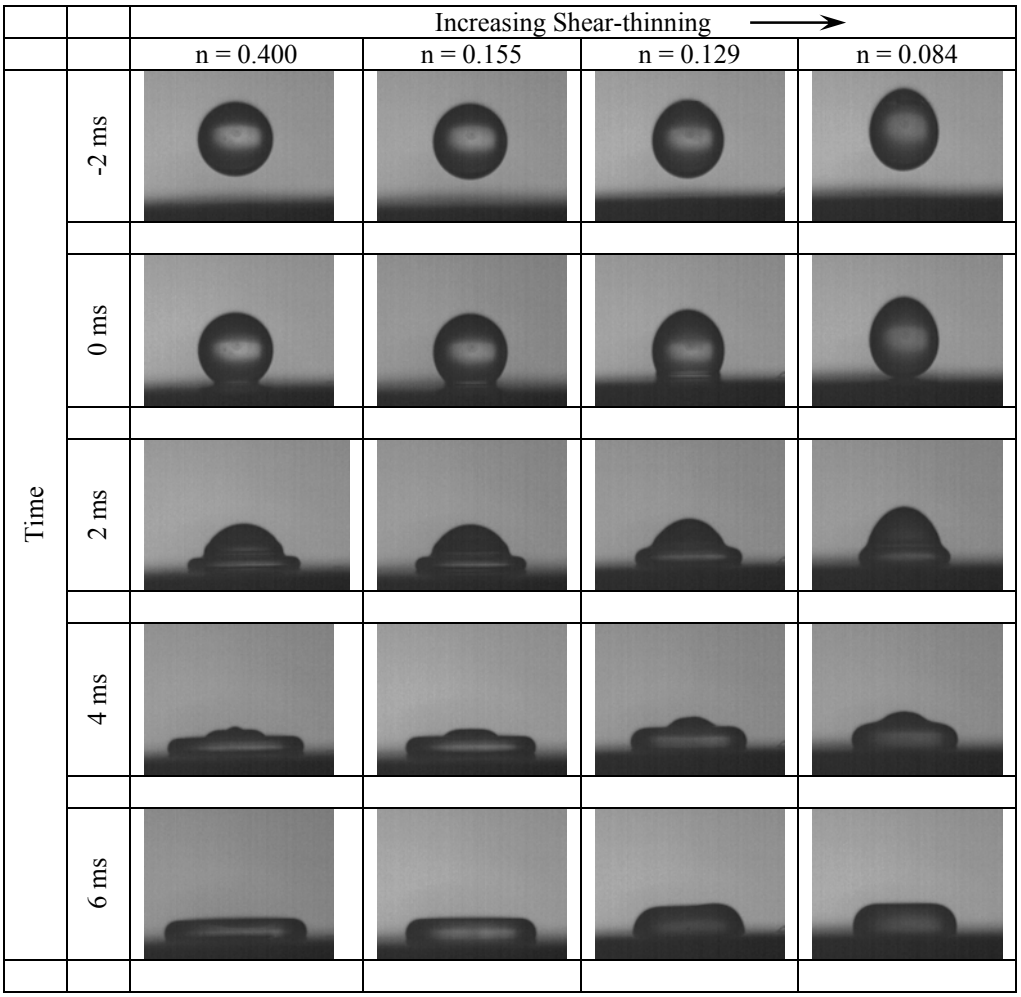

Figure 79. The parametric morphology of shear-thinning fluid drops impacting on a parafilm substrate from a fall height of 25 mm.

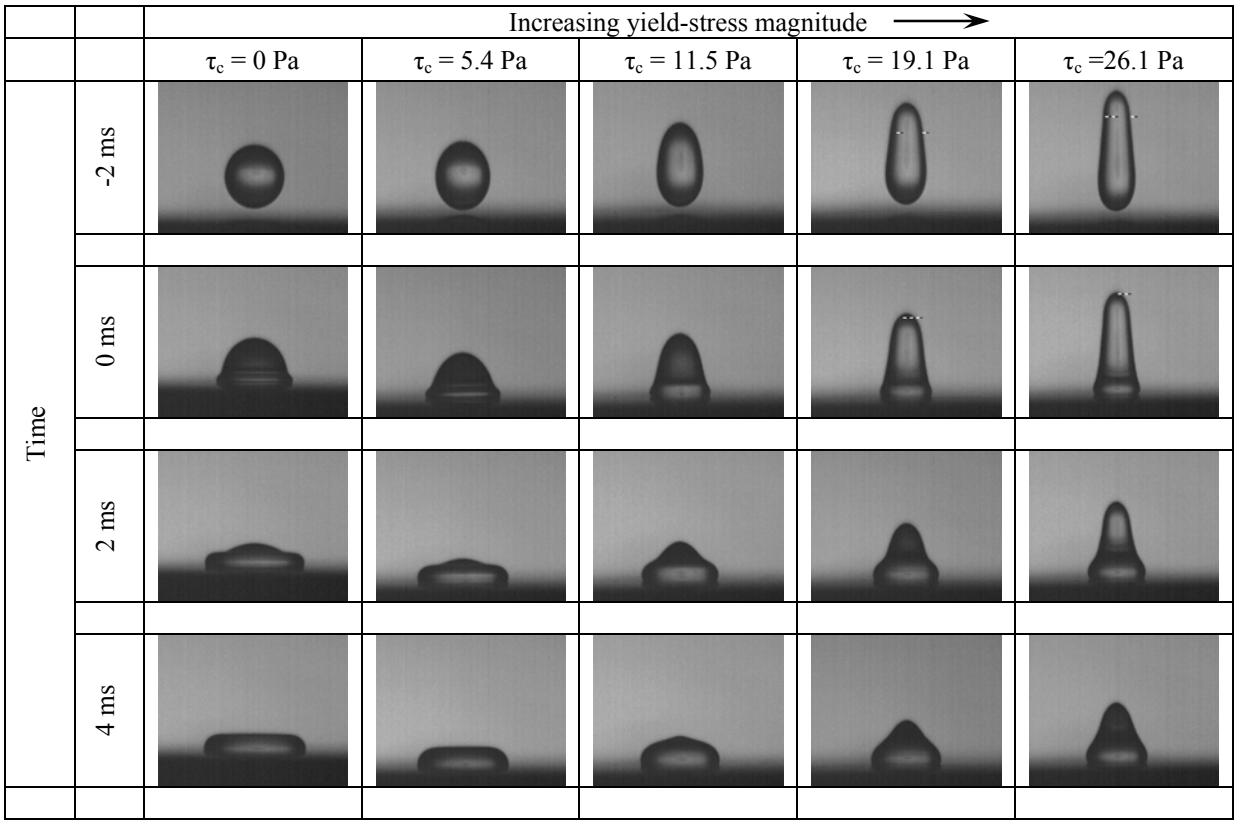

Figure 80. The parametric morphology of yield-stress fluid drops impacting on a parafilm substrate from a fall height of 25 mm.

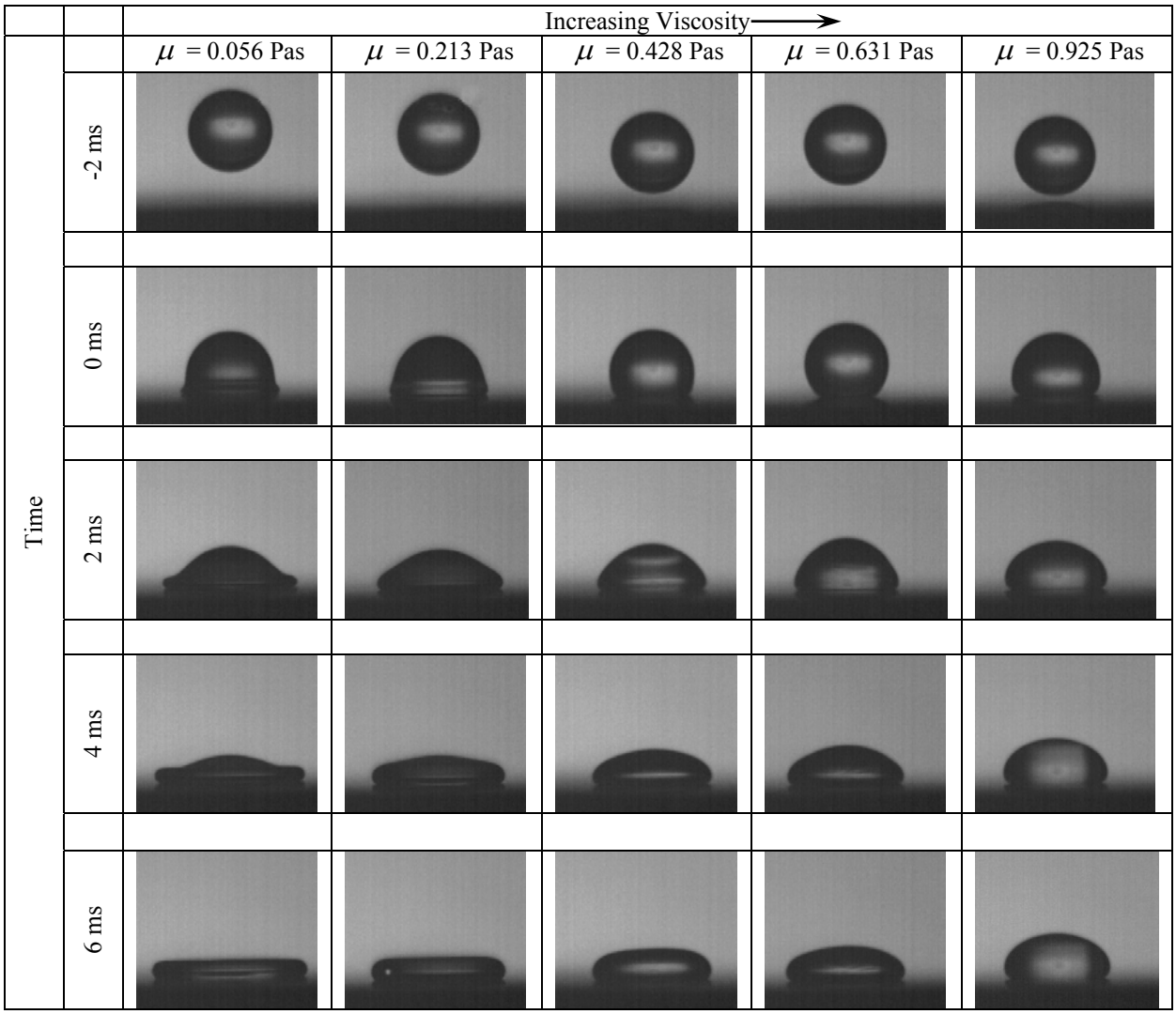

Figure 81. The parametric morphology of viscous Newtonian fluid drops impacting on a parafilm substrate from a fall height of 50 mm.

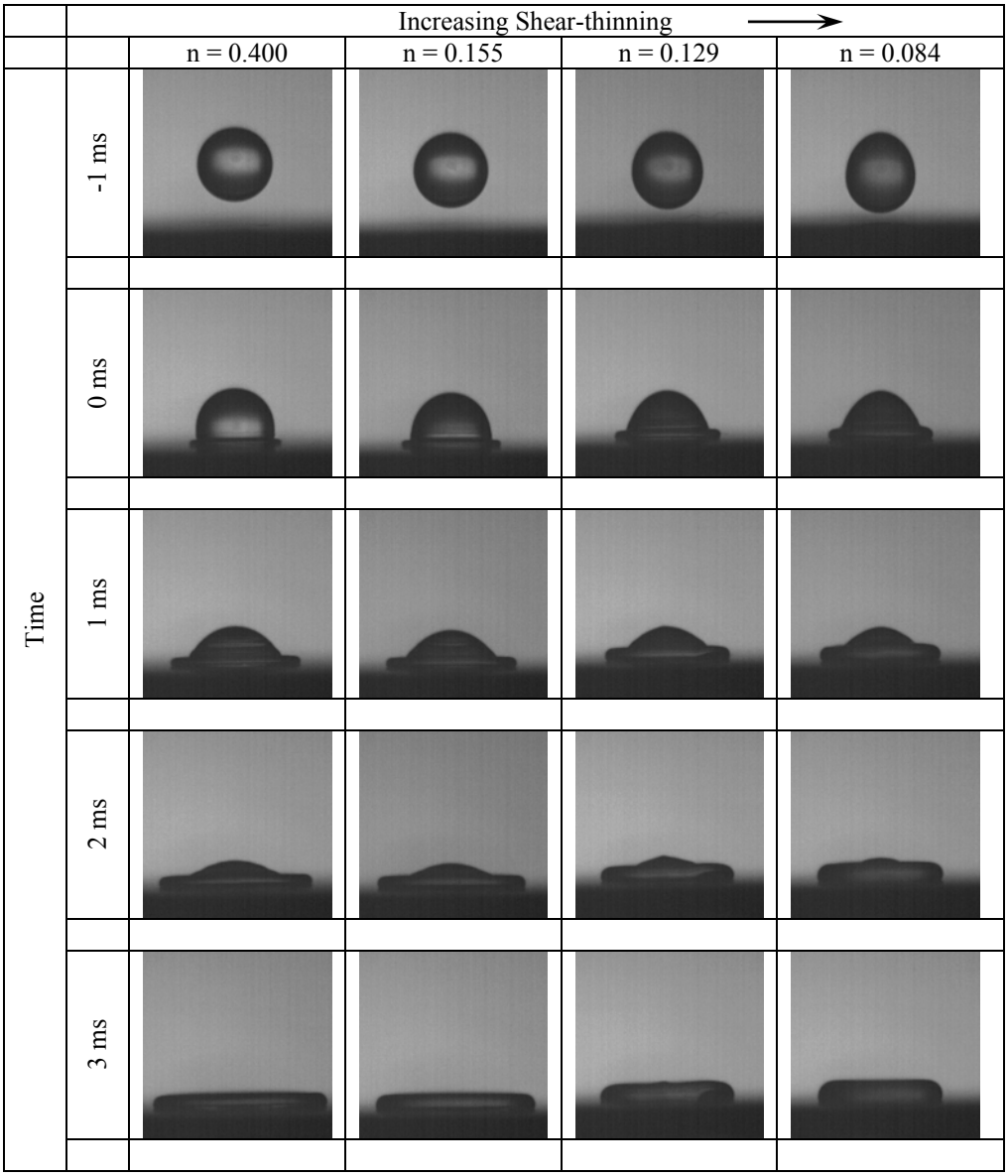

Figure 82. The parametric morphology of shear-thinning fluid drops impacting on a parafilm substrate from a fall height of 50 mm.

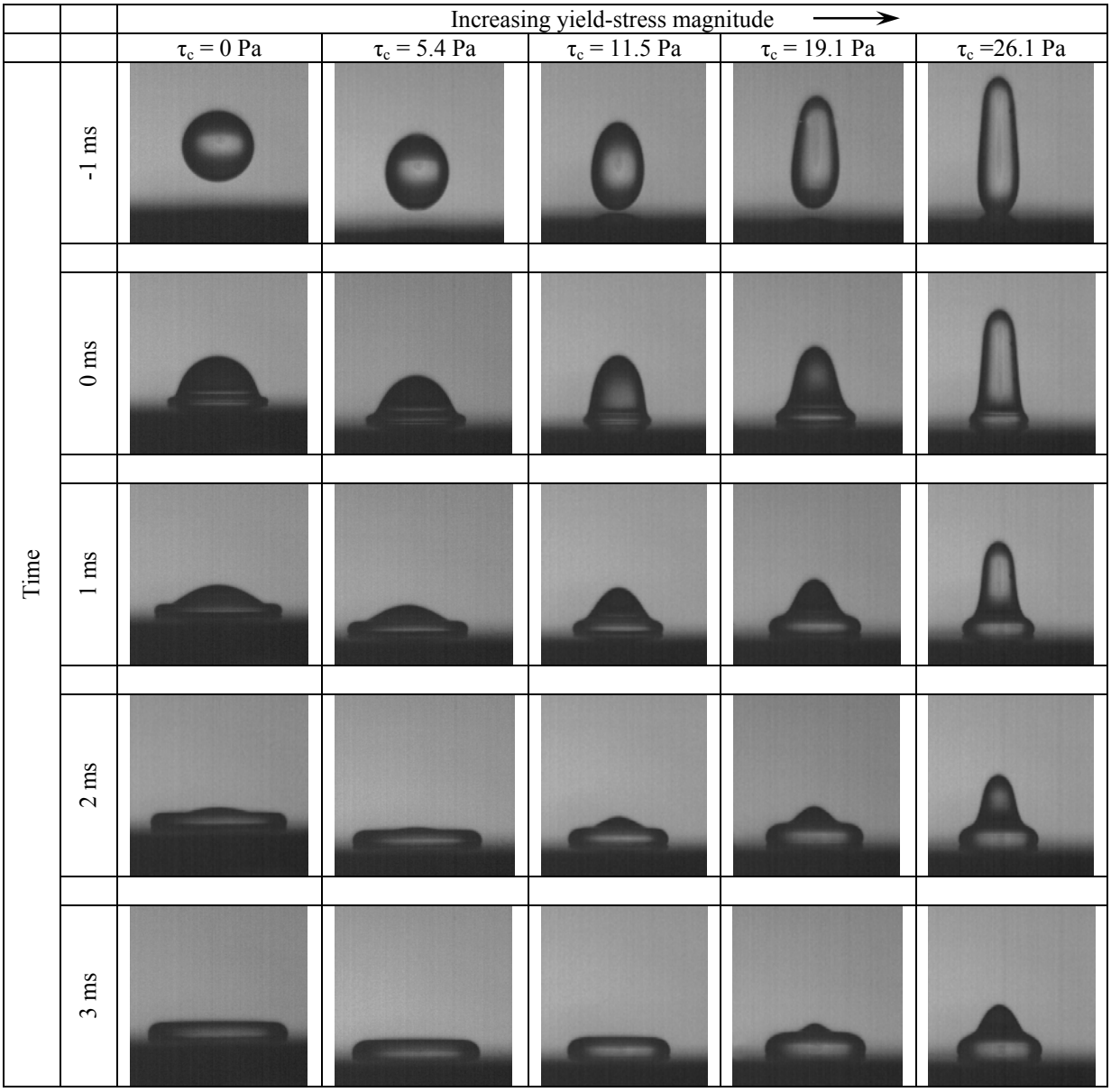

Figure 83. The parametric morphology of yield-stress fluid drops impacting on a parafilm substrate from a fall height of 50 mm.

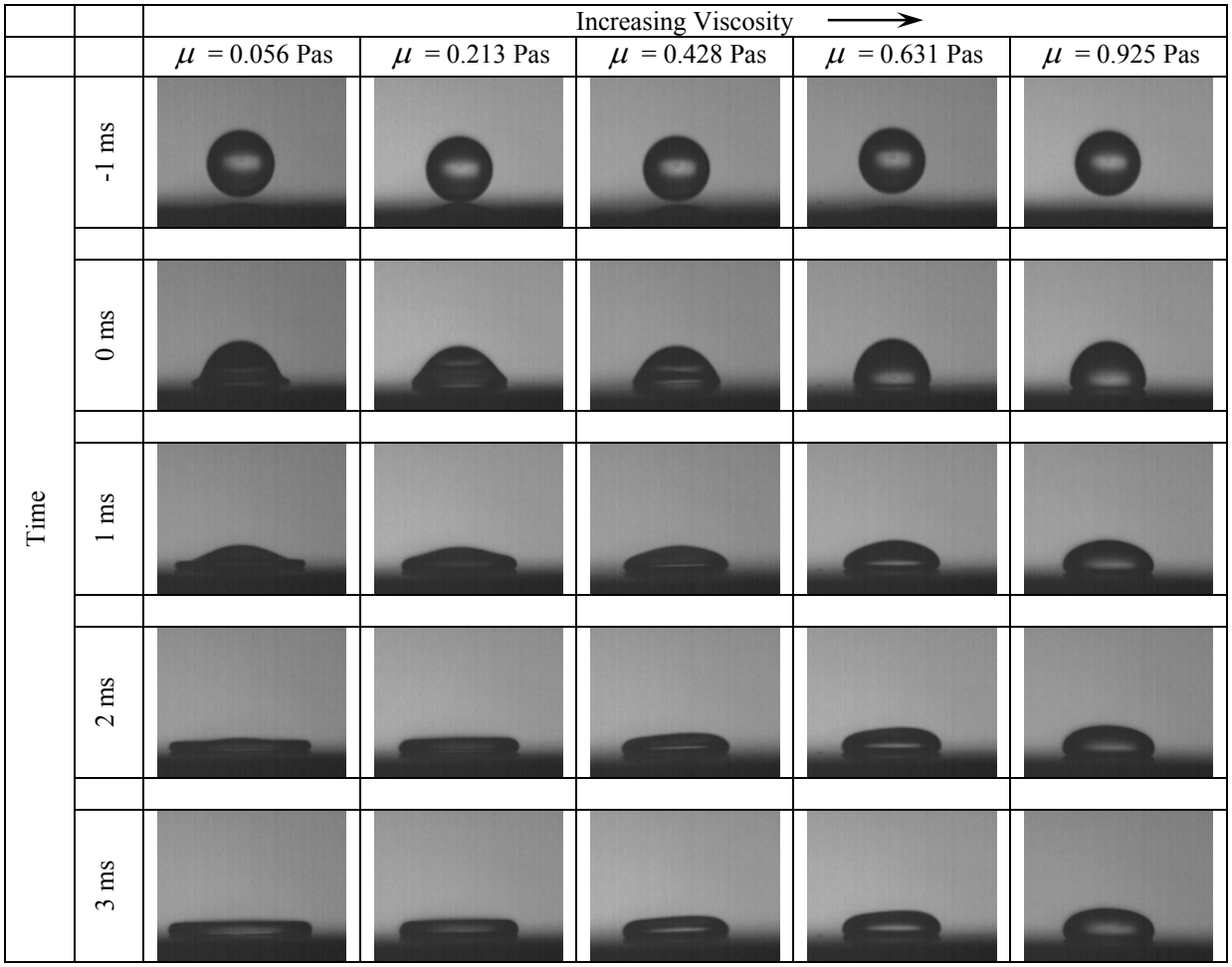

Figure 84. The parametric morphology of viscous Newtonian fluid drops impacting on a parafilm substrate from a fall height of 100 mm.

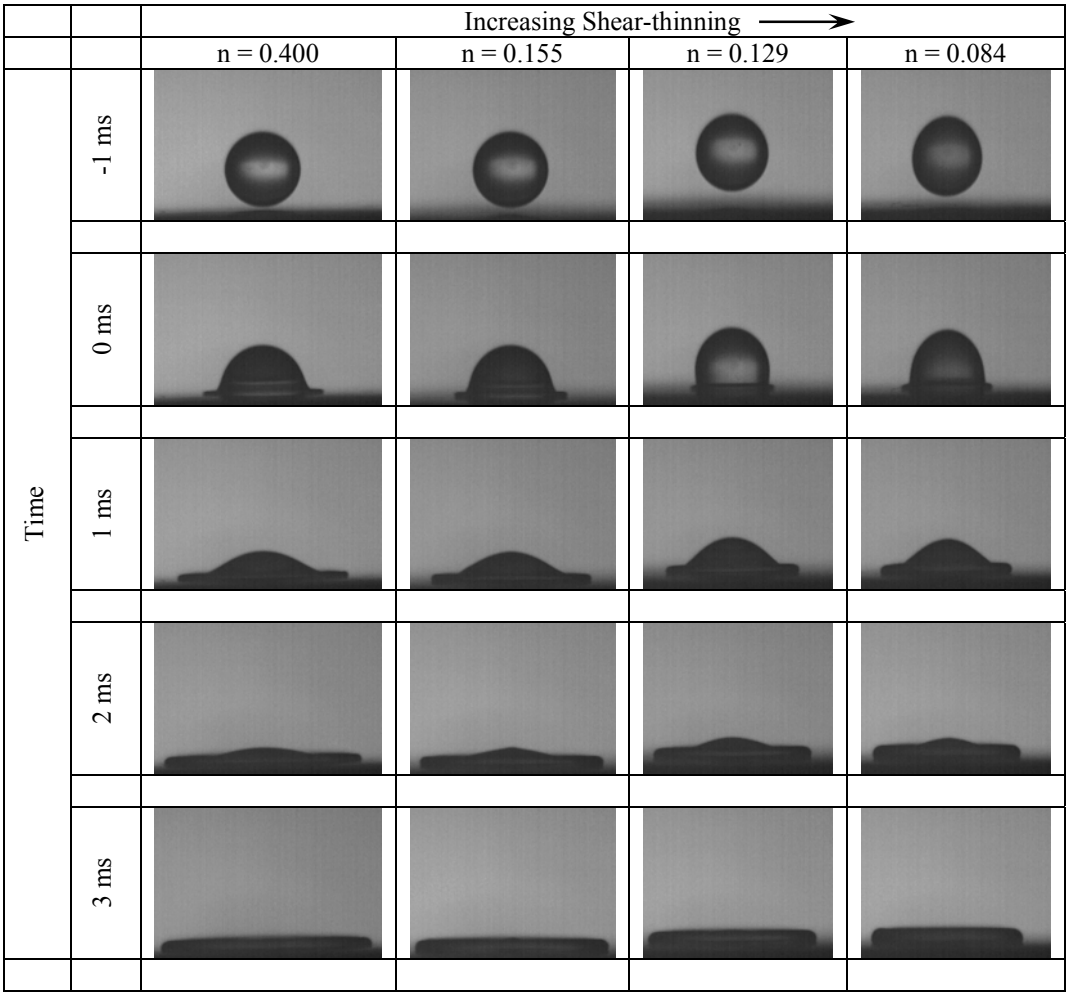

Figure 85. The parametric morphology of shear-thinning fluid drops impacting on a parafilm substrate from a fall height of 100 mm.

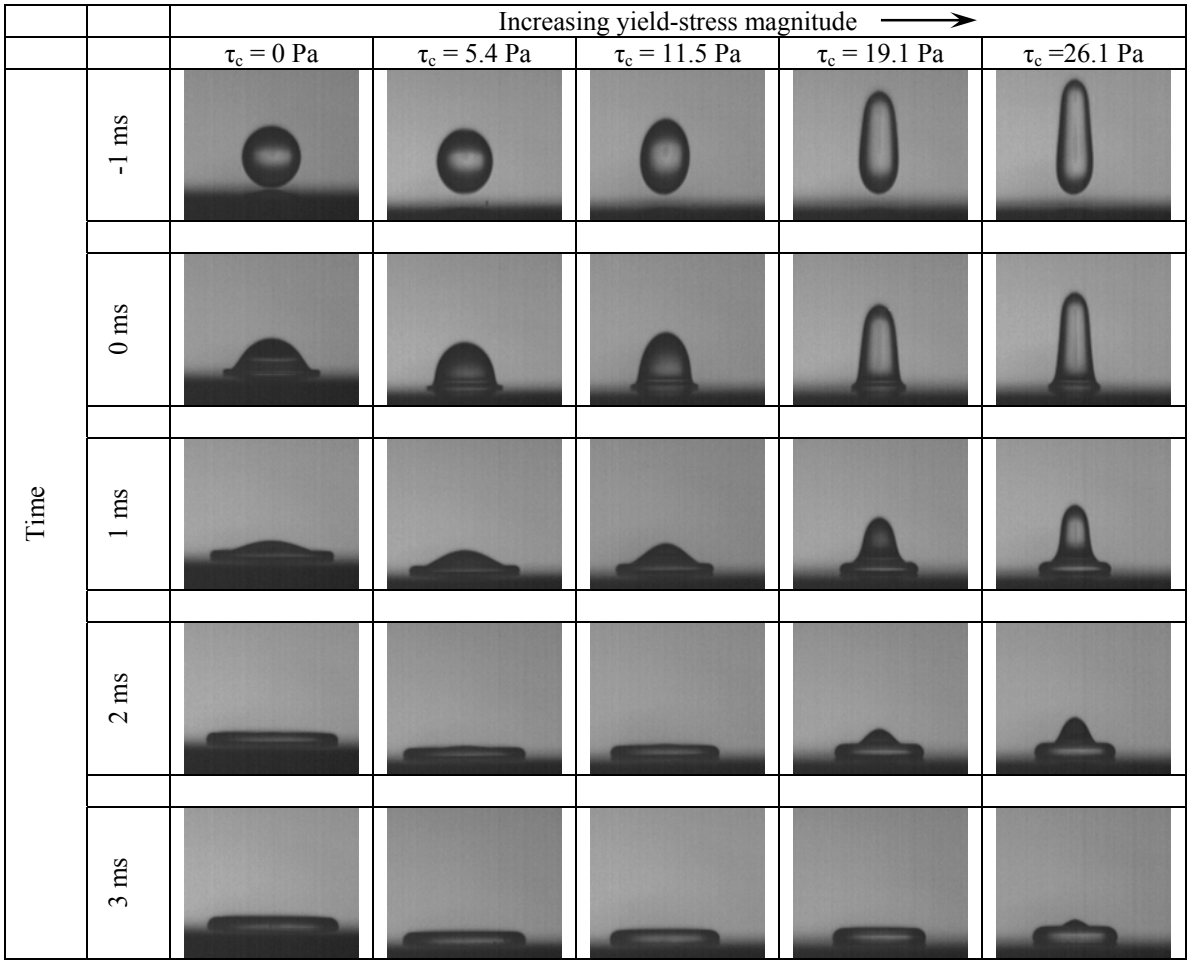

Figure 86. The parametric morphology of yield-stress fluid drops impacting on a parafilm substrate from a fall height of 100 mm.

5.1 The influence of surface wettability on drop impact behaviour

Previous studies have reported differences in the maximum dimensionless spread factor $\beta_m = D_{Max}/D_E$ at the end of the expansion phase for water drops ($\mu = 0.001$ Pas) impacting on substrates with differing wettabilities. Differences of up to ±23.6% were measured by Pasandideh-Fard et al.[43] for drops (of similar size to this investigation) impacting on glass ($\theta_e = 27^o$) and beeswax ($\theta_e = 111^o$) substrates in the ranges $59 \leq We \leq 271$ and $2084 \leq Re \leq 5833$. Differences of ±10.4% were measured by Mao et al.[47] for similar sized drops impacting on glass ($\theta_e = 37^o$) and wax ($\theta_e = 97^o$) substrates in the range $11.3 \leq We \leq 518$ and $1482 \leq Re \leq 10024$. We extend these investigations here by examining the influence of surface wettability on drops of more viscous Newtonian fluids

with $0.056 \leq \mu \leq 0.925$ Pas over the ranges $1.7 \leq We \leq 240$ and $1.1 \leq Re \leq 137$, shear thinning fluids with $0.084 \leq n \leq 0.400$ and $0.208 \leq K \leq 5.064$ Pas^n over the range $0.8 \leq We \leq 194$ and viscoplastic fluids with $0.3727 \leq n \leq 0.4747$, $1.443 \leq K \leq 7.936$ Pas^n and $0 \leq \tau_c \leq 26.1$ Pa over the range $0.7 \leq We \leq 340$.

Equivalent drop impacts on hydrophobic parafilm-M ($\theta_e = 95 \pm 2^o$ for water drops with $\mu = 0.001$ Pas and $D_E = 3.48$ mm) and hydrophilic clean glass ($\theta_e = 0^o$ for identical water drops) surfaces are compared for the Newtonian, shear-thinning and yield-stress fluids by plotting temporal variations in dimensionless inertial spread factor $\beta = D/D_E$. Whilst the viscoplastic fluids exhibit much lower surface tensions and hence smaller equilibrium contact angles than water ($\sigma = 0.034$ Nm^{-1} for viscoplastic fluids, $\sigma = 0.075$ Nm^{-1} for water), characterisation of the surface energy using de-ionised water drops is used here purely to highlight the difference in surface energy between the glass and parafilm substrates. A more detailed analysis of shear-thinning and yield-stress fluid drop equilibrium contact angle is presented in the drop spreading section (**§6.2**). Figures [87] – [89] compare equivalent drop impacts on glass and parafilm substrates for the GLY098 ($\mu = 0.925$ Pas), GLY094 ($\mu = 0.428$ Pas) and GLY080 ($\mu = 0.056$ Pas) Newtonian solutions. Figures [92] – [94] and [97] – [99] display equivalent comparisons for the shear-thinning X0125 ($n = 0.400$, $K = 0.208$ Pas^n), X050 ($n = 0.129$, $K = 2.846$ Pas^n), and X075 ($n = 0.084$, $K = 5.064$ Pas^n) fluids and the viscoplastic YSF020 ($n = 1.443$, $K = 0.475$ Pas^n, $\tau_c = 0$ Pa), YSF030 ($n = 0.378$, $K = 5.53$ Pas^n, $\tau_c = 11.5$ Pa) and YSF040 ($n = 0.373$, $K = 7.94$ Pas^n, $\tau_c = 26.1$ Pa) fluids respectively.

5.1.1 Newtonian fluids

Throughout the inertial expansion phase in Figures [87] – [89], β remains similar for impacts on both glass and parafilm substrates. The similarity of the maximum dimensionless spread and height factors can be observed more clearly in Figures [90] and [91], which plot $\beta_m = D_{Max}/D_E$ and $\xi_m = h_{Min}/D_E$ as a function of We. β_m and ξ_m increase and decrease respectively with increases in We and decreases in viscosity, in agreement with previous observations[41-62]. Unlike the effect of wettability on low viscosity drop impacts (with $\mu \sim 0.001$ Pas), both β_m and ξ_m for fluids with $0.056 \leq \mu \leq 0.925$ Pas do not

vary significantly with substrate wettability within the ranges $1.7 \leq We \leq 240$ and $1.1 \leq Re \leq 137$. The most significant variable between these results and those of Mao et al.[47] and Pasandideh et al.[43] is the viscosity of the test fluids examined. This indicates that whilst substrate wettability will influence the impact dynamics of low viscosity liquids during the expansion phase, the measurable difference will decrease as the viscosity is increased and for Newtonian fluids with $\mu \geq 0.056$ Pas, measured differences fall within experimental error.

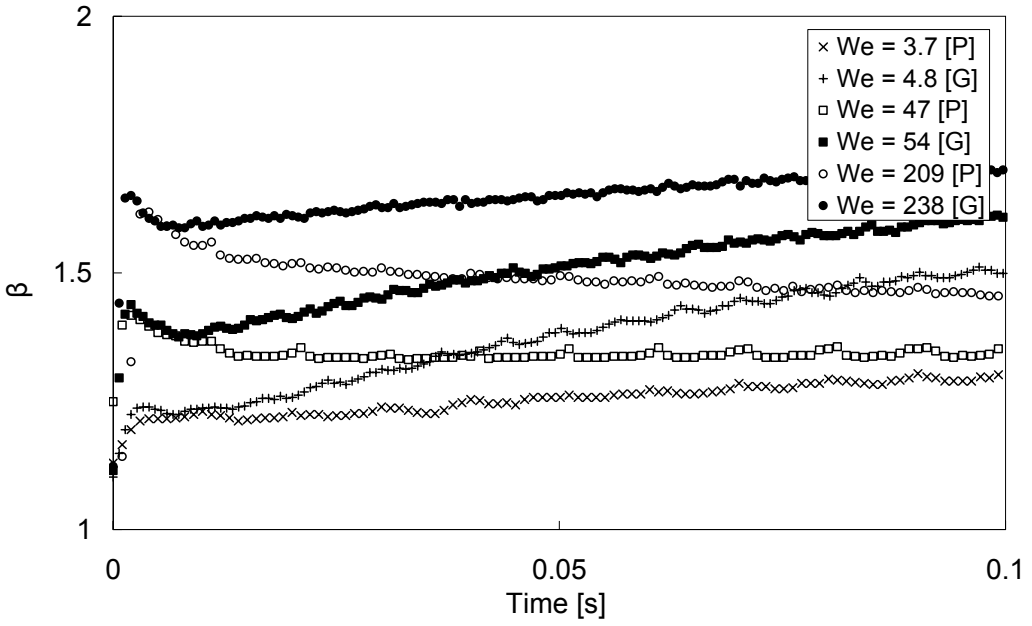

Figure 87. Dimensionless drop diameter β plotted against time for drops of the GLY098 Newtonian fluid ($\mu = 0.925$ Pas) impacting from fall heights of 10 (We ~ 4), 50 (We ~ 45) and 200 mm (We ~ 220) on glass [G] ($\theta_e = 0^o$, solid symbols) and parafilm-M [P] ($\theta_e = 95 \pm 2^o$, open symbols) substrates. Each results set represents the average of 5 drop measurements. Errors are comparable in size to symbol dimensions.

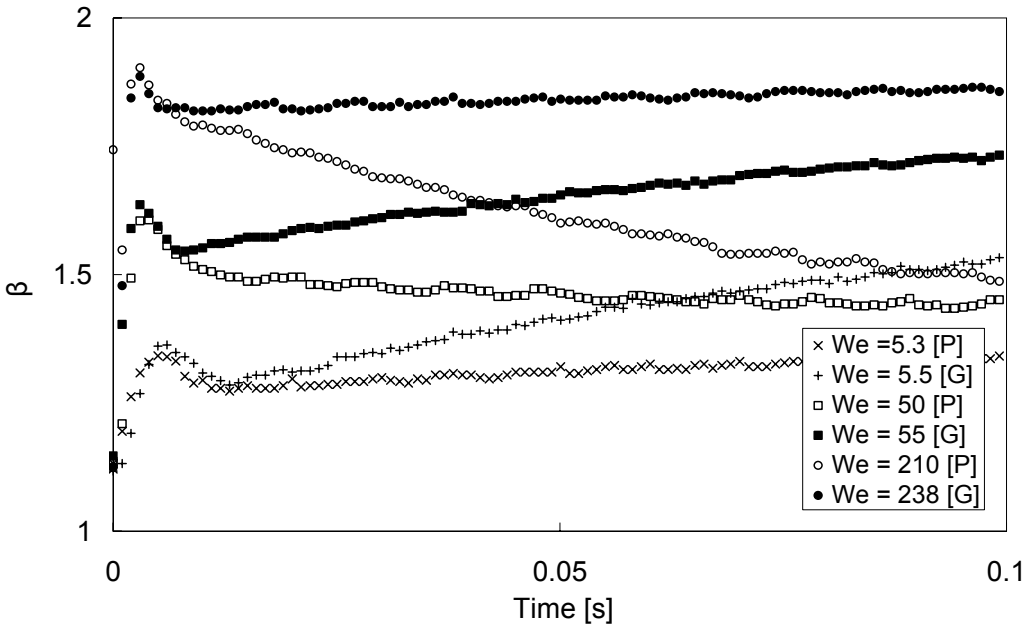

Figure 88. Dimensionless drop diameter β plotted against time for drops of the GLY094 Newtonian fluid (μ = 0.428 Pas) impacting from fall heights of 10 (We ~ 5), 50 (We ~ 50) and 200 mm (We ~ 210) on glass [G] ($\theta_e = 0^o$, solid symbols) and parafilm-M [P] ($\theta_e = 95 \pm 2^o$, open symbols) substrates. Each results set represents the average of 5 drop measurements. Errors are comparable in size to symbol dimensions.

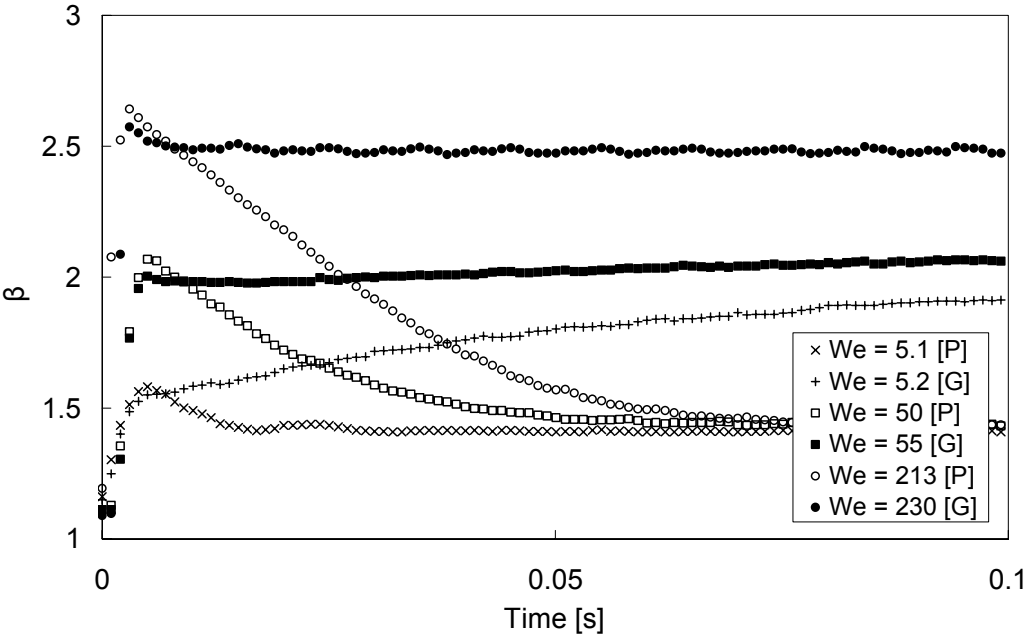

Figure 89. Dimensionless drop diameter β plotted against time for drops of the GLY080 Newtonian fluid (μ = 0.056 Pas) impacting from fall heights of 10 (We ~ 5), 50 (We ~ 50) and 200 mm (We ~ 220) on glass [G] ($\theta_e = 0^o$, solid symbols) and parafilm-M [P] ($\theta_e = 95 \pm 2^o$, open symbols) substrates. Each results set represents the average of 5 drop measurements. Errors are comparable in size to symbol dimensions.

The maximum inertial spread factor of water drops were concluded in a paper by Fukai et al.[65] to decrease as the advancing contact angle, θ_a increased. To extend this conclusion to account for more viscous Newtonian fluid viscosities, θ_a was measured for drops of each solution impacting on the glass and parafilm substrates. θ_a was found to be 135 ± 10^o for impacts of each fluid on both substrates. This indicates that differences in θ_a between the two substrates are small for fluids with $\mu \geq 0.056$ Pas and fall within experimental error.

The influence of substrate wettability on impact dynamics can only significantly be observed after the inertial expansion phase. After β_m is reached, a large retraction phase is typically observed for impacts on the parafilm substrate. In contrast, impacts on the glass surface can show a short initial retraction phase, typically followed by slow spreading driven by capillarity. These characteristics are not true in all cases. Low fall height impacts of high viscosity fluids on a parafilm substrate, such as $H_f = 10$mm for the GLY098 solution (Figure 87) show very little retraction, suggesting that the inertial energy converted to capillary energy during inertial expansion is small and not sufficiently large to produce a retraction phase. This behaviour is consistent for an impact with Re = 1.1, where near parity exists between inertial and viscous forces.

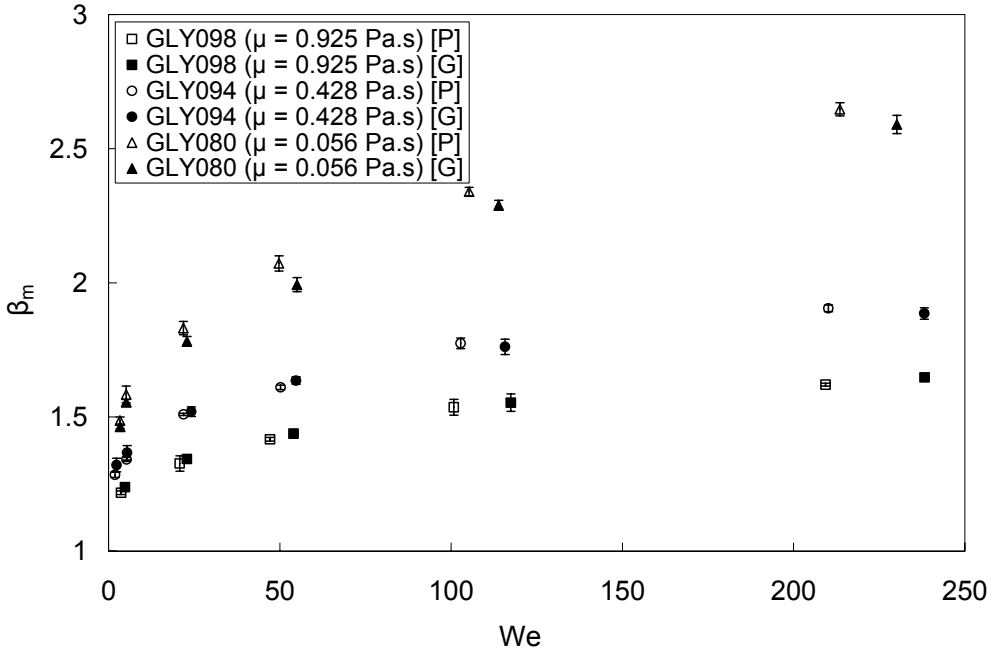

Figure 90. Comparison of maximum dimensionless spread factor β_m for Newtonian fluid drops GL098 (μ = 0.925 Pas, D_E = 3.102 mm), GL094 (μ = 0.428 Pas, D_E = 3.101 mm) and GLY080 (μ = 0.056 Pas, D_E = 3.133 mm) impacting on parafilm [P] ($\theta_e = 95 \pm 2^o$, open symbols) and glass [G] ($\theta_e = 0^o$, solid symbols) substrates. Each results set is based on the average of 5 drop measurements.

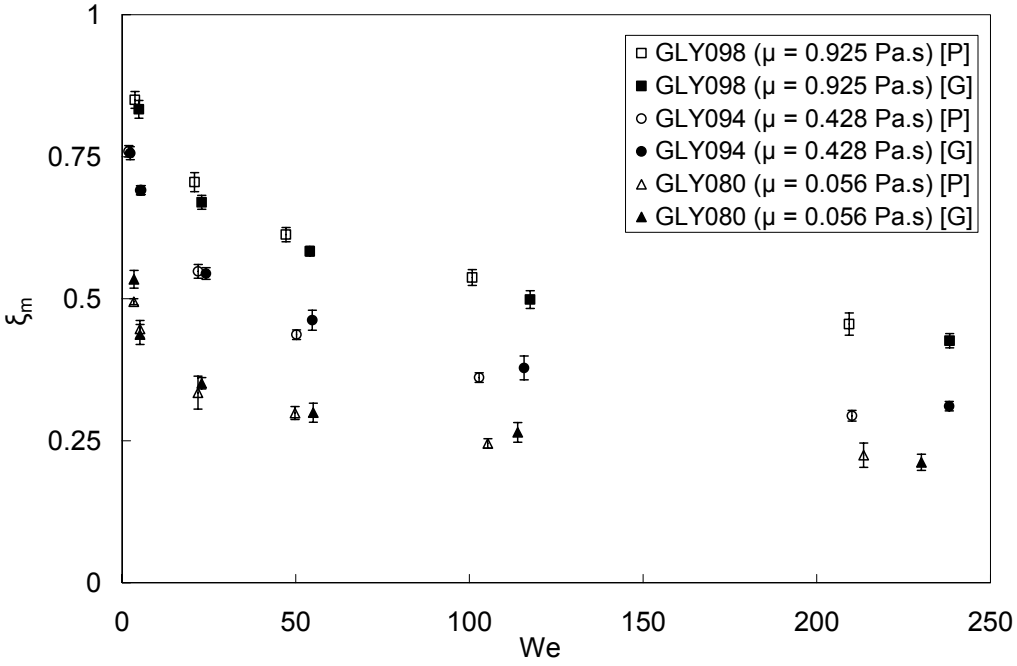

Figure 91. Comparison of the minimum dimensionless height factor ξ_m for Newtonian fluid drops GLY098 (μ = 0.925 Pas, D_E = 3.102 mm), GL094 (μ = 0.428 Pas, D_E = 3.101 mm) and GLY080 (μ = 0.056 Pas, D_E = 3.133 mm) impacting on parafilm [P] ($\theta_e = 95 \pm 2^o$, open symbols) and glass [G] ($\theta_e = 0^o$, solid symbols) substrates. Each results set is based on the average of 5 drop measurements.

5.1.2 Shear-thinning fluids

Equivalent shear-thinning fluid impacts on glass and parafilm substrates (Figures 92 – 94) are very similar during the inertial expansion phase. Noticeable differences can only be observed after maximum inertial spread, whereupon drops on the parafilm surface show significantly larger retraction phases than on the glass surface. Small retraction phases can be observed for drop impacts of the X0125 solution on glass (Figure 92), however this decreases as the impact velocity decreases; similar to that observed for impacts on parafilm. Impacts from fall heights of 10 mm show no visible retraction phase at all and slow capillary driven spreading continues directly after the fast spreading of the inertial expansion phase.

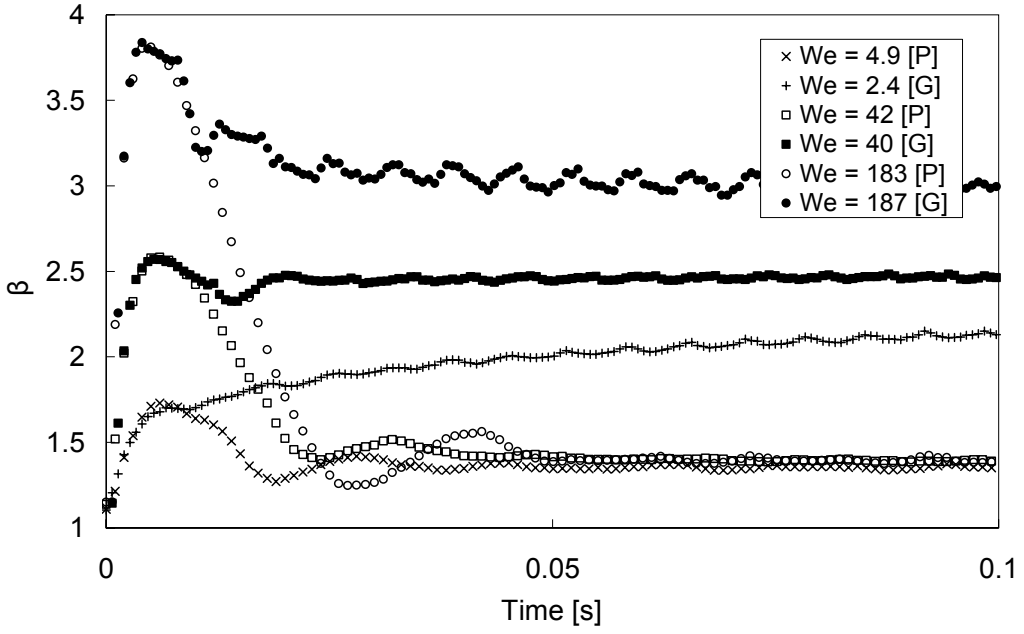

Figure 92. Dimensionless drop diameter β plotted against time for drops of the X0125 shear-thinning fluid (K = 0.208 Pas^n, n = 0.400) impacting from fall heights of 10 (We ~ 3), 50 (We ~ 40) and 200 mm (We ~185) on glass [G] (solid symbols) and parafilm-M [P] (open symbols) substrates. Each results set represents the average of 5 drop measurements. Errors are comparable in size to symbol dimensions.

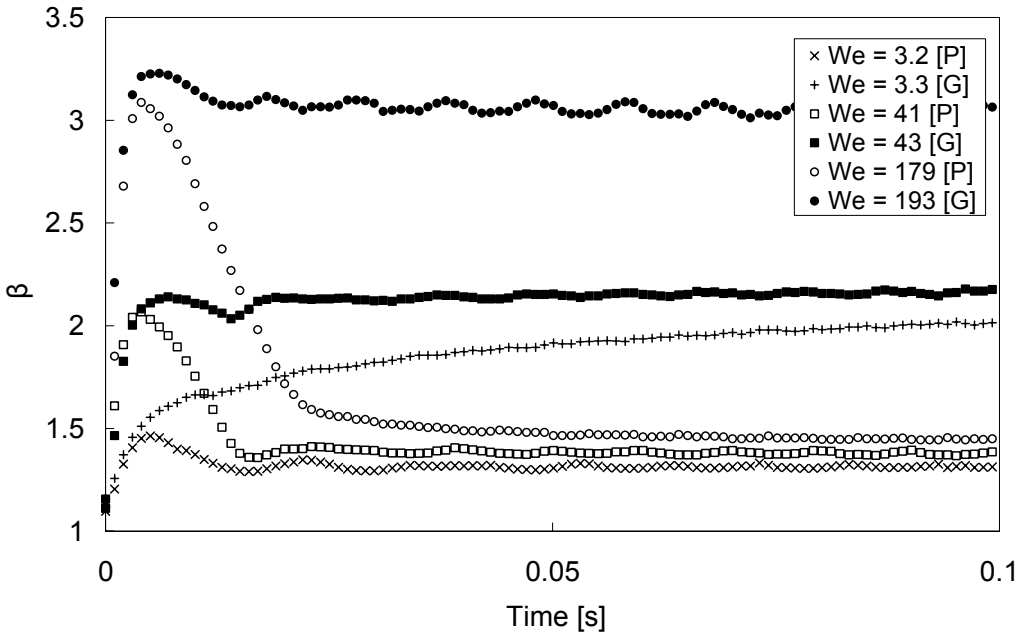

Figure 93. Dimensionless drop diameter β plotted against time for drops of the X050 shear-thinning fluid (K = 2.846 Pas^n, n = 0.129) impacting from fall heights of 10 (We ~ 3), 50 (We ~ 42) and 200 mm (We ~ 185) on glass [G] (solid symbols) and parafilm-M [P] (open symbols) substrates. Each results set represents the average of 5 drop measurements. Errors are comparable in size to symbol dimensions.

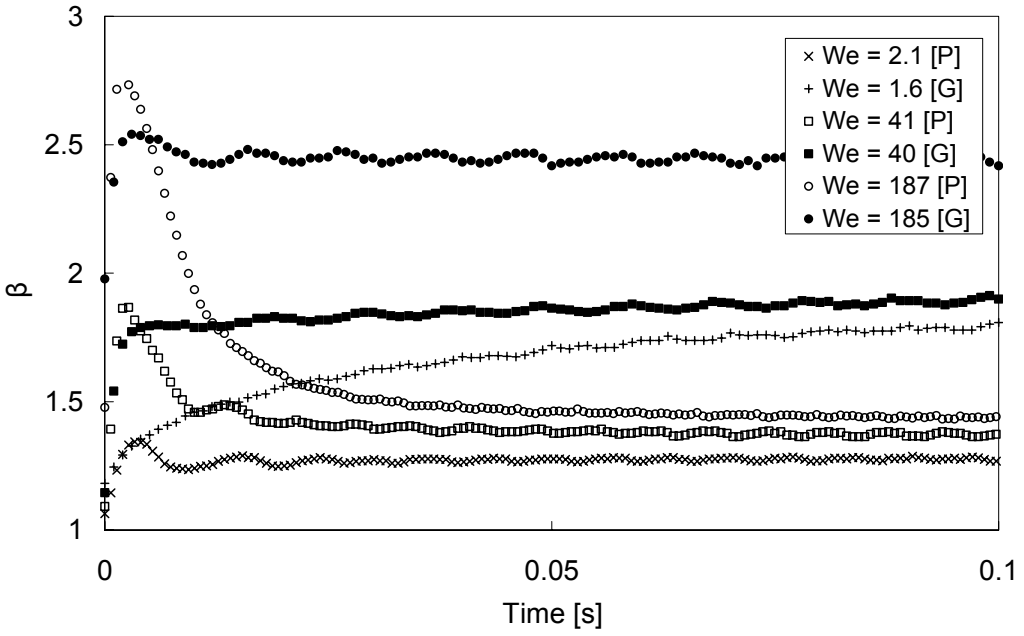

Figure 94. Dimensionless drop diameter β plotted against time for drops of the X075 shear-thinning fluid (K = 5.064 Pas^n, n = 0.084) impacting from fall heights of 10 (We ~ 2), 50 (We ~ 40) and 200 mm (We ~ 186) on glass [G] (solid symbols) and parafilm-M [P] (open symbols) substrates. Each results set represents the average of 5 drop measurements. Errors are comparable in size to symbol dimensions.

Figures [95] and [96] respectively display measurements of β_m and ξ_m plotted against We for drops of the shear-thinning fluid solutions impacting on the two substrates within the range $0.8 \leq We \leq 194$. For equivalent impacts on the two substrates, both height and diameter results agree to within experimental error, indicating that surface wettability does not appear to influence drop impact behaviour during the inertial expansion phase.

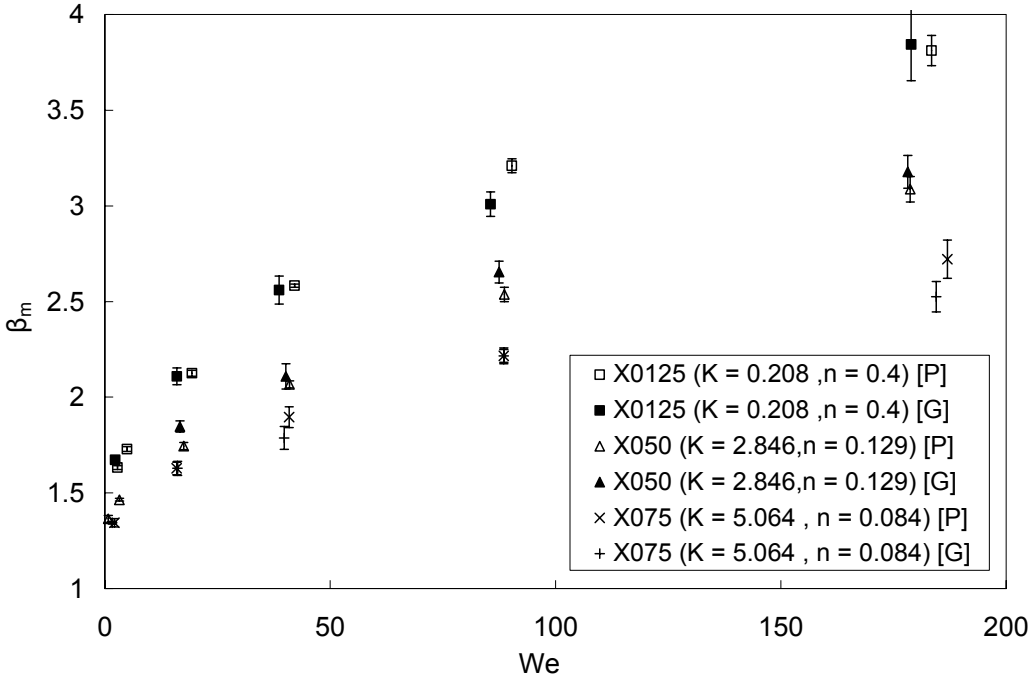

Figure 95. Comparison of the dimensionless diameter β_m at the end of inertial expansion for shear-thinning fluid drops X0125 (K = 0.208 Pas^n, n = 0.400, D_E = 3.474 mm), X050 (K = 2.846 Pas^n, n = 0.129, D_E = 3.428 mm) and X075 (K = 5.064 Pas^n, n = 0.084, D_E = 3.347 mm) impacting on parafilm [P] (open symbols) and glass [G] (solid symbols) substrates. Each results set is based on the average of 5 drop measurements.

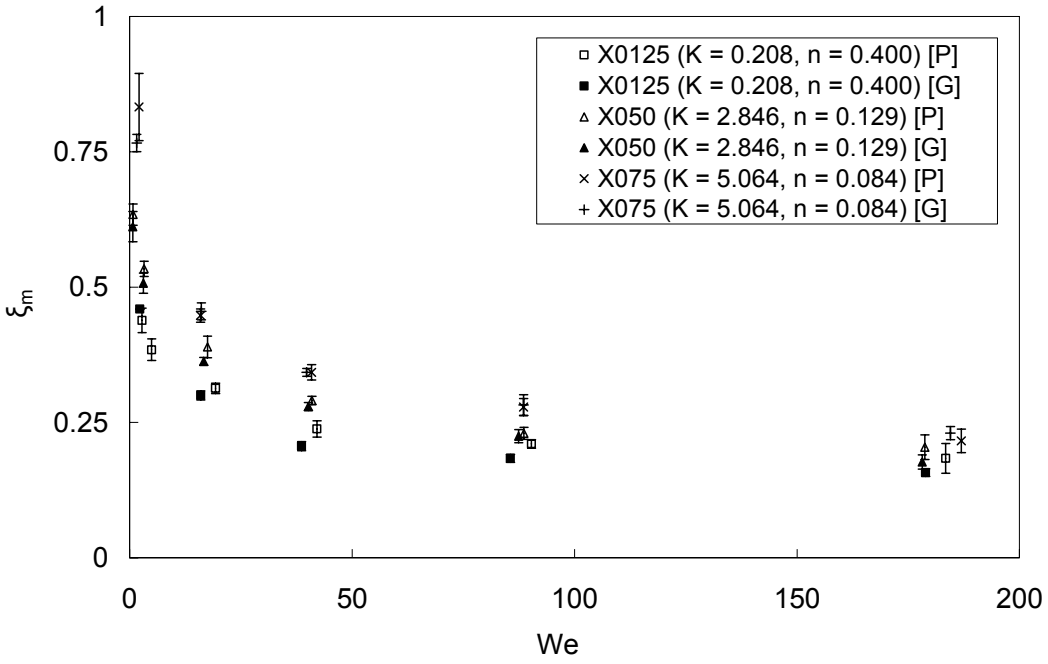

Figure 96. Comparison of the dimensionless apex height ξ_m at the end of inertial expansion for shear-thinning fluid drops X0125 (K = 0.208 Pas^n, n = 0.400, D_E = 3.474 mm), X050 (K = 2.846 Pas^n, n = 0.129, D_E = 3.428 mm) and X075 (K = 5.064 Pas^n, n = 0.084, D_E = 3.347 mm) impacting on parafilm [P] (open symbols) and glass [G] (solid symbols) substrates. Each results set is based on the average of 5 drop measurements.

5.1.3 Viscoplastic fluids

As with the Newtonian and shear-thinning fluids, the influence of surface wettability on drop impacts of viscoplastic fluids in the range $0 \leq \tau_c \leq 26.1$ Pa (Figures 97 – 99) is only noticeable after the end of the inertial expansion stage. Whilst retraction phases are observed after impacts of YSF020 fluid drops on parafilm, fluids with $\tau_c \geq 5.4$ Pa exhibit only small retraction phases similar to those observed for high viscosity Newtonian fluids. Viscoplastic drop impacts on glass show no significant retraction phase and slow capillary driven spreading follows directly on from the fast spreading of inertial expansion for low impact velocity impacts with $H_f < 25$ mm. For fall heights $H_f \geq 50$ mm, drop diameters remain nearly constant after β_m is reached, however Figures [97] – [99] only show periods up to 0.1 s after impact; the influence of yield-stress on spreading after impact is detailed in **§6.2.**

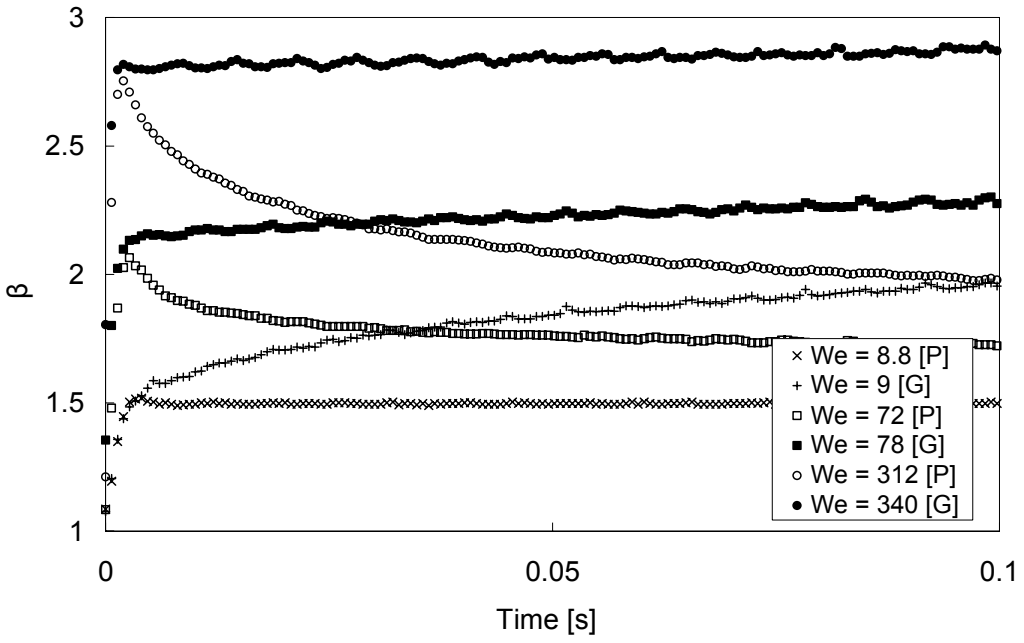

Figure 97. Dimensionless drop diameter β plotted against time for drops of the YSF020 viscoplastic fluid ($K = 1.443$ Pas^n, $n = 0.4747$, $\tau_c = 0$ Pa) impacting from fall heights of 10 (We ~ 9), 50 (We ~ 75) and 200 mm (We ~ 320) on glass [G] (solid symbols) and parafilm-M [P] (open symbols) solid substrates. Each results set represents the average of 5 drop measurements. Errors are comparable in size to symbol dimensions.

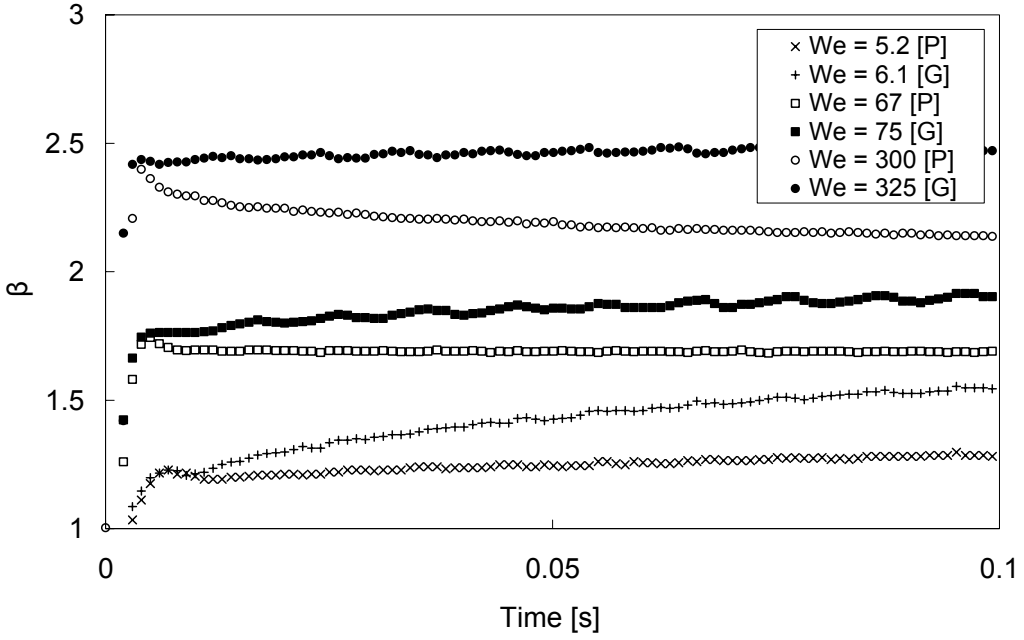

Figure 98. Dimensionless drop diameter β plotted against time for drops of the YSF030 viscoplastic fluid ($K = 5.533$ Pas^n, $n = 0.3775$, $\tau_c = 11.5$ Pa) impacting from fall heights of 10, 50 and 200 mm on glass [G] (solid symbols) and parafilm-M [P] (open symbols) solid substrates. Each results set represents the average of 5 drop measurements. Errors are comparable in size to symbol dimensions.

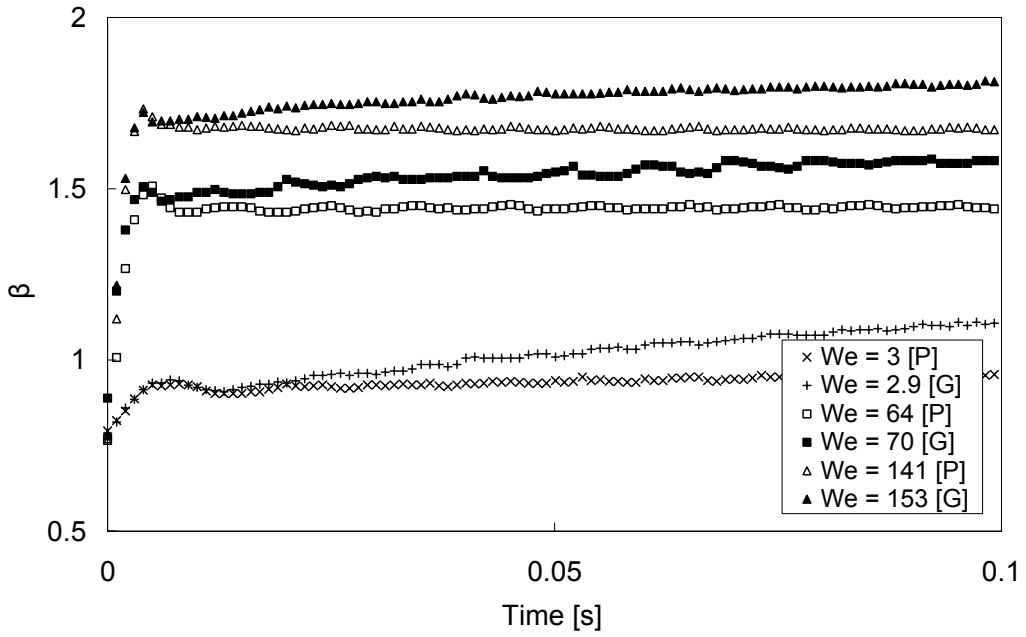

Figure 99. Dimensionless drop diameter β plotted against time for drops of the YSF040 viscoplastic fluid ($K = 7.936$ Pas^n, $n = 0.3727$, $\tau_c = 26.1$ Pa) impacting from fall heights of 10, 50 and 200 mm on glass [G] (solid symbols) and parafilm-M [P] (open symbols) solid substrates. Each results set represents the average of 5 drop measurements. Errors are comparable in size to symbol dimensions.

Figures [100] and [101] respectively compare β_m and ξ_m against We for equivalent impacts of viscoplastic drops with $0 \leq \tau_c \leq 26.1$ Pa on parafilm and glass substrates in the range $0.7 \leq We \leq 340$. Both diameter and height results closely agree, with measured differences falling within experimental error for each solution. Fluid yield-stress effects therefore do not contribute to increases in the influence of surface wettability. Moreover, the similarity of the results also highlights that the phenomena of slip effects, commonly observed in yield-stress fluid flows[133] are also not significant or equally influential on both substrates. This however cannot be quantified.

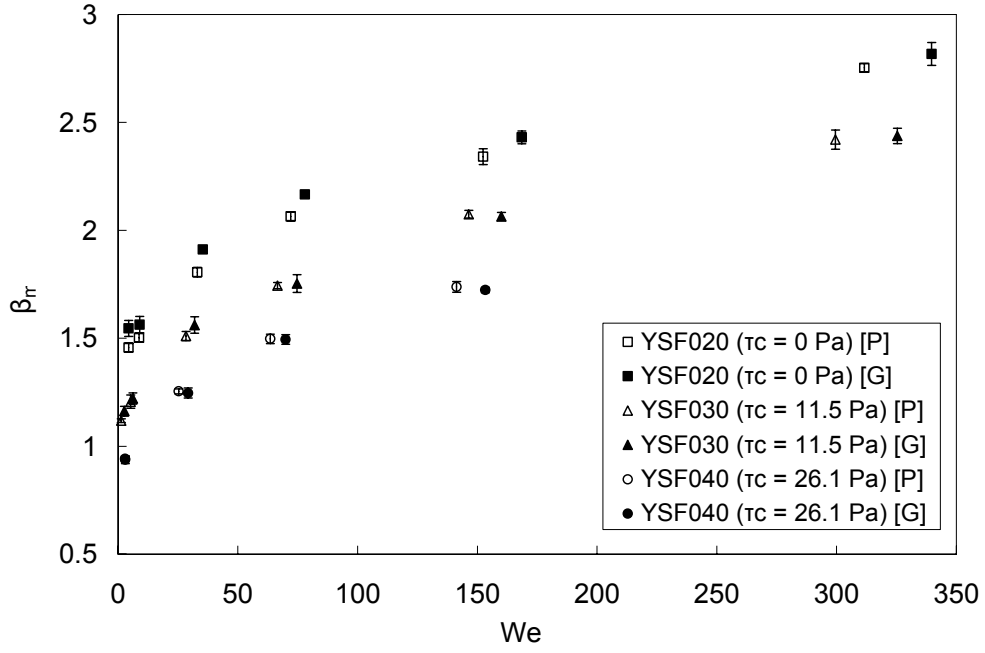

Figure 100. Comparison of β_m at the end of inertial expansion for viscoplastic fluid drops YSF020 (K = 1.443 Pas^n, n = 0.4747, τ_c = 0 Pa, D_E = 2.848 mm), YSF030 (K = 5.533 Pas^n, n = 0.3775, τ_c = 11.5 Pa, D_E = 2.678 mm) and YSF040 (K = 7.936 Pas^n, n = 0.3727, τ_c = 26.1 Pa, D_E = 2.617 mm) impacting on parafilm [P] (open symbols) and glass [G] (solid symbols) substrates. Each results set is based on the average of 5 drop measurements.

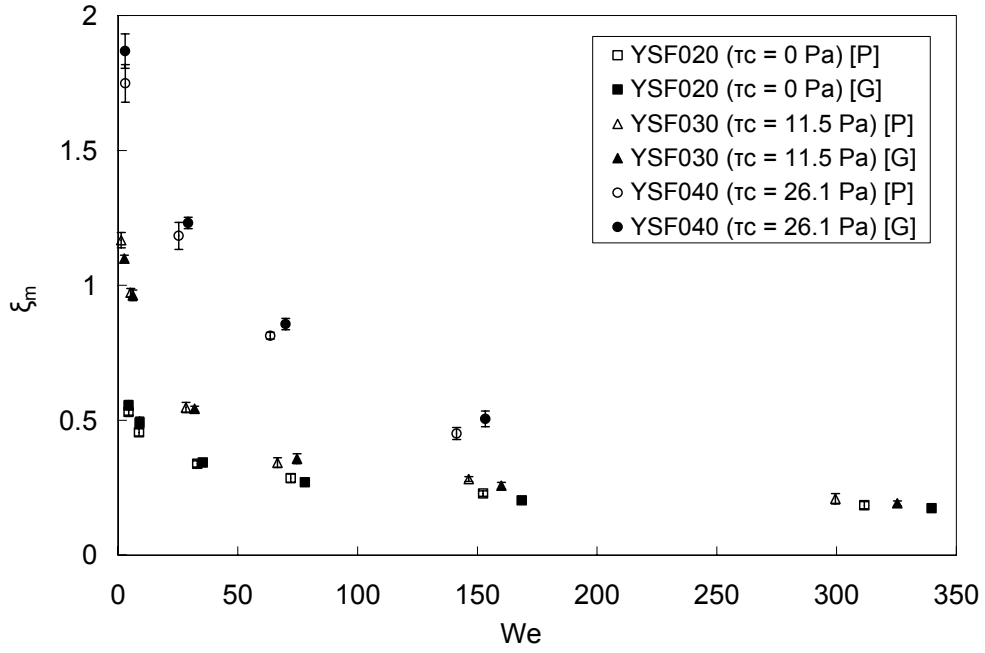

Figure 101. Comparison of ξ_m at the end of inertial expansion for viscoplastic fluid drops YSF020 (K = 1.443 Pas^n, n = 0.4747, τ_c = 0 Pa, D_E = 2.848 mm), YSF030 (K = 5.533 Pas^n, n = 0.3775, τ_c = 11.5 Pa, D_E = 2.678 mm) and YSF040 (K = 7.936 Pas^n, n = 0.3727, τ_c = 26.1 Pa, D_E = 2.617 mm) impacting on parafilm [P] (open symbols) and glass [G] (solid symbols) substrates. Each results set is based on the average of 5 drop measurements.

5.2 Newtonian drop impact behaviour

5.2.1 Experimental studies

Figures [102] - [104] respectively display temporal variations in dimensionless spread factor $\beta = D/D_E$ and dimensionless height $\xi = h/D_E$ for drops of the GLY098 (μ = 0.925 Pas), GLY094 (μ = 0.428 Pas) and GLY080 (μ = 0.056 Pas) fluids impacting from fall heights in the range $7.5 \leq H_f \leq 200$ mm ($3.4 \leq We \leq 214$, $1.1 \leq Re \leq 134$) on to a parafilm-M substrate. It has been well established that the maximum spread diameters of drops vary as a function of the impact velocity and fluid viscosity, most simply characterised by ratios of inertial to viscous (Re) and capillary (We) forces. The underlying relation between impact velocity and contact line radial velocity during inertial spreading has not however been examined in great detail. As a first approximation from simple scaling analyses[50], the contact line velocity of an inviscid drop during inertial spreading has been established to be of the same order of magnitude as the impact velocity, $v_r = O(v_z)$.

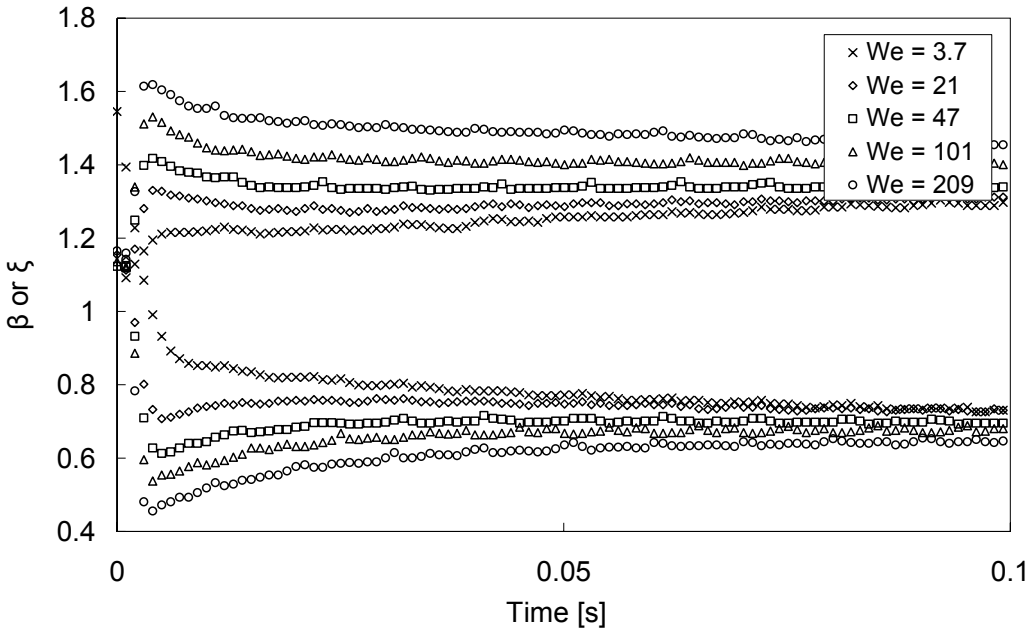

Figure 102. Temporal variations in dimensionless inertial spread diameter β and height ξ for Newtonian GLY098 fluid drops (D_E = 3.10 mm, μ = 0.925 Pas) impacting on a parafilm-M substrate from fall heights in the range 10 mm $\leq H_f \leq$ 200 mm (corresponding to $3.7 \leq We \leq 209$, $1.1 \leq Re \leq 8.1$). Each results set represents the average of 5 drop measurements. Errors are comparable in size to symbol dimensions.

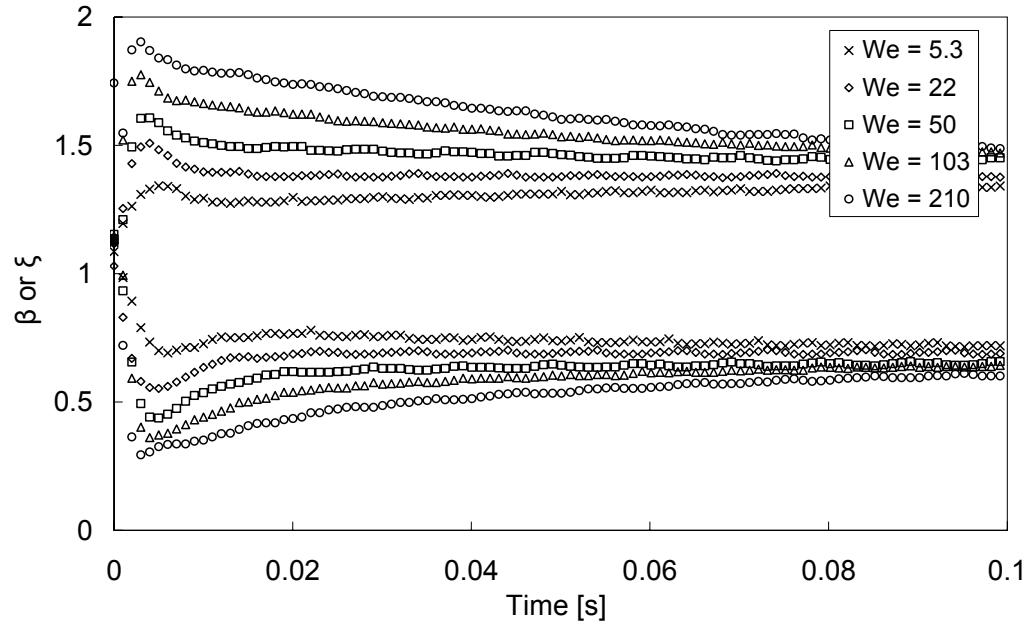

Figure 103. Temporal variations in dimensionless inertial spread diameter β and height ξ for Newtonian GLY094 fluid drops (D_E = 3.10 mm, μ = 0.428 Pas) impacting on a parafilm-M substrate from fall heights in the range 10 mm ≤ H_f ≤ 200 mm (corresponding to 5.3 ≤ We ≤ 210, 1.7 ≤ Re ≤ 18). Each results set represents the average of 5 drop measurements. Errors are comparable in size to symbol dimensions.

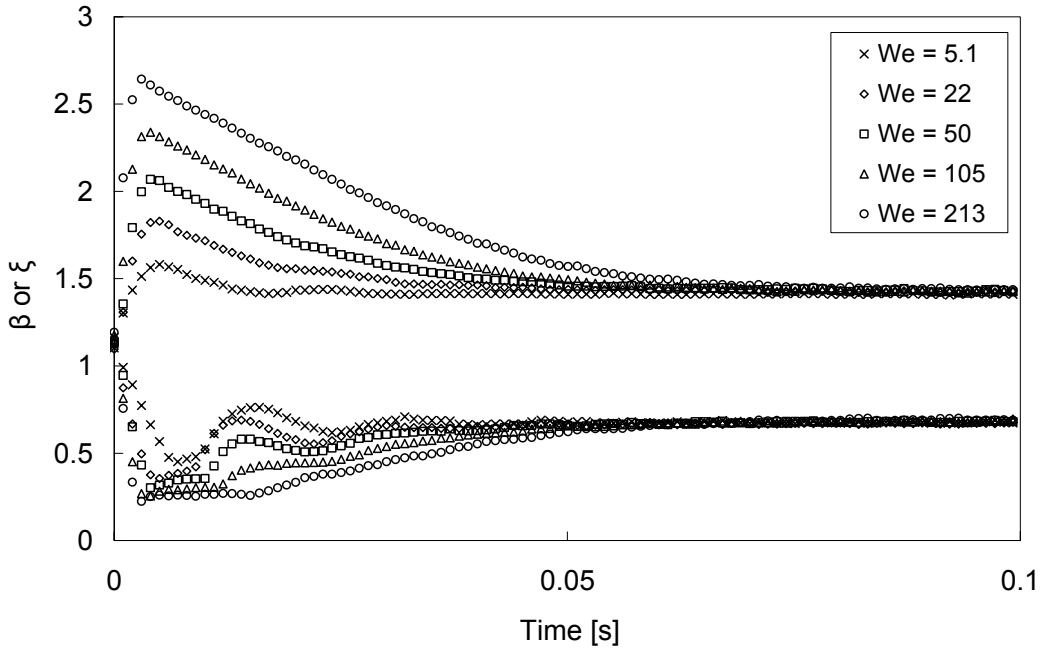

Figure 104. Temporal variations in dimensionless inertial spread diameter β and height ξ for Newtonian GLY80 fluid drops (D_E = 3.13 mm, μ = 0.056 Pas) impacting on a parafilm-M substrate from fall heights in the range 7.5 mm ≤ H_f ≤ 200 mm (corresponding to 3.4 ≤ We ≤ 213, 17≤ Re ≤ 134). Each results set represents the average of 5 drop measurements. Errors are comparable in size to symbol dimensions.

Figure [105] plots the maximum radial spread velocity[9]:

$$v_r \equiv \dot{R}(t) = \max\left\{\frac{D_E \dot{\beta}(t)}{2}\right\} \qquad [67]$$

of drops on both parafilm and glass surfaces during inertial expansion against the impact velocity for fluids with $0.056 \leq \mu \leq 0.925$ Pas in the range $3.7 \leq We \leq 230$. Advancing contact angles were measured to be $\theta_a = 135 \pm 10^o$ for each fluid. For drops of equal viscosity, there is a clear linear variation of v_r with v_z. The line gradients decrease with increasing fluid viscosity. Figure [106] plots the gradient of the lines of best fit against the dimensionless viscosity (the ratio of fluid viscosity, μ, to that of water, μ_{water} at 23°C). A power law of the form:

$$\frac{v_r}{v_z} = 3.645\left(\frac{\mu}{\mu_{water}}\right)^{-0.4} \qquad [68]$$

provides the best fit to the combined results of both substrates. The inviscid scaling law equating the spread velocity to the same order of magnitude as the impact velocity provides a good approximation for low viscosity fluid drops with $\mu << 0.056$ Pas, however this approximation degrades with increasing viscosity.

[9] The radial spread velocity at the beginning of impact can be very large and may not be adequately recorded for each drop impact due to the limiting temporal resolution of the high speed camera (1000 Hz). Impact and radial velocities are based on an average of 5 drop impact processes however, significantly increasing the probability of recording the initial inertial spreading rate. Measurement errors are based on the variance of the maximum recorded radial spread velocity (from 5 impacts) because these are significantly larger than both the spatial image resolution (32.6 μm) error and the temporal resolution (which based on the maximum recorded spread velocity of $v_r \sim 1.5$ ms^{-1} recorded at 1000 Hz gives a spatial resolution of 0.015 m).

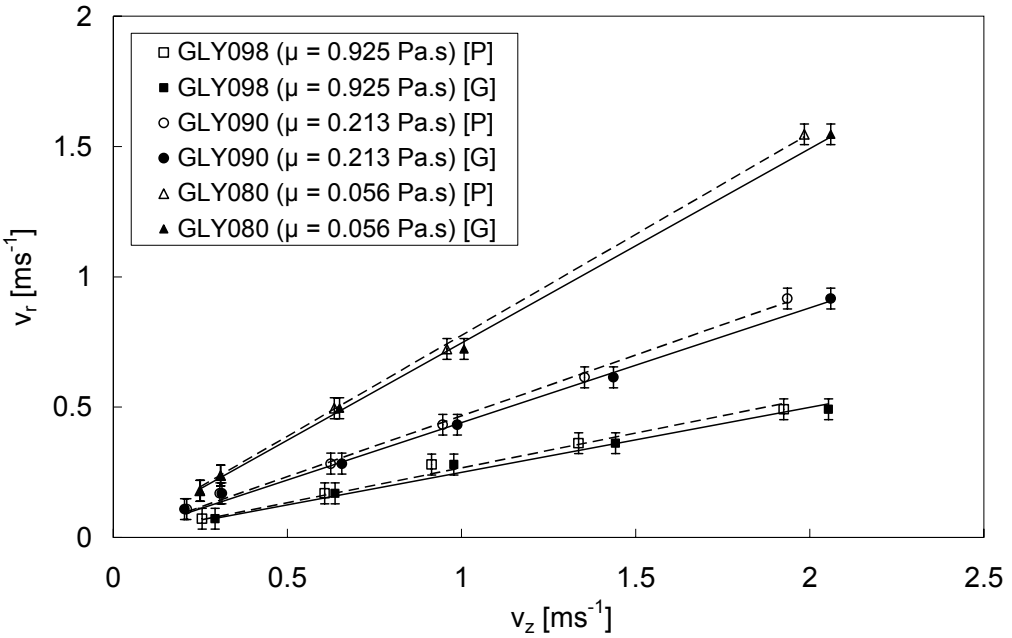

Figure 105. Maximum drop spread velocity (Equation 67) plotted against impact velocity v_z for Newtonian fluids GLY098 (μ = 0.925 Pas), GLY090 (μ = 0.213 Pas) and GLY080 (μ = 0.056 Pas) impacting on glass [G] ($\theta_e = 0^o$, solid symbols) and parafilm [P] ($\theta_e = 95 \pm 2^o$, open symbols) substrates over the range $3.7 \leq We \leq 230$.

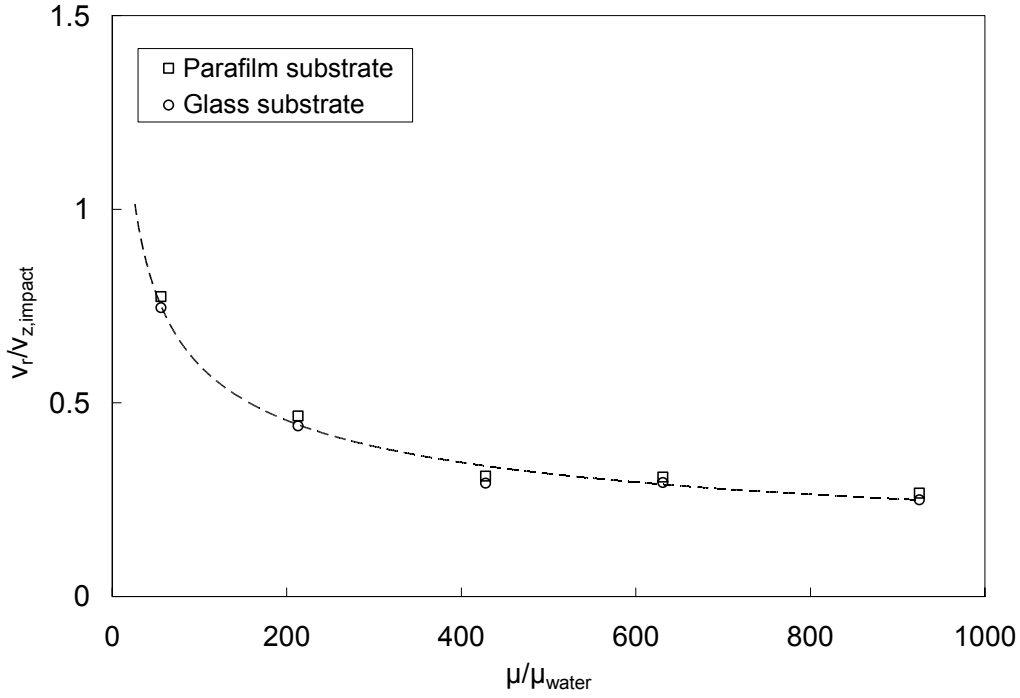

Figure 106. Gradient of linear relationship between spread velocity v_r and impact velocity v_z (Figure 105) plotted as a function of dimensionless viscosity (fluid viscosity scaled by the viscosity of water). The dashed line corresponds to a best fit power law relation described by Equation [68].

Increasing impact velocity on hydrophobic substrates increases β_m and hence the surface energy stored in the lamella available for retraction. In Figure [104], the amount and duration of the retraction phase grows significantly with increasing We. The initial gradient of retraction however appears similar in magnitude for impacts at different We. Figures [107] – [109] plot temporal variations in β, normalised with respect to β_m for GLY098, GLY094 and GLY080 fluid drops impacting on the parafilm surface. For impacts of each fluid across the range $5.1 \leq We \leq 213$, results for the initial retraction period (over the period 5-10 ms after β_m) collapse onto a single curve. Figures [110] – [112] plot the maximum retraction rate $\dot{\chi}$ as a function of We for the GLY098, GLY094 and GLY080 fluids where:

$$\dot{\chi} = \frac{v_r}{R_{Max}} = -\max\left\{\frac{\dot{\beta}(t)}{\beta_m}\right\} \qquad [69]$$

for impacts on the parafilm substrate. The negative sign in Equation [69] indicates that $\dot{\chi}$ is positive for retraction. From the figures, low velocity impacts with $Re < 10$ and $We < 10$ typically show significantly smaller retraction rates (where present) in comparison with high velocity impacts with $Re > 10$ and $We > 10$, where inertial forces are an order of magnitude larger than capillary or viscous forces.

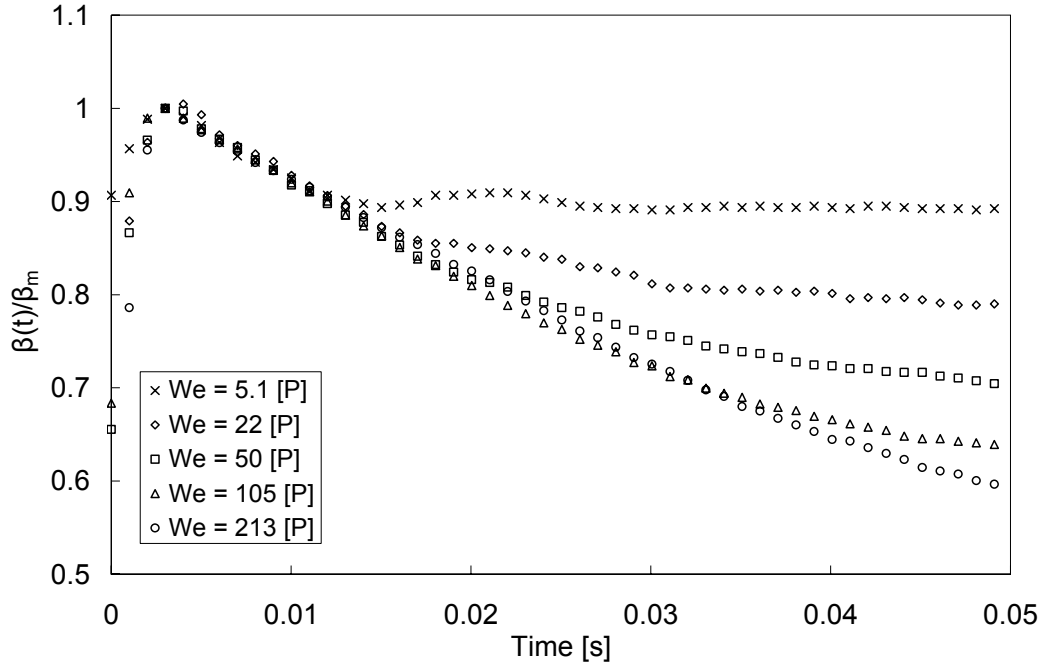

Figure 107. Temporal variations in dimensionless inertial spread diameter β normalised by β_m for GLY080 fluid drops (D_E = 3.13 mm, μ = 0.056 Pas) impacting on a parafilm-M [P] substrate from fall heights in the range 10 mm ≤ H_f ≤ 200 mm (corresponding to 5.1 ≤ We ≤ 213, 21 ≤ Re ≤ 134). Each results set represents the average of 5 drop measurements. Errors are comparable in size to symbol dimensions.

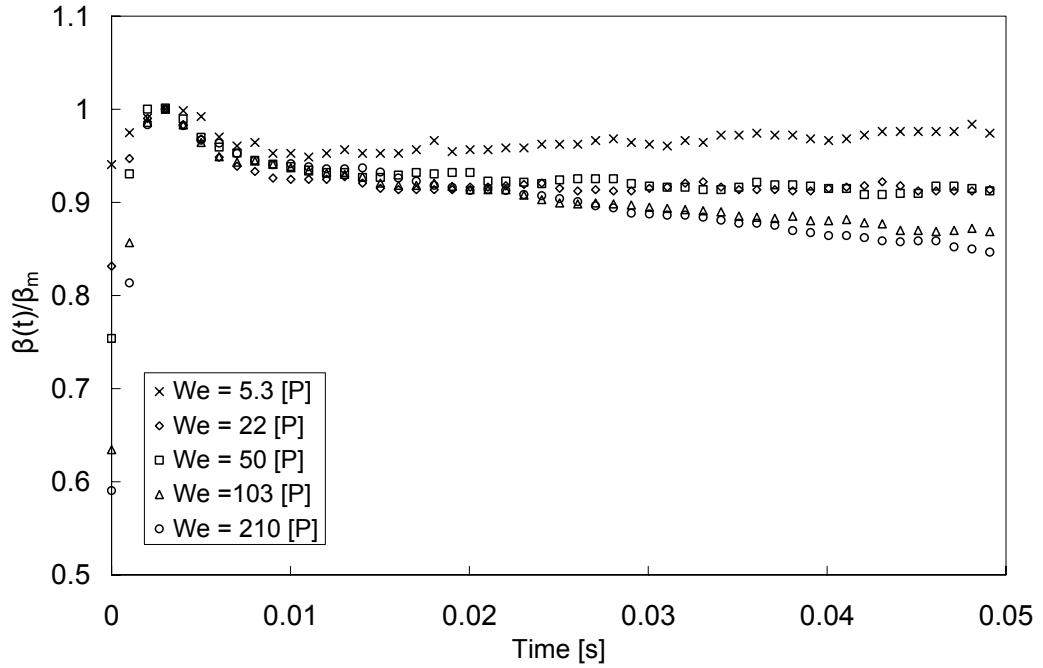

Figure 108. Temporal variations in dimensionless inertial spread diameter β normalised by β_m for GLY094 fluid drops (D_E = 3.10 mm, μ = 0.428 Pas) impacting on a parafilm-M [P] substrate from fall heights in the range 10 mm ≤ H_f ≤ 200 mm (corresponding to 5.3 ≤ We ≤ 210, 2.8 ≤ Re ≤ 18). Each results set represents the average of 5 drop measurements. Errors are comparable in size to symbol dimensions.

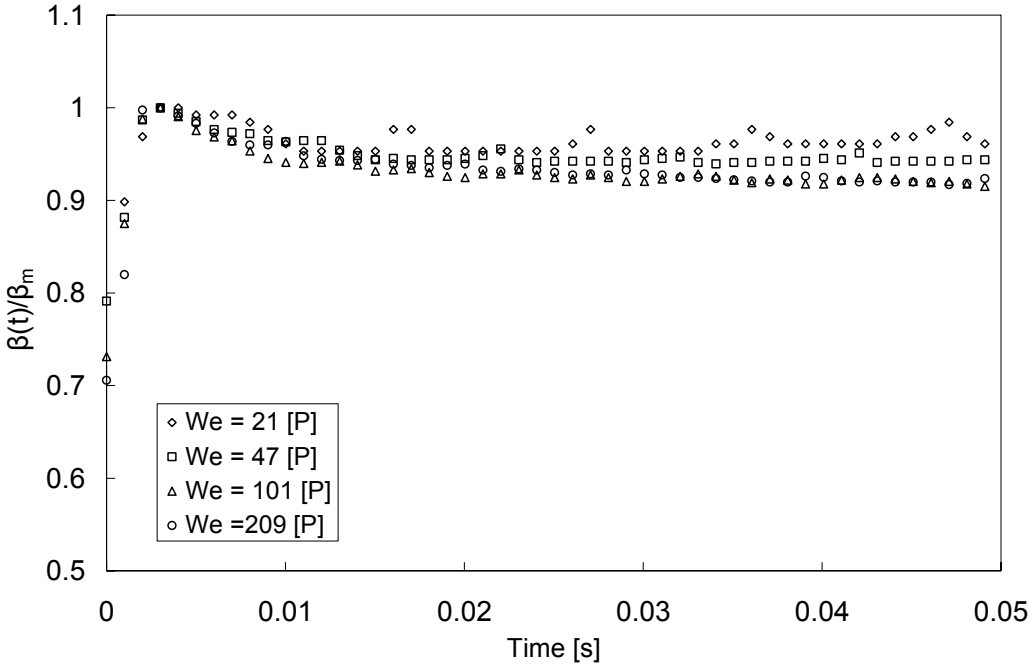

Figure 109. Temporal variations in dimensionless inertial spread diameter β normalised by β_m for GLY098 fluid drops (D_E = 3.10 mm, μ = 0.925 Pas) impacting on a parafilm-M [P] substrate from fall heights in the range 25 mm ≤ H_f ≤ 200 mm (corresponding to 21 ≤ We ≤ 209, 2.6 ≤ Re ≤ 8.1). Each results set represents the average of 5 drop measurements. Errors are comparable in size to symbol dimensions.

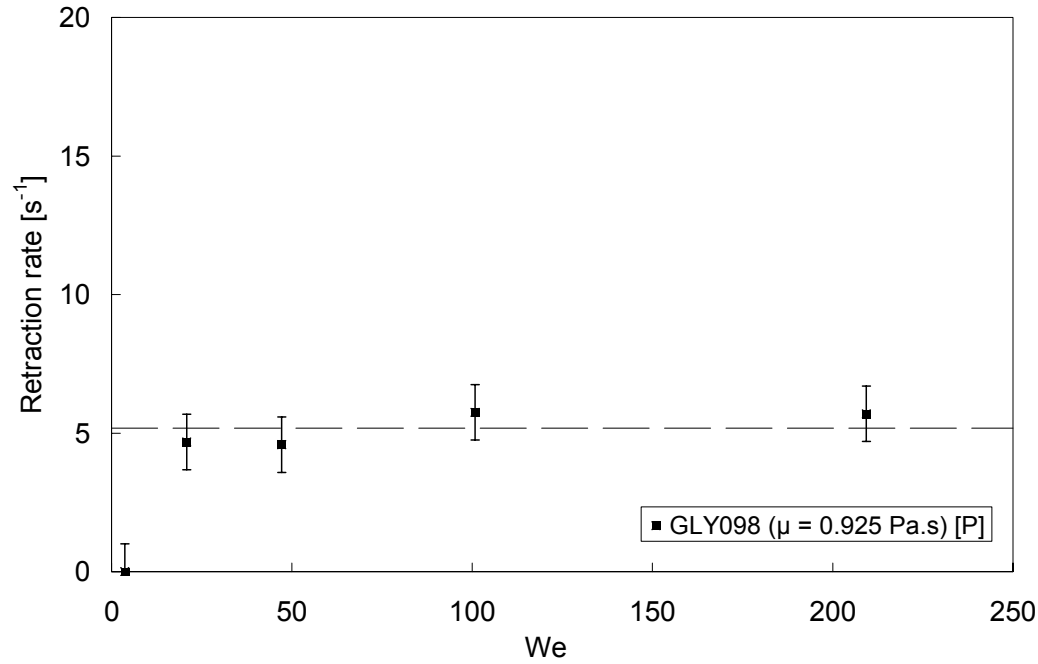

Figure 110. Maximum retraction rate $\dot{\chi}$ plotted against We for GLY098 (μ = 0.925 Pas, D_E = 3.10 mm) fluid drops impacting on a parafilm [P] substrate.

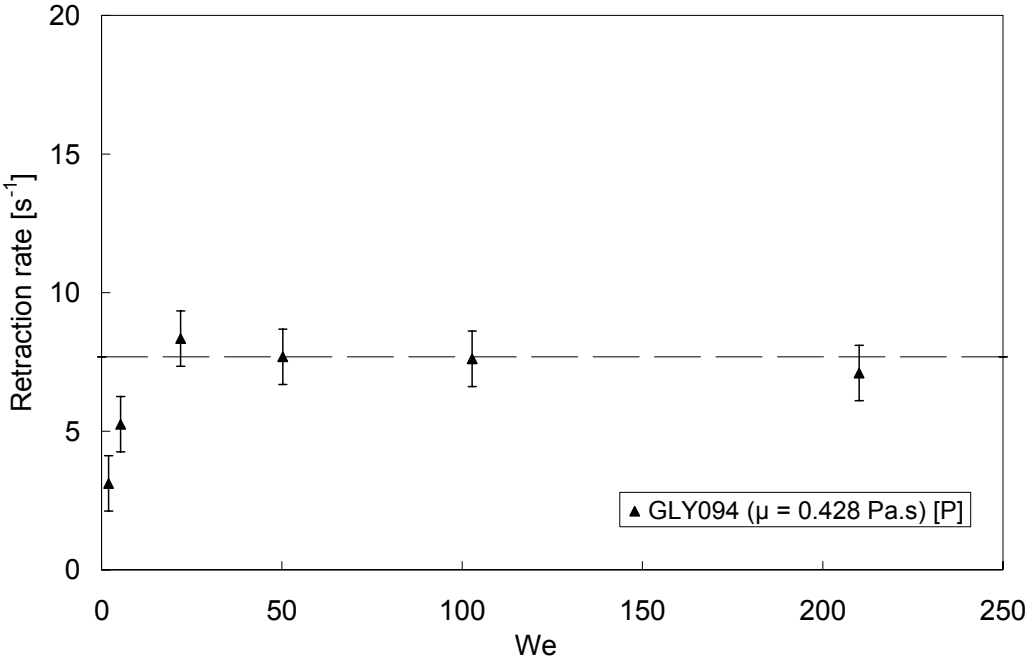

Figure 111. Maximum retraction rate $\dot{\chi}$ plotted against We for GLY094 (μ = 0.428 Pas, D_E = 3.10 mm) fluid drops impacting on a parafilm [P] substrate.

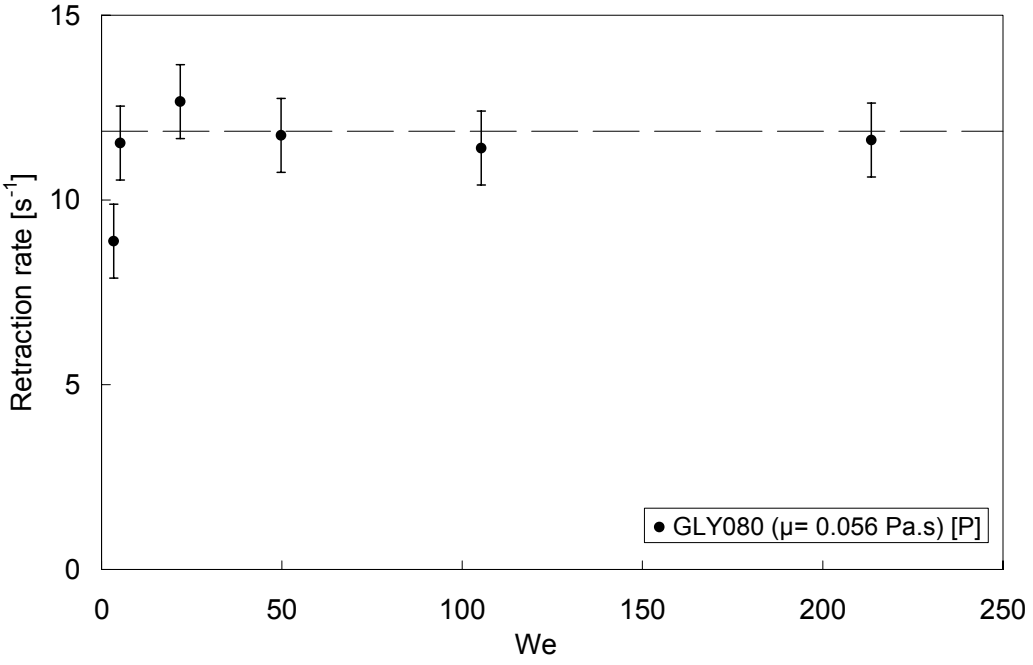

Figure 112. Maximum retraction rate $\dot{\chi}$ plotted against We for GLY080 (μ = 0.428 Pas, D_E = 3.10 mm) fluid drops impacting on a parafilm [P] substrate. A measurable retraction phase was not observed for impacts on the glass substrate.

The long dashed lines in Figures [110] – [112] represent the average $\dot{\chi}$ for drop impacts with We > 10. With the exception of low velocity impacts (We < 10) whose retraction rate decreases as We decreases, measured values of $\dot{\chi}$ agree to within the experimental error of the average, suggesting that the retraction rate remains constant with increasing We for sufficiently large impact velocities.

The maximum retraction rate also varies with fluid viscosity. Drop retraction can be divided into two regimes[98]; an inertial regime, where the non-dimensionalised retraction rate, $\dot{\chi}\,T_I$, for fluids with Oh < 0.05 is independent of viscosity and a viscous regime, where $\dot{\chi}\,T_I$ for fluids with Oh > 0.05 is proportional to Oh^{-1}. A theoretical retraction rate can be established from:

$$\dot{\chi} \approx \left(\frac{3}{25}\right)^{1/3} \frac{(1-\cos\theta_r)^{5/3}}{5\ln\left(\Lambda/\lambda\right)} T_v^{-1} \qquad [70]$$

where θ_r is the drop contact angle during retraction, Λ and λ are respectively the macroscopic and microscopic cut-off length scales from the linear-force-velocity relation by De Gennes[99]:

$$F_V = -\frac{6\pi\mu}{\theta}\ln\left(\frac{\Lambda}{\lambda}\right)R(t)\dot{R}(t) \qquad [71]$$

and $T_v = \mu R_E/\sigma$ is the large-scale relaxation timescale of a viscous drop. Typically Λ is the same order of magnitude as the drop size (O ~ 1mm) and λ is of the order O ~ 1nm. The retraction rate in the viscous regime is then non-dimensionalised by an inertial timescale T_I:

$$T_I = \left(\frac{4}{3}\frac{\pi\rho R_E^3}{\sigma}\right)^{1/2} \qquad [72]$$

denoting the oscillation period of a perturbed inviscid drop. Nondimensionalising $\dot{\chi}$ in Equation [70] with T_I in Equation [72] then gives the relationship $\dot{\chi}T_I \propto Oh^{-1}$.

Measured values of $\dot{\chi}\,T_I$ are plotted against Oh in Figure [113]. Measurements agree with the previously established[98] $\dot{\chi}T_I \propto Oh^{-1}$ relationship to within experimental error. Moreover, this work extends the range of Oh to larger values than previously measured ($0.11 \leq Oh \leq 1.78$, previously $0.0035 \leq Oh \leq 0.85$).

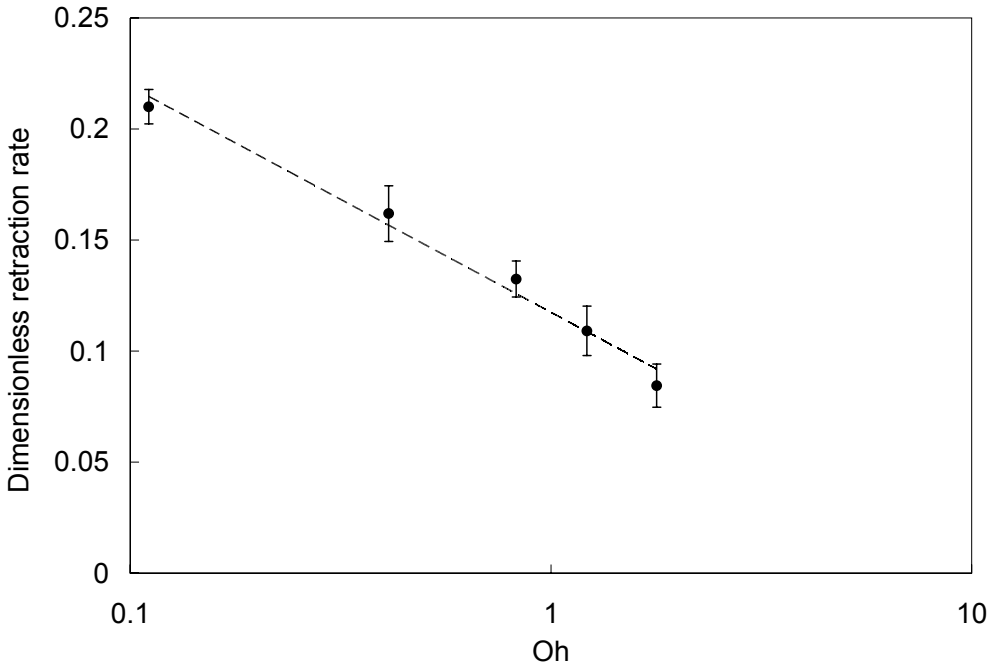

Figure 113. Dimensionless retraction rate $\dot{\chi}\,T_I$ plotted against Oh in the range $0.11 \leq Oh \leq 1.7$ for Newtonian drops during the retraction phase on a parafilm substrate. $\dot{\chi}\,T_I$ shows an inverse linear proportional relationship with Oh for $Oh \leq 0.85$ (short dashed line). For $Oh \geq 0.85$, this linearity breaks down.

Whilst this section provides only a qualitative description of how fluid viscosity, surface wettability and impact velocity influences drop impact behaviour, the following section provides a more quantitative analysis by detailing and reviewing the capability of models that use dimensionless parameters such as We, Re and Oh to characterise and predict drop impact behaviour during inertial expansion.

5.2.2 Prediction models

As highlighted in the literature review, there are several theoretical, empirical and semi-empirical models that attempt to accurately predict the maximum diameter or minimum height of impacting drops on a solid surface at the end of the inertial expansion phase. Models typically utilise common measurable parameters in their prediction including We, Re, Oh, θ_e and θ_a. The advantage of using prediction models in comparison with performing complete three-dimensional numerical solutions using computational methods is the speed with which parameters of interest (in this case β and ξ) can be estimated; useful when designing and optimising engineering applications incorporating spray or drop impact processes. The main disadvantage however is that model predictions are typically very approximate; therefore it is important to understand the predictive capability of each model.

Creating a robust one-dimensional model is challenging, primarily because a number of flow physics assumptions and approximations must be made which are only valid for specific drop impact behaviour. Impact dynamics can vary widely with fluid, impact and substrate properties. We have previously established that drop deformation (excluding splashing phenomena) can be considerable for high We impacts of low viscosity fluids. Drop shape towards the end of inertial expansion can typically be approximated by a thin flat cylinder. Moreover in some high impact velocity cases, the lamella may be bounded by a rim. In contrast however, for low We impacts of moderately high viscosity fluids, the cylindrical approximation described in the literature review becomes invalid and impacting drops exhibit deformations similar in shape to that of a spherical cap. The diversity of drop impact dynamics makes the formulation of a general one dimensional prediction model; valid over large ranges of Oh and We numbers, difficult.

Since the publication of review papers by Bennett and Poulikakos[51] and Healy et al.[74], a number of one-dimensional prediction models have been proposed, ranging from simple order of magnitude studies to more technical energy conservation models, which account for more complex flow physics including deformed drop shape and additional

dissipative effects arising from the rolling motion of liquid near the contact line. Whilst not a review paper, Attané et al.[48] also provide a thorough analysis of some more contemporary models and compare their predictions with both experimental results and a newly proposed AGM model over a larger range of Oh ($0.002 \leq Oh \leq 0.585$) than previously assessed. We propose that there are two remaining regions where additional work would contribute to the existing high quality research already performed in this area. Firstly, details of drop prediction models are dispersed. This section aims to consolidate previous analyses of contemporary models and highlight their attributes and limitations by establishing their predictive capabilities with respect to a standardised set of experimental measurements: drop impact dynamics of Newtonian drops with viscosities in the range $0.001 \leq \mu \leq 0.925$ Pa·s ($0.00195 \leq Oh \leq 1.78$) for impacts with $1.8 \leq We \leq 214$ and $1.1 \leq Re \leq 6889$. Secondly, model predictions are most commonly compared only with experimental results of low viscosity fluid drops (water with $\mu = 0.001$ Pas or $Oh \sim 0.002$) impacting at moderate We ($v_z \geq 1 ms^{-1}$ or $We > 50$). The work presented here focuses more on establishing the predictive capability of models towards higher Oh and lower We, where viscous effects during inertial expansion play a more dominant role. The shape of drops at the end of inertial spreading for high Oh fluids or low We impacts can differ significantly from a cylindrical lamella (an assumption made by a number of energy balance approach models), therefore analyses of model predictive capabilities are more likely to highlight limitations. Moreover, emerging industrial processes such as the manufacture of glass microlenses[162] for the electronics industry, where deposition of fluid drops is made at relatively low We, makes the investigation timely. The review is concluded with a summary of the predictive capabilities of each model, from which the best performing model is established. A further study then investigates empirical modifications to this model to improve the predictive capability at in the low We, high Oh regime.

The models reviewed here are presented in terms of increasing complexity, beginning with simple order of magnitude and scaling law analyses to more complex models that utilise an energy balance approach. The energy balance models themselves can be further divided into those that assume a spherical cap drop shape at the end of the inertial expansion phase and those that assume a cylindrical shape. For the latter type,

models are presented chronologically from the original approach by Chandra and Avedisian[42] through derivative models by Pasandideh-Fard et al.[43] and Mao et al.[47] to the most contemporary energy balance approach formulated by Attané et al.[48], which incorporates aspects that account for more complex flow physics; namely flow circulation close to the contact line during inertial spreading and the presence of a bounding rim for low viscosity, high velocity drop impacts[46].

It should be noted that whilst the complexity of prediction models has increased significantly to incorporate descriptions for more complex flow physics, models typically exhibit good predictions only in a range of Weber and Reynolds numbers (as highlighted in **§5.2.2.3**). Outwith this range (both towards high and low Re and We), predictions degrade. As highlighted by Roisman et al.[166], if Re and We are large enough (such that the effects of viscous forces can be considered negligible), models that are based on the energy balance approach or use a cylindrical shape approximation are incorrect. In this regime, the lamella shape far from the drop edge during impact can be described in terms of a universal law. Moreover, the lamella thickness, velocity and pressure distributions almost become independent of the impact conditions. This conclusion suggests that there is a limit to the predictive capability of models employing an energy balance approach. This review and subsequent empirical model optimization has been included however because prediction models are useful to both academia and industry as a method for estimating drop impact behaviour without using intensive computational methods.

This review is not exhaustive and there exist a number of additional prediction models since the publication of the last review papers that have not been analysed. These include Asai et al.[64], Yarin and Weiss[169] and Kim and Chun[55]. These models each use an energy balance approach with a cylindrical drop shape approximation. Previous research[47,48] has shown however that these models provide poorer predictive capabilities than the respective models they were compared with (and which are reviewed here), therefore they have not been included.

5.2.2.1 Scaling law models.

Scaling law models establish simple theoretical and empirical relationships between the fluid properties and the dimensionless diameter and height factors β_m and ξ_m (see **§2.8.3**). These models do not consider the complex flow physics that occurs during drop impact and as such, their predictive capabilities are often severely limited.

5.2.2.1.1 Bejan and Gobin.

The model proposed by Bejan and Gobin[50] is based upon a purely theoretical order of magnitude argument derived from the principle that flow geometry maximises inertial drop spreading to accelerate the attaining of equilibrium. This theory proposes that inertial spreading ceases when viscous diffusion has swept the entire lamella cross section. At this time the maximum drop spread factor will be:

$$\beta_m \sim 2\left(\frac{\rho v_z D_E}{\mu}\right)^{1/2} \sim 2\,\mathrm{Re}^{1/2} \qquad [73]$$

Equation [73] significantly overpredicts measured maximum spread factors by up to nearly an order of magnitude as displayed in Figure [114]. The limitations of this scaling law originate from the assumptions that immediately after impact, the flow is initially inviscid and all radial flow motion is constant and the same as the velocity at the drop rim, resulting in a toroidal drop shape. This assumption is therefore invalid for low impact velocities and viscous fluids. Spreading ceases when viscous diffusion originating from the contact surface sweeps transversally through the entire drop cross-section. It is recognised however that this scaling law is a means to an end with the objective of the research being to evaluate whether a principle of maximisation of flow access anticipates the splashing phenomenon during drop impact. The onset of splashing is more readily observed for low viscosity fluids, where inertial deformations can result in toroidal and rimmed disk drop shapes, therefore this model is not expected to provide good agreement with drop impacts at high Oh or low We.

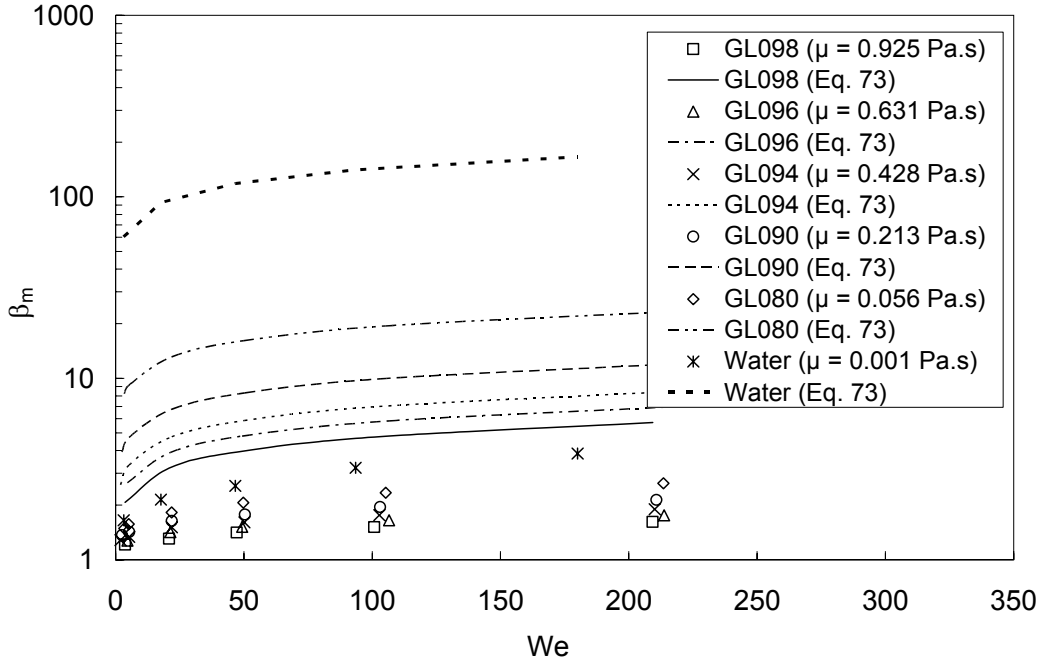

Figure 114. Comparison of measured β_m with predictions using Equation [73] in the range $0.0019 \leq Oh \leq 1.78$ and $1.9 \leq We \leq 214$.

5.2.2.1.2 Clanet et al.

Clanet et al.[44] establishes the maximum drop spread factor to scale as $\beta_m \sim We^{1/4}$ for low viscosity fluids ($\mu = 0.001$ Pas) impacting on super-hydrophobic surfaces. They highlight that this relationship differs from the more classical proposition[42,57] where dissipation of kinetic energy (of the order $\rho D_E^3 v_z^2$) arises from viscous dissipation (energy dissipation scales as $\mu(v_z / h)D_{Max}^3$, where h is the lamella thickness). This order of magnitude argument along with the conservation of drop volume ($hD_{Max}^2 \sim D_0^3$) yields the scaling law:

$$\beta_m \sim \mathrm{Re}^{1/5} \qquad [74]$$

with a corresponding height scale of:

$$\xi_m \sim \frac{1}{\mathrm{Re}^{2/5}} \qquad [75]$$

Moreover, Attané et al.[48] demonstrate that whilst the $We^{1/4}$ power law provides a reasonable description at low Oh, this power law changes to:

$$\beta_m \sim We^{1/6} \quad [76]$$

at higher Oh, with:

$$\xi_m \sim \frac{1}{We^{1/3}} \quad [77]$$

In Figure [115] the $Re^{1/5}$ (Equation 74) scaling law under-predicts measured values of β_m for fluids with $\mu \geq 0.213$ Pas ($Oh \geq 0.412$) and over-predicts β_m for $\mu \leq 0.056$ Pa·s ($Oh \leq 0.109$). The predicted variation of β_m with We exhibits the same trend as that observed in the experimental results, however the largest deviations between them arise towards the lowest Weber numbers. Whilst predictions disagree with experimental measurements by up to ± 136% for low viscosity fluid drops with Oh = 0.00195, predictions agree to within ± 18% for more viscous drops with $0.11 \leq Oh \leq 1.78$ and do not appear to worsen significantly with changes in Oh. Height predictions (Equation 75) in Figure [116] agree with measurements for $0.412 \leq Oh \leq 1.78$ to within ± 15%, however this worsens for Oh = 0.11 where predictions disagree by up to ± 37%. Similarly to predictions of β_m, the variation of ξ_m with We is similar to the experimental results with the largest deviations arising towards lower Weber numbers.

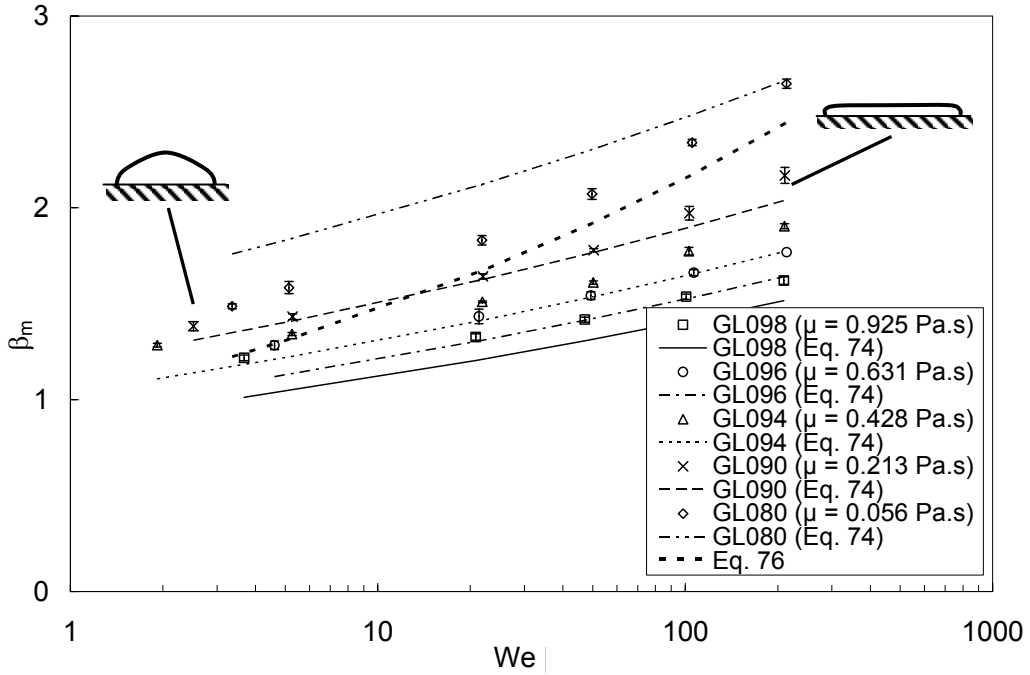

Figure 115. Comparison of measured β_m with scaling law predictions from Clanet et al. and Attané et al. (Equations 74 and 76 respectively) in the range $0.11 \leq Oh \leq 1.78$ and $1.9 \leq We \leq 214$.

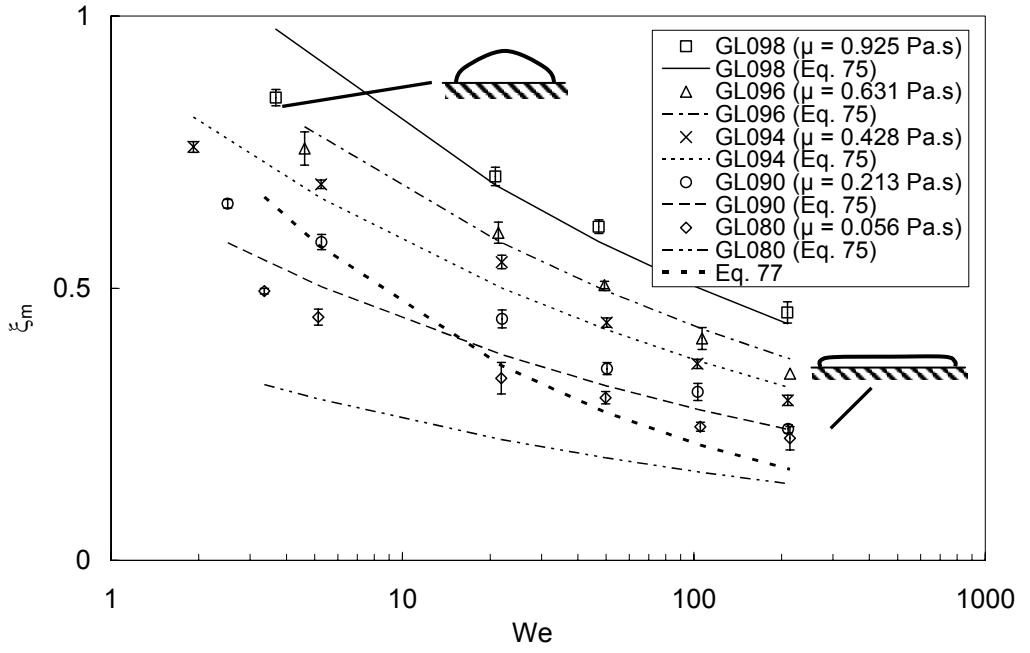

Figure 116. Comparison of measured ξ_m with scaling law predictions from Clanet et al. and Attané et al. (Equations 75 and 77 respectively) in the range $0.11 \leq Oh \leq 1.78$ and $1.9 \leq We \leq 214$.

To further analyse the relationship between β_m, viscosity and how this varies towards low We, measured values of β_m were replotted against μ and power laws were fitted to the experimental results. For impacts with We ~ 211 in Fig [117], β_m scales as

$\mu^{-1/6}$. This viscosity dependence is close to that proposed by Equation [74]. As We decreases however, the relative importance of fluid viscosity on β_m diminishes. For $2.6 \leq We \leq 4.8$, β_m scales between $\mu^{-1/11}$ and $\mu^{-1/14}$. The influence of fluid viscosity on drop impact behaviour therefore varies with We.

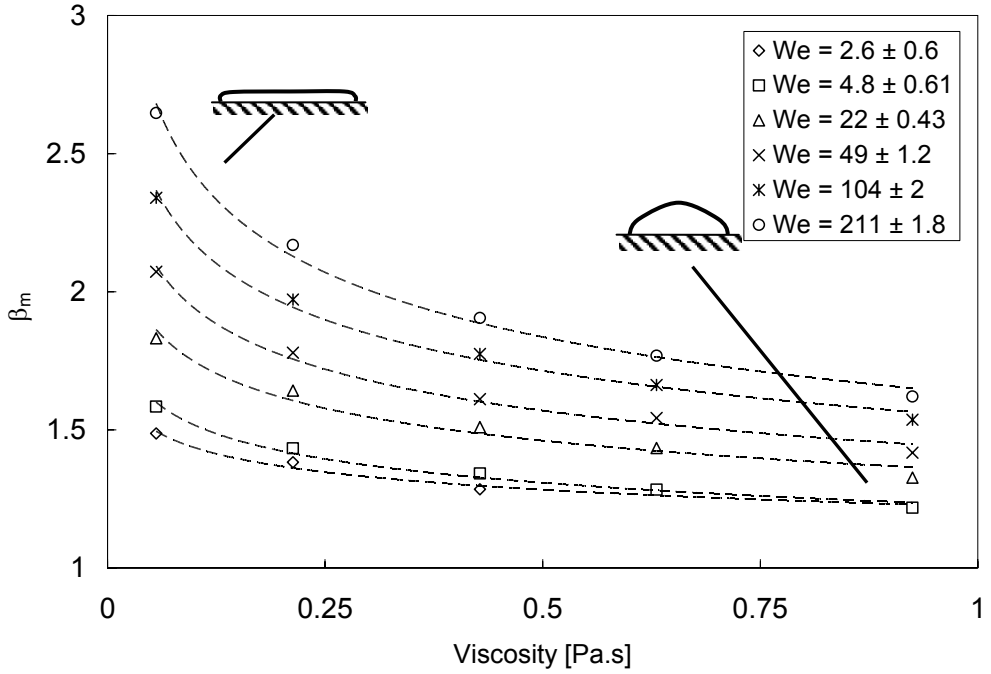

Figure 117. Power law distributions (lines) fitted to measured maximum spreading ratio (symbols) plotted as a function of viscosity for Weber numbers We = 2.6 ± 0.60 (diamond), We = 4.8 ± 0.61 (square), We = 22 ± 0.43 (triangle), We = 49 ± 1.2 (cross), We = 104 ± 2.0 (star) and We = 211 ± 1.8 (circle).

The $We^{1/6}$ (Equation 76) scaling law for super hydrophobic surfaces applicable for high Oh is also compared with experimental results in Figures [115] and [116]. Predictions for Glycerol solutions with $\mu \geq 0.056$, corresponding to the range $0.11 \leq Oh \leq 1.78$ are identical and fall between the experimental results for the GL080 and GL090 solutions ($0.056 \leq \mu \leq 0.213$ Pas). The scaling law does not however show an improved relationship between β_m and We over the classical $Re^{1/5}$ scaling law. Moreover, the significant limitation of this scaling law is the inability to account for variations in fluid viscosity. It should be noted that whilst this scaling law was derived for impacts on superhydrophobic surfaces, the experimental results provided here are for impacts on hydrophobic Parafilm-M surfaces. This comparison is considered valid however because measured differences in β_m between impacts surfaces with varying wettabilities

(Parafilm-M and hydrophilic glass) for Newtonian fluid drops with $\mu \geq 0.056$ Pas ($Oh \geq 0.109$) have previously been found to be small, with differences accountable by experimental error.

5.2.2.2 Energy balance models.

From published literature, one of the most common methods of estimating the maximum spreading ratio β_m has been to utilise an energy balance approach; Kurabayashi[56], Bechtel et al.[49] and Chandra and Avedisian[42] were amongst the first to utilise this method to estimate β_m and ξ_m. In general, the energy balance can be expressed by Equation [20]. Difficulty arises when attempting to estimate the surface tension term at the end of the inertial expansion phase. Most models approximate the shape of the drop at maximum spread to be a cylinder (Equations 21 and 22), however an alternative method is to approximate drop shape to that of spherical cap[49] whereupon the equation used is given in Equation [23].

5.2.2.2.1 Bechtel et al.

Bechtel et al.[49] utilise an energy balance approach with a spherical cap approximation to derive a nonlinear second order differential equation for the drop height. For convenience, they introduce dimensionless time (t^*), surface tension (ST) and viscosity (VIS) parameters, and reduce the differential equation to a first order system of the form:

$$\begin{aligned} \dot{\xi} &= y \\ \dot{y} &= -\frac{\left[C(\xi)y^2 + D(\xi)y + E(\xi)\right]}{2A(\xi)} \end{aligned} \qquad [78]$$

The functions $C(\xi)$, $D(\xi)$ and $E(\xi)$ are given respectively by:

$$\begin{aligned} C(\xi) = &\left(\frac{13\xi^4}{36} + \frac{11\xi}{72} + \frac{\xi^{-2}}{72}\right)\left(\frac{1}{3} + \frac{2\xi^3}{3}\right)^2\left(\frac{\xi}{3} + \frac{\xi^4}{6}\right)^{-2} + \\ &\left(\frac{13\xi^5}{90} + \frac{11\xi^2}{72} + \frac{\xi^{-1}}{36}\right)\left(\frac{1}{3} + \frac{2\xi^3}{3}\right)\left[2\xi^2\left(\frac{\xi}{3} + \frac{\xi^4}{6}\right) - \left(\frac{1}{3} + \frac{2\xi^3}{3}\right)^2\right]\left(\frac{\xi}{3} + \frac{\xi^4}{6}\right)^{-3} \end{aligned} \qquad [79]$$

$$D(\xi) = VIS(\xi^4 - 2\xi + \xi^{-2})\left(\frac{1}{3} + \frac{2\xi^3}{3}\right)^2\left(\frac{\xi}{3} + \frac{\xi^4}{6}\right)^{-2} \quad [80]$$

$$E(\xi) = 2\left[4\xi - \xi^{-2} - ST(2\xi + \xi^{-2})\right] \quad [81]$$

where:

$$ST = -\cos\theta_e$$
$$VIS = \frac{We^{1/2}D_E C}{12\,\mathrm{Re}} = \frac{\sqrt{\pi}}{12}(Oh)^{1/2} \quad [82]$$

The dimensionless time is defined as $t^* = t\left(\rho D_E^3/\sigma\right)^{-1/2}$, and the function C(ξ) includes a boundary layer effect. Equations [78] – [81] were reformulated more concisely by Attané et al.[48] to:

$$\frac{1}{12}\frac{d}{dt}\left[\left(\frac{1+2\xi^3}{2\xi+\xi^4}\right)^2\left(\frac{\xi^{-1}}{9} + \frac{11\xi^2}{18} + \frac{26\xi^5}{45}\right)\left(\frac{d\xi}{dt}\right)^2\right]$$
$$+ \frac{d}{dt}\left[\frac{1}{3}\left(\xi^{-1} + 2\xi^2 - (\xi^{-1} - \xi^2)\cos\theta_e\right)\right] + \frac{\Lambda}{18}Oh\left[\frac{(\xi^3-1)^2(1+2\xi^3)^2}{\xi^4(2+\xi^3)^2}\right]\left[\frac{d\xi}{dt}\right]^2 = 0 \quad [83]$$

where:

$$\Lambda = \sqrt{\pi}Oh^{-1/2} \quad [84]$$

The initial conditions are:

$$\xi\big|_{t=0} = 1$$
$$\left.\frac{d\xi}{dt}\right|_{t=0} = -\sqrt{We} \quad [85]$$

Attané et al.[48] observe that the expression for Λ in Equation [83] was originally incorrectly derived due to a sign error in Equation [79] and propose a more accurate empirical expression given by:

$$\Lambda = 23Oh^{-1/2} \quad [86]$$

Figure [118] compares experimental values of ξ_m with those predicted by Equation [83] using the modified expression for Λ (Equation 86). Figure [119] highlights

the improved agreement between measured and predicted ξ_m for the empirically modified Λ term (Equation 86) in comparison with the original term (Equation 84). Whereas predictions using the original empirical term disagree with experimental measurements by up to ± 72%, this decreases to ± 28% for the modified empirical term. Due to the large errors associated with water drop (Oh = 0.00195) lamella thickness measurements, no comparisons were made with the prediction model.

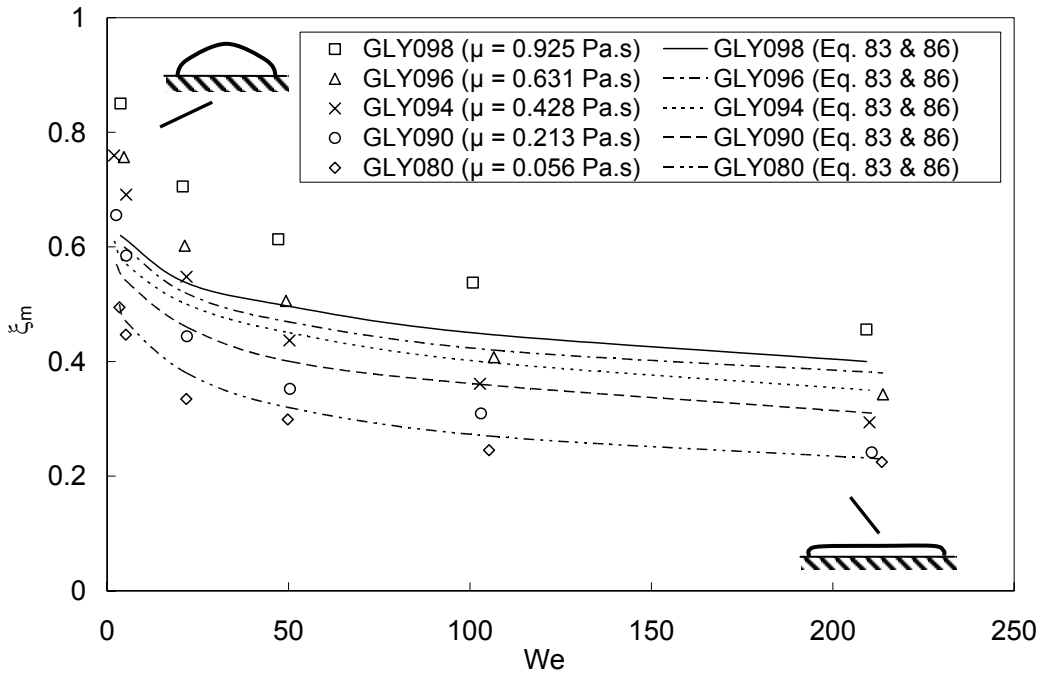

Figure 118. Comparison of measured ξ_m with predictions using the Bechtel et al. model (Equation 83) with the empirically modified Λ term (Equation 86) in the range $0.11 \leq Oh \leq 1.78$ and $1.9 \leq We \leq 214$.

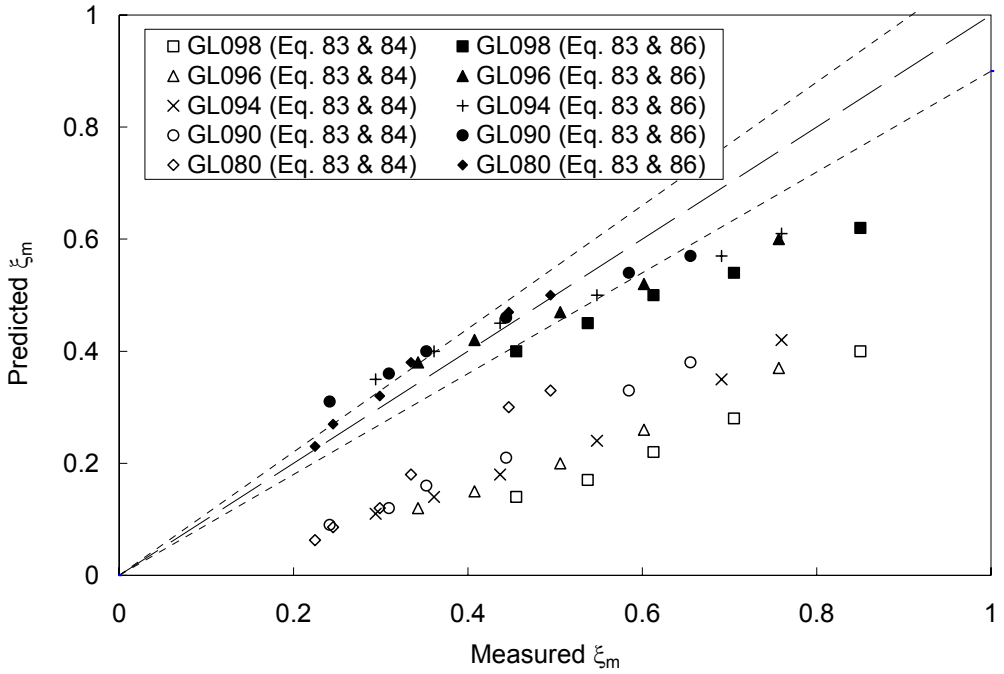

Figure 119. Comparison of measured with predicted ξ_m using Eq, [83] with (i) the original Λ term, Equation [84] (open symbols) and (ii) the empirically modified Λ term, Equation [86] (filled symbols). Short dashed lines correspond to a ± 10% variation.

The predictive capability of this model using the empirically modified Λ term improves with decreasing Oh over the range $0.11 \leq Oh \leq 1.78$. Whereas predictions agree with measured values of ξ_m to within ± 27% for Oh = 1.78, this decreases to ± 14% for Oh = 0.11. This trend initially seems counterintuitive; drop shapes upon inertial impact appear less like the spherical cap approximation for lower Ohnesorge numbers and more cylindrical in shape. The trend is due however to the empirically modified Λ term being optimised for low Oh numbers.

5.2.2.2.2 Chandra and Avedisian.

Whilst this model has been reviewed previously[51, 74], it is included here to provide a baseline comparison from which improvements in more contemporary energy balance prediction models can be highlighted.

The energy balance approach used by Chandra and Avedisian[42] equates the kinetic and surface tension energies of the drop at the moment of impact to the kinetic,

surface tension and viscous dissipation energies at the point of maximum inertial spread. Using a cylindrical approximation for the drop shape at the end of inertial expansion, the resultant expression is:

$$\frac{3}{2}\frac{We}{\mathrm{Re}}\beta_m^4 + (1-\cos\theta_a)\beta_m^2 - (\frac{1}{3}We + 4) \approx 0 \qquad [87]$$

The work done, W, in deforming the drop against viscosity was established as:

$$W = \int_0^{t_c}\int_V \phi dV dt \approx \phi V t_c = \frac{1}{4}\pi\mu\left(\frac{u_z}{h}\right)D_E D_{Max}^2 \qquad [88]$$

where the dissipation function is:

$$\phi = \mu\left(\frac{v_z}{h}\right)^2 \qquad [89]$$

and h is the lamella height.

Figure [120] compares predictions of β_m with experimental results over the range $1.9 \leq We \leq 214$. For low viscosity fluids ($\mu = 0.001$ Pas, corresponding to $Oh = 0.0019$), the model significantly overpredicts β_m by up to 29%. The opposite is true however for fluids with $\mu \geq 0.056$ ($0.11 \leq Oh \leq 1.78$), where the model underpredicts experimental results by up to 29%; the greatest deviation occurring at the highest Ohnesorge numbers. Moreover, the greatest deviations occur in each case for predictions at higher Weber numbers.

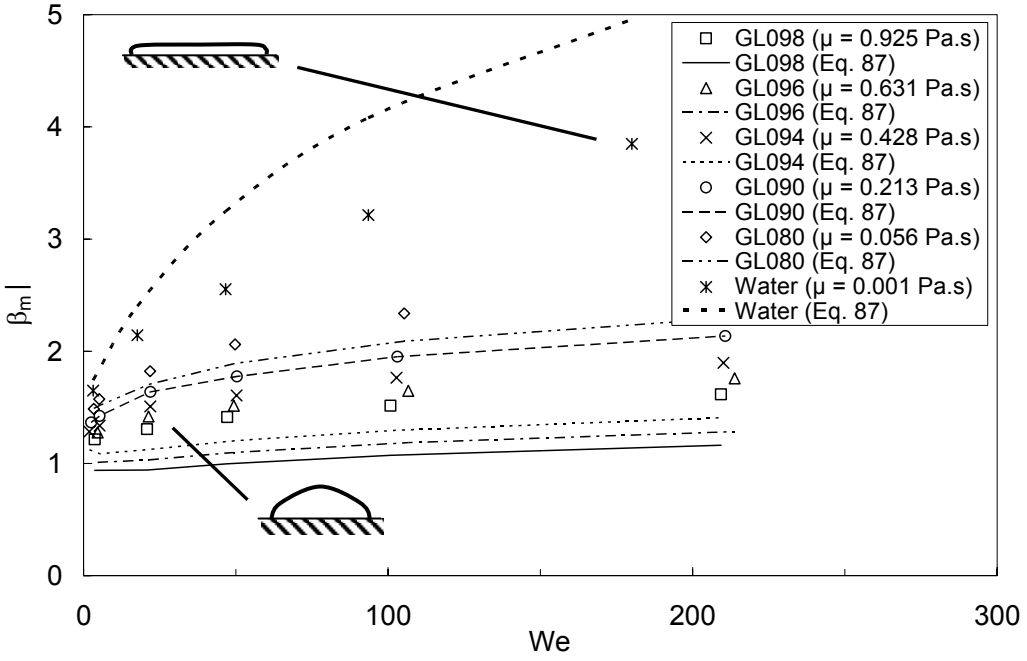

Figure 120. Comparison of measured β_m with predictions using Equation [87] in the range $0.0019 \leq Oh \leq 1.78$ and $1.9 \leq We \leq 214$.

5.2.2.2.3 Pasandideh-Fard et al.

Pasandideh-Fard et al.[43] recognised that the results of Chandra and Avedisian overestimated β_m by up to 40% for low viscosity fluids and instead of using the lamella height h as the length scale associated with the viscous dissipation term, proposed it instead to be the boundary layer thickness, δ, determined from the analytical solution of an axisymmetric stagnation point flow. The expression for β_m using this approach is given by:

$$\beta_m = \sqrt{\frac{We + 12}{3(1 - \cos\theta_a) + 4(We/\sqrt{\mathrm{Re}})}} \qquad [90]$$

In the published paper, predictions using Equation [90] were compared with experimental results from their own measurements as well as those by Ford and Furmidge[53], Madjeski[79], Fukanuma and Ohmori[54] and Bhola and Chandra[81] for drop impacts with $26 \leq We \leq 641$, $213 \leq Re \leq 35339$, $0.000573 \leq Oh \leq 0.0239$ and $20 \leq \theta_a \leq 140^o$. The agreement between measured and predicted results was less than ± 15% in most cases with the largest deviation of ± 21% occurring at the largest Oh.

Figure [121] compares predictions using Equation [90] with measured values of β_m from the present investigation. Whilst the model agrees to within ± 6% over $3 \leq We \leq 180$ for low viscosity fluids (μ = 0.001 Pas, Oh = 0.0019), predictions worsen significantly for higher viscosities ($Oh \geq 0.109$) and disagree with experimental results by up to ± 47% over the range $1.8 \leq We \leq 213$. This is due to the incorrect estimation of the boundary-layer thickness. For $We \leq 50$, predictions even show decreases in β_m with increases in We. These observations confirm a previous comparison[47] showing that Equation [90] significantly underpredicts the maximum spread of viscous liquids.

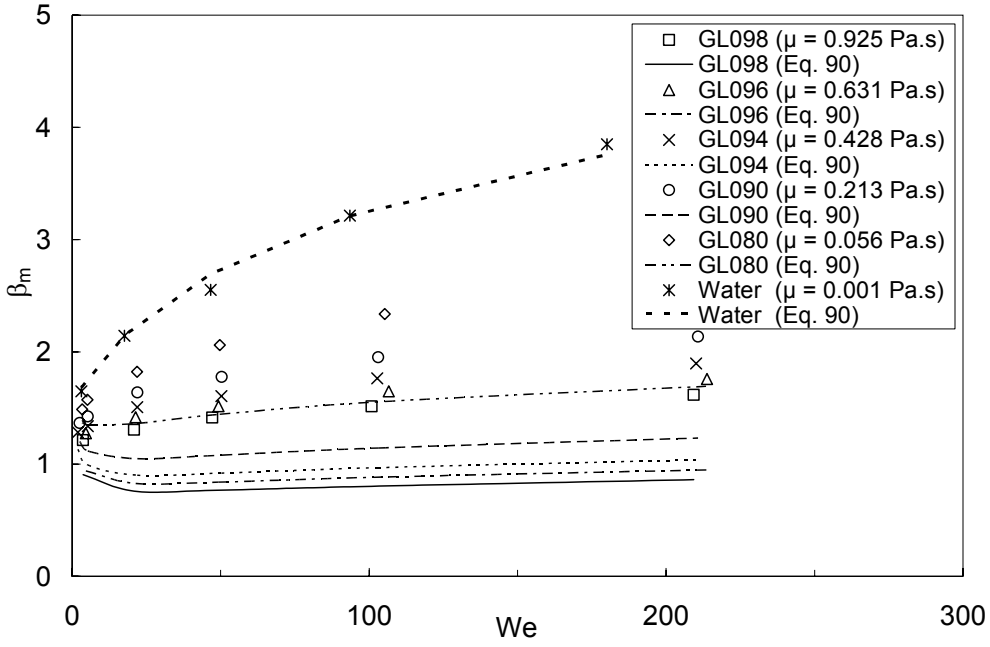

Figure 121. Comparison of measured β_m with predictions using Equation [90] in the range $0.0019 \leq Oh \leq 1.78$ and $1.9 \leq We \leq 214$.

5.2.2.2.4 Mao et al.

Mao et al.[47] developed their model in a number of ways from the Chandra and Avedisian original. Firstly, surface tension estimations at maximum spread were derived as a function of the static contact angle instead of the advancing contact angle (Equation 22) since it is uniquely related to the surface energies. Secondly, whilst the boundary layer thickness δ was calculated using an analytical solution to the stagnation point flow, they recognised that for highly viscous fluids, δ was larger than the flattened drop height

h. The flow regime when $\delta < h$ would therefore be different to when $\delta > h$ and were considered separately. Viscous dissipation models were developed for each regime and jointly used to develop a general maximum spread model, given by:

$$\left[\frac{1}{4}(1-\cos\theta_e)+0.2\frac{We^{0.83}}{\mathrm{Re}^{0.33}}\right]\beta_m^3-\left(\frac{We}{12}+1\right)\beta_m+\frac{2}{3}=0 \qquad [91]$$

Mao et al. compared predictions using this semi-empirical model with their own experimental measurements and those from Cheng[52], Scheller[60], Ford and Furmidge[53], Asai et al.[64] and Fukai et al.[63]. A good agreement was found to within ± 10% for a wide range of impact velocities ($1 \leq v_z \leq 6$ m/s), static contact angle ($30 \leq \theta_e \leq 120^o$) and droplet sizes ($1.5 \leq D_E \leq 3.5$ mm), however the range of viscosities was limited to relatively low viscosity fluids ($\mu \leq 0.1$ Pas). Comparisons of the proposed model were also made with previous empirical (Asai et al.; Scheller and Bousfield[45]) and semi-empirical models (Chandra and Avedisan[42]; Pasandideh-Fard et al.[43]), and found to agree more closely with experimental measurements.

Figure [122] shows the predictive capability of Equation [91] to be best for low viscosity (Oh = 0.0019) fluids over $3 \leq We \leq 180$. Predictions agree to within ± 9 % of the experimental results. The model underpredicts β_m at higher viscosities ($Oh \geq 0.11$) however, by up to ± 33% over $1.9 \leq We \leq 214$. Predictions decrease in accuracy for impact velocities less than 1 m/s since for impacts with lower inertial energy, surface tension plays an increasingly greater role on the spreading dynamics and the flat disk assumption and stagnation point flow analogies cannot be assumed to be appropriate.

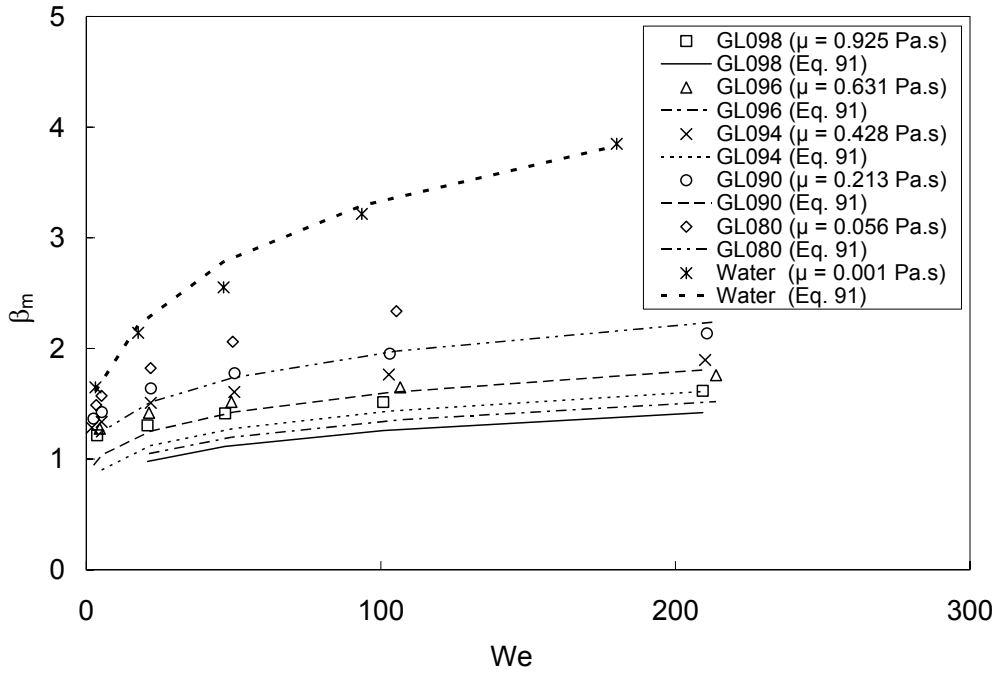

Figure 122. Comparison of measured β_m with predictions using Equation [91] in the range $0.0019 \leq Oh \leq 1.78$ and $1.9 \leq We \leq 214$.

5.2.2.2.5 Attané et al.

The model proposed by Attané et al.[48], henceforth denoted as the AGM model is currently one of the most contemporary energy balance approach models. This model focuses primarily on providing more accurate predictions of low Oh fluids at high impact velocities. Model developments include incorporating shear flow descriptions from Madjeski[79] and the rimmed disk model developed by Roisman et al.[46].

Typically, for low Oh fluids (Oh ~O[10^{-3}]) impacting with We > 200, toroidal rims are observed that are thicker than the more central liquid. The authors highlight that a cylindrical approximation is no longer sufficiently descriptive. To account for this, the AGM model replaces the standard cylindrical shape approximation with that of a rimmed disk, where the rim is of typical dimension L x αL with volume $2\pi\alpha RL^2$ and α is an adjustable parameter function of the fluid viscosity that takes into account the differences observed between fluids drops of different viscosities. The model is not expected to hold for L << h and L >> h, where h is the lamella height. The L << h case is representative of

when drops adopt a spherical cap shape upon deformation and not a cylindrical disk. With regard to the present investigation, this is the most significant limitation of the AGM model. The use of an approximation more closely resembling a cylindrical lamella instead of a spherical cap is justified by the assumptions that the description of the dissipation at the very beginning of the impact is less important than a correct description of the dissipation for spread factors over 1 and that a cylindrical shape provides a good general representation of the deformed drop shape for a majority of impacts over a large range of We. The focus of the present study however includes the drop impact behaviour of fluids with Oh >> 10^{-3}, where cylindrical and rimmed-cylindrical assumptions do not adequately represent the deformed drop shape. The AGM model is not expected to provide accurate predictions for high Oh fluids impacting at low We.

The other significant development of this semi-empirical model was the inclusion of a term into the dissipative work that accounts for additional dissipation arising from rolling fluid motion near the contact line; a characteristic necessary for the triple line to advance[125]. This term is specifically aimed at low viscosity fluid drops with $\beta_m > 3$

Attané et al. review the derivations of a number of existing 1D energy balance approach prediction models and compare the proposed AGM model predictions with an extensive selection of literature data (Mao et al.[47], Kim and Chun[55], Clanet et al.[44] Scheller and Bousfield[45] and Rioboo et al.[58]) encompassing a diverse range of drop impact dynamics over approximately $0.002 \leq Oh \leq 0.585$, $6 \leq We \leq 1100$ and $5 \leq \theta_e \leq 100^o$.

The AGM model differential equation is given by:

$$\frac{1}{12}\frac{d}{dt}\left\{\left[\frac{2}{3}+\frac{1}{45}\frac{1}{r^6}\right]\left(\frac{dr}{dt}\right)^2\right\}+\frac{d}{dt}\left[r^2(1-\cos\theta_e)+\frac{1}{3r}\right] + 4Oh\left[3r^4+\frac{2}{3r^2}+sr\right]\left(\frac{dr}{dt}\right)^2=0, \quad [92]$$

with the initial conditions:

$$1 = \left[r_0^2 \left(1 - \cos\theta_e\right) + \frac{1}{3r} \right] \quad [93]$$

$$\left.\frac{dr}{dt}\right|_0 = \sqrt{We}\left[\frac{2}{3} + \frac{1}{45}\frac{1}{r_0^6} \right]^{-1/2} \quad [94]$$

where $r = \beta_m/2$ and r_0 is the initial spread factor. The first initial condition is derived from the approximation that the drops assumes a cylindrical shape upon deformation but the initial value of the surface energy (derived using the surface area of a cylinder) must equal that of the surface energy of a spherical drop. Attané et al. also highlight that Equation [93] has no real positive root of r_0 for $\theta_e > 109.4^o$, however using a value of $r_0 = 0.39$ provides an evaluation of the initial surface energy to within 16% irrespective of θ_e. The term s in Equation [92] is an adjustable parameter defined as:

$$s = 1.41 Oh^{-2/3} \quad [95]$$

and constitutes the only empirical term.

Predictions of β_m for the AGM model were determined by solving the differential equation (Equation 92) with initial conditions given by Equations [93] and [94]. Whereas explicit solutions for β_m exist for impacts where a retraction phase exists, predictions of β_m for impacts where spreading continues after a maximum inertial expansion spread factor is reached are ambiguous and were taken as the midpoint between the fast inertial spreading rate and the slower rate corresponding to capillary driven spreading.

Figure [123] compares AGM model predictions of β_m with experimental results for $0.0019 \leq Oh \leq 1.78$ within the range $1.9 \leq We \leq 214$. Whilst predictions of β_m for liquid drops with a low viscosity (μ = 0.001 Pas, Oh = 0.0019) agree closely with experimental results to within ± 9%, predictions worsen for more viscous fluids with $\mu \geq$ 0.056 Pas (corresponding to $Oh \geq 0.11$) and can disagree with experimental measurements by up to ± 34%.

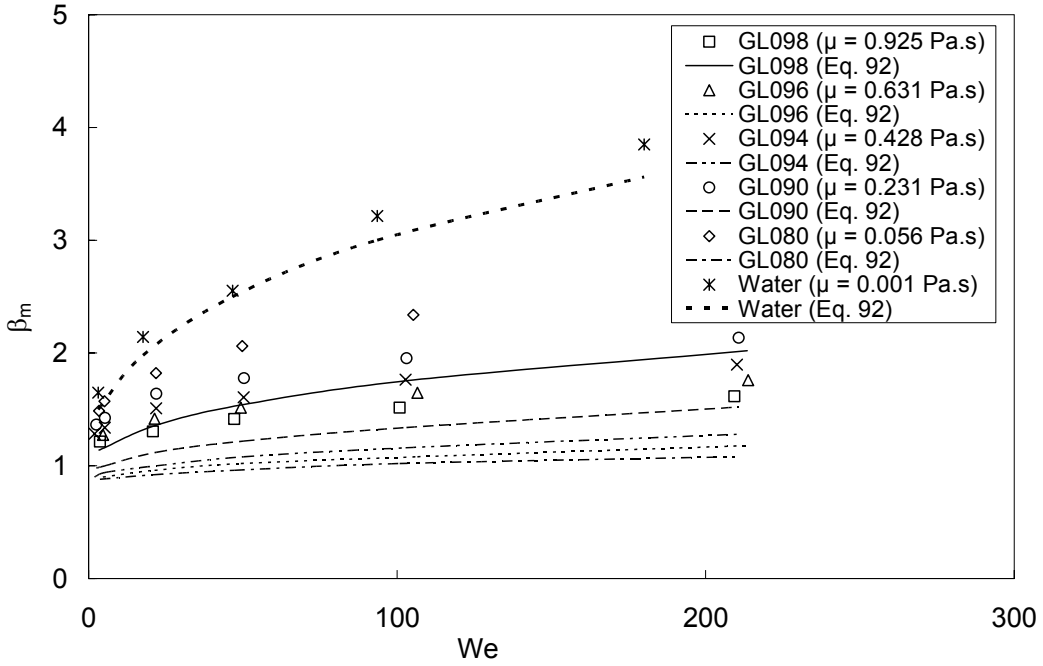

Figure 123. Comparison of experimental β_m with predictions using Equation [92] in the range $0.0019 \leq Oh \leq 1.78$ and $1.9 \leq We \leq 214$.

5.2.2.3 Summary of models.

Tables [12] and [13] summarise the characteristics and predictive capabilities of each model for fluids with $0.00195 \leq Oh \leq 1.78$ impacting within the range $1.9 \leq We \leq 214$ and $1 \leq Re \leq 6889$. Table [13] highlights the model publication date, approach taken during the derivation of the model, drop shape approximation used for the energy balance approach models when deriving the surface tension energy at the end of inertial expansion, the predicted parameter, the model format and the solution type; where T, E and SE corresponds to theoretical, empirical and semi-empirical respectively. Table [13] summarises the predictive capability of each model by quantifying the maximum percentage deviation of predictions away from equivalent experimental measurements; the values in bold correspond to the best model predictive capability for the specified Ohnesorge number.

Table 12. – Summary of prediction models. Abbreviations E, SE and T represent empirical, semi-empirical and theoretical solution types respectively.

Model	Model approach	Drop shape approximation	Model Derivation	Model format	Prediction parameter
Bejan and Gobin (2006)	scaling law	-	T	algebraic	β_m
Clanet et al. - Attané et al. (2007)	scaling law	-	E	algebraic	β_m
Chandra and Avedisian (1991)	scaling law	-	T	algebraic	β_m
Bechtel et al. (1981)	Energy balance	Spherical cap	SE	differential	ξ_m
Chandra and Avedisian (1991)	Energy balance	cylindrical	SE	algebraic	β_m
Pasandideh-Fard et al. (1996)	Energy balance	cylindrical	SE	algebraic	β_m
Mao et al. (1997)	energy balance	cylindrical	SE	algebraic	β_m
Attané et al. (2007)	energy balance	cylindrical	SE	differential	β_m
Modified Mao et al. (2008)	energy balance	cylindrical	SE	algebraic	β_m
Kurabayashi - Yang with Healy et al. modification (2000)	energy balance	cylindrical	SE	algebraic	β_m

Table 13. Model predictive capabilities upon comparison with experimental results for fluid drops with $0.056 \leq \mu \leq 0.925$ Pas impacting with $1.9 \leq We \leq 214$. Values in bold type constitute the best predictive capability of all the models assessed.

Model	Maximum % variation between predicted and experimental in range $1.8 \leq We \leq 213$					
	Oh					
	0.00195	0.109	0.403	0.8	1.167	1.718
Bejan and Gobin (2006)	4539	779	456	341	294	250
Clanet et al. – Attané et al. (2007	38	17	15	27	37	48
Chandra and Avedisian (1991)	136	18	4.5	13	12	16
Bechtel et al. (1981)	-	14	28	20	21	27
Chandra and Avedisian (1991)	29	13	22	27	28	29
Pasandideh-Fard et al. (1996)	6	36	42	45	46	47
Mao et al. (1997)	9	21	31	33	26	25
Attané et al. (2007)	9	26	32	34	34	33
Modified Mao et al. (2008)	17	**6**	**2**	**2**	**2**	**5**
Kurabayashi - Yang with Healy et al. modification (2000)	22	19	21	20	18	16

5.2.2.4 Empirical adjustments for low Weber numbers and high viscosities.

5.2.2.4.1 Kurabayashi-Yang Model.

Empirical modifications to existing prediction models have previously been proposed. In order to improve model predictive capabilities for impacts with We ≤ 150, an empirical correction was made by Healy et al.[74] to the semi-empirical prediction model initially proposed by Kurabayashi[56] and later modified by Yang[76]:

$$\frac{We}{2} = \frac{3}{2}\beta_m^2\left[1 + \frac{3We}{\mathrm{Re}}\left(\beta_m^2 \ln \beta_m - \frac{\beta_m^2 - 1}{2}\right)\left(\frac{\mu}{\mu_{wall}}\right)^{0.14}\right] - 6 \qquad [96]$$

μ_{drop} is the fluid viscosity evaluated at the initial drop temperature and μ_{wall} is the fluid viscosity evaluated at the substrate temperature. The purely empirical modification:

$$\beta_{m,corr} = \beta_m\left(\frac{45}{\theta_e}\right)^{0.241} \qquad [97]$$

was derived to account purely for surface wettability effects (the original Kurabayashi-Yang model does not take into account contact angle), where $\beta_{m,corr}$ is the corrected spread factor, β_m is the spread factor derived using Equation [96] and θ_e is the sessile contact angle of the drop. Healy et al. chose this model to modify after comparing it against those proposed by Chandra and Avedisian[42], Madjeski[79], Shi and Chen[59], Bechtel et al.[49] and Naber[78] and finding predictions to agree most closely with the experimental results. The correction was established for impacts with 25 ≤ We ≤ 150 and 1000 ≤ Re ≤ 7500 for fluids with 30 ≤ θ_e ≤ 90^o and 0.000386 ≤ μ ≤ 0.001 Pas. Healy et al. found the modification improved predictive capability for low viscosity fluid impacts at low We from greater than ± 20% to within approximately ± 10% when compared with a selection of experimental results including Chandra and Avedisian, Ford and Furmidge[53] and Fukai et al.[63].

Figure [124] plots the predicted results from Equation [96] (where μ and μ_{wall} are assumed to be identical) incorporating the correction from Equation [97] (with $\theta_e = 90^o$, the close to the measured value of $\theta_e = 95^o$) against experimental results from the current investigation for impacts with We ≤ 150. Over the range 0.0019 ≤ Oh ≤ 1.78, predictions agree with experiment to within ± 20%, however this significantly improves to within ± 10% for We ≤ 25.

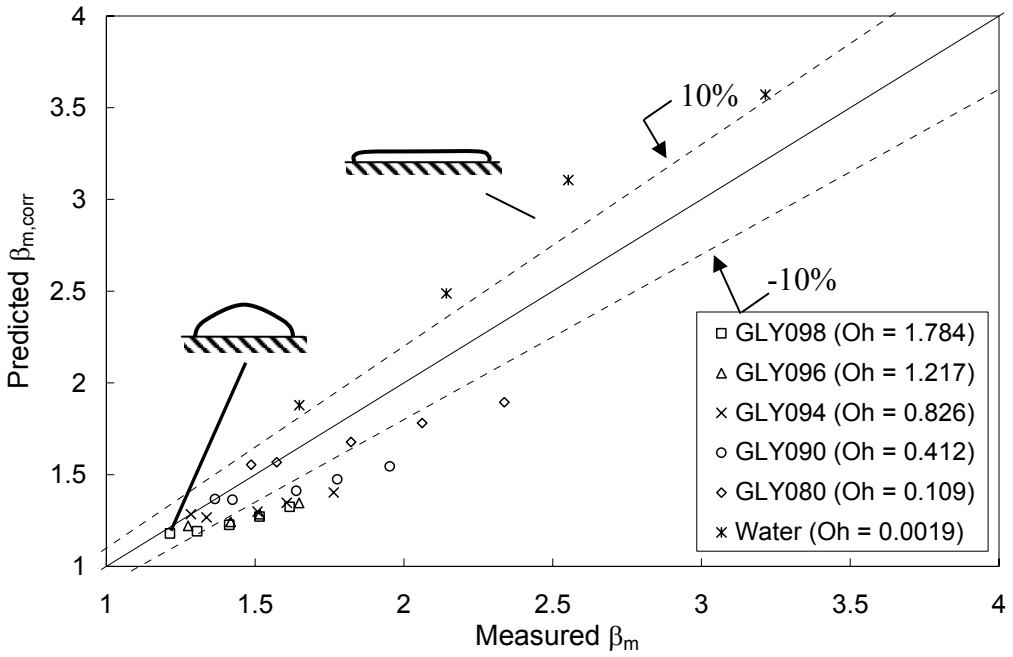

Figure 124. Comparison of predicted β_m against experimental results for Equation [96] using the empirical correction of Equation [97].

The combined prediction model with empirical modification has a number of limitations. Firstly, the correction factor given by Equation [97] varies by up to 30% in the range $30 \leq \theta \leq 90^o$ for fluids with Oh ≥ 0.109 and cannot be used at all when the fluid is completely wetting ($\theta_e = 0^o$). This variation is not observed in equivalent experimental results where values of β_m are observed not to vary significantly with surface wettability (**§5.1.1**). Secondly, the empirical power term has been derived for low viscosity fluids with $\mu \leq 0.001$ Pas, therefore is unlikely to accurately predict β_m for more viscous fluids. In contrast, the more contemporary energy balance approach models of Attané et al. and Mao et al. account for drop contact angle within their formulation. Whilst the Healy-Kurabayashi-Yang model does provide more accurate predictions over these two models for We ≤ 25 and equivalent predictions for 25 ≤ We ≤ 200, the previously cited

limitations are sufficient enough to warrant the examination of empirical modifications to the other models in order to establish a more generalised prediction method with an improved predictive capability for low Weber number impacts across a wide range of fluid viscosities. Empirical modifications were therefore chosen to be made to the model that provided the best predictive capability for We ≤ 200.

5.2.2.4.2 Modified Mao et al. model.

In comparison with the model proposed by Mao et al., the AGM model has been shown[48] to provide more accurate predictions of β_m for Oh ≤ 0.035 within the range 10 ≤ We ≤ 1100 and Oh ≤ 0.535 in the range 100 ≤ We ≤ 1000. These models are further compared in Fig [125]. For fluids with Oh ≥ 0.109 impacting in the range 1.9 ≤ We ≤ 214, both models underpredict β_m with differences exceeding ± 10%. Within this range however, the Mao et al. model predictions agree more closely with the experimental results: the differences in predictive capability becoming more evident with increasing Oh. Whilst both models are semi-empirical and have the potential for modification to improve predictions at low We and high Oh by adaptation of the empirical parameters; based on this comparison the Mao et al. model was chosen to be modified.

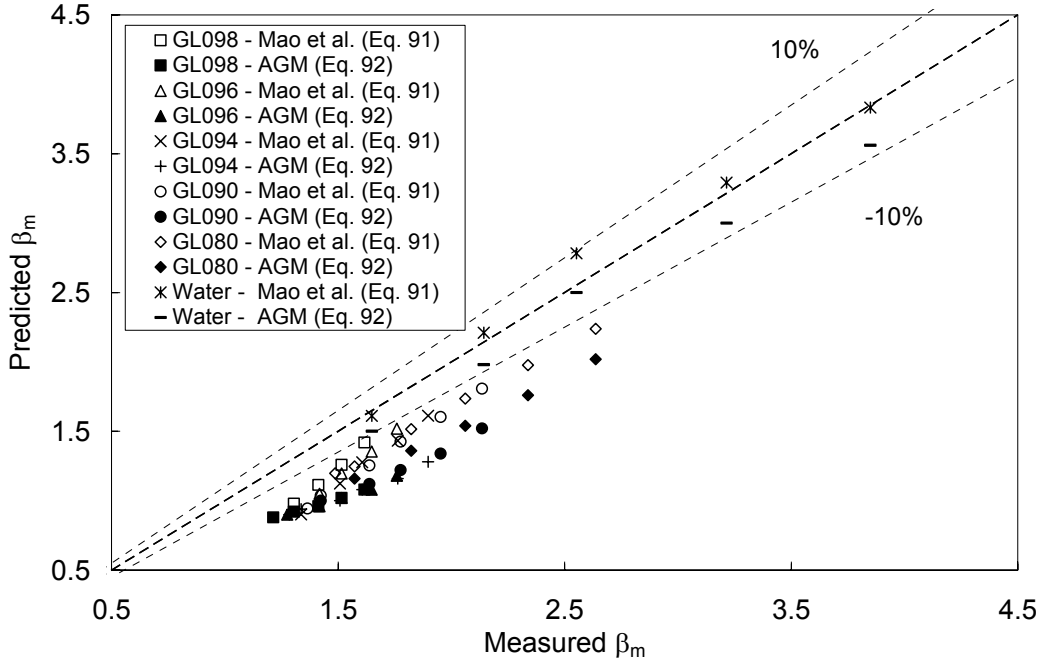

Figure 125. Comparison of predicted β_m against experimental results for (i) the AGM model (Equation 92, filled symbols) and (ii) the Mao et al. model (Equation 91, open symbols).

Adjustments to the Mao et al. model (Equation 91) were made through an iterative process of optimising the empirically based powers of We and Re and the empirical constant term (2^{nd} term in the cubic polynomial) by minimising differences between predicted and experimental β_m for each Newtonian solution over the range $1.9 < We < 214$.

Small variations in the Reynolds number power term were found to result in minor improvements, the optimised value varying as a function of Oh. More significant improvements were obtained however by varying the empirical constant, with the optimal value varying as a function of We. Changing the Weber number power term was found not to improve predictions. These modifications result in a revised model of the form:

$$\left[\frac{1}{4}(1-\cos\theta)+\psi\frac{We^{0.83}}{\mathrm{Re}^{\kappa}}\right]\beta_m^3-\left(\frac{We}{12}+1\right)\beta_m+\frac{2}{3}=0\,, \qquad [98]$$

where $\kappa = 0.45\mathrm{Oh}^{0.05}$ replaces the analogous exponent $\kappa = 0.33$ in Equation [91], and $\psi = 0.07\mathrm{We}^{0.2}$ replaces a constant empirical coefficient. The Reynolds number power term

remains nearly identical to the original model for low viscosities, however for more viscous fluids the power term increases, representative of the increased importance of viscous effects during drop impact. The replacement for the empirical constant term varies in the range $0.083 \leq \psi \leq 0.213$ for $1.9 \leq We \leq 214$ and remains close to the original value of 0.2 for $We > 100$.

Figure [126] compares predictions of β_m from both the original Mao et al. model (Equation 91) and the empirically adjusted model Equation [98]. The modifications result in improved predictions for fluids drop impacts over $1.9 \leq We \leq 214$ and $0.11 \leq Oh \leq 1.78$; consistently agreeing with experimental results to within ±10%. This predictive capability reduces however for low fluid viscosities, where for $Oh = 0.00195$, predictions exceed 10% and the original model is more accurate.

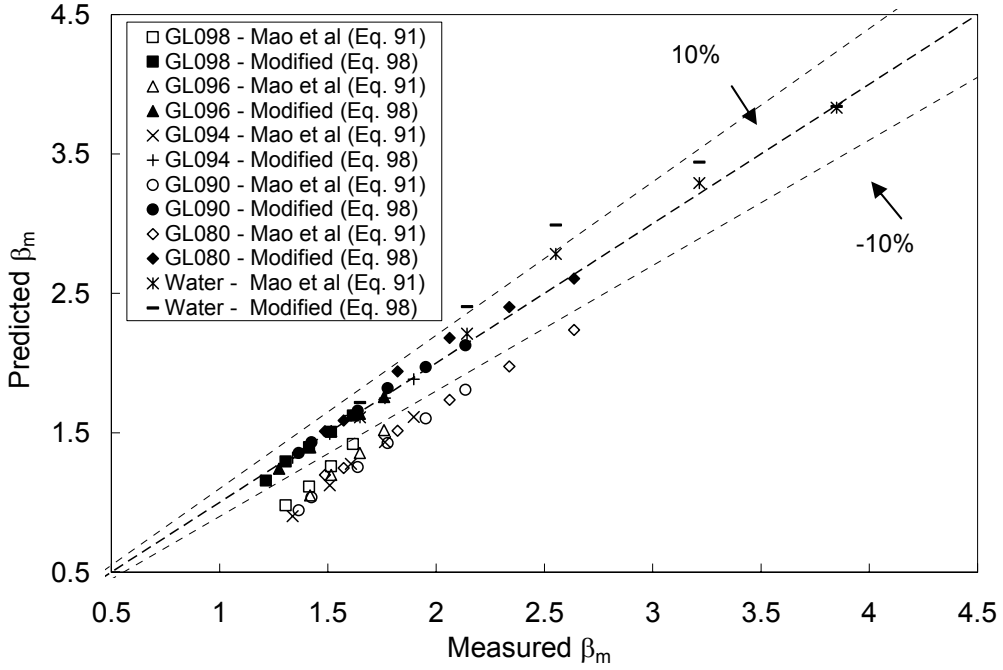

Figure 126. Comparison of predicted β_m against experimental results for the original (Equation 91) (open symbols) and modified (Equation 98) (filled symbols) Mao et al. models.

In comparison with the Healy-Kurabayashi-Yang model, the influence of surface wettability on β_m for fluids with $0.109 \leq Oh \leq 1.718$ is significantly reduced in the modified Mao et al. model; variations of less than 15% are predicted for changes in equilibrium contact angle over $30 \leq \theta \leq 99^o$. Overall, the modifications significantly

improve predictions for low We, high Oh drop impacts, where the original model underpredicts β_m by up to ±33%.

5.3 Shear-thinning drop impact behaviour

Figures [127] and [128] display temporal variations in β and ξ for drops of the X0125 (n = 0.4 K = 0.208 Pas^n) and X075 (n = 0.084 K = 5.064 Pa^ns) shear-thinning fluids during impact on a hydrophobic surface. These fluids respectively exhibit the least and most shear-thinning fluid characteristics.

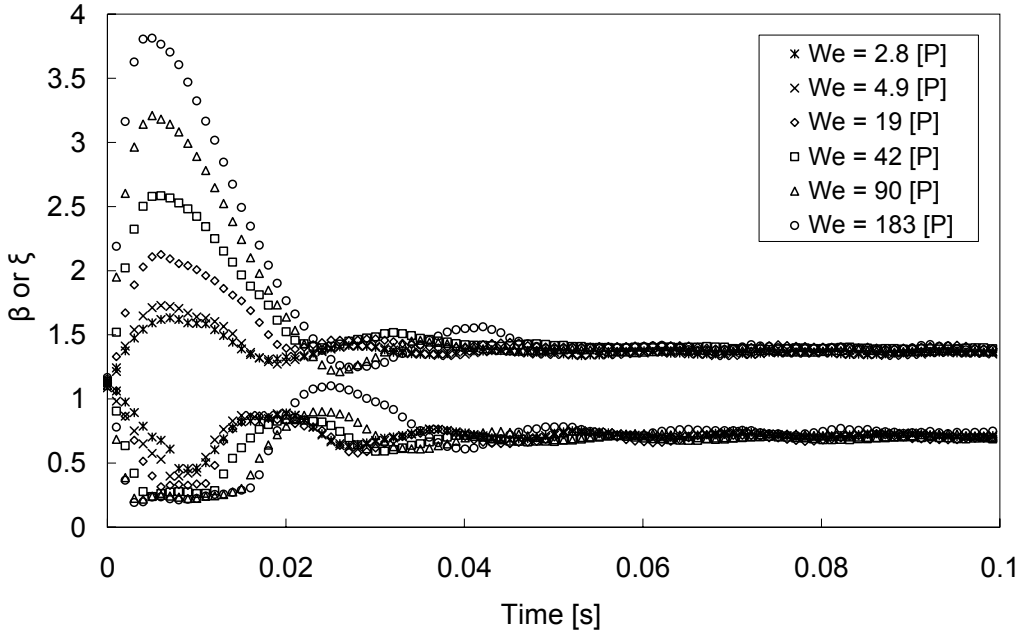

Figure 127. Temporal variations in dimensionless inertial spread factor β and height factor ξ for shear-thinning X0125 fluid drops (D_E = 3.47 mm, n = 0.400 , K = 0.208 Pas^n) impacting on a parafilm-M substrate from fall heights of 7.5 mm ≤ H_F ≤ 200 mm (corresponding to 2.8 ≤ We ≤ 183). Each set of results corresponds to an average of five drop impacts. To aid visual clarity, experimental errors are not shown, however they are comparable with symbol size.

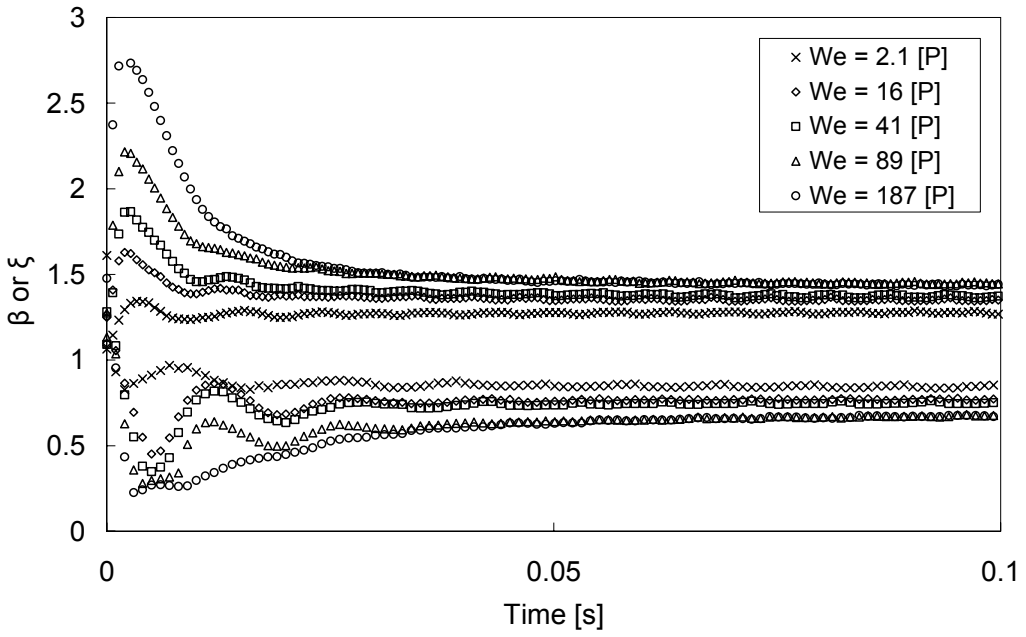

Figure 128. Temporal variations in dimensionless inertial spread factor β and height factor ξ for shear-thinning X075 fluid drops (D_E = 3.34 , n = 0.084 , K = 5.064 Pas^n) impacting on a parafilm-M substrate from fall heights of 7.5 mm ≤ H_f ≤ 200 mm (corresponding to 2.1 ≤ We ≤ 187). Each set of results corresponds to an average of five drop impacts. To aid visual clarity, experimental errors are not shown, however they are comparable with symbol size.

Increasing We results in increases in β_m and decreases in ξ_m for impacts on a parafilm surface, similar to the behaviour of Newtonian fluids. This is more clearly observed in Figures [95] and [96], which plot β_m and ξ_m against We respectively. Drop impact dynamics on both substrates are very similar during the inertial expansion phase with substrate wettability having previously been established (**§5.1**) not to measurably influence drop impact behaviour during this phase for fluids in the ranges 0.084 ≤ n ≤ 0.4 and 0.208 ≤ K ≤ 5.064 $Pas^{n.}$ across 0.7 ≤ We ≤ 193.

Unlike Newtonian fluids, whose viscometric properties are characterised only by viscosity, shear-thinning fluids are characterised most simply with the consistency coefficient K and power law index n parameters from the power law rheological model (Equation 37). Figures [129] - [131] replot temporal variations of β and ξ for the four shear-thinning fluids for impacts at We = 3.65 ± 1.1 (H_f = 10 mm), We = 43.2 ± 1.4 (H_f = 50 mm) and We = 191.6 ± 2.7 (H_f = 200 mm) on a parafilm substrate to highlight the influence of viscous properties on impact dynamics.

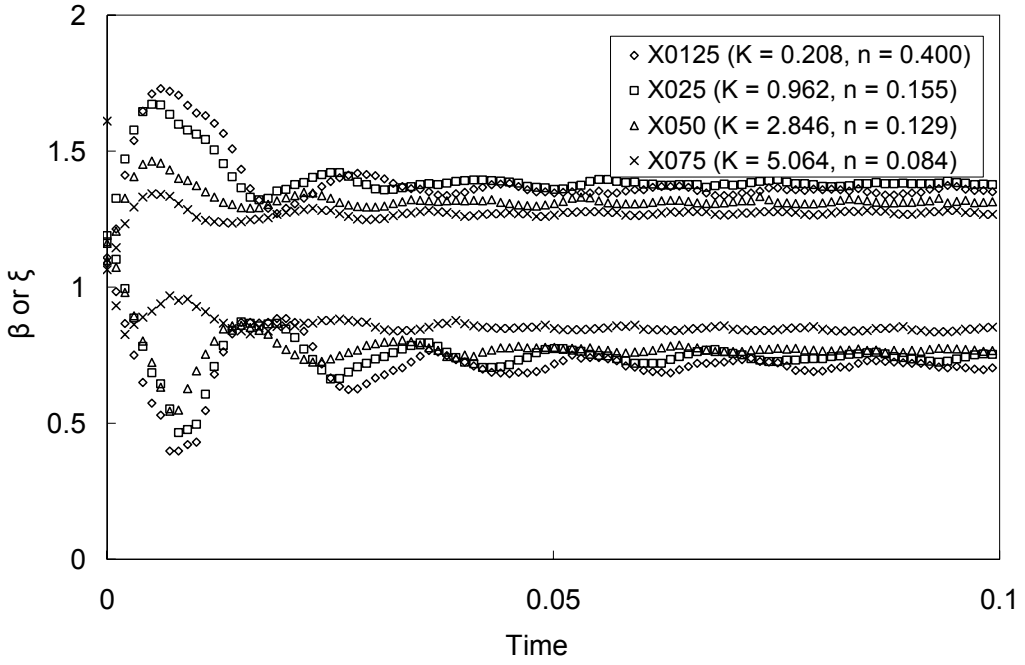

Figure 129. Temporal variations in β and ξ for drops of the four shear-thinning fluids with $0.084 \leq n \leq 0.400$ and $0.208 \leq K \leq 5.064$ Pas^n impacting from $H_f = 10$ mm ($We = 3.65 \pm 1.1$) on a parafilm substrate. Each results set is based on the average of 5 drop measurements. To aid visual clarity, experimental errors are not shown, however they are comparable with symbol size.

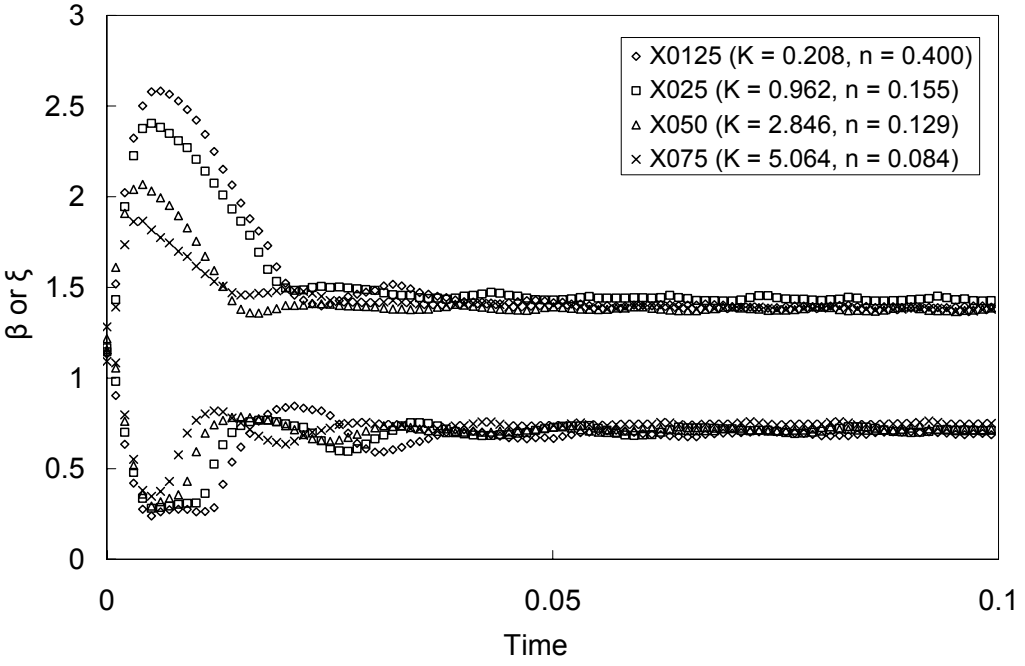

Figure 130. Temporal variations in β and ξ for drops of the four shear-thinning fluids ($0.084 \leq n \leq 0.400$, $0.208 \leq K \leq 5.064$ Pas^n) impacting from $H_f = 50$ mm ($We = 43.2 \pm 1.4$) on a parafilm substrate. Each results set is based on the average of 5 drop measurements. To aid visual clarity, experimental errors are not shown, however they are comparable with symbol size.

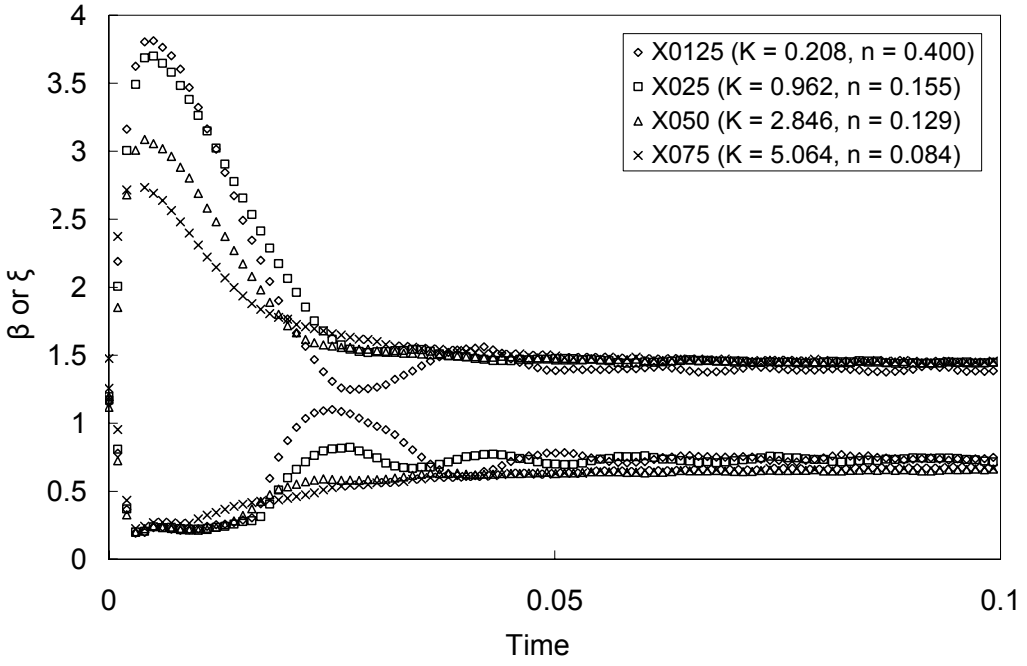

Figure 131. Temporal variations in β and ξ for drops of the four shear-thinning fluids ($0.084 \leq n \leq 0.400$, $0.208 \leq K \leq 5.064$ Pas^n) impacting from $H_f = 200$ mm (We = 191.6 ± 2.7) on a parafilm substrate. Each results set is based on the average of 5 drop measurements. To aid visual clarity, experimental errors are not shown, however they are comparable with symbol size.

Increasing the mass fraction of Xanthan gum decreases β_m, however ξ_m for each fluid remains very similar at each fall height, indicative of thin cylindrical lamella formation where variations in drop height and the variation of height with impact velocity are both small. Increasing the mass fraction increases the consistency coefficient K, however it also decreases the power law index n. In other words, fluids become more shear-thinning with increased mass fraction.

In order to separate the effects of K and n a thought experiment is performed. For two identical fluid drops with equal values of K and differing power law indices subject to equivalent impacts, the fluid exhibiting the greatest degree of shear-thinning (n closest to 0) would be expected to exhibit lower local viscosities during inertial expansion and therefore increased β_m. Figures [129] - [131] show the opposite trend; β_m increases for less shear-thinning fluids. This suggests that whilst shear-thinning effects may influence the impact behaviour, the influence of the consistency coefficient K (whose relationship with β_m and ξ_m is expected to be similar to that of Newtonian viscosity) appears to dominate.

An alternative perspective can be achieved by modelling the viscous characteristics in terms of the Cross model (Equation 38), where C is the Cross time constant, (1-m) is the rate constant and μ_0 and μ_1 are the high and low shear rate finite dynamic viscosities. This model characterises shear-thinning properties using a dynamic viscosity range ($\mu_0 - \mu_1$). During impact, a shear-thinning drop exhibiting axisymmetric spreading (with a central stagnation point) will produce a range of viscosities between μ_o and a minimum μ' where $\mu_1 \leq \mu'$. For high velocity impacts where shear rates are very large, μ' is expected to be similar to μ_1. From Table [14], increasing the mass fraction of Xanthan gum increases the dynamic viscosity range, primarily by increasing μ_0. For two drops subject to equivalent impacts, the higher mass fraction fluid will therefore exhibit larger average viscosities and hence a decrease in β_m in a similar fashion to increasing μ for Newtonian fluids.

Table 14. Cross model parameters for shear-thinning fluids.

Shear-thinning solution	μ_0 [Pas]	μ_1 [Pas]	(1-m)	R^2 fit
X0125	0.597 ± 0.068	0.0048 ± 0.00083	0.23666 ± 0.025	0.99841
X075	14.436 ± 0.417	0.0068 ± 0.00081	0.0648 ± 0.0032	0.99998

The analysis of shear-thinning fluid drops during impact is made increasingly complex because viscosity is not constant and varies as a function of the shear-rate, which itself varies both with radial position in the drop and time. Newtonian prediction models (**§5.2.2**) that characterise impact behaviour using dimensionless numbers such as Re, Oh and Ca cannot therefore be easily modified to predict shear-thinning fluid behaviour without losing their original simplicity and requiring iterative methods to obtain a solution. Moreover, it is not possible to produce fluids with equal consistency coefficients and varying power law indices, therefore like-with-like experimental comparisons to establish the independent effects of shear-thinning on drop impact dynamics cannot be performed. This limits the amount of experimental analyses that can be completed. Qualitatively however, some effects of fluids shear-thinning can be examined.

β_m for each shear-thinning fluid (Figure 95), is typically much larger than those observed for the Newtonian fluids (Figure 90). The consistency coefficient K provides an

indication of the maximum fluid viscosity that each shear-thinning fluid exhibits; this ranges between $0.208 \leq K \leq 5.064$ Pas^n. The X075 ($K = 5.064$ Pas^n) fluid can thus exhibit much larger viscosities than the most viscous GLY098 Newtonian fluid ($\mu = 0.925$ Pas), however values of β_m at similar We are similar in magnitude to the least viscous GLY080 ($\mu = 0.056$ Pas) Newtonian fluid. This suggests that fluid shear-thinning has an effect on impact behaviour. For high velocity impacts where shear-rates are large, shear-thinning has the effect of increasing the maximum spread factor considerably.

Drop retraction characteristics on hydrophobic substrates can also be examined using a similar method to that used for the Newtonian fluids. Figures [132] and [133] display temporal variations in β normalised by β_m for drop impacts of the X0125 and X075 fluids in the range $16 \leq We \leq 187$. The retraction phase for impacts with $We > 20$ collapse on to a single curve for periods up to 10 ms after the end of inertial expansion.

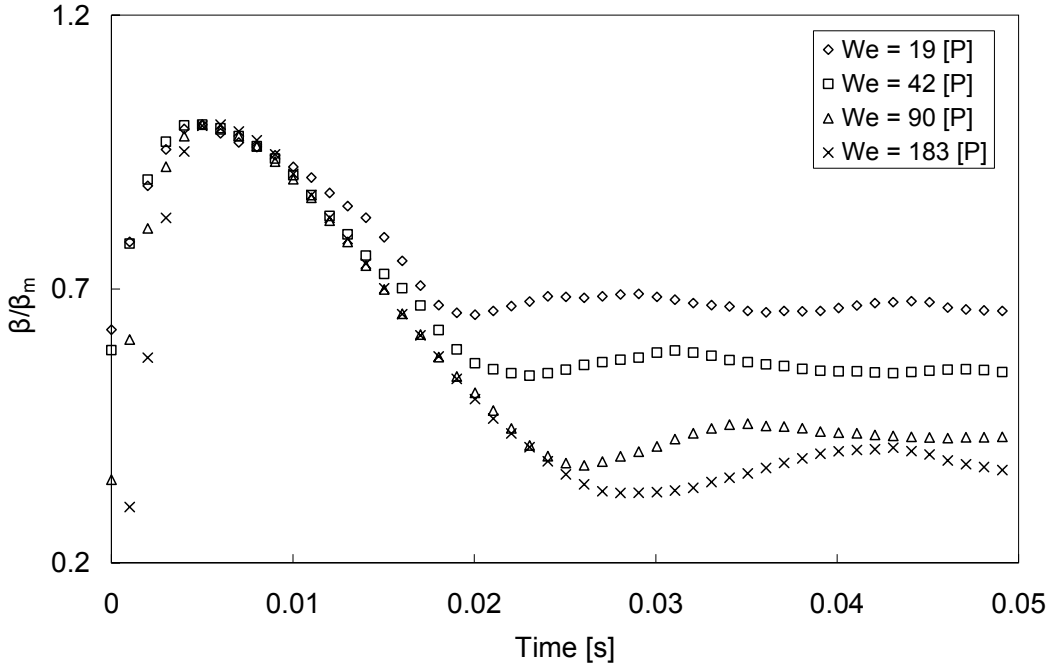

Figure 132. Temporal variations in β/β_m for X0125 fluid drops impacting in the range $19 \leq We \leq 183$ on a parafilm surface. Each results set is based on the average of 5 drop measurements. To aid visual clarity, experimental errors are not shown, however they are comparable with symbol size.

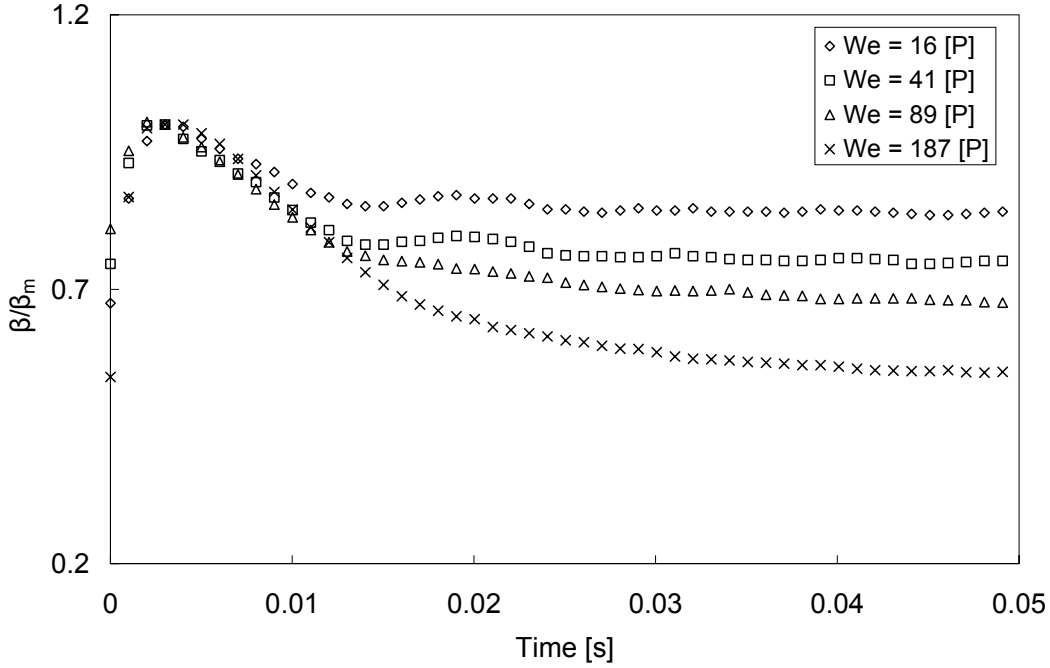

Figure 133. Temporal variations in β/β_m for X075 fluid drops impacting in the range $16 \leq We \leq 187$ on a parafilm surface. Each results set is based on the average of 5 drop measurements. To aid visual clarity, experimental errors are not shown, however they are comparable with symbol size.

Figures [134] – [136] display the maximum measured retraction rate $\dot{\chi}$ (Equation 69) during this period for the X0125, X050 and X075 fluids. Dashed lines correspond to the average $\dot{\chi}$ for impacts with $We \geq 20$. Impacts with $We < 20$ typically show smaller retraction rates in comparison with this average and decrease further as We reduces. For $We \geq 20$, $\dot{\chi}$ remains constant and independent of We for each fluid; measurements agree with the average to within experimental error. This characteristic is also observed for Newtonian fluids. Moreover, $\dot{\chi}$ decreases with increasing Xanthan gum mass fraction (increasing K, decreasing n).

An inverse linear relationship between the dimensionless retraction rate $\dot{\chi} T_I$ and the consistency coefficient K is displayed in Figure [137], where T_I is the oscillation period of a perturbed inviscid drop (Equation 70). This variation is similar to that observed between $\dot{\chi} T_I$ and μ (for $Oh \leq 0.85$) for the Newtonian fluids (Figure 113 in **§5.2.1)**. Whilst establishing a relationship between $\dot{\chi} T_I$ and Oh is not possible for shear-thinning fluids because μ and hence Oh varies both spatially and temporally during

retraction, the $\dot{\chi} T_I \propto K^{-1}$ relationship does suggest that increases in K act to increase the average fluid viscosity during retraction and hence reduce the retraction rate based on increased energy dissipation.

$\dot{\chi}$ T_I and n shows the opposite trend to that of the relationship between $\dot{\chi}$ T_I and K, with $\dot{\chi}$ T_I increasing with n. This again suggests that the magnitude of the initial retraction rate is governed more by the viscosity of each fluid at low shear-rates rather than their degree of shear-thinning.

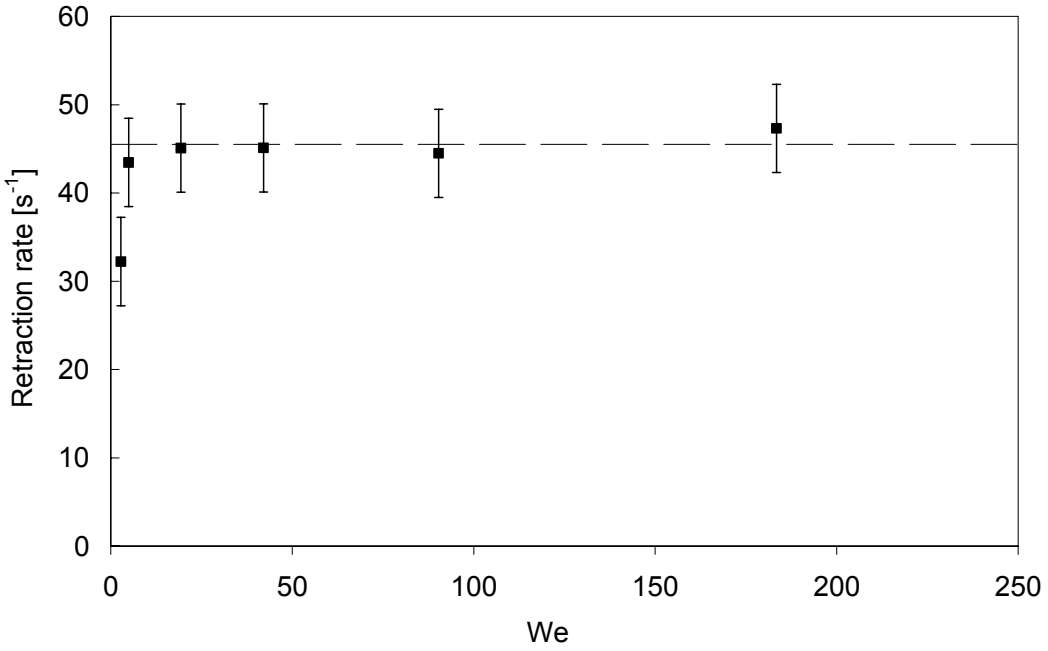

Figure 134. Maximum retraction rate $\dot{\chi}$ plotted against We for the X0125 (K = 0.208 Pas^n, n = 0.400, D_E = 3.474 mm) shear-thinning fluid in the range 2.8 ≤ We ≤ 183. The dashed line corresponds to the average $\dot{\chi}$ for We > 20.

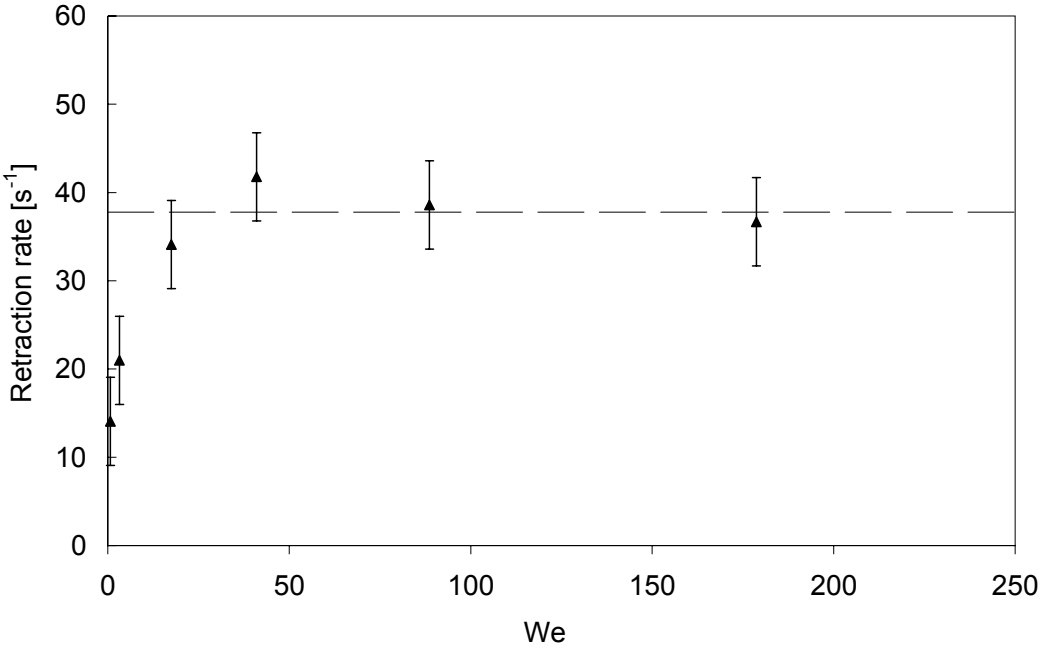

Figure 135. Maximum retraction rate $\dot{\chi}$ plotted against We for the X050 (K = 2.846 Pas^n, n = 0.129, D_E = 3.428 mm) shear-thinning fluid in the range 0.7 ≤ We ≤ 179. The dashed line corresponds to the average $\dot{\chi}$ for We > 20.

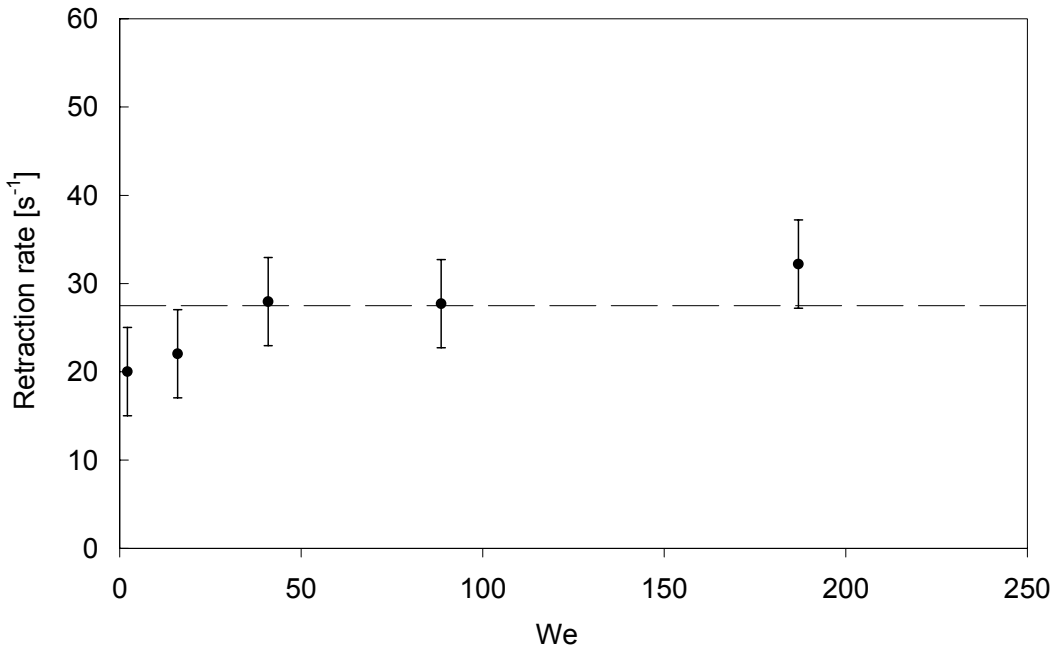

Figure 136. Maximum retraction rate $\dot{\chi}$ plotted against We for the X050 (K = 5.064 Pas^n, n = 0.084, D_E = 3.347 mm) shear-thinning fluid in the range 2.1 ≤ We ≤ 187. The dashed line corresponds to the average $\dot{\chi}$ for We > 20.

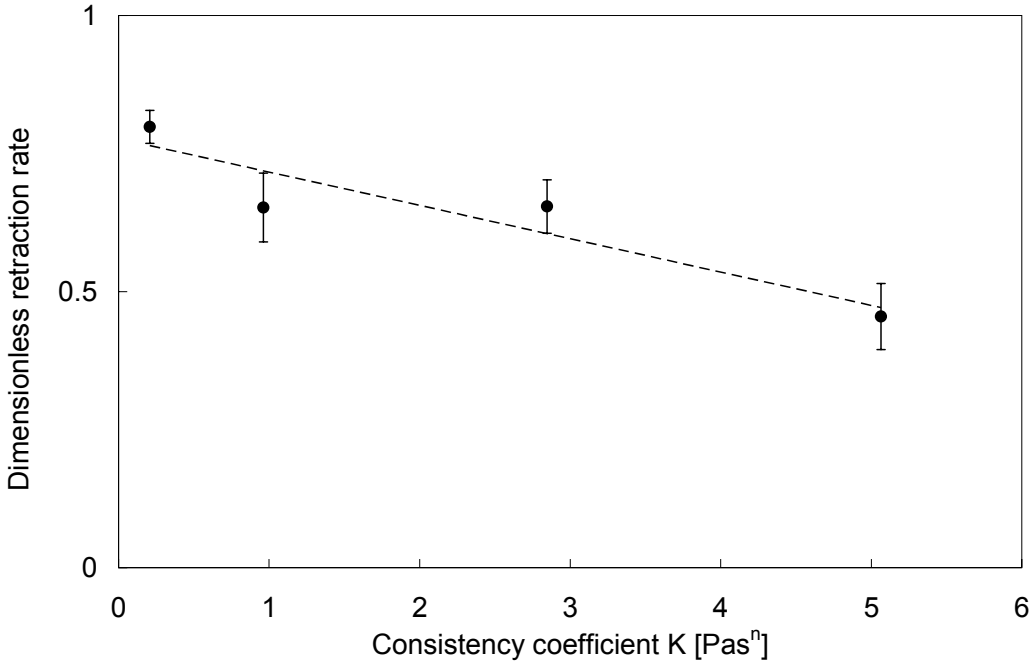

Figure 137. Average dimensionless retraction rate $\dot{\chi}\, T_I$ for impacts with We > 20 plotted against consistency coefficient K for shear-thinning fluids with $0.084 \leq n \leq 0.400$ and $0.208 \leq K \leq 5.064$ Pas^n. The dashed line corresponds to a linear best fit.

5.4 Yield-stress drop impact behaviour

Figures [138] and [139] display β_m and ξ_m (respectively) plotted against We for viscoplastic fluids with $0 \leq \tau_c \leq 26.1$ Pa impacting on a parafilm substrate in the range $0.68 \leq We \leq 312$. Measured values of ξ_m for viscoplastic fluids with $\tau_c \geq 11.5$ Pa are significantly larger than both the shear-thinning and Newtonian fluids over similar We ranges. This is due to the combined effect of incomplete drop deformation during impact and the prolate shape of drops prior to impact.

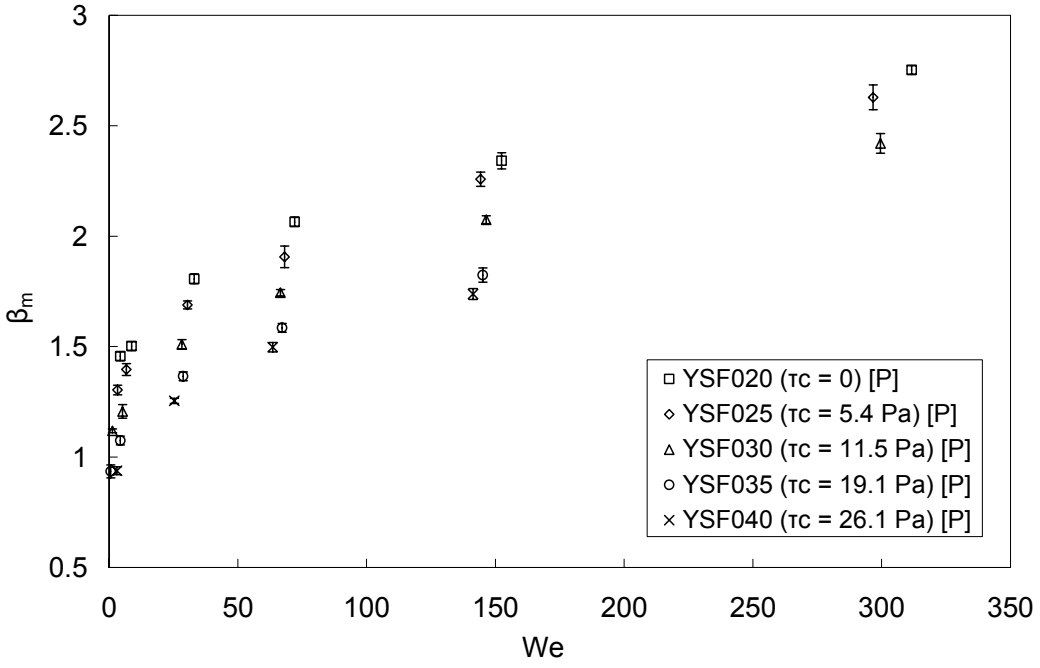

Figure 138. β_m plotted against We for viscoplastic fluid drops with $0 \leq \tau_c \leq 26.1$ Pa impacting on a parafilm substrate in the range $0.68 \leq We \leq 312$. Each results set is based on the average of 5 drop measurements.

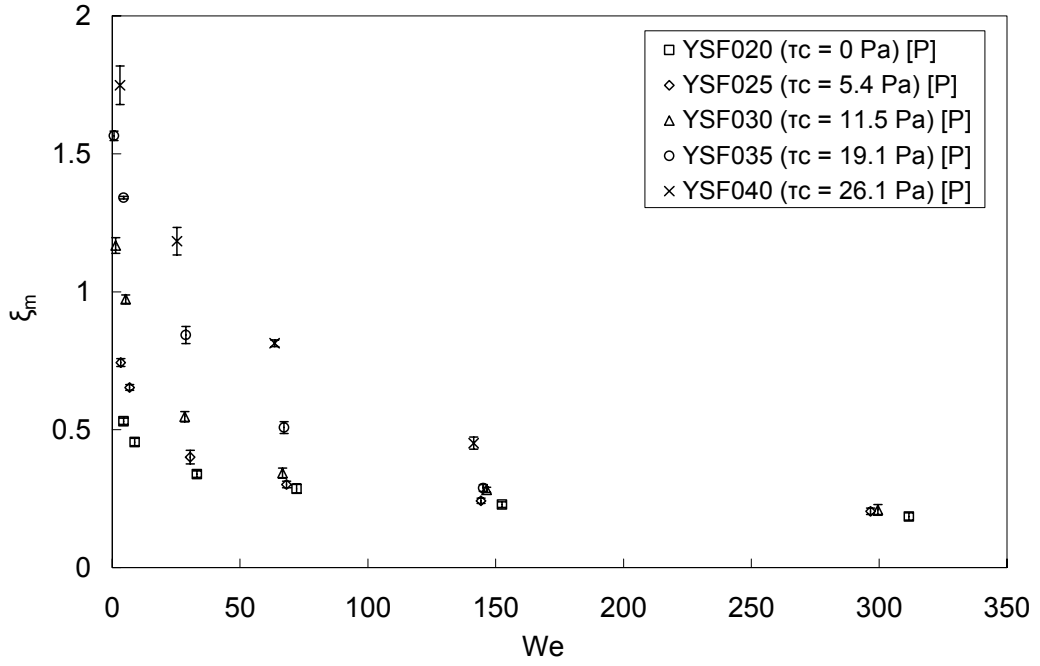

Figure 139. ξ_m plotted against We for viscoplastic fluid drops with $0 \leq \tau_c \leq 26.1$ Pa impacting on a parafilm substrate in the range $0.68 \leq We \leq 312$. Each results set is based on the average of 5 drop measurements.

Figure [140] displays β_m re-plotted as a function of the yield-stress magnitude. For each viscoplastic fluid, the relationship appears linear across the full range of We. Whilst this indicates a consistent inversely proportional relationship, the effects of shear-thinning have not been accounted for, therefore this relationship is not entirely accurate.

Viscoplastic drop impacts are influenced both by shear-thinning and yield-stress characteristics, making qualitative and quantitative assessments of the independent influence of yield-stress magnitude on drop impact dynamics difficult to establish. Moreover, it is not possible to determine the independent influence of yield-stress on impact dynamics by direct comparison of experimental results because the viscometric characteristic of the shear-thinning and yield-stress fluids differ, therefore like-with-like comparisons[10] cannot be made. One aspect that can be further scrutinised however is the presence of viscoplastic drop peaks at the end of inertial expansion. Neither shear-thinning or Newtonian fluid drops are observed to exhibit this morphological characteristic, therefore it is considered entirely related to viscoplasticity.

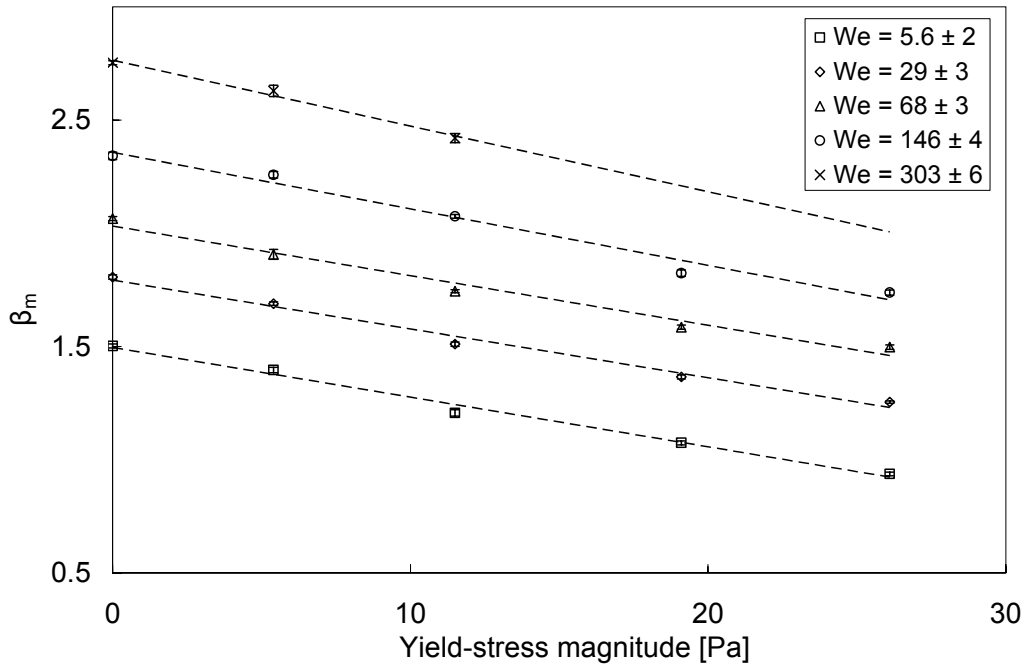

Figure 140. β_m plotted against τ_c for viscoplastic fluid drops with $0 \leq \tau_c \leq 26.1$ Pa impacting on a parafilm substrate in the range $0.68 \leq We \leq 312$.

[10] It is not possible to produce viscoplastic ($\tau_c > 0$ Pa) and shear-thinning ($\tau_c = 0$ Pa) fluids with identical shear-thinning viscometric properties. Therefore a direct experimental comparison of β_m and ξ_m cannot be made to establish the independent influence of fluid yield-stress on impact dynamics.

The presence of yield-stress fluid drop peaks can more clearly be observed in Figure [139]. Whereas the largest difference in ξ_m for impacts of the YSF020 solution (τ_c = 0 Pa) in the range $4.4 \leq We \leq 312$ is small with $\Delta\xi_m = 0.35$ (and similar to equivalent height differences of the Newtonian ($0.27 \leq \Delta\xi_m \leq 0.47$ for $0.056 \leq \mu \leq 0.925$ Pas) and shear-thinning fluids ($0.25 \leq \Delta\xi_m \leq 0.62$ for $0.208 \leq K \leq 5.064$ Pas^n, $0.084 \leq n \leq 0.4$) across similar ranges in We), height differences increase significantly with increasing τ_c; the maximum difference for the YSF040 solution (τ_c = 26.1 Pa) is $\Delta\xi_m = 1.3$ over $3 \leq We \leq 141$. This value exceeds unity and is due to the presence of a central peak in the drop (Figures 77, 80, 83 and 86). Drop peaks are present due to incomplete drop deformation during impact; the upper region of impacting drops do not significantly deform from their original prolate shape during free-fall. For impacts at similar We, peak heights increase with τ_c. Moreover, for low velocity impacts (H_f = 10 mm) deformation is small for fluids with $\tau_c \geq 11.5$ Pa and peaks can account for most of the drop volume. This suggests that radial flow will be inhibited within a threshold radius where shear stresses arising during impact fall below the yield-stress magnitude.

Dimensionless drop peak diameters, $\beta_{Peak} = D_{Peak}/D_{Max}$, are determined by measuring the intersection of the drop peak and lamella surface tangents, as shown in Figure [27]. Measurable drop peaks are present after impacts of the YSF035 and YSF040 fluids for $H_f \leq 100$ mm and for the YSF045 and YSF050 fluids for $H_f \leq 150$ mm. Whilst peaks exist at low fall heights for each of these solutions, deformations are small and surface tangent intersections and drop heights at the rim cannot not be accurately measured, therefore have not been analysed. Moreover, complete drop deformation is observed for fluids with $\tau_c \leq 19.1$ Pa over the full range of We.

To establish a relationship between peak diameter and yield-stress magnitude, measured values of β_{Peak} were compared with a theoretical threshold diameter, $\beta_T = D_T/D_{Max}$, where D_T is defined as the radial drop diameter where maximum shear-stresses arising in the lamella during inertial spreading equal the yield-stress magnitude of the fluid. During the expansion phase, the radial velocity, v_r, will be at a maximum close to the drop rim[46]. The maximum shear-rate and shear-stress can be therefore be approximated respectively by:

$$\dot{\gamma}_{Max} \approx \left. \frac{v_{r\max}}{h_{rim}(r)} \right|_{R_{Max}} \quad [99]$$

and:

$$\tau_{Max} = \tau_c + K\dot{\gamma}^n = \tau_c + K\left(\frac{v_{r\max}}{h_r(r)} \right)^n \Bigg|_{R_{Max}} \quad [100]$$

where $h_{rim}(R_{Max})$ is the lamella height at the rim, r is the radial position and the viscosity term has been replaced by a Herschel-Bulkley model. v_r will vary with time during the impact process, therefore this term represents the maximum average radial velocity during inertial spreading. This is used to provide an upper limit to the shear rate and stress terms. v_r for each drop is directly extracted from measurements.

Whilst it is not known how the radial velocity, shear-rates or shear-stresses vary across the lamella during impact, upon assuming the deforming drop has rotational symmetry about the vertical axis, each of these terms will decrease from a maximum near the rim to zero at the lamella centre. As a first approximation, we assume this variation to be linear. The dimensionless threshold diameter β_T can therefore be defined as where the shear stress will equal the fluid yield-stress magnitude:

$$\beta_T = \frac{D_T}{D_{Max}} = \frac{\tau_c}{\tau_{Max}} = \frac{\tau_c}{\tau_c + K\left(\frac{v_{r\max}}{h_r(r)} \right)^n \Big|_{R_{Max}}} \quad [101]$$

Within this perimeter, shear-stresses will be too small to cause deformation during impact and the drop shape will remain undeformed, resulting in a drop peak.

Figure [141] compares β_T (Equation 101) with measured values of β_{Peak}. Predictions are confined within a range limited by an upper level above which inertial forces result in the complete deformation of impacting drops (such that no central peak is observed) and a lower limit below which drops exhibit only small deformations and measured values of the drop rim height cannot be measured. The predictions agree with

the measured drop peak diameters to within ± 20%. It is also noted that only fluids with $\hat{B} > 1$ exhibit peaks.

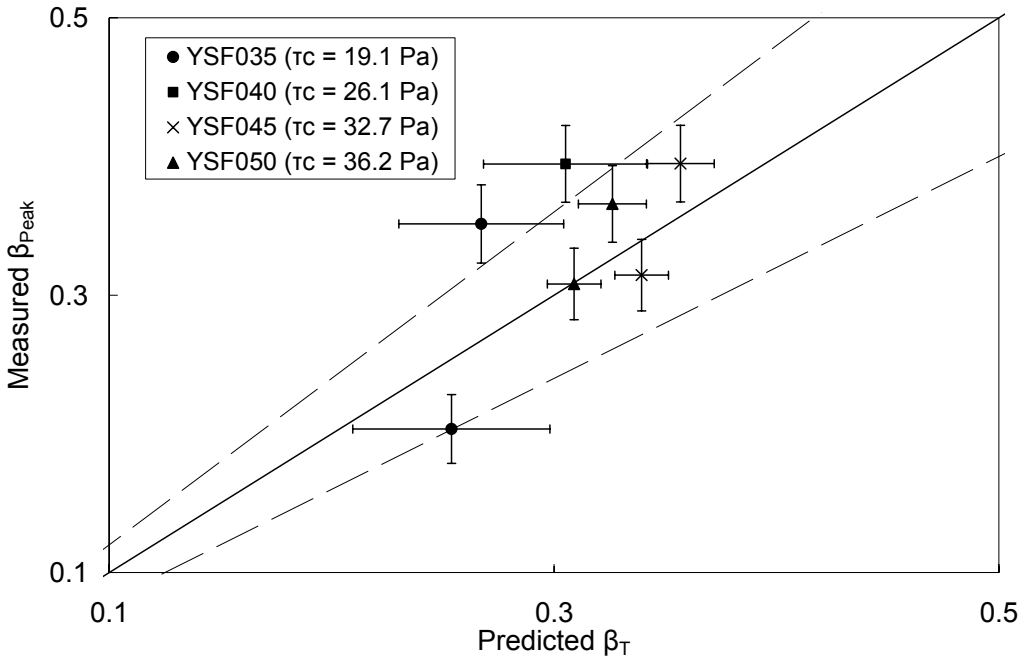

Figure 141. Measured drop peak diameter β_{Peak} plotted against predicted threshold diameter β_T (denoting the perimeter inside which shear-stresses during impact are smaller than the yield-stress) for yield-stress fluid drops with $19.1 \leq \tau_c \leq 36.2$ Pa impacting on a parafilm substrate within the range $67 \leq We \leq 203$. Long dashed lines correspond to a deviation of ± 20% from predictions.

The similarity of predicted threshold diameters with measurements appears to confirm the hypothesis that fluid yield-stress will influence drop impact dynamics by inhibiting fluid motion within a definable region during the expansion phase. Predictions also highlight that the threshold region will vary in size both with τ_c and We. As We increases, the maximum shear stresses near the drop rim will rise and (based on the approximated linear radial variation of shear-stress from the centre to the lamella edge) the threshold region of yield-stress influence will decrease in size, eventually resulting in complete deformation of the impacting drop and the disappearance of the drop peak. Observed changes in measured drop peak sizes confirm these trends. Whilst yield-stress effects may continue to influence inertial spreading behaviour for higher velocity impacts, where drops completely deform and peaks are no longer present, this cannot be established from the analysis. Moreover, larger drop peak sizes are observed for equivalent impacts of fluids with increasing τ_c, indicative of an increase in the threshold diameter.

6 Results and Discussion - Drop spreading dynamics

This section focuses on extending well established research into spreading dynamics of Newtonian and shear-thinning fluids, as detailed in **§1.2.5** and **§1.2.6.1**, by examining the drop spreading behaviour of viscoplastic fluids. The investigation can be split into two distinct topics; the influence of yield-stress magnitude on the dynamic spreading rate of drops on wettable substrates and the influence of fluid yield-stress on sessile drop shapes on surfaces of varying wettability.

Whilst Newtonian fluid drop shapes at the end of inertial expansion vary both with viscosity and impact velocity (Figures 75, 78, 81 and 84)), the final sessile shape is independent of both these parameters, although it does vary with substrate wettability. The same characteristic is also observed for the shear-thinning fluids. Figure [142] compares the shape of viscoplastic fluid drops with $0 \leq \tau_c \leq 26.1$ Pa at the end of inertial expansion (which is similar for impacts on different wettability substrates as detailed in **§5.1.3**) with sessile drop shapes after impacts from 10, 25, 50 and 100 mm on a hydrophilic (light grey outline) and hydrophobic (white outline) substrate. Whilst low yield-stress fluid drops show similar characteristics to the Newtonian and shear-thinning fluids with equilibrium drop shapes varying only with substrate wettability, the final sessile drop shapes of higher yield-stress magnitude fluid drops vary with yield-stress magnitude, impact velocity and substrate wettability.

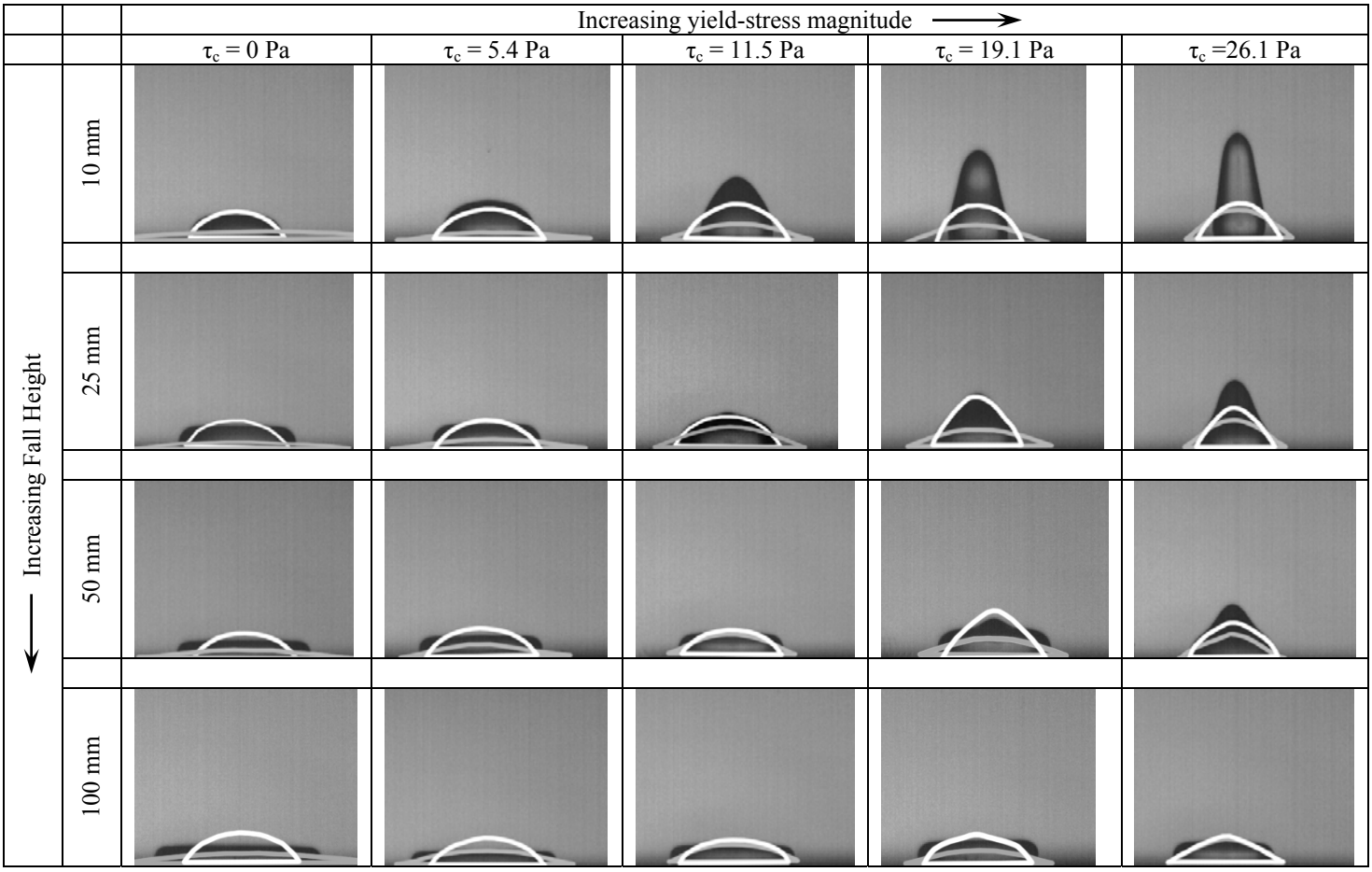

Figure 142. A comparison of viscoplastic fluid drop shape at the end of inertial expansion with sessile drop shape. Light grey outlines indicate sessile drop shapes on hydrophilic glass. White outlines indicate sessile drop shapes on hydrophobic parafilm-M. Comparisons are made with viscoplastic fluids with $0 \leq \tau_c \leq 26.1$ Pa impacting from fall heights of 10, 25, 50 and 100 mm.

6.1 The influence of fluid shear-thinning and yield-stress on spreading.

To understand any effects fluid yield-stress may have on the spreading of drops it is first necessary to examine the effects of fluid shear-thinning. Whilst significant research has been performed on this topic[152,154,156], the most relevant here is the theoretical analysis performed by Starov et al.[154] and the experimental investigation of shear-thinning drop spreading performed by Rafaï et al.[156].

As detailed in **§1.2.6.1**, Starov et al.[154] examined the spreading of non-Newtonian liquid drops on nearly complete (small θ_e) and completely wetting ($\theta_e = 0^o$) horizontal solid substrates. Theoretical analyses were performed for both gravitationally driven (R_E

> a) and capillary driven (R_E < a) spreading regimes. The evolution of drop shapes for each regime were deduced to have self-similar solutions, from which spreading laws were obtained. For the case of an axisymmetric non-Newtonian drop within the capillary spreading regime, a self-similar relationship of the form given in Equation [44] was established. The temporal spreading exponent p is obtained from Equation [45].

Temporal variations in drop radius R(t) were measured for each of the four shear-thinning fluids from impacts of H_f = 10 mm on a glass substrate. A best fit power law curve of the form $R(t) = At^p$ was then fitted to each set of results. Figures [143] and [144] display variations in R(t) for drops of the X0125 (n = 0.400) and X075 (n = 0.084) fluids respectively, along with their best fit power law curves (short dashed line). Each results set constitutes the average of five drop measurements.

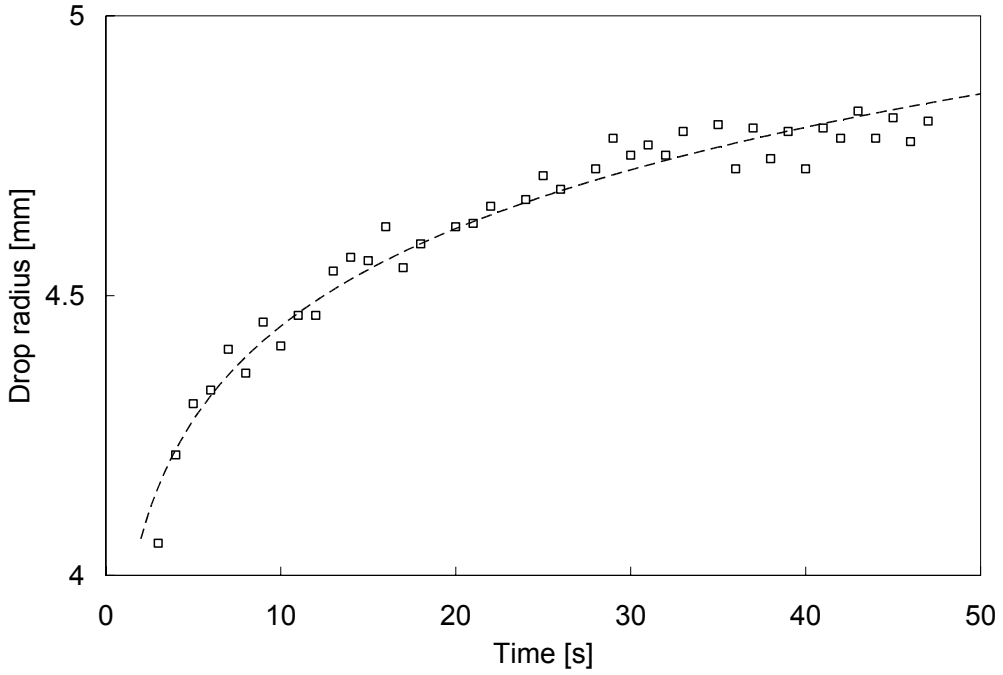

Figure 143. Drop radius plotted against time for impacts of the X0125 fluid (K = 0.208 Pas^n, n = 0.400, D_E = 3.474 mm) from H_f = 10 mm (We = 4.9) on to a glass substrate. The short dashed line corresponds to a best fit power law of the form $R(t) = At^p$. The results displayed here are an average of 5 separate drop spreading measurements. To aid visual clarity, measurement errors are not displayed, however are comparable with the symbol size.

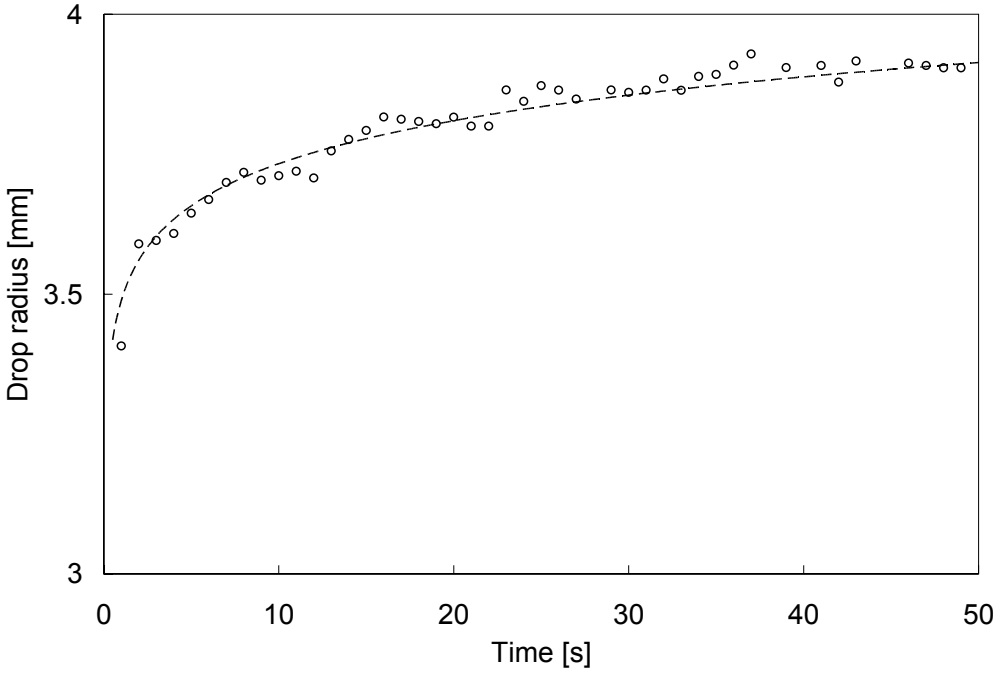

Figure 144. Drop radius plotted against time for impacts of the X0125 fluid (K = 0.208 Pas^n, n = 0.400, D_E = 3.347 mm) from H_f = 10 mm (We = 2.1) on to a glass substrate. The short dashed line corresponds to a best fit power law of the form $R(t) = At^p$. The results displayed here are an average of 5 separate drop spreading measurements. To aid visual clarity, measurement errors are not displayed, however are comparable with the symbol size.

Figure [145] compares measured values of the spreading exponent p with those predicted by Equation [45], denoted by the long dashed line. The solid line represents the constant spreading exponent derived for Newtonian fluids using Tanner's law (Equation 35). An experimental investigation by Rafaï et al.[156] also compared measured spreading exponents against those predicted by Equation [45] for shear-thinning fluids with $0.3 \leq n \leq 0.94$. These results are reproduced in Figure [145]. For fluids with $n \geq 0.6$, Rafaï et al. measured spreading exponents slightly smaller than the Newtonian exponent (p = 0.1) from Tanner's law. Moreover, experimental results were found to agree with those predicted by Starov et al. for all except the most shear-thinning (n = 0.3) fluid, whose measured exponent was notably larger than the predicted result.

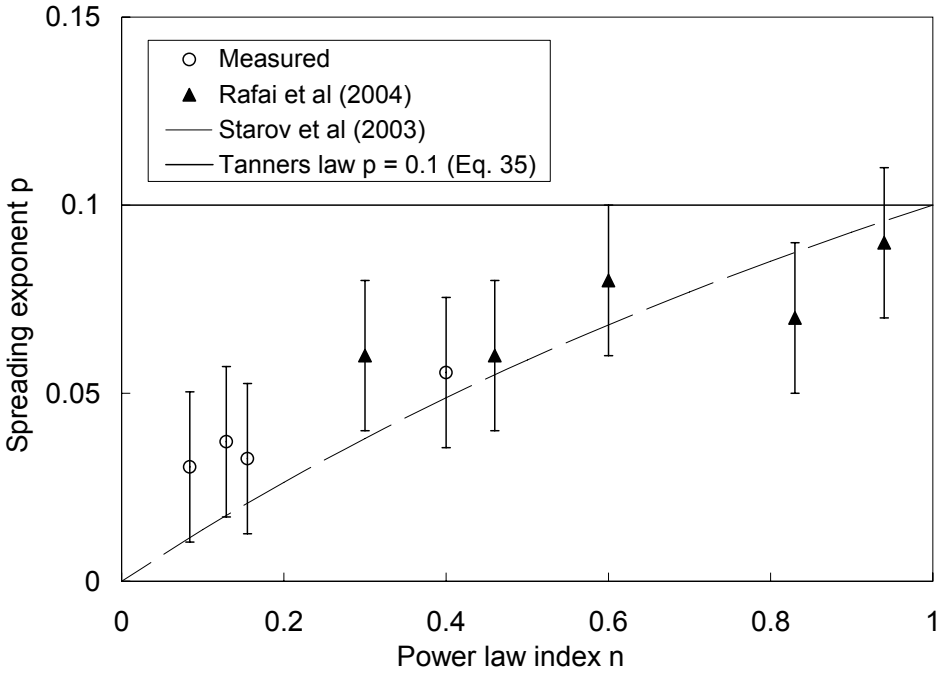

Figure 145. Drop spreading coefficient p ($R(t) = At^p$) plotted against shear-thinning power law index n (Equation 37) for measurements of the four shear-thinning fluids with $0.084 \leq n \leq 0.400$ (open square symbol) and measurements reproduced from Rafaï et al.[156] for shear-thinning fluids with $0.3 \leq n \leq 0.9$ (filled triangle symbol). The dashed line corresponds to predictions using Equation [45] from Starov et al.[154]. The solid line corresponds to the spreading exponent p = 0.1 established by Tanner for the spreading of Newtonian fluid drops (Equation 35).

The results from Rafaï et al. are not sufficiently accurate to provide conclusive evidence supporting Equation [45]; the exponent for the n = 0.3 fluid differs from predictions by a margin in excess of the experimental error and for less-shear-thinning fluids ($n \geq 0.6$), error margins are sufficiently large for measurements to agree with predictions by both Starov et al. and Tanner's law (p = 0.1). In contrast, the results from the current investigation provide evidence unambiguously supporting the theory by Starov et al. to within experimental error and extend measurements towards lower power law indices, highlighting the validity of the theory for highly shear-thinning fluids.

Variations in drop radius with time are now plotted for the yield-stress fluids in the range $0.3727 \leq n \leq 0.475$, $0 \leq \tau_c \leq 26.1$ Pa. As with the shear-thinning fluids, best fit power law curves are fitted to the results to establish the temporal spreading exponent p. Figures [146] – [148] display the results and best fit curves for the YSF020, YSF030 and YSF040 fluids impacting from fall heights of $H_f = 10$ mm on a glass substrate.

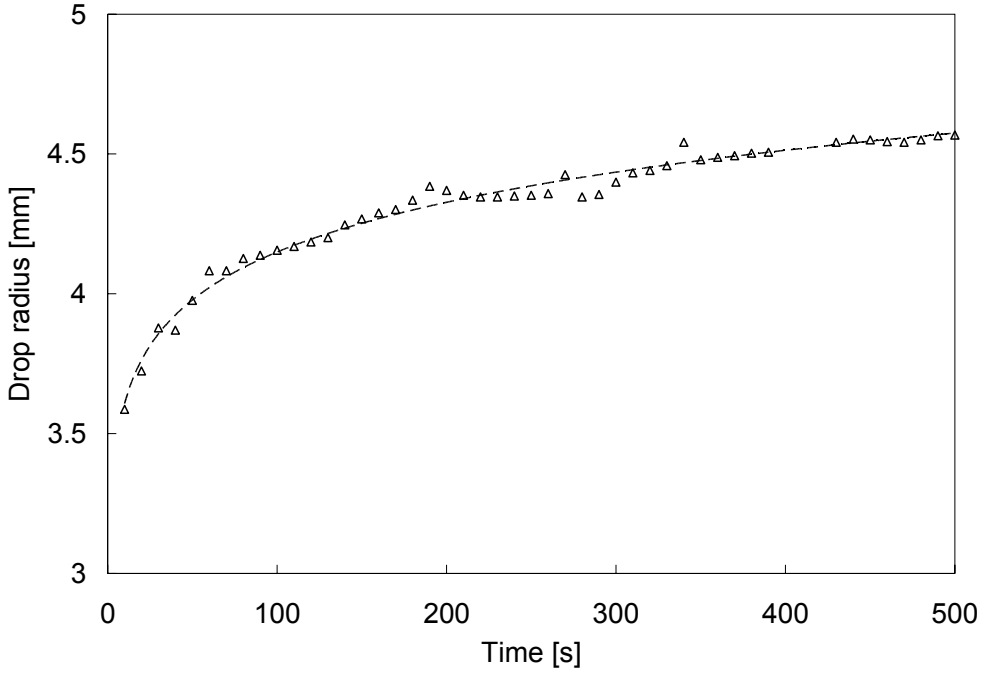

Figure 146. Drop radius plotted against time for impacts of the YSF020 fluid (K = 1.44 Pas^n, n = 0.475, τ_c = 0 Pa, D_E = 2.848 mm) from H_f = 10 mm (We = 8.8) on to a glass substrate. The results displayed here are an average of 5 separate drop spreading measurements. To aid visual clarity, measurement errors are not displayed, however are comparable with the symbol size.

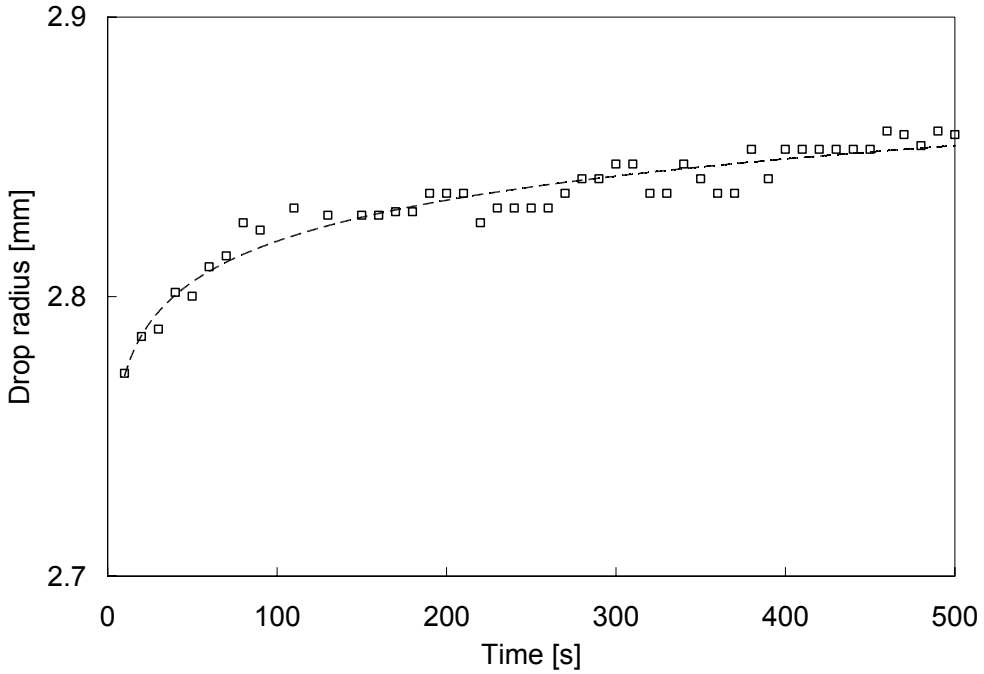

Figure 147. Drop radius plotted against time for impacts of the YSF030 fluid (K = 5.53 Pas^n, n = 0.378, τ_c = 11.5 Pa, D_E = 2.678 mm) from H_f = 10 mm (We = 5.2) on to a glass substrate. The results displayed here are an average of 5 separate drop spreading measurements. To aid visual clarity, measurement errors are not displayed, however are comparable with the symbol size.

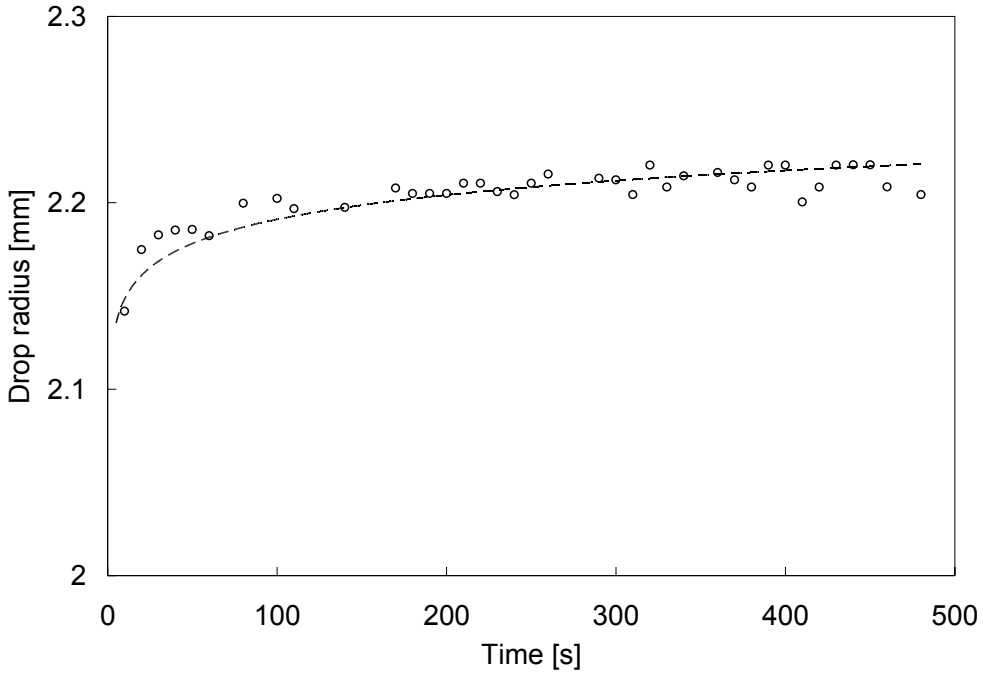

Figure 148. Drop radius plotted against time for impacts of the YSF040 fluid (K = 7.94 Pas^n, n = 0.373, τ_c = 26.1 Pa, D_E = 3.347 mm) from H_f = 10 mm (We = 3.0) on to a glass substrate. The results displayed here are an average of 5 separate drop spreading measurements. To aid visual clarity, measurement errors are not displayed, however are comparable with the symbol size.

Figure [149] plots the measured spreading exponent p as a function of the shear-thinning power law index n for the viscoplastic fluids. Whilst the measured exponent agrees with predictions by Starov et al. (dashed line, Equation 45) for the YSF020 fluid (τ_c = 0 Pa) to within experimental error, fluids with τ_c > 0 Pa show significantly smaller values than the predictions. The YSF020 fluid has no measurable yield-stress and as such, behaves characteristically like a shear-thinning fluid. In contrast, the exponent values of fluids with τ_c > 0 indicate that spreading rates are retarded by fluid yield-stress forces acting against the capillary driven spreading. Moreover the retardation rate increases with yield-stress magnitude. The resultant influence on final sessile drop shape is assessed in the following section.

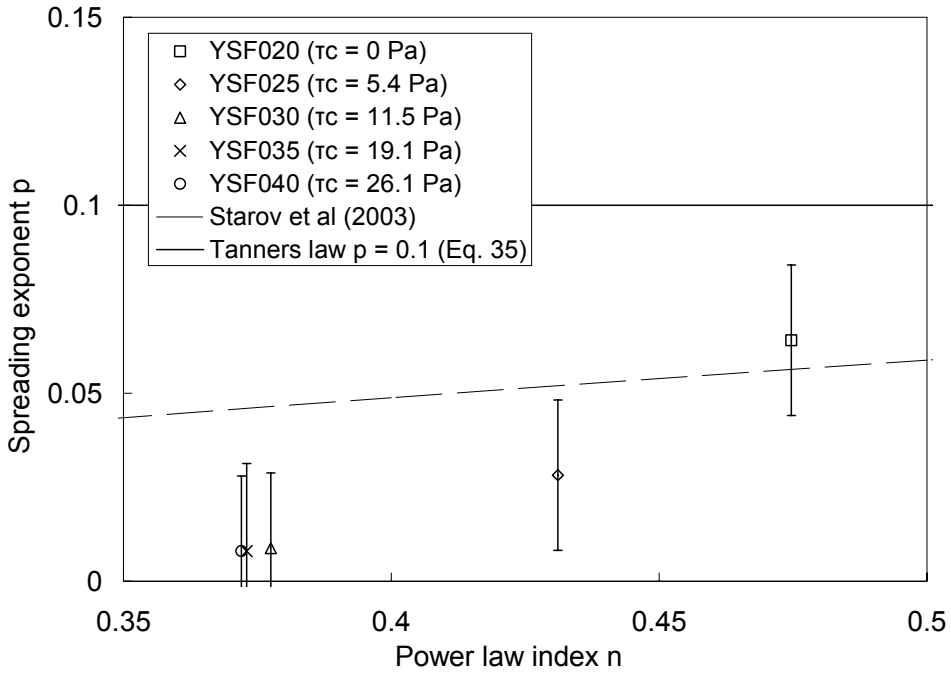

Figure 149. Drop spreading coefficient p ($R(t) = At^p$) plotted against shear-thinning power law index n (Equation 37) for viscoplastic fluids with $0.373 \leq n \leq 0.475$ and $0 \leq \tau_c \leq 26.1$. The dashed line corresponds to predictions using Equation [45] from Starov et al. The solid line corresponds to the spreading exponent p = 0.1 established by Tanner for the spreading of Newtonian fluid drops (Equation 35).

6.2 The influence of yield-stress magnitude on sessile drop shape.

To establish the influence of yield-stress magnitude on the final sessile state of impacting drops, the effect of viscous fluid characteristics are first assessed, Measurements of $\beta_{Sessile} = D_{Sessile}/D_E$ and the static contact angle θ_e are taken for the shear-thinning fluids after impacts on both glass and parafilm substrates from a range of fall heights. Figures [150] and [151] respectively plot $\beta_{Sessile}$ and θ_e against the power law index n for drops of the four shear-thinning fluids in the range $3.5 \leq We \leq 183$. Error margins are not displayed in either figure to aid visual clarity, however both $\beta_{Sessile}$ and θ_e results agree with the averaged values of $\beta_{Sessile} = 2.75$ and $\theta_e = 95.5^o$ to within experimental error. Whilst the results are compared here against n, a similar independence is also obtained when comparing measurements with the consistency coefficient K. Changes in n, K and We therefore do not significantly influence either the final drop spread factor or sessile contact angle for impacts on parafilm. The same conclusion can be attributed to impacts on the glass substrate, where shear-thinning drops

were found to be completely wetting ($\theta_e = 0^o$). Variations in final drop shape for the viscoplastic fluids can therefore be attributed to yield-stress effects.

The results for shear-thinning drop equilibrium contact angles are similar to those established by Mao et al.[47] for Newtonian drops. They observed that fluid viscosity and We do not influence the equilibrium contact angle of drops after impact.

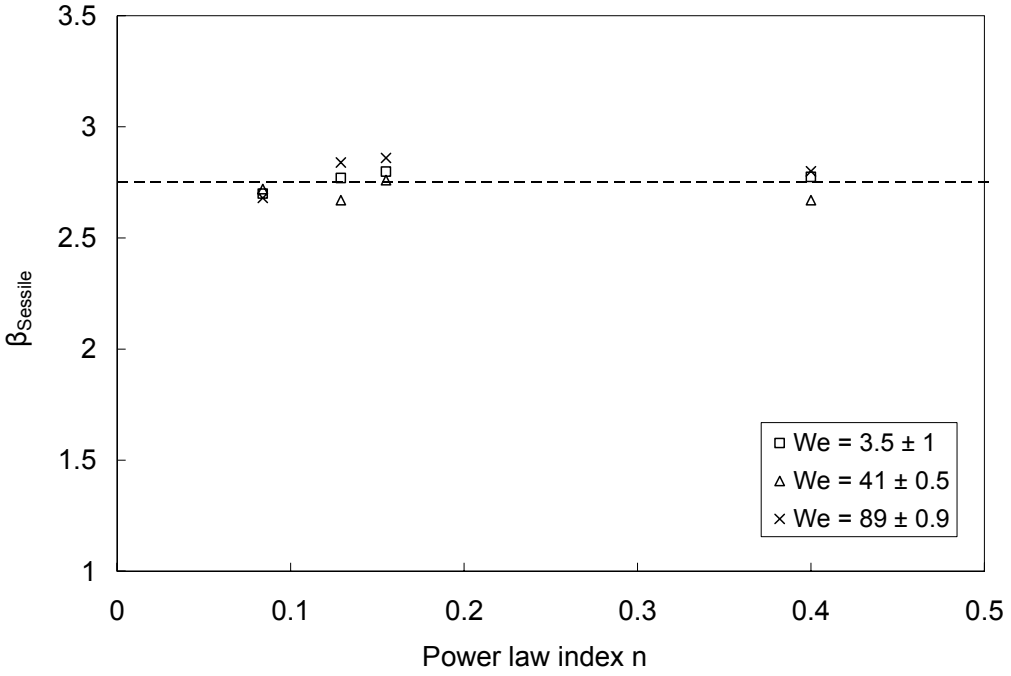

Figure 150. Sessile drop spread factor $\beta_{Sessile}$ plotted against shear-thinning power law index n (Equation 37) for impacts from $H_f = 10$ mm (We = 3.5 ± 1), $H_f = 50$ mm (We = 41 ± 0.5) and $H_f = 100$ mm (We = 89 ± 0.9) on a parafilm substrate. Error margins are not displayed for visual clarity, however measurements agree with the average $\beta_{Sessile} = 2.75$ to within experimental error.

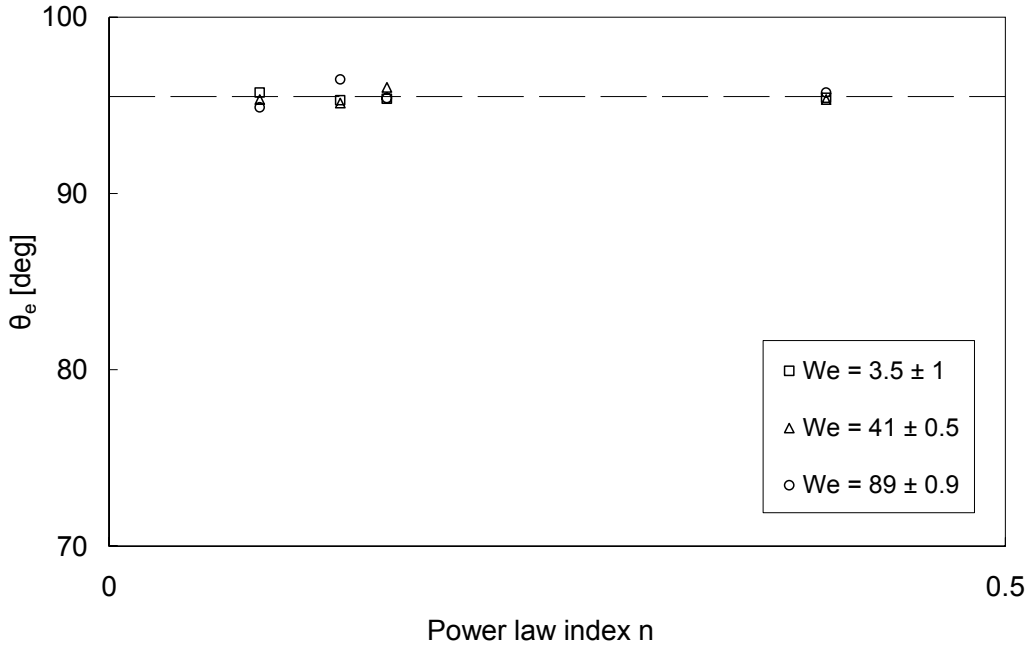

Figure 151. Sessile drop contact angle θ_e plotted against shear-thinning power law index n (Equation 37) for impacts from H_f = 10 mm (We = 3.5 ± 1), H_f = 50 mm (We = 41 ± 0.5) and H_f = 100 mm (We = 89 ± 0.9) on a parafilm substrate. Error margins are not displayed for visual clarity, however measurements agree with the average $\theta_e = 95.5^o$ to within experimental error.

Fluids with a yield-stress above a threshold magnitude (related to the size of the drop) have previously been established to influence the formation of spherical drops during free-fall **(§4.3)** and inhibit inertial drop spreading during the expansion phase of impact (**§5.4**). We make the further conjecture that fluid yield-stress may also inhibit the spreading of drops, preventing the formation of drop shapes governed by Equation [26]. In order to verify this conjecture, $\beta_{Sessile}$ and θ_e for each viscoplastic fluid are plotted against the yield-stress magnitude τ_c for each impact We; Figures [152] and [153] display results for impacts on the parafilm and glass substrates respectively.

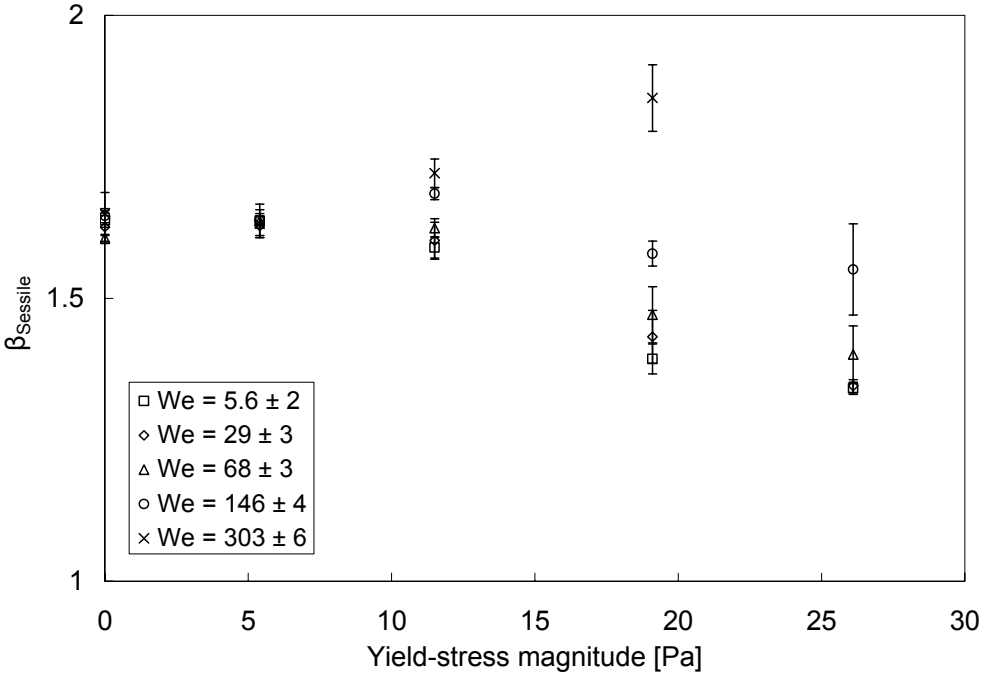

Figure 152. Sessile drop spread factor $\beta_{Sessile}$ plotted against fluid yield-stress magnitude τ_c for impacts in the range 10 mm ≤ H_f ≤ 200 mm (5.7 ≤ We ≤ 303) on a parafilm substrate. Each data point is the average of five separate drop measurements.

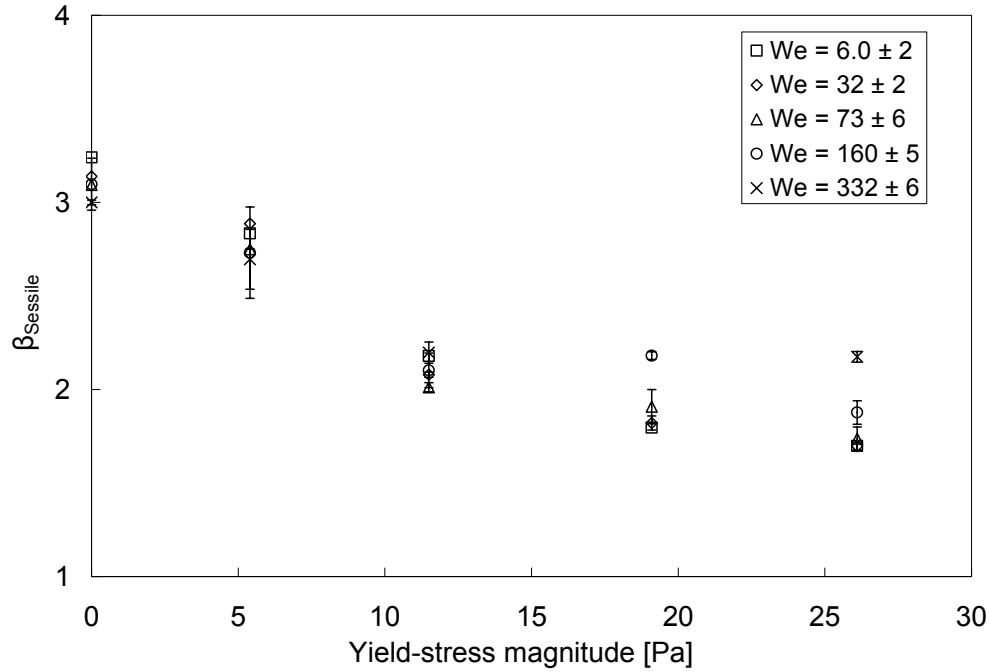

Figure 153. Sessile drop spread factor $\beta_{Sessile}$ plotted against fluid yield-stress magnitude τ_c for impacts in the range 10 mm ≤ H_f ≤ 200 mm (6.0 ≤ We ≤ 332) on a glass substrate. Each data point is the average of five separate drop measurements.

For drops spreading on the parafilm surface in Figure [152], $\beta_{Sessile}$ remains independent of impact velocity for low yield-stress magnitude fluids with $\tau_c < 11.5$ Pa, similar to the results observed for the Newtonian and shear-thinning fluids. For $\tau_c > 11.5$ Pa however, there is a clear variation in final sessile drop diameter for impacts at different velocities, indicative of $\beta_{Sessile}$ varying with We. This indicates that fluid yield-stress prevents drops from forming similar sessile drop shapes by inhibiting spreading or retraction. For impacts on glass in Figure [153], $\beta_{Sessile}$ for fluids with $\tau_c \leq 5.4$ Pa are similar in magnitude, although the YSF025 fluid shows slightly smaller values of $\beta_{Sessile}$ in comparison with the YSF020 fluid ($\tau_c = 0$ Pa). As τ_c increases above $\tau_c = 11.5$ Pa, $\beta_{Sessile}$ decreases notably for impacts at similar We, indicating that spreading becomes increasingly inhibited.

A more clear understanding of the inhibiting effect of yield-stress on drop spreading is provided in Figure [154]. This displays the measured difference between $\beta_{Sessile}$ for equivalent impacts on the glass and parafilm substrates, denoted $\Delta\beta_{Sessile}$. Results are plotted against τ_c for impacts in the range $5.8 \leq We \leq 317$.

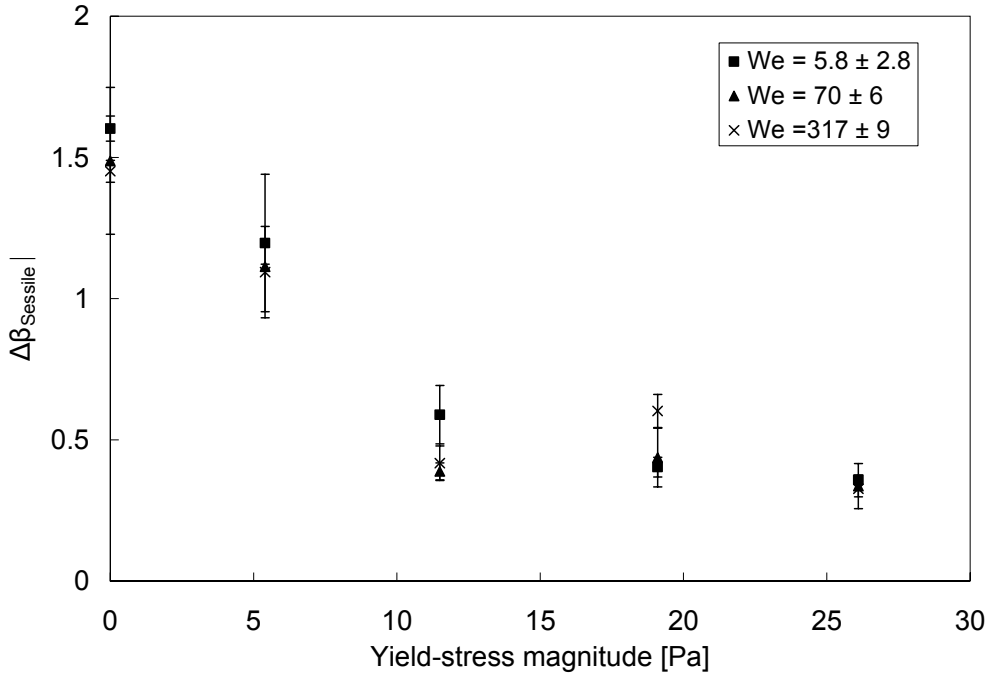

Figure 154. The difference between $\beta_{Sessile}$ for equivalent drop impacts on a glass and parafilm substrate, $\Delta\beta_{Sessile}$,, plotted against yield-stress magnitude for impacts at $H_f = 10$ mm (We = 5.8 ± 2.8), $H_f = 50$ mm (We = 70 ± 6) and $H_f = 100$ mm (We = 317 ± 9).

Low yield-stress magnitude fluids with $\tau_c \leq 5.4$ Pa exhibit a similar characteristic to both the Newtonian and shear-thinning fluids upon examination of $\Delta\beta_{Sessile}$. Fluid drops are completely or nearly completely wetting on glass substrates and partially wetting on parafilm. $\Delta\beta_{Sessile}$ for each fluid type is large and similar in magnitude irrespective of We and the viscous characteristics of the fluid. In contrast for viscoplastic fluids with $\tau_c > 5.4$ Pa, $\Delta\beta_{Sessile}$ is reduced and decreases with increased τ_c. The spread factor at the end of inertial expansion (β_m) for these fluids is the same on both substrates (**§5.1.3**), therefore these results indicate that as yield-stress magnitudes increase, the amount of spreading/retraction after impact reduces and sessile drop shapes become more similar, irrespective of the substrate wettability.

This analysis provides a qualitative assessment of the influence of fluid yield-stress on spreading. A more quantitative approach cannot be made however because whilst $\beta_{Sessile}$ is independent of viscous fluid characteristics (whilst varying as a function of τ_c), the maximum spread factor at the end of inertial expansion is dependent on the viscous characteristics of the fluid. An analysis of the difference between β_m and $\beta_{Sessile}$ to establish how much drops spread after inertial expansion therefore cannot be disassociated from viscous fluid properties.

Figures [155] and [156] respectively display sessile drop contact angles for viscoplastic fluids after impacts from varying fall heights on parafilm and glass substrates. For impacts at similar We, increasing the yield-stress magnitude over the range $0 \leq \tau_c \leq 26.1$ Pa results in increases in θ_e on both substrates. Increases of $10.4 \leq \Delta\theta_e \leq 13.6^o$ are observed for the parafilm substrate ($5.6 \leq We \leq 146$) and $27.6 \leq \Delta\theta_e \leq 33.4^o$ ($6 \leq We \leq 160$) for the glass substrate. The short dashed line in Figure [155] corresponds to the measured sessile contact angle of water drops containing a Polysorbate 20 additive at concentrations greater than 10X C.M.C ($\theta_e = 53 \pm 2.6^o$). The surface tension of these drops are equal ($\sigma = 0.034$ Nm^{-1}) to those measured for the viscoplastic fluids, however only values of θ_e for the YSF020 and YSF025 fluids agree closely and to within experimental error of the water drop measurements.

The variation of θ_e with We is small for low yield-stress fluids and similar to that observed for the Newtonian and shear-thinning fluids, where θ_e for non-splashing drops is similar and independent of the impact velocity. Variations increase however as τ_c increases. For the YSF040 fluid ($\tau_c = 26.1$ Pa), θ_e varies by 3.9^o for impacts (in the range $3 \leq We \leq 141.3$) on the parafilm substrate and 6.5^o (in the range $2.9 \leq We \leq 153.3$) for the glass substrate. This indicates that final sessile drop shapes become increasingly influenced by impact conditions as τ_c increases.

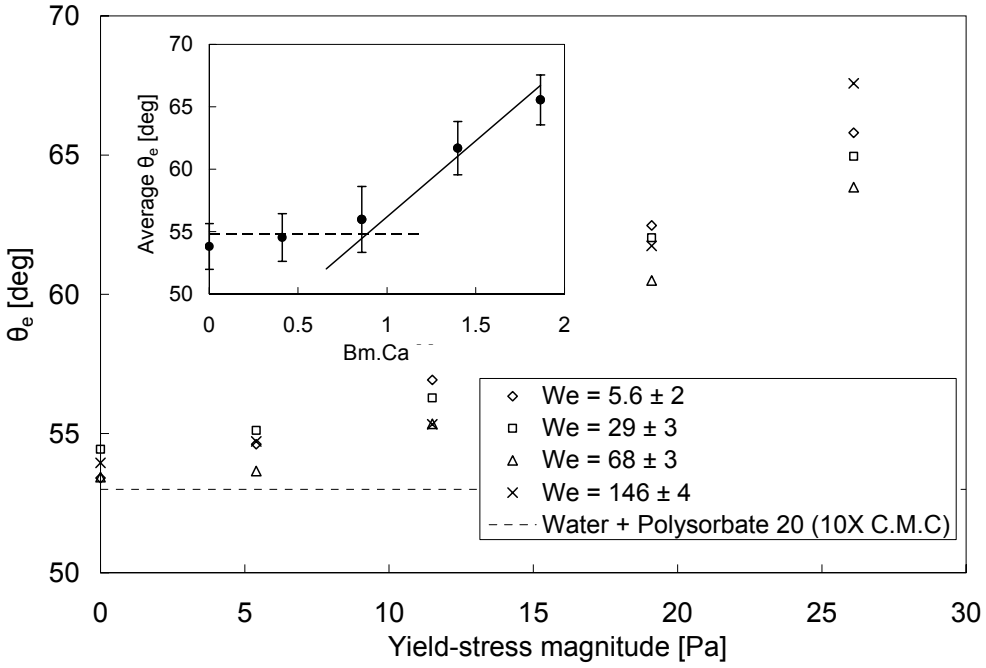

Figure 155. Sessile drop contact angle θ_e plotted against yield-stress magnitude for viscoplastic fluids with $0 \leq \tau_c \leq 26.1$ Pa impacting on a parafilm substrate from $H_f = 10$ mm (We = 5.6 ± 2), $H_f = 25$ mm (We = 29 ± 2), $H_f = 50$ mm (We = 68 ± 3) and $H_f = 100$ mm (We = 146 ± 4). The short dashed line corresponds to the sessile state contact angle of water drops with a Polysorbate 20 additive at greater than 10X C.M.C ($\sigma = 0.034$ Nm^{-1}). Errors margins are not displayed to aid visual clarity. (Inset) average θ_e for drops of each viscoplastic fluid (averaged over the four fall heights) plotted against Bingham-Capillary number $\hat{B}$. The average of measurements for $\hat{B} < 1$ is denoted by the long dashed line. The line of best fit for fluids with $\hat{B} \geq 1$ (including the YSF030 fluid where $\hat{B} \sim 1$) is denoted by the solid line. Error bars are equal to the standard deviation of relative errors from each set of data points at a fixed yield-stress magnitude.

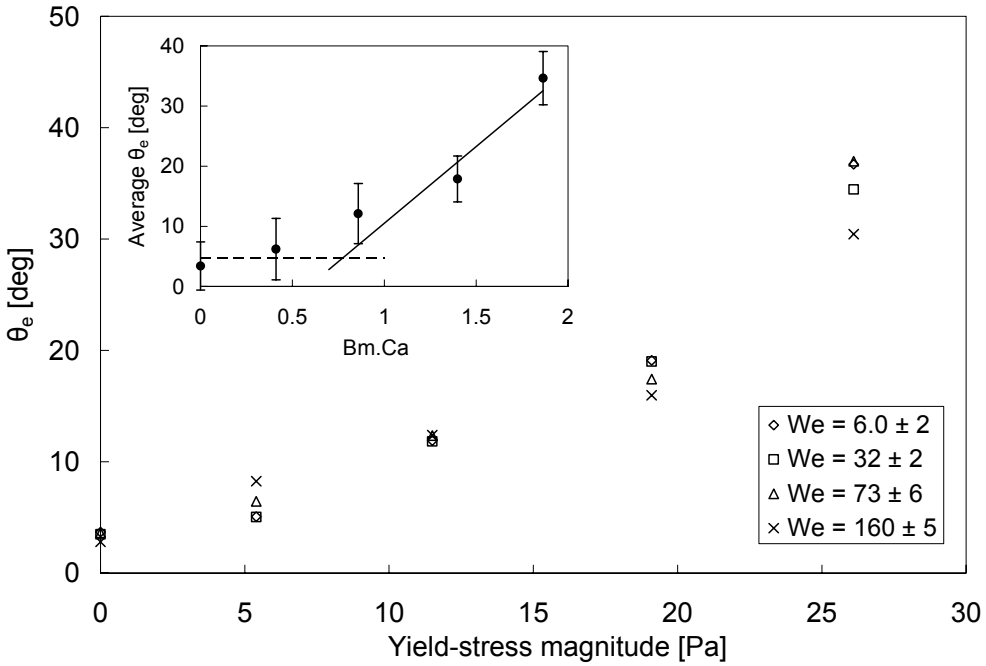

Figure 156. Sessile drop contact angle θ_e plotted against yield-stress magnitude for viscoplastic fluids with $0 \leq \tau_c \leq 26.1$ Pa impacting on a glass substrate from $H_f = 10$ mm (We = 6.0 ± 2), $H_f = 25$ mm (We = 32 ± 2), $H_f = 50$ mm (We = 73 ± 6) and $H_f = 100$ mm (We = 160 ± 5). Errors are not displayed to aid visual clarity. (Inset) average θ_e for each fluid (averaged over the four fall heights) plotted against Bingham-Capillary number $\hat{B}$. The average of measurements for $\hat{B} < 1$ is denoted by the long dashed line. The line of best fit for fluids with $\hat{B} \geq 1$ (including the YSF030 fluid where $\hat{B} \sim 1$) is denoted by the solid line. Error bars are equal to the standard deviation of relative errors from each set of data points at a fixed yield-stress magnitude

Inset in both Figures [155] and [156] are plots of the average θ_e for each fluid (over impacts at the different We) plotted against the Bingham-Capillary number $\hat{B}$ (Equation 63). For viscoplastic fluids with $\hat{B} < 0.5$, variations in θ_e are small and agree with the averaged value of $\theta_e = 54.8^o$ for the parafilm substrate and $\theta_e = 4.8^o$ for the glass substrate (long dashed lines) to within experimental error. Fluids with $\hat{B} > 1$ however show deviations away from this value; increasing in size with increasing τ_c. A line of best fit made to these results (including the YSF030 fluid with $\hat{B} \sim 1$) is denoted by the solid line. The intersection of these lines occurs at $\hat{B} \sim 0.9$ for the parafilm substrate and $\hat{B} \sim 0.8$ for the glass substrate, close to the expected value of $\hat{B} = 1$ in both cases. This value indicates a regime change from capillary governed to yield-stress governed flow behaviour.

For fluids with $\hat{B} < 1$, capillary forces appear to dominate over yield-stress forces and the sessile state contact angle remains near constant and unchanging with yield-stress magnitude, power law index n or consistency coefficient K. This is the same as what is observed for shear-thinning fluids. For fluids with $\hat{B} > 1$ however, θ_e increases with τ_c, indicating that yield-stress effects influence the sessile drop shape with the influence becoming more apparent with increasing yield-stress magnitude.

7 Conclusion.

Systematic experiments show that viscoplastic fluid drops can exhibit peculiar behaviour during detachment, free-fall, impact and subsequent spreading on a solid, horizontal substrate. An investigation was completed that examined the morphological aspects of viscoplastic fluid drops during these processes. Viscoplastic fluids exhibit shear-thinning fluid behaviour when the applied stress exceeds a certain threshold value, called the yield-stress. Below this threshold however, the fluid exhibits elastic solid characteristics. This behaviour can be described using the Herschel-Bulkley rheological model. In order to separate the effects of yield-stress from viscous effects, comparisons were made with Newtonian and shear-thinning fluid drop behaviour. The rheological properties of each fluid type were measured using a Haake-Mars rotational rheometer.

High speed imaging at 1000 Hz. was used to record the dynamics of drops during the fast detachment, free-fall and impact processes. Spreading occurs over much longer timescales however, therefore imaging was performed at slower frame-rates of 1 Hz.

Unlike Newtonian and shear-thinning fluids, which assume a spherical equilibrium drop shape during free-fall, viscoplastic fluid drops can exhibit a non-spherical equilibrium shape, with an aspect ratio that varies as a function of the yield-stress. The behaviour of these drops can be characterised by a dimensionless number which is the product of the Bingham and the capillary numbers, and represents the ratio of the Laplace pressure (which acts to minimise the surface energy) to the yield-stress. In drops where the Laplace pressure exceeds the yield-stress a spherical equilibrium drop shape is obtained; otherwise drops are prolate, and their aspect ratio grows linearly with the yield-stress magnitude in the explored range of experimental parameters. We name this dimensionless number the Bingham-Capillary number and abbreviate it to $\hat{B}$.

Prior to free-fall, viscoplastic fluid drops grow and detach from a flat ended capillary tube. Their behaviour during this process can differ significantly from Newtonian and shear-thinning fluids with drops appearing increasingly more prolate with yield-stress magnitude. Drops grow at the end of a capillary tube until a critical threshold is reached. They then become unstable and detach. This stability threshold can be characterised by a variant of $\hat{B}$,

characterising the ratio of extensional yield-stress to capillary pressure. This variant is used because flow in the drop neck is nearly purely extensional. For viscoplastic drops where the capillary pressure is greater than the extensional yield-stress, the tensile stress at critical breakup remains nearly constant. A similar characteristic is also observed for Newtonian and shear-thinning fluids. When the extensional yield-stress exceeds the capillary pressure the maximum tensile stress at critical breakup increases linearly with yield-stress magnitude. This relationship is consistent with the von Mises yield criterion, which relates the extensional yield-stress to the yield-stress in pure shear.

The inertial spreading of drops after impacting on a solid surface exhibits some features that can be related to the fluid rheology. In particular, at the end of the expansion phase, the fluids with the higher yield-stresses exhibit peaks at the centre of the lamella. This suggests that the drop deformation is localised in the external part, while the central part remains undeformed because the stress is smaller than the yield point of the fluid. Predictions defining a threshold diameter wherein shear-stresses (which are assumed during impact to vary linearly from zero at the axisymmetric drop centre to a maximum at the lamella rim) equal the yield-stress magnitude show reasonable agreement with measured drop peak diameters. More direct quantitative comparisons are difficult because one must also take into account the potential effects of shear thinning.

The final sessile shapes of drops after spreading are also influenced by fluid yield-stress and can be characterised with the Bingham-Capillary number. Quantitative measurements show fluid yield-stress can act to inhibit spreading driven by capillarity. On a hydrophilic substrate, increasing the yield-stress magnitude decreases the final sessile drop diameter. This characteristic differs from Newtonian and shear-thinning fluids which both completely wet the substrate. For drops where the capillary pressure is greater than the yield-stress, equilibrium contact angles remain similar to that of a Newtonian fluid (with an equivalent surface tension) and independent of the impact velocity or yield-stress magnitude. For drops where the yield-stress exceeds the capillary pressure, the contact angle appears to grow linearly with yield-stress.

8 Further Work

There are a number of regions where further research outwith the scope of the current investigation would improve our understanding of viscoplastic fluid drop behaviour. Firstly, as this research has highlighted, it is difficult to produce fluids with viscometric properties that enable systematic comparisons to be performed. Specifically, the effect of yield-stress magnitude on the amount of inertial spreading during impact cannot be directly established. Moreover, the independent influences of (shear-thinning) power law index n and consistency coefficient K on drop impact behaviour cannot be determined from the existing research. Numerical studies would therefore contribute towards a better understanding of the behaviour. By incorporating viscoplastic bi-viscosity (Eq. 50) or Herschel Bulkley models (Eq. 46) into the viscosity terms of a robust computational fluid dynamics code (FLUENT, STAR CCM) using a volume of fluid conservation approach, investigations analysing the independent effects of power law index, consistency coefficient and yield-stress magnitude on free-fall and impact behaviour could be performed. Investigations should initially focus on validating the fluid dynamics equations for Newtonian fluid drop impacts where only one viscosity term is required. The AGM model in **§5.2.2.2.5** would be a good starting point because it includes aspects describing more complex fluid flow. This or an alternative model could then be modified to include shear-thinning behaviour. Numerical results could be directly compared with experimental results presented in this thesis for validation purposes. The rheological model employed (Power law, Cross, Carreau) should first be analysed to find which provides numerical predictions closest to the experimental results. The influence of the degree of shear-thinning (e.g power law index n and consistency coefficient K in the power law model) should then be analysed in detail. Once this study is complete, the rheological model most accurately predicting viscoplastic behaviour should be studied (Herschel-Bulkley or bi-viscosity model). A parametric study analysing the effect of yield-stress magnitude and the degree of shear-thinning should then be completed. This analysis should asses the validity of the central viscoplastic peak prediction equation (Eq. 101). This research would be timely and a natural progression from existing numerical and theoretical analyses of viscoplastic drop detachment[145-147]. Validation of the results

could be made by comparing predictions with the experimental results presented within this thesis.

Further experimental studies into drop free-fall behaviour could potentially be achieved with the use of diamagnetic levitation techniques[167]. Currently drop free-fall behaviour is observed with the drop in a moving reference frame with respect to the camera. This limits the period of observation. Diamagnetic levitation techniques would allow the drop to remain indefinitely within the field of view of the camera. Interfacial oscillations and damping behaviour of drops could then be examined more thoroughly as well as the equilibrium prolate shapes of the viscoplastic drops over longer timescales. The results of this experiment would contribute towards a better understanding of fluid yield-stress. For instance if drop shapes varied over long timescales instead of remaining in an equilibrium shape, this would suggest a bi-viscosity model, rather than a Herschel-Bulkley model is more suitable in characterising viscoplasticity.

References

[1] S. C. Yao and V. E. Schrock, 'Heat and mass transfer from freely falling drops', J. Heat. Trans. **98**, p 120 (1976).
[2] M. Pasandideh-Fard, V. Pershin, S. Chandra and J. Mostaghimi, 'Splat shapes in a thermal spray coating process: Simulations and experiments', J. Thermal Spray Tech. **11**(2), p206 (2002).
[3] V. Bergeron, 'Designing intelligent fluids for controlling spray applications', C. R. Phys. **4**(2), p211 (2003).
[4] M. Dahlback, "Behaviour of nebulizing solutions and suspensions," J. Aerosol Med.-Depos. Clear. Eff. Lung **7**, S13 (1994).
[5] A. Maranghides, R. Anleitner, J. Montgomery, H. Burchell, J. Fleming, and R.S. Sheinson, 'Water mist visualisation and droplet size analysis in large scale fire suppression research', Halon options technical working conference, p397, (2001).
[6] S. L. Manzello and J. C. Yang, 'Collision dynamics of a liquid fire suppressant upon a heated wax surface', 9th International conference on liquid atomization and sprays (2003).
[7] A. Asai, M. Shioya, S. Hirasawa and T. Okazaki, 'Impact of an ink drop on paper', J. Imaging Sci. Technol. **37**, p205 (1993).
[8] D. B. van Dam and C. Le Clerc, 'Experimental study of the impact of an ink-jet printed droplet on a solid substrate' Phys. Fluids **16**(9), p3403 (2004).
[9] B. Chan, N. J. Balmforth and A. E. Hosoi, 'Building a better snail: Lubrication and adhesive locomotion' **17** 113101 (2005)
[10]Leonardo Da Vinci, Codex Leicester, (1506-1510).
[11]J. Eggers and E. Villermaux, 'Physics of liquid jets', Rep. Prog. Phys. **71**(3) 036601 (2008).
[12] P. S. de Laplace, Méchanique Celeste*,* Supplément au Xieme Livre, Courcier, Paris (1805).
[13] T. Young, , Philos. Trans. R. Soc. London, **95**, p65 (1805).
[14] F. Savart, Ann. Chim. 53, p337; plates in vol. **54**, (1833)[11].
[15]J. A. F. Plateau, 'Statique expérimentale et théorique des liquides soumis aux seules forces moléculaires, Gauthiers-Villars, Paris (1873).
[16] Lord Rayleigh, 'On the Capillary phenomena of jets', Proc. Royal Society of London. **29,** 71 (1879).
[17] J. Eggers, 'Nonlinear dynamics and breakup of free-surface flows', Rev. Mod. Phys. **69**(3), p865 (1997).
[18] S. Chandrasekhar, 'Hydrodynamic and hydromagnetic stability' Oxford University, New York/London 1961, reprint 1981 (Dover, New York).
[19] R. J. Donnelly and W. Glaberson, 'Experiments on the capillary instability of a liquid jet,' Proc. R. Soc. Lond. Ser. A-Math. Phys. Eng. Sci., **290**(1423), p547 (1966).
[20] E. F. Goedde and M. C. Yuen, 'Experiments on liquid jet instability,' J. Fluid Mech., **40**(3), p495 (1970).
[21] A. Rothbert, R. Richter and I. Rehberg, 'Formation of a drop: viscosity dependence of three flow regimes', New J. Phys. **5**, p59-1 (2003).
[22] J. Eggers, 'Universal pinching of 3D axisymmetric free-surface flows', **71**(21), p3458 (1993).
[23] D. T. Papageorgiou, 'On the breakup of viscous liquid threads', Phys. Fluids **7**(7), p1529 (1995).
[24] D.F. Zhang and H.A. Stone, 'Drop formation in viscous flows at a vertical capillary tube', Phys. Fluids, **9**(8), p2234 (1997).
[25] X. D. Shi, M. P. Brenner, and S. R. Nagel, 'A cascade of structure in a drop falling from a faucet,' Science **265**, p219 (1994).
[26] T. Tate, 'On the magnitude of a drop of liquid formed under different circumstances,' Philos. Mag., **27**, p176 (1864).
[27] W. D. Harkins and F. E. Brown, 'The determination of surface tension and the weight of falling drops: the surface tension of water and benzene by the capillary height method,' J. Am. Chem. Soc., **41**, p499 (1919).
[28] M. C. Wilkinson, 'Extended use of, and comments on, the drop-weight (drop-volume) technique for the determination of surface and interfacial tensions', J. Colloid Interface Sci., **40**, p14 (1972).
[29] L. Rayleigh, 'Investigations in capillarity', Philos. Mag., **48** ,p321 (1899).
[30]A. Ferguson, 'Some notes on the drop-weight method for the measurement of surface tension', J. Sci. Instrum., **6**, p163 (1929).
[31] O. E. Yildrim, Q. Xu and O. A. Basaran, 'Analysis of the drop weight method', Phys. Fluids **17**(6) 062107 (2005).

[11] Unable to verify details by viewing the source material. Reference extracted from J. Eggers[11].

[32] J. Eggers and T. F. Dupont 'Drop formation in a one-dimensional approximation of the Navier-Stokes equation', J. Fluid Mech., **262**, p205 (1994).
[33] X. Zhang and O. A. Basaran 'An experimental study of dynamics of drop formation', Phys. Fluids, **7**(6), p1184 (1995).
[34] Lord Kelvin, 'Oscillations of a liquid sphere' Mathematical papers, **3**, p 384 (1890).
[35] H. Lamb, Hydrodynamics, 6th edn. Cambridge University Press (1932).
[36] G. J. Schoessow and K. J. Baumeister, 'Liquid drop model vibrations and simulated fission', Chem. Engng. Prog. Symp. Ser., **62**, p47 (1966).
[37] A. Prosperetti, 'Free-oscillations of drops and bubbles: the initial value problem', J. Fluid Mech, **100**, p333 (1980).
[38] O. Reynolds, 'On the action of the rain to calm the sea', Papers on Mechanical and Physical Subjects, **1**, p86 (1900).
[39] A. M. Worthington, 'On the forms assumed by drops of liquids falling vertically on a horizontal plate', Proc. Roy. Soc. Lond., **25**, p261 (1876).
[40] H.*E.* Edgerton and J.R. Killian, 'Flash!: Seeing the Unseen By Ultra High-speed Photography', Hale-Cushman & Flint, Boston, (1939).
[41] C. D. Stow and M. G. Hadfield, 'An experimental investigation of fluid-flow resulting from the impact of a water drop with an unyielding dry surface', Proc. R. Soc. London Ser. A-Math. Phys. Eng. Sci., **373** , p419 (1981).
[42] S. Chandra and C. T. Avedisian, 'On the collision of a droplet with a solid surface', Proc. R. Soc. Lond. Ser. A-Math. Phys. Eng. Sci., **432**, p13 (1991).
[43] M. Pasandideh Fard, Y. M. Qiao, S. Chandra, 'Capillary effects during droplet impact on a solid surface', Phys. Fluids, **8**, p650 (1996).
[44] C. Clanet, C. Beguin, D. Richard, 'Maximal deformation of an impacting drop', J. Fluid Mech., **517**, p199 (2004).
[45] B. L. Scheller and D. W. Bousfield, 'Newtonian drop impact with a solid-surface', Aiche J., **41**, p1357 (1995).
[46] I. V. Roisman, R. Rioboo, and C. Tropea, 'Normal impact of a liquid drop on a dry surface: model for spreading and receding', Proc. R. Soc. London Ser. A-Math. Phys. Eng. Sci., **458**, p1411 (2002).
[47] T. Mao, D.C.S. Kuhn, and H. Tran, 'Spread and rebound of liquid droplets upon impact on flat surfaces', Aiche J. **43**, p2169 (1997).
[48]P. Attané, F. Girard and V. Morin, 'An energy balance approach of the dynamics of drop impact on a solid surface', Phys. Fluids. **19**, 012101 (2007).
[49] S.E. Bechtel, D.B. Bogy and F.E. Talke, 'Impact of a liquid drop against a flat surface', IBM J. Res. Develop., **25**, p963 (1981).
[50] A. Bejan and D. Gobin, 'Constructal theory of droplet impact geometry', Int. J. Heat Mass Transfer. **49**(15-16), p2412 (2006).
[51] T. Bennett and D. Poulikakos, 'Splat-quench solidification: estimating the maximum spreading of a droplet impacting a solid surface', J. Mater. Sci. **28**, p963 (1993).
[52] L. Cheng, 'Dynamic spreading of drops impacting onto a solid surface', Ind. Eng. Chem. Process Des. Div., **16**(2), p192 (1997).
[53] R.E. Ford and C.G.L. Furmidge, 'Impact and spreading of spray drops on foliar surfaces', Wetting. Soc. Chem. Industry Monograph. **25**,p417 (1967).
[54] H. Fukanuma and A. Ohmori, 'Behaviour of molten droplets impinging on flat surfaces', Proceedings of the 7th National Thermal Spray Conference, p563 (1994).
[55] H.-Y. Kim and J.-H. Chun, 'The recoiling of liquid droplets upon collision with solid surfaces', Phys. Fluids, **13**, p643 (2001).
[56] T. Kurabayashi, T. Karasawa and K. Iida, 'Impact of liquid droplets on a solid surface', Japan Soc. Mech. Eng. **175**, p153 (1967).
[57] M. Rein, 'Phenomena of liquid-drop impact on solid and liquid surfaces', Fluid Dyn. Res. **12**(2), p61 (1993).
[58] R. Rioboo, M. Marengo and C. Tropea, 'Time evolution of liquid drop impact onto solid, dry surfaces', Exp. Fluids, **33**, p112 (2002).
[59] M.H. Shi and J.C. Chen, 'Behaviour of a liquid droplet impinging on a solid surface', 1983 Winter Annual Meeting Preprint **83**-WA/HT/104 (1983).
[60] B.L. Scheller, 'Drop formation and the spreading behaviour of Newtonian and shear-thinning liquid drops impacting a solid surface, Ph.D Thesis, Univ. of Maine, Orono (1993).

[61]S. Sikalo, M. Marengo, C. Tropea and E.N. Ganic, 'Analysis of impact of droplets on horizontal surfaces', Exp. Therm. Fluid Sci., **25**, p503 (2002).
[62] A.L. Yarin, 'Drop impact dynamics: Splashing, spreading, receding, bouncing', Annu. Rev. Fluid Mech. **38**, p159 (2006).
[63] J. Fukai, Z. Zhao, D. Poulikakos, C. M. Megaridis and O. Miyatake, 'Modeling of the deformation of a liquid droplet impinging upon a flat surface', Phys. Fluids A **5**(11), p2588 (1993).
[64] A. Asai, M. Shioya, S. Hirasawa and T. Okazaki, 'Impact of an ink drop on paper', J. Imaging Sci. Technol. **37**, p205 (1993).
[65] J. Fukai, Y. Shiiba, T. Yamamoto, O. Miyatake, D. Poulikakos, C.M. Megaridis and Z. Zhao, 'Wetting effects on the spreading of a liquid droplet colliding with a flat surface – experiment and modeling', Phys. Fluids **7**, p236 (1995).
[66] C. Ukiwe and D. Kwok, 'On the maximum spreading diameter of impacting droplets on well-prepared solid surfaces', Langmuir, **21**, p266 (2005).
[67] J. J. Cooper-White, R. C. Crooks, and D. V. Boger, 'A drop impact study of worm-like viscoelastic surfactant solutions', Colloid Surf. A-Physicochem. Eng. Asp., **210**, p105 (2002).
[68] X. G. Zhang and O. A. Basaran, 'Dynamic surface tension effects in impact of a drop with a solid surface', J. Colloid Interface Sci., **187**, p166 (1997).
[69] R. Crooks, J. Cooper-White, and D. V. Boger, 'The role of dynamic surface tension and elasticity on the dynamics of drop impact', Chem. Eng. Sci. **56**, p5575 (2001).
[70] N. Mourougou-Candoni, B. Prunet-Foch, F. Legay, M. Vignes-Adler and K. Wong, 'Influence of dynamic surface tension on the spreading of surfactant solution droplets impacting onto a low-surface-energy solid substrate', J. Colloid Interface Sci., **192**, p129 (1997).
[71] S. Sikalo and E. N. Ganic, 'Phenomena of droplet-surface interactions', Exp. Therm Fluid Sci., **31,** p97 (2006).
[72] A. S. Moita and A. L. N. Moreira, 'The deformation of single droplets impacting onto a flat surface', J. Fuels Lubricants, **2002-01-2749** (2002).
[73] K. Range and F. Feuillebois, 'Influence of surface roughness on liquid drop impact', J. Colloid Interface Sci., **203,** p16 (1998).
[74] W.M. Healy, J.G. Hartley and S.I. Abdel-Khalik, 'Surface wetting effects on the spreading of liquid droplets impacting a solid surface at low Weber numbers', Int. J. Heat Mass Tran., **44**, p235 (2000).
[75] J. G. Leidenfrost 'De aquae communis nonullis qualitatibus tractatus—On the fixation of water in divers fire. A tract about some qualities of common water'(translated into English by C. Wares), Int. J. Heat Mass Trans., **9**, p1167 (1966).
[76] W.-J. Yang, 'Theory on vaporization and combustion of liquid drops of pure substances and binary mixtures on heated surfaces', Institute of Space and Aeronautical Science, Report 535 (1975).
[77] V. Bertola, ' Drop impact on a hot surface: effect of a polymer additive', Exp. Fluids, **37**, p653 (2004).
[78] J.D. Naber, 'Droplet impinging on a heated surface', Ph.D. Thesis, University of Wisconsin (1992).
[79] J. Madjeski, 'Solidification of droplets on a cold surface', Int. J. Heat Mass Transfer, **19**, p1009 (1976).
[80] H. Fukanuma and A. Ohmori, 'Behaviour of molten droplets impinging on flat surfaces', Proceedings of the 7th National Thermal Spray Conference, p563 (1994).
[81] R. Bhola and S. Chandra, 'Freezing of droplets colliding with a cold surface', ASME HTD, **306**, p181 (1995).
[82] R. Bhola and S. Chandra, 'Parameters controlling solidification of molten wax droplets falling on a solid surface', J. Materials Sci., **34**, p4883 (1999).
[83] L. Xu, W. W. Zhang and S. R. Nagel, 'Drop splashing on a dry smooth surface', Phys. Rev. Lett., **94**(18) 184505 (2005).
[84] R. L. Vander Wal, G. M. Berger and S. D. Mozes, 'The splash/non-splash boundary upon a dry surface and thin film fluid', Exp. Fluids, **40**, p53 (2006).
[85] A. Prosperetti and H. N. Oguz, 'The impact of drops on liquid surfaces and the underwater noise of rain', Annu. Rev. Fluid Mech., **25**, p577 (1993).
[86] A. Rozhkov, B. Prunet-Foch and M. Vignes-Adler, 'Impact of water on small targets', Phys. Fluids **14**, p3485 (2002).
[87] T. C. Avedisian and J. Koplik, 'Leidenfrost boiling of methanol droplets on hot porous ceramic surfaces', Int J. Heat Mass Trans., **30**(2), p379 (1987).
[88] J. S. Uehara, M. A. Ambroso, R. P. Ojha and D. J. Durian, 'Low-speed impact craters in loose granular media', Phys. Rev. Lett., **90**(19), 4301-1 (2003).

[89] R. Rioboo, C. Tropea and M. Marengo, 'Outcomes from a drop impact on solid surfaces', At. Sprays, **11** p155 (2001).
[90] G. K. Batchelor, 'An introduction to fluid dynamics', Cambridge University Press (1967).
[91] T. A. Elliot and D. M. Ford, 'Dynamic contact angles' J. Chem. Soc., Faraday Transactions 1, p1814 (1972).
[92] G. E. P. Elliot and A. C. Riddiford, 'Dynamic contact angles): I-The effect of impressed motion', J. Colloid Interface Sci., **23**, p389 (1967).
[93] K. F. Loehr, 'Etalement et eclatement de gouettes', Diplom de Doctorat de l'Universite Pierre et Marie Curie, Paris, (1990).
[94] F. H. Harlow and J. P. Shannon, 'The splash of a liquid drop', J. Appl Phys., **38**(10), p3855 (1967).
[95] P. Savic and G. T. Boult, 'The fluid flow associated with the impact of liquid drops with solid surfaces', National Research Council of Canada. Report No. Mt-26 (1955).
[96] Z. Levin and P. V. Hobbs, 'Splashing of water drops on solid and wetted surfaces: Hydrodynamics and charge separation', Phil. Trans. R. Soc. London A, **269**, p555 (1971).
[97] C. D. Stow and R. D. Stainer, 'The physical products of a splashing water drop', J. Meteorological Soc. Japan, **55**(5), p518 (1981).
[98] D. Bartolo, C. Josserand and D. Bonn, 'Retraction dynamics of aqueous drops upon impact on non-wetting surfaces', J. Fluid Mech., **545**, p329 (2005).
[99] P. G. De Gennes, 'Wetting: statics and dynamics', Rev. Mod. Phys., **57**(3), p827 (1985).
[100]A.-L. Biance, F. Chevy, C. Clanet, G. Lagubeau and D. Quere, 'On the elasticity of an inertial shock', J. Fluid Mech., **554**, p47 (2006).
[101] S. Schiaffino and A. A. Sonin, 'Molten droplet deposition and solidification at low Weber numbers', Phys. Fluids, **9**(11), p3172 (1997).
[102] T. Kurabayashi, T. Karasawa and K. Iida, 'Impact of liquid droplets on a solid surface', Preprints No. 175, Japan Society of Mechanical Engineers, p153 (1967).
[103]O.G. Engel, 'Waterdrop collisions with solid surfaces, *J. Res. NBS* **54**(5), p281 (1955).
[104] Z.-N. Wu, 'Modelisation et calcule implicite multidomaine d'ecoulements diphasiques gaz-gouttelettes', PhD Thesis, Universite Pierre et Marie Curie (1992).
[105] C. H. R. Mundo, M Sommerfeld and C Tropea, 'Droplet-wall collisions: experimental studies of the deformation and breakup process', Int J Multiphase Flow, **21**, p151 (1995).
[106] P. Walzel, 'Zerteilgrenze beim Tropfenprall' Chem. Int. Tech., **52**(4), p338 (1980).
[107] G. E. Cossali, A Coghe and M. Marengo, 'The impact of a single drop on a wetted solid surface' Exp. Fluids **22**, p463 (1997).
[108] L. H. J. Wachters and N. A. J. Westerling, 'The heat transfer from a hot wall to impinging water drops in the spheroidal state', Chem. Eng. Sci., **21**, p1047 (1966).
[109] V. Bertola and K. Sefiane, 'The reflection of liquid droplets off hot surfaces', Proc. 23rd UIT National Heat Transfer Conference, Parma, Italy, June 20-22, (2005).
[110] A.-B. Wang, C.-H. Lin and C.-C. Chen, 'The critical temperature of dry impact for tiny droplet impinging on a heated surface', Phys of Fluids, **12**(6), p1622 (2000).
[111] S.C. Yao and K. Y. Cai, 'The dynamics and Leidenfrost temperature of drops impinging on a hot surface at small angles', Experimental Thermal and Fluid Sci., **1**, p363 (1988).
[112] M.L. Sawyer, S. M. Jeter and S. I. Abdel-Khalik., 'A critical heat flux correlation for droplet impact cooling', Int. J. Heat Mass Tranfer., **40**(9), p2123 (1997).
[113] C. Marangoni, 'Uber die Ausbreitung der tropfen einer Flussigkeit auf der Oberflache einer anderen', Ann. Phys. (Leipzig), **143,** p.337 (1871).
[114] C. D. Dushkin and T. H. Iliev, 'Dynamic surface tension of micellar solutions studied by the maximum bubble pressure method: 2. Theory of the solutions below C.M.C.', Colloid Polymer Science, **272**, p1157 (1994).
[115] G. Geeraerts and P. Joos, 'Dynamic surface tension of micellar Triton X-100 solutions', Colloids Surf. A, **90**, p149 (1994).
[116] N. Mourougou-Candoni, B. Prunet-Foch, F. Legay and M. Vignes-Adler, 'Retraction phenomena of surfactant solution drops upon impact on a solid substrate of low surface energy', American Chemical Soc., **15**(19), p6563 (1999).
[117] J. Lampe, R. DiLalla, J. Grimaldi and J. P. Rothstein, 'Impact dynamics of drops on thin films of viscoelastic wormlike micelle', J. J. Non-Newtonian Fluid Mech., **125**(1), p11 (2005).
[118] R. N. Wenzel, 'Resistance of solid surface to wetting by water', Ind. Eng. Chem., **28**, p988 (1936).

[119] W. D. Harkins and A. Feldman, 'Films. The spreading of liquids and the spreading coefficient', J. Am. Chem. Soc., **44,** p2665, (1922).
[120] J. S. Rowlinson and B. Widom, 'Molecular theory of capillarity', Clarendon press: Oxford (1982).
[121] J. Hyppia, 'Measurement of Rates of Spread of Solutions of Surface Active Agents', Anal. Chem., 20, p1039 (1948).
[122] M. Lelah and A. Marmur, 'Spreading kinetics of drops on glass', J. Colloid Interface Sci., **82**, p518 (1981).
[123] L. H. Tanner, 'The spreading of silicone oil drops on horizontal surfaces', J. Phys. D: Appl. Phys., **12**, p1473 (1979).
[124] R. Hoffman, 'A study of the advancing interface. I. Interface shape in liquid—gas systems', J. Colloid Interface Sci., **50**, p228 (1975).
[125] V. E. Dussan and S. Davis., 'On the motion of a fluid-fluid interface along a solid surface', J. Fluid Mech., **65**, p71 (1974).
[126] M. Renardy, 'Mathematical analysis of viscoelastic flows', Ann. Rev. Fluid Mech., **21** p21 (1989).
[127] R. B. Bird, R. C. Armstrong and O. Hassager, 'Dynamics of polymeric liquids: Volume 1 Fluid Mechanics', John Wiley and Sons (1977).
[128] D. V. Boger and R. Crooks, 'Influence of fluid elasticity on drops impacting on dry surfaces', J. Rheol. **44**(4), p973 (2000).
[129] M. M. Cross, 'Rheology of non-Newtonian fluids: a new flow equation for pseudoplastic systems', J. Colloid Sci, **20**, p417 (1965).
[130] P. J. Carreau, Ph.D Thesis, University of Wisconsin, Madison (1968).
[131] M. Reiner, 'Deformation, strain and flow: an elementary introduction to rheology', London, H. K. Lewis (1960).
[132] C. W. Macosko, 'Rheology principles, measurements and applications', Wiley-VCH (1994).
[133] V. Bertola, 'Wicking with a yield-stress fluid', J. Phys. Condens. Matter, **21**, 035107, p1 (2009).
[134] W. H. Herschel and R. Bulkley, 'Konsistenzmessungen von Gummi-Benzol-Lösungen', Kolloid Z., **39**, p291 (1926).
[135] H. A. Barnes, "The yield stress - a review or 'παητα ρει' - everything flows?," J. Non-Newton. Fluid Mech. **81**, p133 (1999).
[136] E. C. Bingham, "An investigation of the laws of platic flow," U.S. Bur. of Standards Bull. **13**, p309 (1916).
[137] N. Casson, 'Rheology of disperse systems', C. C. Mill, Ed.: Pergamon:London, p84 (1959).
[138] P. Coussot, 'Rheophysics of pastes: a review of microscopic modeling approaches' Royal Soc. Chem.: Soft matter, **3**, p528 (2007).
[139] Q. D Nguyen and D. V. Boger, 'Measuring the flow properties of yield stress fluids', Annu. Rev. Fluid Mech., **24**, p47 (1992).
[140] T. Schwedoff, 'La rigidite des fluides', Rapp. Congress Phys. **1**, p478 (1900).
[141] S Blair, 'On the Nature of ``Yield-Value"', J. Applied Phys. **4**, p113 (1933).
[142] J. Ferguson and Z. Kemblowski, 'Applied Fluid Rheology', Kluwer Academic Pub (1991).
[143] A.Ya. Malkin, 'Rheology Fundamentals', ChemTec Publishing, Toronto-Scarborough, (1994).
[144] M. Reiner, *'The Deborah Number'*, Physics Today, **17**(1), p62 (1964).
[145] M. R. Davidson and J. J. Cooper-White, 'Pendant drop formation of shear-thinning and yield stress fluids', Appl. Math. Model. **30**, p1392 (2006).
[146] P. Coussot and F. Gaulard, 'Gravity flow instability of viscoplastic materials: The ketchup drip', Phys. Rev. E **72**, p5 (2005).
[147] M. A. M. Al Khatib and S. D. R. Wilson, 'Slow dripping of yield-stress fluids', J. Fluid. Eng., **127**, p687 (2005).
[148] S. Nigen, "Experimental investigation of the impact of an (apparent) yield-stress material," Atom. Sprays **15**, p103 (2005).
[149] D. A. Weiss, A. Reinl and D. M. Binding, 'Spray impact on solid walls on non-Newtonian fluids, including yield stress and thixotropic behaviour', XXI ICTAM (2004).
[150] P. Coussot, Q. D. Nguyen, H. T. Huynh and D. Bonn, 'Avalanche behaviour in yield stress fluids', Phys. Rev. Lett., **88**(17), p5501 (2002).
[151] N. Maleki-Jirsaraei, A. Lindner, S. Rouhani and D. Bonn, 'Saffman-Taylor instability in yield-stress fluids' J. Phys.: Condens. Matter, **17**, S1219 (2005).
[152] A. Carre and F. Eustache, 'Spreading kinetics of shear-thinning fluids in wetting and dewetting modes', J. Am. Chem. Soc., 16, p2936 (2000).

[153] A.-M. Cazabat, M. A. Cohen-Stuart, 'Dynamics of wetting: effects of surface roughness', J. Phys Chem., 90(22), p5845 (1986).
[154] V.M. Starov, A.N. Tyatyushkin, M.G. Velarde and S.A. Zhdanov, 'Spreading of non-Newtonian liquids over solid substrates'*, J.* Colloid Interface ***Sci.,*** **257**(2)**,** p284 (2003).
[155] D. E. Weidner and L, W. Schwartz, 'Contact-line motion of shear-thinning liquids', Phys. Fluids, **6**(11), p3535 (1994).
[156] S. Rafaï, D. Bonn and A. Boudaoud, 'Spreading of non newtonian fluids on hydrophilic surfaces', J. Fluid Mech., **513**, p77 (2004).
[157] K. L. Mittal, 'Determination of CMC of Polysorbate 20 in aqueous-solution by surface tension method', J. Pharm. Sci. **61**, p1334 (1972).
[158] Ecole Polytechnique Federale de Lausanne, Big>Drop software downloaded from http://bigwww.epfl.ch/demo/dropanalysis/.
[159] Y. Amarouchene, D. Bonn, J. Meunier, and H. Kellay, 'Inhibition of the Finite-Time Singularity during Droplet Fission of a Polymeric Fluid', Phys. Rev. Lett., **86**(16), p3558 (2001).
[160]C. R. Beverly and R. I. Tanner, 'Numerical analysis of three-dimensional Bingham plastic flow', J. Non-Newtonian Fluid Mech., **47**, p211 (1992).
[161] D. Richard, C. Clanet and D. Quere. 'Contact time of a bouncing drop',. Nature, **417**, p811 (2002).
[162] S. Biehl, R. Danzebrink, P. Oliveira and M.A. Aegerter, 'Refractive Microlens Fabrication by Ink-Jet Process' Journal of Sol-Gel Science and Technology, **13**(1-3), p177 (1998).
[163] R. Von Mises, 'Mechanik der Festen Korper im plastisch deformablen Zustand'. Göttin. Nachr. Math. Phys., **1**, p582 (1913).
[164] R. G. Larson and J. J. Magda, 'Coil-stretch transitions in mixed shear and extensional flows of dilute polymer solutions', Macromolecules, **22**, p3044 (1989).
[165] C. Wagner, Y. Amarouchene, Daniel Bonn and J. Eggers, 'Droplet Detachment and Satellite Bead Formation in Viscoelastic Fluids', Phys. Rev. Lett., **95**, 164504 (2005).
[166] I. V. Roisman, E. Berberović and C. Tropea, 'Inertia dominated drop collisions. 1. On the universal flow in the lamella'. Phys. Fluids, **21**, 052103 (2009).
[167] R. J. A. Hill and L. Eaves, 'Nonaxisymmetric Shapes of a Magnetically Levitated and SpinningWater Droplet', Phys. Rev. Lett. **101**, 234501 (2008).
[168] S. I. Betelu´ and M. A. Fontelos, ' Capillarity driven spreading of power-law fluids', Appl. Math. Lett., **16**, p1315 (2003).
[169] D. A. Weiss and A. L. Yarin, 'Single drop impact onto liquid films: neck distortion, jetting, tiny bubble entrainment, and crown formation', J. Fluid Mech., **385**, p229 (1999).
[170] C. Weber, 'Zum zerfall eines fluessigkeitsstrahles', Z. Angew. Math. Mech., **2**, p136 1931.
[171] M. J. Ruijter, T. D. Blake and J. De Coninck, 'Dynamic wetting studied my molecular modeling simulations of droplet spreading', Langmuir, **15**, p7836 (1999).

Appendix A

Appendix A – Acrylic Case

(all dimensions in mm)

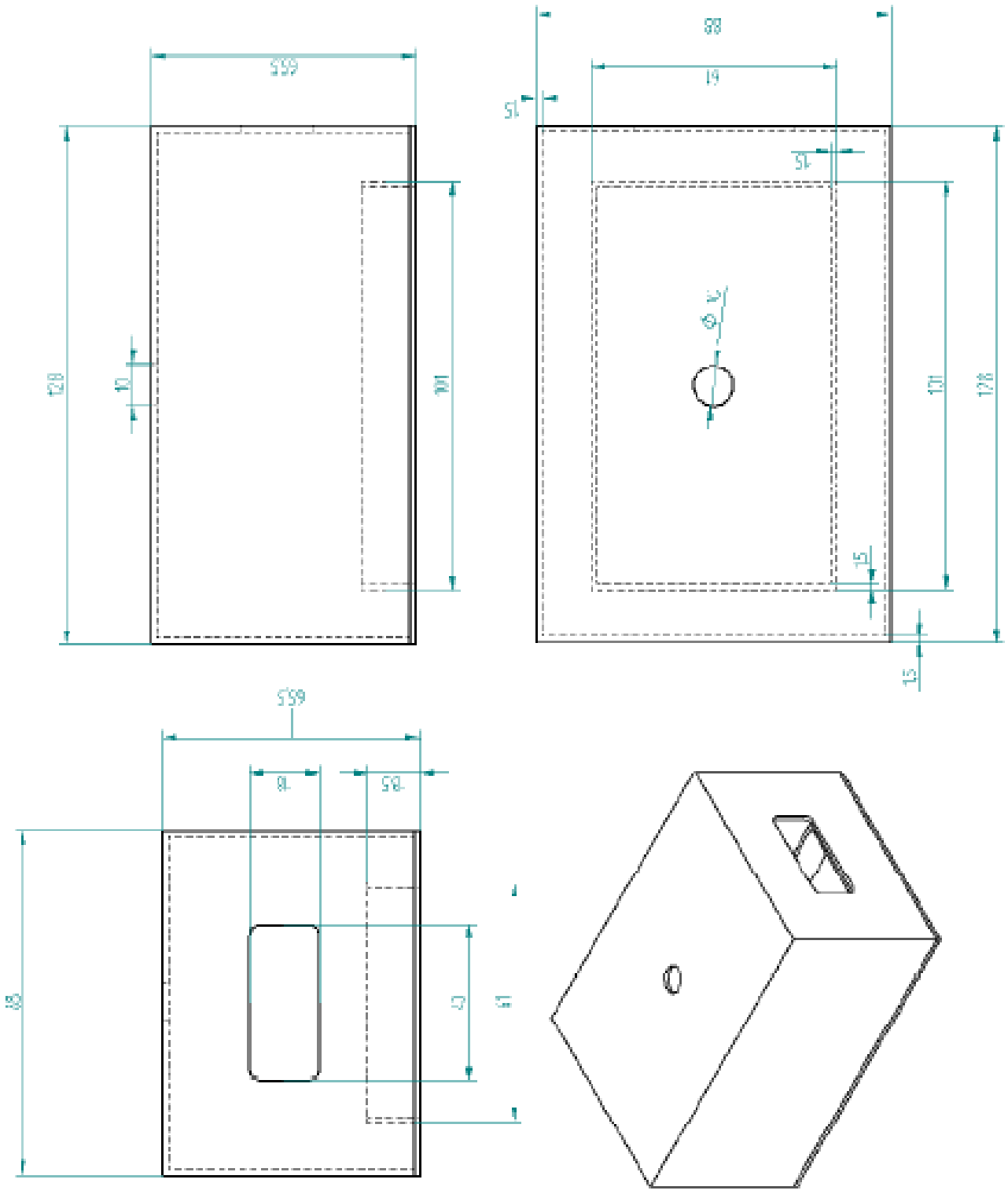
65.5
128
10
101
88
51
15
61
Ø 12
171
178
15
15
65.5
18
58
88
57
61

Appendix B

Labview Post-processing routines:

Labview post-processing routine schematic – Figure [19]

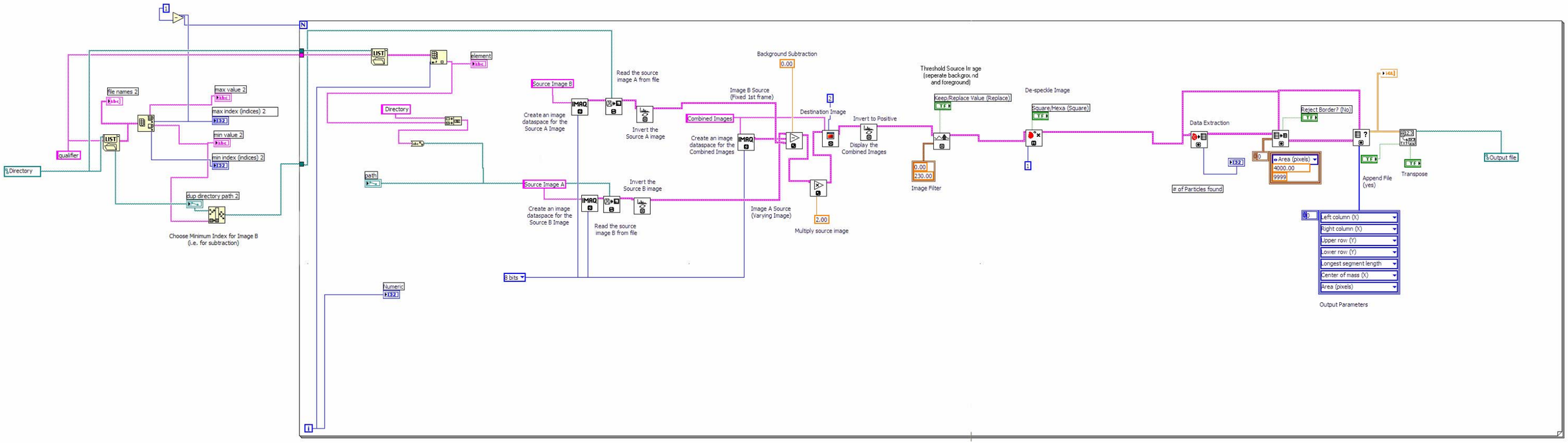

Labview post-processing routine schematic – Figure [20]

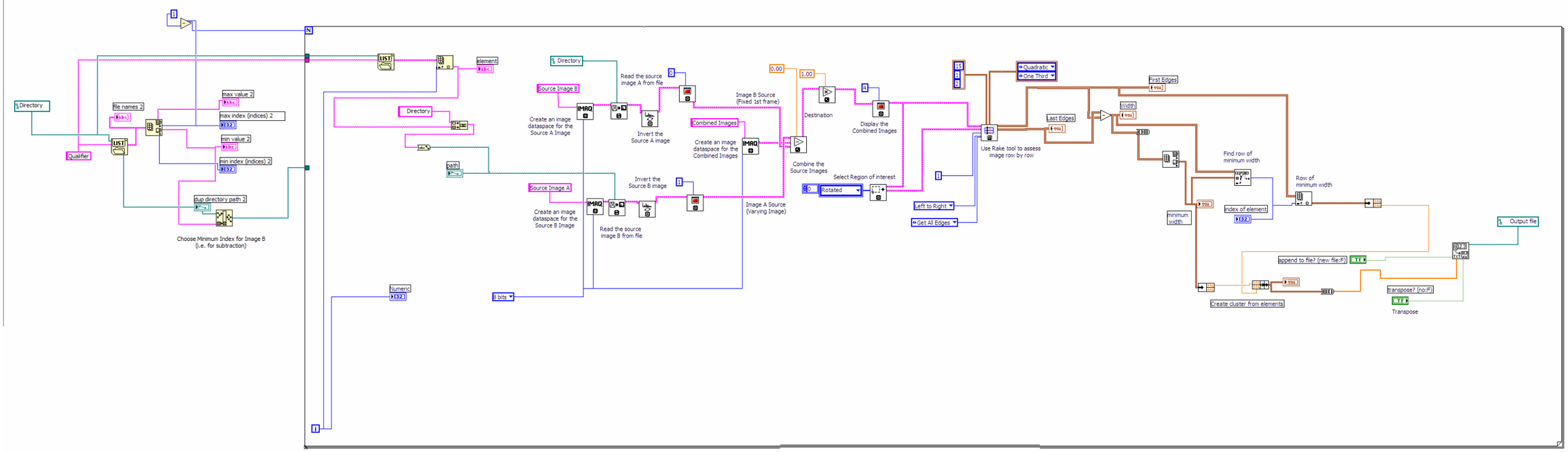

Glossary of useful terms

Glossary of useful terms

Please consult the nomenclature for a description of all terms used in equations.

Bingham number

Non-dimensional number characterising the ratio of yield-stress to capillary forces.

$$Bm = \frac{\tau_c D_E}{\mu\, v_z}$$

Bingham model (rheology)

The Bingham rheological model assumes a linearly elastic solid-like behaviour for applied shear-stresses less than the yield-stress. Above the yield stress, the viscoplastic fluid exhibits Newtonian fluid flow:

$$\tau = G\gamma \quad for\ \tau \le \tau_c$$
$$\tau = \tau_c + \mu\dot{\gamma} \quad for\ \tau \ge \tau_c$$

Bingham-Capillary number (shear)

A dimensionless number that is the ratio of the yield-stress to the capillary pressure.

$$\hat{B} = \frac{\tau_c D_E}{\sigma}$$

This term is the product of the dimensionless Capillary and Bingham numbers.

Bingham-Capillary number (extensional)

This term is more significant for extensional flows such as those found in the neck filament during drop detachment. The dimensionless term is the ratio of the extensional yield stress to capillary pressure. Based on von-Mises criterion. The extensional yield-stress of a viscoplastic fluid is $\sqrt{3}$ times larger than the shear-stress in purely shear flow. The term is thus a modification of the Bingham-Capillary number, such that:

$$\hat{B}_E = \frac{\zeta_{crit} D_E}{\sigma} = \frac{\sqrt{3}\tau_c D_E}{\sigma}$$

Capillary length

A drop with a radius smaller than the capillary length can be considered a low Bond number surface, wherein gravitational effects are not dominant. A sessile drop on a solid surface will take the shape of spherical cap; the solution to the Young equation with gravity absent. Drops with a radius greater than the capillary length will differ increasingly from typical impact behaviour.

$$a = \sqrt{\frac{\sigma}{\rho g}}$$

Capillary number

A dimensionless number characterising the ratio of viscous to capillary forces.

$$Ca = \frac{v_x . \mu}{\sigma}$$

Carreau model (rheology)

A common model used for shear-thinning fluids. This model defines the liquid as having low and high shear rate Newtonian regions. In between these regions, fluid exhibits shear-thinning. This model is nearly identical to the Cross model (the Cross model is a simplification of this model), with only one extra term. It has been found that the utilisation of this extra term, a, improves the fit with experimental data.

$$\frac{\mu - \mu_\infty}{\mu_0 - \mu_\infty} = \frac{1}{\left[1 + (C\dot{\gamma})^a\right]^{(1-m)/a}}$$

Casson model (rheology)

The Casson model is similar to the Bingham model, only with a more gradual transition from the Newtonian to the solid-like regime.

$$\sqrt{\tau} = \sqrt{\tau_c} + \sqrt{\mu\dot{\gamma}} \quad for\ \tau \geq \tau_c$$

Complex fluid - see non-Newtonian fluid

Cross model (rheology)

A common model used for shear-thinning fluids. This model defines the liquid as having low and high shear rate Newtonian regions. In between these regions, fluid exhibits shear-thinning. This model is a simplification of the Carreau model.

$$\frac{\mu - \mu_\infty}{\mu_0 - \mu_\infty} = \frac{1}{1 + (C\dot{\gamma})^{1-m}}$$

Deborah number

A dimensionless number used in rheology to characterize how "fluid" a material is. It is defined as the ratio of the material relaxation time (characterizing the intrinsic fluidity of the material) to the characteristic time scale of the experiment probing the response of the material. The smaller the Deborah number, the more fluid the material appears.

Dimensionless number

As the name suggests, a dimensionless number has no dimensional units and usually describes a ratio of forces (e.g. surface tension, yield stress, viscous or inertial) or timescales (see Deborah number). These terms are usually used to characterise fluid behaviour.

Dynamic surface tension

All fluids have a surface tension, which acts at the interface of the fluid. Whilst the magnitude of the surface tension does not ordinarily vary, the addition of surfactants into the fluid can alter surface energies. Surfactants have a hydrophilic head and a hydrophilic tail. They find it energetically favourable to move to the fluid interface. This results in a reduction of surface energy. In equilibrium, the fluid interface has a constant surface tension value, however non-equilibrium situations can exist where new surface regions are formed more quickly than the surfactants can migrate to the interface and the surface tension may vary with position. Eventually the surfactant/fluid system will form an equilibrium. The temporal variation in surface energy is called dynamic surface tension.

Ellis model (rheology)

Shear-thinning models such as the Cross or Carreau model define low and high shear Newtonian regimes. The Ellis model also defines a low shear Newtonian regime, however now, the fluid viscosity tends to zero at high shear-rates. This model is typically used for materials such as polymer melts where the high shear rate Newtonian region is not observed. The model is also typically expressed in terms of a stress variable.

$$\frac{\mu_0}{\mu} = 1 + \left(\frac{\tau}{\tau_{1/2}} \right)^{n-1}$$

Herschel-Bulkley model (rheology)

This is the most commonly used rheological model for viscoplastic fluids. Below the yield-stress, the fluid is modeled as a linearly elastic solid. Above the yield stress, the fluid is modeled as a shear-thinning fluid.

$$\tau = G\gamma \qquad for\ \tau < \tau_c$$
$$\tau = \tau_c + K\dot{\gamma}^n \qquad for\ \tau \geq \tau_c$$

Newtonian fluid

A fluid where the ratio of applied shear-stress to shear-rate, called the viscosity, is constant.

Non-Newtonian fluid

A fluid where the viscosity (the relationship between shear-stress and shear-rate) is not constant (unlike a Newtonian fluid). The most common fluids are

- *Shear-thinning/Pseudoplastic fluid* – Apparent viscosity increases with increased stress
- *Shear-thickening/Dilatant fluid* – Apparent viscosity increases with increased stress
- *Thixotropic fluid* – Apparent viscosity decreases with duration of stress
- *Rheopectic fluid* – Apparent viscosity increases with duration of stress
- *Viscoelastic fluid* – A fluid which is viscous but which also exhibits certain elastic properties such as the ability to store energy of deformation.
- *Viscoplastic fluid* – exhibits solid like characteristics when the applied shear-stress is below the yield-stress. For applied shear-stresses above the yield-stress, fluid-like behaviour is observed. Typically this fluid behaviour is shear-thinning.

Ohnesorge number

A dimensionless number characterising the ratio of viscous to capillary forces in terms of the drop size.

$$Oh = \frac{\mu}{(\rho.\sigma.D_E)^{1/2}} = \frac{We^{1/2}}{\mathrm{Re}}$$

Power law model (rheology)

The most simple rheological model describing shear-thinning fluid behaviour. Unlike the Cross and Carreau models, this model does not describe low or high shear Newtonian regimes.

$$\mu = K\dot{\gamma}^{n-1}$$

Reynolds number

A dimensionless number characterizing the ratio of inertial to viscous forces.

$$\mathrm{Re} = \frac{\rho.D_E.v_z}{\mu}$$

Shear-thinning - see Non-Newtonian fluid

Surfactant – see Dynamic surface tension

Yield-stress (shear and extensional)

This defines the shear or tensile (for extensional flow) stress above which a viscoplastic fluid will exhibit fluid-like properties

Von-Mises yield criterion

The von-Mises yield criterion states that the yielding of plastic materials begins when the second deviatoric stress tensor reaches a critical value. In the case of the generalized Herschel-Bulkley rheological model, this is the square of the yield-stress magnitude. Moreover, the shear stress at the onset of yielding is $\sqrt{3}$ times smaller than the tensile stress in the case of simple tension at the yield criterion.

$$\zeta_{crit} = \sqrt{3}\tau_c$$

Weber number

A dimensionless number characterising the ratio of inertial to capillary forces.

$$We = \frac{\rho . D_E . v_z^{\,2}}{\sigma}$$

Wettability

A fully wetting substrate is one in which a fluid drop will readily spread on the surface. Accordingly, a partially wettable substrate is one in which a fluid drop will (if the drop radius is less than the capillary length) form a spherical cap shape. The final shape of the drop on the surface will depend on the drop size and the fluid and substrate surface energies.